

**Studies on the Structural Organizations and  
Dynamics of Some Deep Eutectic Solvents and Room  
Temperature Ionic Liquids in the Absence and  
Presence of Electrolyte and Biomolecule by Various  
Spectroscopic Methods**

*By*

**SAHADEV BARIK  
CHEM11201804005**

**National Institute of Science Education and Research  
Bhubaneswar, Odisha**

*A thesis submitted to the  
Board of Studies in Chemical Sciences  
In partial fulfilment of requirements  
For the degree of*

**DOCTOR OF PHILOSOPHY  
of  
HOMI BHABHA NATIONAL INSTITUTE**



**MAY, 2023**

# Homi Bhabha National Institute

## Recommendations of the Viva Voce Committee

As members of the Viva Voce Committee, we certify that we have read the dissertation prepared by Mr. Sahadev Barik entitled "*Studies on the Structural Organizations and Dynamics of Some Deep Eutectic Solvents and Room Temperature Ionic Liquids in the Absence and Presence of Electrolyte and Biomolecule by Various Spectroscopic Methods*" and recommend that it may be accepted as fulfilling the thesis requirement for the award of Degree of Doctor of Philosophy.

Chairman –

(Name: Dr. Sanjib Kar)

Date: 09/10/2023

Guide / Convener –

(Name: Dr. Moloy Sarkar)

Date: 09/10/2023

Co-guide –

Examiner –

(Name: Dr. Ashok Kumar Mishra) Date - 09/10/2023

Member 1 –

(Name: Dr. Himansu Sekhar Biswal)

Date: 09/10/2023

Member 2 –

(Name: Dr. Arindam Ghosh)

Date: 09/10/2023

Member 3 –

(Name: Dr. Yatendra Singh Chaudhary)

Date: 09/10/2023

Final approval and acceptance of this thesis is contingent upon the candidate's submission of the final thesis copies to HBNI. I/We hereby certify that I/we have read this thesis prepared under my/our direction and recommend that it may be accepted as fulfilling the thesis requirement.

Date: 09/10/2023

Signature

Signature

Place: NISER Bhubaneswar Co-guide (if any)

Guide

## STATEMENT BY AUTHOR

This dissertation has been submitted in partial fulfilment of requirements for an advanced degree at Homi Bhabha National Institute (HBNI) and is deposited in the library to be made available to borrowers under rules of the HBNI. Brief quotations from this dissertation are allowable without special permission, provided that accurate acknowledgement of source is made. Requests for permission for extended quotation from or reproduction of this manuscript in whole or in part may be granted by the Competent Authority of HBNI when in his or her judgment the proposed use of the material is in the interests of scholarship. In all other instances, however, permission must be obtained from the author.

*Sahadev Barik*

**Sahadev Barik**

## DECLARATION

I, hereby declare that the investigation presented in the thesis has been carried out by me. The work is original and has not been submitted earlier as a whole or in part for a degree/diploma at this or any other Institution / University.

*Sahadev Barik*

**Sahadev Barik**

## LIST OF PUBLICATIONS

1. # **Barik, S.;** Chakraborty, M.; Sarkar, M.; How Does Addition of Lithium Salt Influence the Structure and Dynamics of Choline Chloride-Based Deep Eutectic Solvents? *J. Phys. Chem. B* **2020**, 124, 14, 2864–2878.
2. # **Barik, S.;** Chakraborty, M.; Mahapatra, A.; Sarkar, M.; Choline Chloride and Ethylene Glycol Based Deep Eutectic Solvent (DES) versus Hydroxyl Functionalized Room Temperature Ionic Liquids (RTILs): Assessing the Differences in the Microscopic Behaviour Between DES and RTILs. *Phys. Chem. Chem. Phys.*, **2022**, 24, 7093-7106.
3. # **Barik, S.;** Preeyanka, N.; Chakraborty, M.; Mahapatra, A.; Sarkar, M.; Temperature-dependent ultrafast solvation dynamics of choline chloride-based deep eutectic solvent (DES) and hydroxyl functionalized room temperature ionic liquids (RTILs): Exploring the difference in solvent response between DES and RTILs. *J. Mol. Liq.*, **2022**, 367, 120545.
4. # **Barik, S.;** Mahapatra, A.; Jena, D.; Sarkar, M.; Assessing the Impact of Increase in the Number of Hydroxyl Groups on the Microscopic Behaviors of Ammonium-based Room Temperature Ionic Liquids: A Combine Fluorescence Up-conversion, Fluorescence Correlation and NMR Spectroscopic Study. *J. Photochem. Photobiol. A*, **2023**, 437, 114505.
5. # **Barik, S.;** Mahapatra, A.; Preeyanka, N.; Sarkar, M.; Assessing the Impact of Choline Chloride and Benzyltrimethylammonium Chloride-Based Deep Eutectic Solvents on the Structure and Conformational Dynamics of Bovine Serum Albumin: A Combined Steady-State, Time-Resolved Fluorescence and Fluorescence Correlation Spectroscopic Study" *Phys. Chem. Chem. Phys.*, **2023**, 25, 20093-20108.
6. Islam, M.M.; **Barik, S.;** Sarkar, M.; Probing the Interactions of 1-Alkyl-3-methylimidazolium Tetrafluoroborate (Alkyl = Octyl, Hexyl, Butyl, and Ethyl) Ionic Liquids with Bovine Serum Albumin: An Alkyl Chain Length-Dependent Study. *J. Phys. Chem. B* **2019**, 123, 7, 1512–1526.
7. Islam, M.M.; **Barik, S.;** Preeyanka, N.; Sarkar, M.; Interaction of Lysozyme with Monocationic and Dicationic Ionic Liquids: Toward Finding a Suitable Medium for Biomacromolecules. *J. Phys. Chem. B* **2020**, 124, 6, 961–973.

8. Mahapatra, A.; Chakraborty, M.; **Barik, S.**; Sarkar, M.; Comparison between pyrrolidinium-based and imidazolium-based dicationic ionic liquids: intermolecular interaction, structural organization, and solute dynamics. *Phys. Chem. Chem. Phys.*, **2021**, 23, 21029-21041.
9. Chakraborty, M.; **Barik, S.**; Mahapatra, A.; Sarkar, M.; Binary mixtures of ionic liquids: Ideal, non-ideal, or quasi-ideal? *J. Chem. Phys.*, **2021**, 154, 224507.
10. Chakraborty, M.; **Barik, S.**; Mahapatra, A.; Sarkar, M.; Effect of Lithium-Ion on the Structural Organization of Monocationic and Dicationic Ionic Liquids. *J. Phys. Chem. B* **2021**, 125, 47, 13015–13026.
11. Majhi, D.<sup>†</sup>; Chakraborty, M.<sup>†</sup>; **Barik, S.**; Mahapatra, A.; Sarkar, M.; Understanding the Microscopic Structural Organization of Neat Ammonium Based Ionic Liquids through Resonance Energy Transfer (RET) Studies. *Chem. Phy. Impact*, **2021**, 3, 100034.
12. Mahapatra, A.; **Barik, S.**; Chakraborty, M.; Lakkoji, S.; Sarkar, M.; Assessing the Suitability of a Dicationic Ionic Liquid as a Stabilizing Material for the Storage of DNA in Aqueous Medium. *Langmuir* **2022**, 125, 47, 13015-13026.
13. Pradhan, K.C.; **Barik, S.**; Singh, B.C.; Mohapatra, P.; Kisan, H.K.; Pal, S.; Synthesis, characterization and theoretical studies of a series of Iridium (III) heteroleptic complexes with Schiff base ligands. *J. Mol. Struct.*, **2020**, 1211, 128058.
14. Pradhan, K.C.; Jadab, M.; **Barik, S.**; Behera, N.; Bag, B.; Pal, S.; Pyridine aldoxime ligation to iridium(III) centre: An innocent ancillary ligand in a series of organometallic complexes. *J. Mol. Struct.*, **2022**, 1271, 133998.
15. Maity, M.; **Barik, S.**; Biswas, R.; Natarajan, R.; Dinda, J.; N-Heterocyclic Carbene (NHC) Boosted Photoluminescence; Synthesis, Structures and Photophysical Properties of bpy/phen-Au (III)-NHC Complexes. *App. Organomet. Chem.*, **2022**, 36,10, e6854.
16. Maity, M.; **Barik, S.**; Kisan H.K.; Jana, A.; Isab A.A.; Dinda, J.; ‘Optimized Route’ to Synthesis Isoelectronic and Isostructural Au(III)- and Pt(II)-NHC Complexes; Synthesis, Structure, Spectral Properties, Electrochemistry, and Molecular Docking Studies. *New J. Chem.*, **2023**, 47, 284-296.
17. Mahapatra, A.; Samantara, A. **Barik, S.**; Sahoo, M.K.; Behera. J. N.; Sarkar, M.; Insight into the Structure and Transport Properties of Pyrrolidinium-based Geminal Dicationic-Organic Ionic Crystals: Unravelling the Role of Alkyl-Chain Length. *Soft Matter*, **2023**, 19, 3510-3518.

18. Sahu, P.; Jena, A.B.; **Barik, S.**; Kisan H.K.; Isab A.A.; Dandapat, J.; Dinda, J.; Gold(III) assisted C-N bond dissociation; Synthesis, structure, photoluminescence, and pharmacokinetic studies of 1,10/- phenanthroline-gold(III)-N-heterocyclic carbene". *J. Mol. Struct.*, **2023**, 1258, 135442.
19. Mahto, A.; Kuldeep, K.; **Barik, S.**; Gajula, R.; Sarkar, M.; Madda, J.; Enhancement of fluorescence emission intensity with metal salts in a sulfonyl hydrazide derivative of tri(biphenyl-4-yl)amine in the solid state via dipole-ion interactions: combined experimental and computational studies. *Chemistry Select*, **2023**, 8, 23, e202301601.
20. Mahapatra, A.; Ghosh, J.; **Barik S.**; Parida, S.; Sarkar, M.; Understanding the Influence of Ethylene Glycol on the Microscopic Behavior of Imidazolium-based Monocationic and Dicationic Ionic Liquid. *Chemical Physics Impact*, **2023** (Accepted).

*Sahadev Barik*

**Sahadev Barik**

## CONFERENCE/SYMPOSIUM

1. Presented poster in Trombay International Symposium on Radiation and Photochemistry 2020 (TSRP-2020) organized by Indian Society for Radiation and Photochemistry (5th to 9th January 2020).
2. Delivered oral presentation in “National Workshop on Fluorescence and Raman Spectroscopy” (FCS-2020) December 7 - 12, 2020, organized by IIT Bombay and Fluorescence Society of India.
3. Presented flash talk as a part of poster presentation at the International Conference on Advance Materials for Better Tomorrow (AMBT 2021) organized by Indian Institute of Technology (BHU), Varanasi in association with Society of Interdisciplinary research in Materials and Biology (SIRMB) from July 13th - 17th 2021.

*Sahadev Barik*

**Sahadev Barik**

**Dedicated  
to**

*My Beloved Parents*

## ACKNOWLEDGEMENT

*I want to express my sincere gratitude to my supervisor Dr. Moloy Sarkar, who has been a constant support, both professionally and personally, during my Ph.D. tenure. He helped me to grow individually as a researcher, starting from designing the projects to writing the manuscript. He made me believe that though things take time but can be achieved.*

*I would like to thank Prof. Sudhakar Panda (Director, NISER) and Prof. T.K. Chandrasekhar (Founder Director, NISER) for establishing well-equipped research facilities in NISER. I would thank Dr. Pranay Swain, (Dean of academic affairs, NISER) for understanding and supporting in various academic issues. I would also like to thank my thesis committee members: Dr. Sanjib Kar, Dr. Arindam Ghosh, Dr. Himansu Sekhar Biswal, and Dr. Yatendra Singh Chaudhary, for their valuable suggestions during my Ph.D. tenure. I also like to acknowledge my course instructor Dr. Upakarasamy Louderaj, Dr. A. Srinivasan for their useful discussion with me during my course work. I acknowledge present (Dr. Sharanappa Nembenna) and former (Dr. Himansu S. Biswal, and Dr. Alagar Srinivasan) Chairpersons (SCS) during my research tenure in NISER. I am also thankful to all other faculty members, scientific officers (Dr. Arun Sir and Dr. Priyanka mam) and the non-teaching staff of our SCS department for providing a healthy environment. I am grateful to NISER, Bhubaneswar, for providing financial support and proper infrastructure for research.*

*I extend my heartfelt gratitude to both my current and former lab members for fostering a friendly and enjoyable research environment. I extend my sincere gratitude to my former colleagues, Dr. Prabhat K. Sahu and Dr. Debashis Majhi, for their invaluable support and enlightening conversations regarding the scientific work conducted in our laboratory. My deepest gratitude goes to Dr. Muhaiminul Islam, whose guidance has greatly enriched my understanding of biological studies. Additionally, I am grateful to Manjari and Somnath bhaiya*

*for their invaluable support in the initial stages. Preeyanka didi has been a constant source of support, both in scientific and non-scientific discussions, and for that, I am truly thankful. I have created lasting and cherished memories with my fellow lab mates Amit and Debabrata, which I will always treasure. Amita's timely aid whenever I have sought it will forever be ingrained in my gratitude. I would also like to extend a special token of thanks to all the past and present Integrated M.Sc students, namely Aman, Biswa, Aditya, Nilesh, Aradhana, Dinesh, Ramya, Subhakanta, Rashmita, and Yashaswini. Working alongside all of you has been truly remarkable and has added immense value to my journey. I would like to extend a special acknowledgment to Biswa, Dinesh and Subhakant, who collaborated with me on their M.Sc projects. I also thank Dr. L. Satish for his association with me during his postdoctoral work.*

*My Ph.D. journey has been truly remarkable, thanks to the invaluable contributions of Tanmoy, Abhisek, Sam, Krishna, Subhrakant, and many others. Tanmoy, in particular, holds a special place in my heart as a brother figure, and our association will be cherished for a lifetime. The late-night discussions we had, alongside Debu and Amit, will forever remain vivid memories etched in my mind. I am immensely grateful for the special moments and connections I have forged with remarkable individuals at NISER. I would also like to express my gratitude to my dear friends Debasish and Bikash for their unwavering moral support. Our friendship dates back decades, and I am grateful for the enduring bond we share. Additionally, I would like to extend my thanks to all the teachers who have imparted knowledge during my school, college, and university days. In particular, Dr. Satyanarayan Pal and Dr. Joydev Dinda, working with you has always been a delightful experience, filled with enjoyment and growth.*

*Last but certainly not least, I am deeply grateful to my family members, whose unwavering support has made my journey peaceful and memorable. My father, Mr. Gangadhar Barik, has been a pillar of constant support, never questioning my decisions and believing in me wholeheartedly. The unconditional love and blessings from my mother, Mrs. Ahalya Barik,*

*have propelled me to reach the heights I stand at today. I am also grateful to all my sisters and brothers-in-law for their unwavering support on a personal level. In particular, I extend my heartfelt thanks to Mrs. Nandita Barik and Mr. Narayan Pradhan for introducing me to the world of science and encouraging me to pursue a career in this field. I am also indebted to all my elder cousins for their timely assistance and support, not only to me but also to my family. Their contributions have made a significant impact, for which I am forever grateful.*

*Lastly, I extend my gratitude to every person I have encountered throughout my journey. Each and every one of them, in their own unique way, has contributed to my growth and development and collectively helped me become a better version of myself.*

*Above all, I offer my heartfelt prayers and wishes for Lord Shiva to bless and take care of my beloved parents.*

*Sahadev Barik*

**Sahadev Barik**

## CONTENT

		<b>Page No.</b>
<b>SYNOPSIS</b>		<b>xvi</b>
<b>List of Schemes</b>		<b>xxix</b>
<b>List of Figures</b>		<b>xxx</b>
<b>List of Tables</b>		<b>xxxiii</b>
<b>Appendices</b>		<b>xxxv</b>
<b>Glossary of Acronyms</b>		<b>xxxvii</b>
<b>Chapter 1</b>		
<b>Introduction</b>		
1.1.	Solvents - a brief introduction	2
1.2.	Ionic Liquids (ILs)	4
1.3.	Deep eutectic solvents (DESs)	7
1.3.1	Classification of DESs	10
1.4.	General Physical Properties of RTILs and DESs	12
1.4.1	Melting Point	13
1.4.2.	Thermal Decomposition temperature	14
1.4.3.	Density	14
1.4.4.	Viscosity	15
1.4.5.	Conductivity	16
1.4.6.	Electrochemical Potential Window (EPW)	16
1.4.7	Polarity	17
1.5.	ILs versus DESs	18
1.6.	Applications of ILs and DESs	19
1.7.	Structure and Dynamics of RTILs and DESs	23
1.8.	Photophysical Process in RTILs and DESs	27
1.9.	NMR Investigations on RTILs and DESs	40
1.10.	Objective of the Thesis Work	41
1.11.	Organization of the Thesis	41
<b>Chapter 2</b>		
<b>Materials, Experimental Techniques, and Methods</b>		
2.1.	Materials	38
2.2.	Synthesis and Characterization of DESs and RTILs	46
2.2.1	General procedure for synthesis of different hydroxyl functionalized ionic liquids (HFILs)	46
2.2.2.	General procedure for the synthesis of DESs	49
2.2.3.	Water Content Measurements of DESs and RTILs	50
2.3.	Instruments	51
2.3.1.	Instrumentations used for characterization of samples	51
2.3.2.	Instrumental Technique for Steady-State Absorption and Fluorescence Measurements	51

2.3.2.1.	Steady-State Absorption Spectroscopy	51
2.3.2.2	Steady-State Fluorescence Spectroscopy	52
2.3.3.	Instrumental Techniques for Time-Resolved Studies	53
2.3.3.1.	Fluorescence Lifetime Measurements	53
2.3.3.2.	Basic Principle of TCSPC Instrument	54
2.3.3.3.	Fluorescence Upconversion Spectroscopy (FLUPS)	57
2.3.4.	Experimental Technique for Single-Molecule Studies	59
2.3.4.1.	Time-Resolved Confocal Fluorescence Microscopy	59
2.3.4.2.	Fluorescence Correlation Spectroscopy (FCS)	60
2.4.	Methods	61
2.4.1.	Analysis of the Fluorescence Decay Curves	61
2.4.1.1.	Data Analysis	61
2.4.1.2.	Reduced chi-square ( $\chi^2$ ) Values	63
2.4.1.3.	Distribution of Weighted Residuals	63
2.4.2.	Construction and fitting of TRES	63
2.4.3.	Solvation Dynamics and Missing Component (MC) Calculation	64
2.4.4.	Time-resolved Fluorescence Anisotropy Measurements	66
2.4.5.	FCS Data Analysis	68
2.4.6.	Pulsed Field Gradient NMR Techniques	70
2.5.	Calculation of Limit of Detection and Limit of Quantification	71
2.6.	Standard Error Limits	71
<b>Chapter 3A</b>		
<b>Understanding the Differences in the Microscopic Behaviour between Deep Eutectic Solvents and Room Temperature Ionic Liquids</b>		
3A.1.	Introduction	73
3A.2.	Experimental Sections	77
3A.3	Results and Discussions	77
3A.3.1.	Steady-State Spectral Measurements	77
3A.3.2.	Rotational Relaxation Dynamics	84
3A.3.3.	FCS Studies	92
3A.3.4.	PFG-NMR Studies	95
3A.4.	Conclusion	98
3A.5.	Appendix	100
<b>Chapter 3B</b>		
<b>Studies on the Temperature-Dependent Ultrafast Solvation Dynamics in Deep Eutectic Solvents and Room Temperature Ionic Liquids</b>		
3B.1.	Introduction	105
3B.2.	Experimental Sections	108
3B.3.	Results and Discussions	108
3B.3.1.	Steady-State Measurements and Solvation Energy	108
3B.3.2.	Ultrafast Solvation Dynamics	110

3B.3.3.	Temperature-Dependent Ultrafast Solvation Dynamics	120
3B.4	Conclusion	125
3B.5.	Appendix	127
<b>Chapter 4</b>		
<b>Probing the Impact of Increase in the Number of Hydroxyl Groups on the Structure and Dynamics of Ammonium-Based Room Temperature Ionic Liquids</b>		
4.1.	Introduction	131
4.2.	Experimental Sections	134
4.3.	Results and Discussions	135
4.3.1.	Steady-State Spectral Measurements	135
4.3.2.	Ultrafast Solvation Dynamics	137
4.3.3.	Rotational Relaxation Dynamics	144
4.3.4.	FCS Studies	154
4.3.5.	PFG-NMR Studies	158
4.4.	Conclusions	161
5.4	Appendix	162
<b>Chapter 5</b>		
<b>Influence of Lithium Salt on the Structure and Dynamics of Deep Eutectic Solvents</b>		
5.1.	Introduction	166
5.2.	Experimental Sections	169
5.3.	Results and Discussions	169
5.3.1	Steady-State Spectral Measurements	169
5.3.2.	Solvation Dynamics	175
5.3.3	Rotational Relaxation Dynamics	180
5.3.4.	PFG-NMR Studies	187
5.3.5.	Arrhenius Behaviour	189
5.4.	Conclusion	191
<b>Chapter 6</b>		
<b>Assessing the Influence of Deep Eutectic Solvents on the Structure and Conformational Dynamics of BSA</b>		
6.1.	Introduction	194
6.2.	Experimental Sections	198
6.3.	Results and Discussions	199
6.3.1.	Quenching of the Intrinsic Fluorescence of BSA in the Presence of DES	199
6.3.2.	Steady-State and Time-Resolved Fluorescence of BSA-FITC	208
6.3.3.	FCS Studies of BSA-FITC in the Presence of DESs	213
6.3.4.	Conformational Studies of BSA through CD Spectroscopy	221
6.4.	Conclusion	227
6.5.	Appendix	228
<b>Summary and Future Prospects</b>		233
<b>REFERENCES</b>		236

## SYNOPSIS

Design and development of novel and sustainable solvent systems for their applications across chemical, biological, industrial, and food processing sectors.<sup>1-2</sup> To full fill this objective, researchers from both academia and industries have devoted themselves. In this context, in recent times, room temperature ionic liquids (RTILs) and deep eutectic solvents (DESs) have emerged as potential substitutes for the common volatile organic solvents (CVOS).<sup>3-9</sup> RTILs are salts with low melting points, usually liquid at ambient temperature and pressure, and are composed of bulky and asymmetric organic cations and organic or inorganic anions.<sup>3-6</sup> On the other hand, DESs are eutectic mixture having the lowest melting point, and are usually formed by the combination of hydrogen bond acceptor (HBA) such as quaternary ammonium or phosphonium salts with hydrogen bond donor (HBD) such as acid, amides or alcohol functionalities.<sup>7-12</sup> Owing to the extensive interspecies hydrogen bonding interaction between HBA and HBD, a large decrease in the freezing point temperature is observed and the resulting mixture becomes liquid at room temperature.<sup>7-9</sup> As both DESs and RTILs share many interesting physicochemical properties DESs are often referred as a subclass of ILs.<sup>7-9</sup> However, both DESs and RTILs may not necessarily behave in a similar manner at the microscopic level.<sup>12-13</sup> Apart from this, even though DESs are believed to have significant potentials for their usage in energy and bio-related applications, the structural and dynamical behaviour of DESs in presence of electrolytes and the stability and conformational dynamics of protein in presence of DESs are still not well understood.<sup>7-9,14-17</sup> Considering this, the main objective behind the current thesis is to understand the microscopic behaviour in terms of intermolecular interaction, micro-structural organisation and dynamics of various DESs and RTILs in the absence and presence of electrolytes and biomolecule through various spectroscopic investigations.<sup>18</sup> Specifically, the solute-solvent dynamics i.e., rotational and translational diffusion dynamics of few selected solutes have been studied by employing the

time-resolved fluorescence anisotropy and fluorescence correlation spectroscopy techniques. Both time-correlated single photon counting (TCSPC) and fluorescence up-conversion spectroscopy (FLUPS) techniques have been used to study the ultrafast solvent response of both DESs and RTILs. Apart from this, the translational self-diffusion dynamics of both DESs and RTILs have also been carried out with the help of nuclear magnetic resonance (NMR) techniques. Lastly, the structural and conformational dynamics of the protein in the presence of DESs, as well as the mechanism of protein-DES interaction have also been investigated.

### **Organization of thesis**

The present thesis has been divided into six chapters. A brief description of the contents of different chapters of the thesis are provided below.

### **Chapter 1: Introduction**

Chapter 1 starts with a brief introduction about ionic liquids (ILs) and deep eutectic solvents (DESs). Different classes of ILs and DESs and their physicochemical properties are also presented in this chapter. Further, the applications of ILs and DESs in various fields ranging from chemical, biological to material sciences have also been highlighted. Next, a brief discussion about the structure and dynamics of ILs and DESs have been discussed by providing recent literature reports. After this, various phenomena that are used while studying the microscopic behaviour of various DESs and ILs have been discussed in details. Particularly, excitation wavelength dependent emission behaviour, solvation and rotational relaxation dynamics, translational diffusion dynamics of both DESs and ILs are provided in detail. Finally, the current challenges in DESs and ILs research and the objective behind the present thesis work have been outlined at the end of this chapter.

## **Chapter 2: Instrumentation and Methods**

This chapter outlines the basic principles of different experimental techniques related to both ensemble average and single molecule measurements employed in the current thesis work. Various spectroscopic techniques such as absorption spectroscopy, steady-state and time-resolved emission spectroscopy have been demonstrated briefly in this chapter. Specifically, the fundamental working principle of time-correlated single photon counting (TCSPC), fluorescence up-conversion spectroscopy (FLUPS) and single molecule fluorescence spectroscopic technique have been discussed in details. Additionally, measurements of self-diffusion coefficient through pulsed-field-gradient NMR (PFG-NMR) techniques have also been provided. Apart from this, various methodologies to obtain the fluorescence decay parameters, time-resolved emission plots, solvation and rotational relaxation time scale, and translational diffusion time have been demonstrated. Moreover, analysis of the rotational relaxation time in light of hydrodynamic model have also been discussed. The error limits corresponding to different experimental parameters are provided in the end of this chapter.

## **Chapter 3a: Understanding the Differences in the Microscopic Behaviour between Deep Eutectic Solvents and Room Temperature Ionic Liquids**

Although DESs are considered a subclass of ILs, they may not necessarily behave similarly at the microscopic level. This is due to the fact that in RTILs, apart from some non-covalent interaction, the coulombic force of interaction between the cation and anion governs the structure-property relationship, whereas in DESs, the extensive interspecies hydrogen bonding interactions between HBA and HBD are believed to be the main cause for the observed physicochemical properties.

In this chapter we have tried to understand the differences in the microscopic behaviors in terms of structure, dynamics, intra and inter molecular interactions of deep eutectic solvents (DESs) and room temperature ionic liquids (RTILs). For this purpose, a choline chloride-based

DES (ethaline) and three hydroxyls functionalized ILs (Chart 1), are employed and investigated by exploiting steady-state and time-resolved fluorescence, EPR, NMR and FCS techniques. The hydroxyl group based ILs have been chosen purposefully so that apart from the role of hydroxyl group, various other factors which account for the difference in the microscopic behavior of both DES and ILs can be clearly understood. EPR spectral measurements have revealed that the polarity of hydroxyl ILs employed in this study are significantly high, whereas polarity of ethaline is found to be close to that of aliphatic poly-hydroxy alcohols. Investigation of rotational and translational diffusion dynamics of selected probes have indicated that the extent of solute-solvent interaction is relatively higher in the DES in comparison to that in hydroxyl ILs. Interestingly, diffusions studies have also depicted that the decoupling of solute dynamics with medium viscosity is found to be more for hydroxyl ILs than that for ethaline indicating the extent of dynamic heterogeneity is more in hydroxyl ILs as compared to that in ethaline. Measurements and analysis of self-diffusion coefficient through NMR have suggested that ethaline have larger hydrodynamic radius as compared to the hydroxyl ILs indicating more associated structure in ethaline. Essentially, all the results obtained from these investigations have demonstrated that despite having similar functional moieties, different intra/intermolecular interaction (such as solute-solvent interaction, specific hydrogen bonding interaction, coulombic interaction etc.) operating at microscopic level are considerably different between DES and hydroxyl ILs. The outcome of this work further highlights that all these interactions and energetics lead to a distribution of relaxation rate as well as spatial rearrangement which are different for DES and hydroxyl ILs and are primarily responsible for observing the difference in the micro-heterogeneous behaviour between DES and hydroxyl ILs.

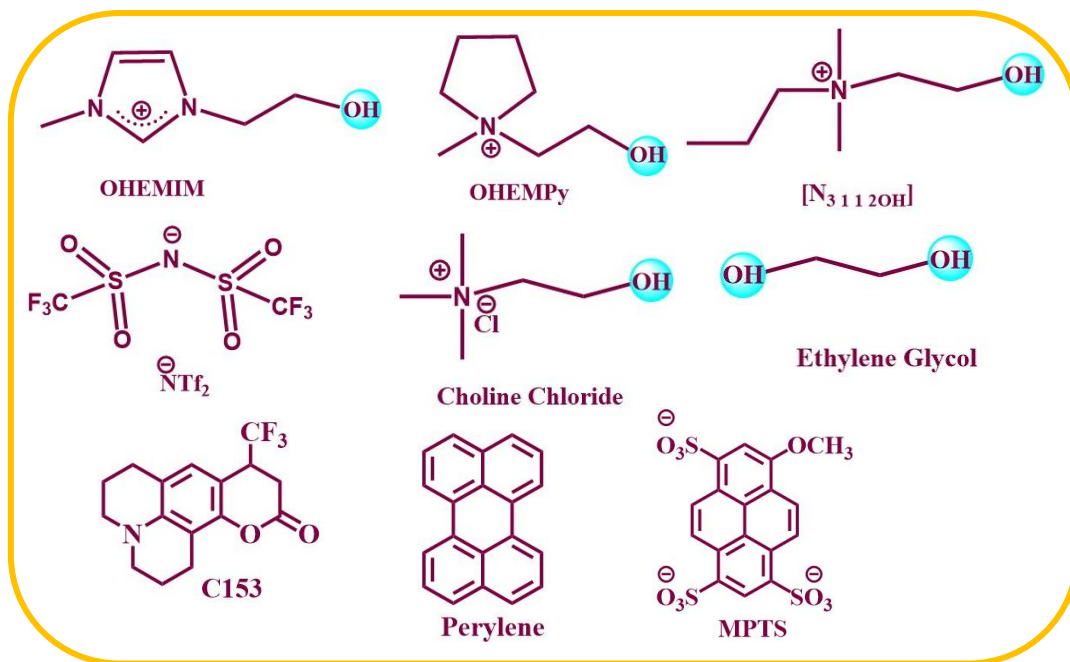


**Chart 1.** Molecular structures of ILs, constituents of the DES and the probes used in the study.

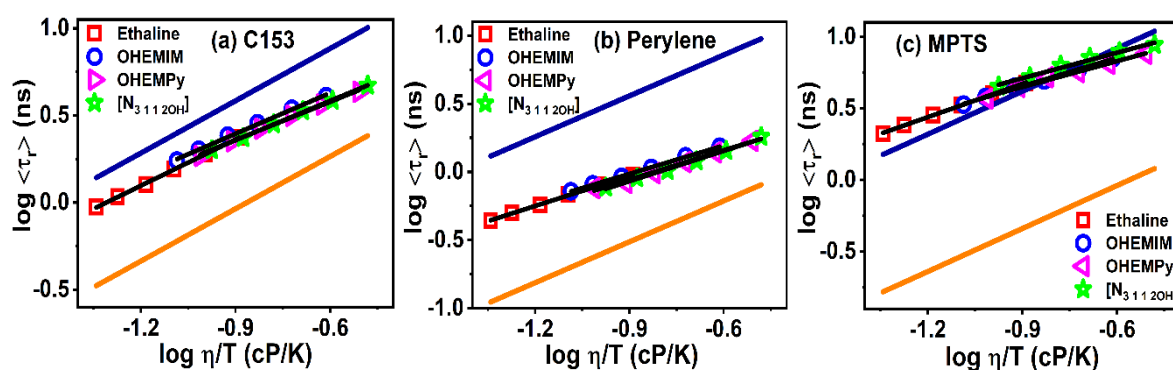


**Figure 1:** log-log plot of  $\tau_r$  versus  $\eta/T$  of C153 (a), perylene (b) and MPTS (c) in both DES and hydroxyl ILs. Solid orange and blue line represent the slip and stick boundary condition respectively. Solid black line represents linear fit to the data points.

### Chapter 3b: Studies on the Temperature-Dependent Ultrafast Solvation Dynamics in Deep Eutectic Solvents and Room Temperature Ionic Liquids

This chapter describes the difference in the solvent relaxation behavior between DESs and RTILs at both shorter (ultrafast) as well as longer time scale. For this purpose, dynamics of solvation have been investigated in a choline chloride-based DES and three hydroxyl functionalized ILs (keeping the hydroxyl functionalities same in both classes of solvent systems), so that the role of various inter/intra molecular interaction including hydrogen

bonding interaction on the solvent relaxation behavior can be understood. Fluorescence up-conversion spectroscopy techniques (FLUPS) coupled with time correlated single photon counting (TCSPC) techniques have been exploited to study the complete Stokes shift dynamics of a dipolar probe, coumarin 153 (C153) dissolved in these media. The solvent response functions generated from the complete dynamic Stokes shift data reveal a bimodal solvent relaxation behaviour having a very fast sub-picosecond and a relatively slower picosecond to sub-nanosecond solvation time component for both DES and hydroxyl ILs. The relatively slower solvation time component which correlates with bulk viscosity of the concerned medium is found to arise due to the diffusional motion of the constituents of both DES and hydroxyl ILs. However, temperature dependent solvent relaxation measurement has revealed that at iso-viscous condition the solvent relaxation is much faster in the DES as compared to that in hydroxyl IL indicating the appreciable differences in the solvent relaxation behaviour between these two classes of solvent systems at longer time scale. Interestingly, when the early part of the dynamics is monitored, the amplitude associated with the ultrafast component for the DES is observed to increase significantly with increase in temperature, whereas the same remain almost unchanged for the hydroxyl IL. This behaviour essentially indicates that even at shorter time scale, the process of solvent relaxation is considerably different for both DES and hydroxyl ILs. Overall, all these investigations pertaining to this work have essentially demonstrated that despite having similar functionalities, different motion related to the solvent relaxation, operating at microscopic level in both these classes of solvents are significantly different from each other. Molecular structure of the constituents of both RTILs and DES are shown in chart 1.

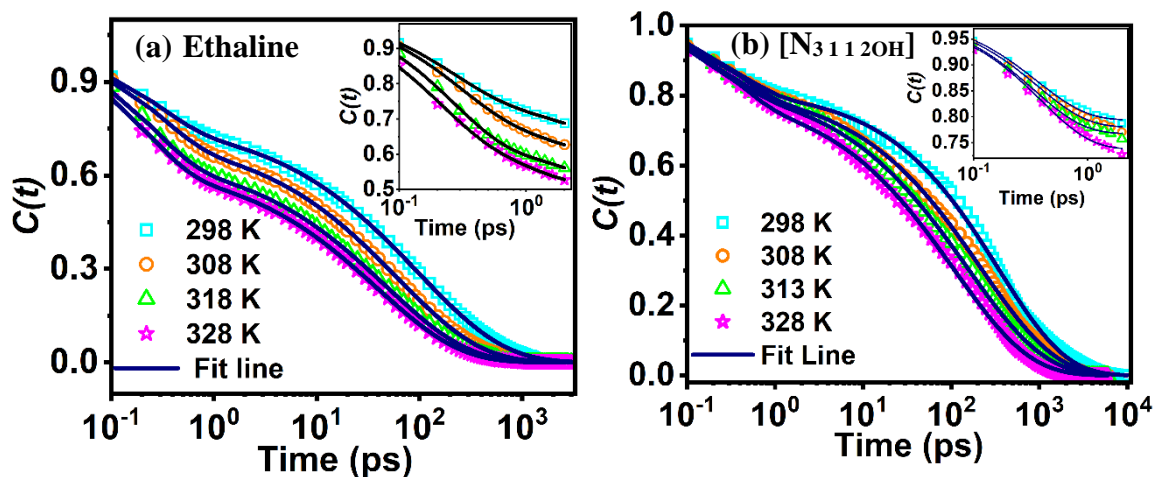


**Figure 2.** Spectral shift correlation function  $C(t)$  decay with time for C153 in (a) ethaline and (b)  $[N_{3,1,1,2OH}][NTf_2]$  at different temperature. The solid line represents fit to the data point.

#### **Chapter 4: Probing the Impact of Increase in the Number of Hydroxyl Groups on the Structure and Dynamics of Ammonium-Based Room Temperature Ionic Liquids**

Having understood that hydroxyl functionalities play crucial role in controlling the structure and dynamics of both DESs RTILs, in this chapter we have tried to understand the impact of variation in the number of hydroxyl groups on the cationic head of ammonium-based room temperature ionic liquids (RTILs) towards inter/intra molecular hydrogen bonding interaction, local structural organization and dynamics of the solvent systems. For this purpose, behaviour of three hydroxyl functionalized ammonium based RTILs (HFILs) bearing different numbers of hydroxyl groups on the cationic head as well as a non-hydroxyl ammonium based RTIL have been examined using both ensembled average and single-molecule spectroscopy techniques. The solvent relaxation dynamics of all the concerned RTILs have been investigated by combining the TCSPC and FLUPs techniques, and it has been found that all of the RTILs exhibit a bimodal solvent relaxation behaviour with a very fast sub-picosecond and a relatively slower picosecond to nanosecond solvation time component. Interestingly, the investigations on the rotational and translational diffusion dynamics of a few particular solutes have revealed that the solvent-solvent interaction in the poly-hydroxyl-based HFILs is substantially stronger than the solute-solvent interaction prevailing in that media. More interestingly, analysis of the

rotational diffusion data have shown that all RTILs exhibit significant dynamic heterogeneity, which increases with increase in the number of hydroxyl groups on the cationic head of HFILs. Moreover, PFG-NMR study have revealed that the HFILs had considerably larger hydrodynamic radii than the non-hydroxyl RTILs, which is likely due to the result of stronger hydrogen bonding interaction between the hydroxyl groups and the constituent of the HFILs. The outcomes of all these investigations have clearly demonstrated that subsequent addition of hydroxyl functionalities to the cationic head of the RTILs significantly alter the intra/inter molecular interaction, local structural organisation and heterogeneity of the medium.

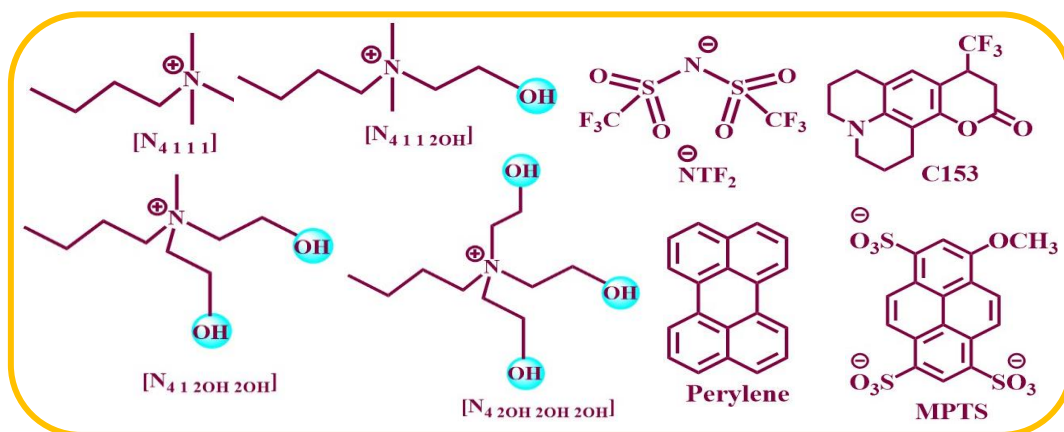


**Chart 2.** Molecular structures of ILs and probes used in the study.

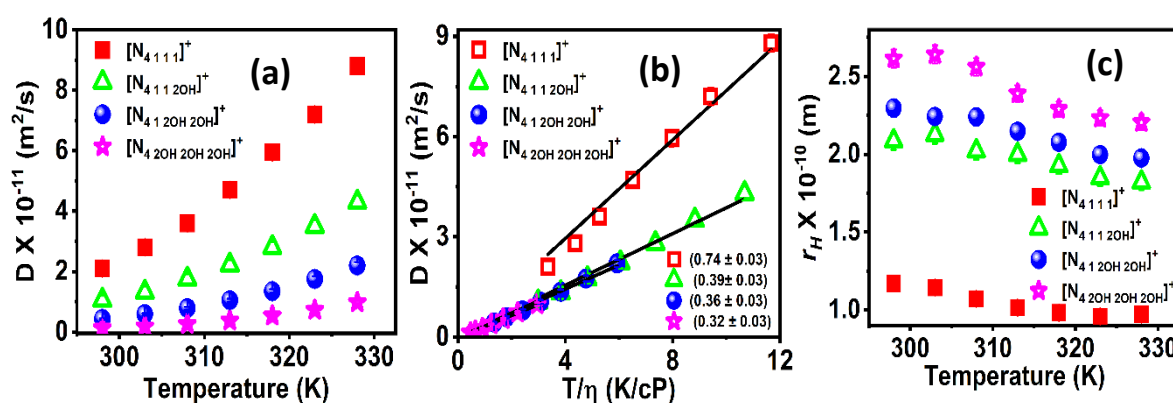


**Figure 3.** (a) Temperature dependent variation of the self-diffusion coefficients of the RTILs (b)  $D$  vs  $T/\eta$  plot of RTILs, (c) hydrodynamic radii of cationic species calculated through SE equation.

## **Chapter 5: Influence of Lithium Salt on the Structure and Dynamics of Deep Eutectic Solvents**

As DESs are known to possess large electrochemical potential windows, and negligible water electrolysis capacity, they are expected to be very attractive candidates for electrochemical applications. However, the influence of electrolytes on the structure, dynamics and heterogeneity of DES are still not explored.

Considering this, in chapter 5, attempts have been made to understand the intermolecular interaction, structural organisation and dynamics of two DES systems in absence and presence of lithium salt so that the potential of these mixtures in electrochemical application is realised. For this purpose, the structural and dynamical behaviour of two DESs (Ethaline and Glyceline) and their mixture with lithium bis(trifluoromethylsulfonyl) imide ( $\text{LiNTf}_2$ ) have been investigated by employing steady state, time resolved fluorescence, EPR and NMR spectroscopic techniques. EPR spectral measurements have revealed that the polarities of the medium are closed to that of aliphatic poly-hydroxy alcohol and the same is found to increase with increase in the concentration of lithium salt for both DESs. Studies on dynamic of solvation have shown an increase in the average solvation time with increase in the concentration of lithium salt. Interestingly, correlation of average solvation time and conductivity of the concerned media have indicated that ethaline, as compared to glyceline, may serve as a relatively better candidate for electrochemical uses. Subsequent investigations of rotational dynamics through time resolved fluorescence anisotropy and measurements of self-diffusion coefficient through NMR of both DESs have suggested significant perturbation in the structural organisation of these solvent systems in presence of lithium salt. All these investigations have categorically demonstrated that the structural organisation of both ethaline and glyceline are significantly different from each other and addition of lithium salt considerably perturb the nano/micro structural organisation of the solvent systems. The

outcome of this study is expected to be helpful in realizing the potential of these media for various electrochemical applications including application in lithium-ion battery.

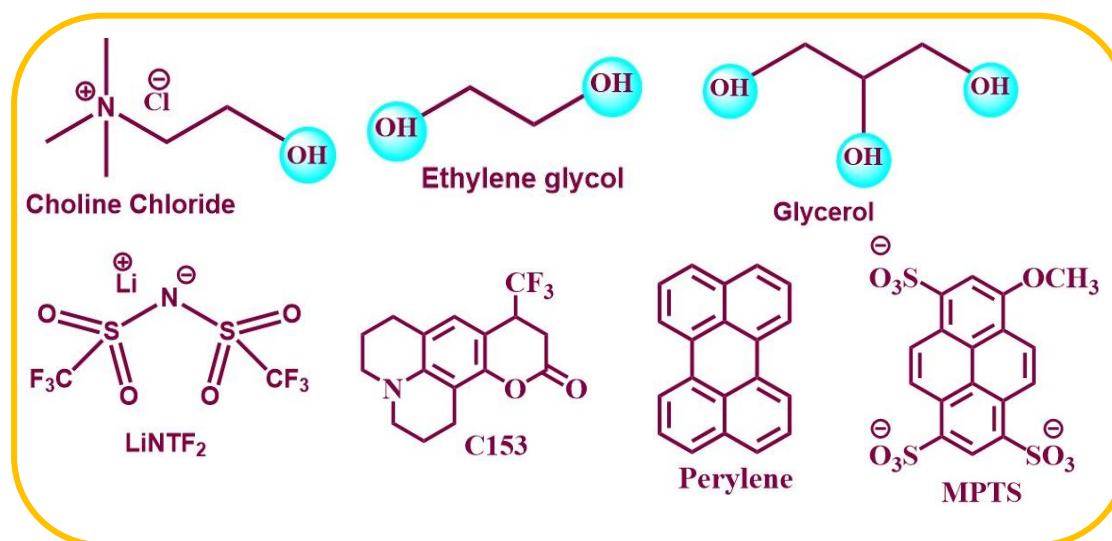


**Chart 3.** Molecular structures of the constituents of DESs and the probes used in the study.

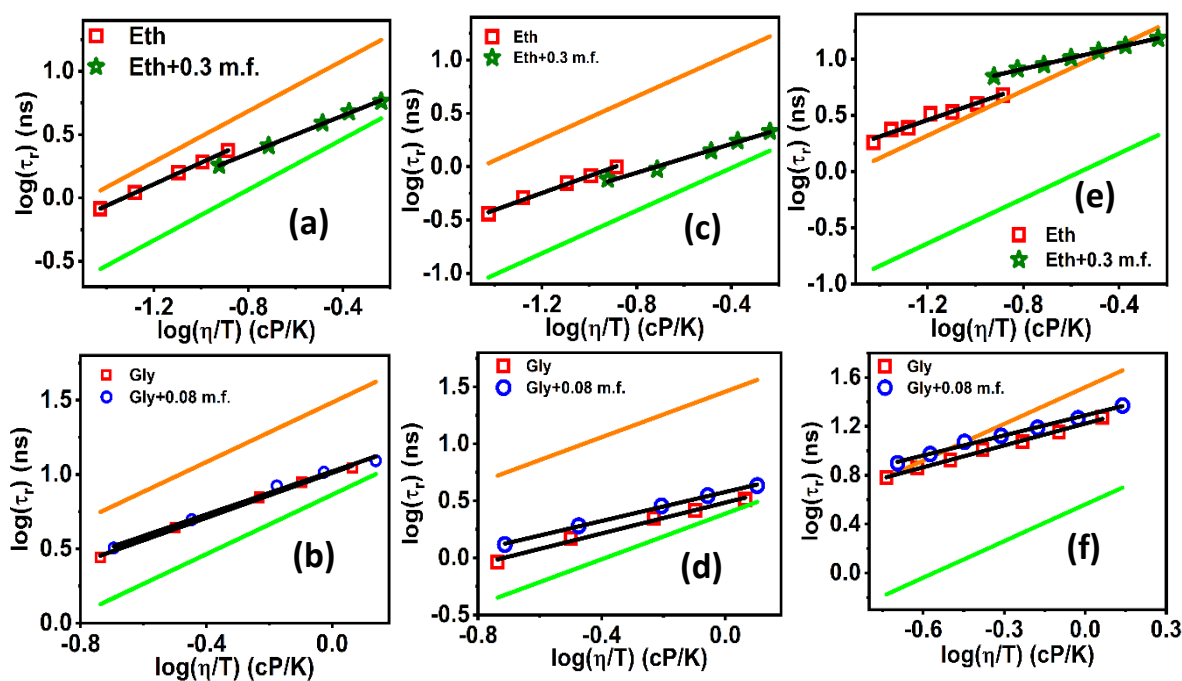


**Figure 4.** log- log plot of  $\tau_r$  versus  $\eta/T$  of C153 (a), (b); Perylene (c), (d) and MPTS (e), (f). upper panel is for ethaline and lower panel is for glyceline in the absence and presence of lithium salt. Solid Brown and green line represent the slip and stick boundary condition respectively. Solid black line represents linear fit to the data points.

## **Chapter 6: Assessing the Influence of Deep Eutectic Solvents on the Structure and Conformational dynamics of Bovine Serum Albumin**

Although deep eutectic solvents (DESs) are believed to be superior alternatives to both ionic liquids and conventional organic solvents for their application in the storage and processing of biomolecules, it is still unclear whether all DESs or only specific types of DESs will be suitable for the said purpose. Additionally, in order to develop new and sustainable DESs for bio-related applications, it is also very important to have a molecular level understanding of the mechanism of protein-DES interactions.

In view of this, the current chapter aims to provide a comprehensive understanding on the mechanism of protein-DES interaction as well as the structural and conformational stability of a protein (BSA) in the presence of DESs. For this purpose, two DESs, namely Ethaline (Choline chloride: ethylene glycol) and BMEG (benzyltrimethyl ammonium chloride: ethylene glycol), having the same hydrogen bond donor but with distinct hydrogen bond acceptor are chosen, so that how a small change in one constituent of a DES alter the protein-DES interaction at the molecular level can be understood. The protein-DES interaction is investigated by exploiting both ensemble averaged measurements like steady-state and time-resolved fluorescence spectroscopy, circular dichroism (CD) spectroscopy and single molecule measurements techniques like fluorescence correlation spectroscopy (FCS). Both steady-state and time-resolved fluorescence measurements have shown that BSA interacts more strongly with BMEG as compared to ethaline, and the BSA-BMEG interaction is primarily governed by hydrophobic interactions. Interestingly, a thorough analysis of FCS data have revealed that while a small quantity of BMEG can completely unfold the native structure of the protein, the protein can remain in partially unfolded state even in the presence of very high concentration of ethaline. More interestingly, it has also been observed that at very high BMEG concentration, favourable interaction among the unfolded protein can enhanced the protein-

protein interaction resulting in the aggregation of BSA. All the results obtained from both ensemble average and single molecule measurements are found to be in perfect agreement suggesting that both protein-DES interaction and interspecies interaction among the constituent of DESs regulate the overall stability and conformational dynamics of the protein in DESs. Moreover, as BMEG causes aggregation of the protein and protein aggregation are linked with many neurodegenerative disorders, the outcome of the current study also clearly points out that not all DESs can be treated as an alternative media for the storage of biomolecules. The current investigations at both single molecular and ensemble average condition is expected to be helpful in the judicious selection, design, and development of novel DESs for protein storage and applications.

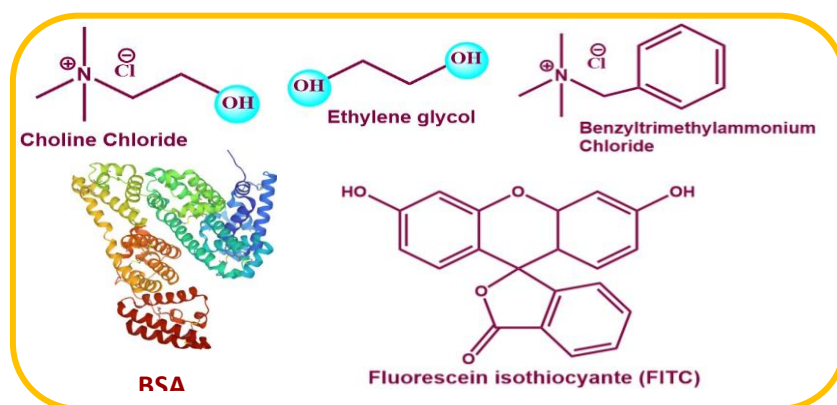


**Chart 4.** Molecular structures of the constituents of DESs, structure of BSA in native state and the probe used in the study.

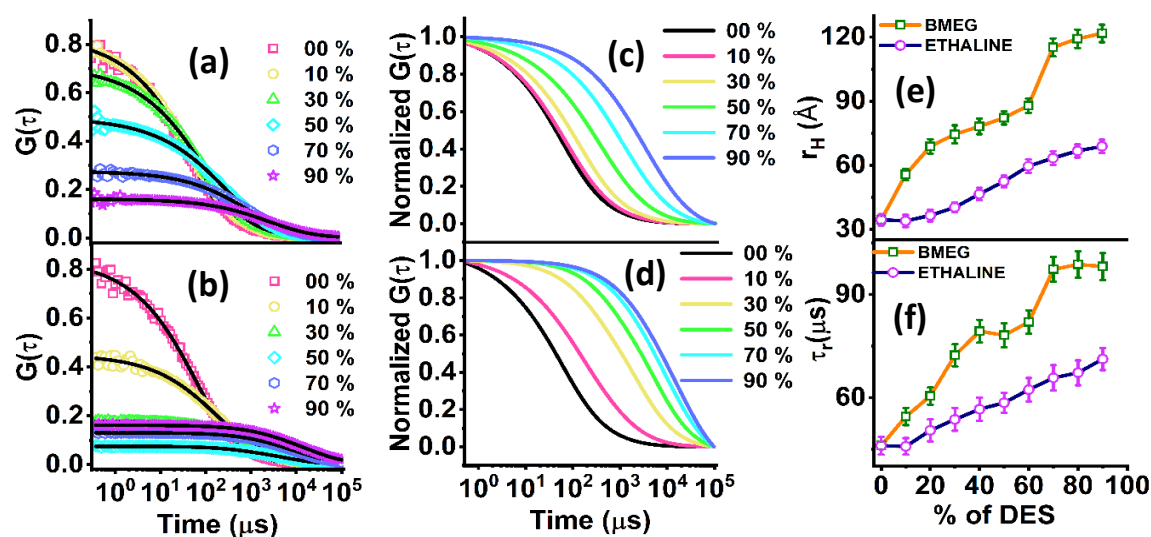


**Figure 5.** FCS traces of BSA-FITC in presence of (a) Ethaline and (b) BMEG, solid black line shows the fitting of the FCS traces. Normalized fitted FCS traces of BSA-FITC in (c) Ethaline and (d) BMEG. Variation of (e) hydrodynamic radii and (f) conformational time ( $\tau_R$ ) in presence of different quantity of DESs.

## References

1. T. W. Johannes, H. Zhao, *Curr. Opin. Microbiol.*, **2006**, 9, 261-267.
2. J. M. Woodley, *Trends Biotechnol.*, **2008**, 26, 321-327.
3. R. A. Sheldon, *Green Chem.*, **2017**, 19, 18-43.
4. R. D. Rogers, and K. R Seddon, *Science*, **2003**, 302, 792-793.
5. R. Hayes, G. G. Warr and R. Atkin, *Chem. Rev.*, **2015**, 115, 6357–6426.
6. Y.L. Wang, B. Li, S. Sarman, F. Mocci, Z.Y. Lu, J. Yuan, A. Laaksonen, M. D. Fayer, *Chem. Rev.*, **2020**, 120, 5798–5877
7. 9. A. P. Abbott, R. C. Harris, K. S. Ryder, C. D'Agostino, F. L. Gladden, M. D. Mantle, *Green Chem.*, **2011**, 13, 82-90.
8. 10. Q. Zhang, K. D. O. Vigier, S. Royer, F. Jérôme, *Chem. Soc. Rev.*, **2012**, 41, 7108-7146.
9. 11. E. L. Smith, A. P. Abbott, K. S. Ryder, *Chem. rev.*, **2014**, 114, 11060-11082..
10. 12. A. Das, R. Biswas, *J. Phys. Chem. B*, **2015**, 119, 10102–10113.
11. 13. S. Barik, M. Chakraborty, M. Sarkar, *J. Phys. Chem. B*, **2020**, 124, 2864-2878.
12. 15. S. Barik, M. Chakraborty, A. Mahapatra, M. Sarkar, *Phys. Chem. Chem. Phys.*, **2022**, 24, 7093-7106.
13. J. P. Wasylika, M. de la Guardia, V. Andruch and M. Vilková, *Microchem. J.*, **2020**, 159, 105539.
14. C.A.Nkuku, R.J. LeSuer, *J. Phys. Chem. B*, **2007**, 111, 13271.
15. P. Jiang, L. Chen, H. Shao, S. Huang, Q. Wang, Y. Su, X. Yan, X. Liang, J. Zhang, J. Feng, Z. Liu, *ACS Energy Lett.*, **2019**, 4, 1419– 1426.
16. S. S. Hossain, S. Paul, A. Samanta, *J. Phys. Chem. B*, **2021**, 125, 5757-5765.
17. N. Subba, N. Das, P. Sen, *J. Phys. Chem. B*, **2020**, 124, 31, 6875.
18. J. R. Lakowicz, *Principles of Fluorescence Spectroscopy*, 3<sup>rd</sup> ed.; Springer, Singapore, **2006**.

## List of Schemes

<b>Sl. No.</b>	<b>Scheme No.</b>	<b>Title</b>	<b>Page No.</b>
1.	Scheme 1.1	(a) Phase diagram for the combination of choline chloride with urea at different mol % of urea. (b) Proposed complexation occurring in ChCl:urea DES (1:2 molar ratio)	8
2.	Scheme 1.2	Comparison of the solid-liquid equilibrium (SLE) of a simple ideal eutectic mixture (represented in red) and a deep eutectic mixture (represented in blue)	9
3.	Scheme 1.3	Pictorial Representation of Red-Edge-Excitation Phenomena.	29
4.	Scheme 1.4	Pictorial representation of the process of dynamics of solvation through time-dependent dynamic Stokes shift measurement.	31
5.	Scheme 2.1	Synthesis scheme of HFILs.	48
6.	Scheme 2.2	A schematic diagram for the working principle of TCSPC setup.	55
7.	Scheme 2.3	A schematic representation of the up-conversion setup, Fluomax from IB photonics.	57
8.	Scheme 2.4	Time-resolved confocal fluorescence microscope setup.	60
9.	Scheme 2.5	(a) Diffusion of fluorophores through the confocal volume, (b) fluctuations in the relative fluorescence intensities and (c) correlation of the fluctuation in fluorescence intensities at different time interval.	69

## List of Figures

Sl. No.	Figure No.	Figure title	Page No.
1.	Figure 3A.1	Normalized absorption (left side) and emission spectra (right side) of C153 in Ethaline and HFILs	78
2.	Figure 3A.2	EPR spectra of TEMPO (Blue sphere) in DES and HFILs	80
3.	Figure 3A.3	Plot of $a_N/G$ vs. $E_T(30)$ values of TEMPO in both DES and HFILs	81
4.	Figure 3A.4	Plots of $\lambda_{em}^{max}$ versus $\lambda_{ex}$ of ANF at 298 K of DES and HFILs	84
5.	Figure 3A.5	Time-resolved fluorescence anisotropy decay for (a) C153, (b) perylene and (c) MPTS in DES and HFILs at 298 K.	85
6.	Figure 3A.6	log-log plot of $\tau_r$ versus $\eta/T$ of C153 (a), perylene (b) and MPTS (c) in both DES and HFILs	87
7.	Figure 3A.7	Plot of $G(\tau)$ vs time for C153 (a, b) and MPTS (d, e) in ethaline fitted through anomalous diffusion model. (c) and (f) are the normalized FCS decay curve for C153 and MPTS respectively in both DES and HFILs.	93
8.	Figure 3A.8	(a) Temperature dependent variation of the self-diffusion coefficients of DES and HFILs, (b) $D$ vs $T/\eta$ plot of DES and HFILs. The value of slope (in $\text{JK}^{-1}\text{m}^{-1}$ ) for different solvents have been shown in the legends, (c) hydrodynamic radii of cationic species calculated through SE equation	96
9.	Figure 3B.1	Fluorescence decay profiles of C153 ( $\lambda_{ex} = 405$ nm) at 298 K in Ethaline (a, c) and $\text{N}_{3112\text{OH}}$ (b, d) measured through FLUPS (upper panel) and TCSPC (lower panel) techniques respectively.	111
10.	Figure 3B.2.	Normalized TRES plot at different time interval for (a) ethaline and (b) $[\text{N}_{3112\text{OH}}][\text{NTf}_2]$ .	112
11.	Figure 3B.3.	Spectral shift correlation function $C(t)$ decay with time for C153 in (a) ethaline (b) $[\text{OHEMIM}][\text{NTf}_2]$ (c) $[\text{OHEMPy}][\text{NTf}_2]$ (d) $[\text{N}_{3112\text{OH}}][\text{NTf}_2]$ at 298K	115
12.	Figure 3B.4.	Variation of (a) long time and (b) short time component against the bulk viscosity of the solvents at 298 K.	118
13.	Figure 3B.5.	Spectral shift correlation function $C(t)$ decay with time for C153 in ethaline and $[\text{N}_{3112\text{OH}}][\text{NTf}_2]$ at different temperature	121
14.	Figure 3B.6.	(a) log-log plot of $\tau_{st}$ versus $\eta/T$ . The solid line represents fit to the data point. (b) amplitude associated with the sub-picosecond component versus temperature.	123
15.	Figure 4.1	(a) Normalized absorption and (b) emission spectra of C153 in both non-hydroxyl and hydroxyl ILs. $\lambda_{ex} = 405$ nm.	136
16.	Figure 4.2	Fluorescence decay profiles of C153 ( $\lambda_{ex} = 405$ nm) at 298 K in $[\text{N}_{4111}][\text{NTf}_2]$ (a, c) and $[\text{N}_{412\text{OH}2\text{OH}}][\text{NTf}_2]$ (b, d) measured through FLUPS (upper panel) and TCSPC (lower panel) techniques respectively	138
17.	Figure 4.3	Normalized TRES plots at different time interval for (a) $[\text{N}_{4111}][\text{NTf}_2]$ and (b) $[\text{N}_{412\text{OH}2\text{OH}}][\text{NTf}_2]$ . Solid line represents	139

		the log-normal line shape fitting of the corresponding data and the dotted line represents the steady-state fluorescence spectrum of C153 in the corresponding HFILs. (c) Spectral shift correlation function $C(t)$ decay with time at 298K for C153 in all the RTILs utilized in the study. The solid line represents fit to the data point.	
18.	Figure 4.4	Time-resolved fluorescence anisotropy decay for (a) perylene and (b) MPTS in all the RTILs at 298 K.	145
19.	Figure 4.5	log- log plot of $\tau_r$ versus $\eta/T$ of (a) perylene and (b) MPTS in all the RTILs. Solid orange and green line represent the stick and slip boundary condition respectively. Solid black line represents linear fit to the data points	148
20.	Figure 4.6	Plot of $G(\tau)$ vs time for (a) Perylene and (b) MPTS in $[N_{411}][NTf_2]$ . (c) and (d) are the normalized FCS decay curve for perylene and MPTS respectively in the relevant RTILs.	154
21.	Figure 4.7	(a) Temperature dependent variation of the self-diffusion coefficients of the RTILs (b), hydrodynamic radii of cationic species calculated through SE equation, (c) $D$ vs $T/\eta$ plot of RTILs.	159
22.	Figure 5.1	Normalized absorption (left side) and emission spectra (right side) of C153 in both DESs containing different mole fraction of lithium salt.	170
23.	Figure 5.2	EPR spectra of TEMPO in both DESs in the absence and presence of LiNTf <sub>2</sub> .	172
24.	Figure 5.3	Plot of $a_N/G$ vs. $E_T(30)$ values of TEMPO in both DES and HFILs vs. $E_T(30)$ values of TEMPO in both DESs in absence and presence of LiNTf <sub>2</sub>	173
25.	Figure 5.4	Plots of $\lambda_{ex}$ versus $\lambda_{em}^{max}$ of ANF at 298 K of both DESs medium in the absence as well as in presence of LiNTf <sub>2</sub> .	174
26.	Figure 5.5	(a), (b) Fluorescence decay of C153 at three different wavelengths in both DESs and (c), (d) TRES plots for both DESs in neat condition.	175
27.	Figure 5.6	Spectral shift correlation function $C(t)$ decay with time for C153 in ethaline and glyceline in absence and presence of LiNTf <sub>2</sub> at 298K. The solid line represents biexponential fit to the data point.	177
28.	Figure 5.7	Time-resolved fluorescence anisotropy decay for C153, perylene and MPTS in ethaline in the absence and presence of LiNTf <sub>2</sub> at 298 K.	181
29.	Figure 5.8	log- log plot of $\tau_r$ versus $\eta/T$ of C153 (a), (b); Perylene (c), (d) and MPTS (e), (f). Left side panel is for ethaline and right-side panel is for glyceline. Different mole fraction of LiNTf <sub>2</sub> added to both DESs are shown in the legends	183
30.	Figure 5.9	Temperature-dependent variation of the self-diffusion coefficients of neat DES and (DES + Li salt) mixture.	188
30.	Figure 5.10	Arrhenius fitting to (a) translational diffusion coefficient, (b) Viscosity (c) rotational diffusion coefficient of C153 in both DESs.	190

31.	Figure 6.1	Fluorescence emission spectra ( $\lambda_{ex}= 295\text{nm}$ ) of BSA in absence and presence of gradual addition of (a) ethaline and (b) BMEG. (c) Stern-Volmer plot for BSA-BMEG and BSA-ethaline at 298K. (d) Stern-Volmer plot for BSA-BMEG at 3 different temperatures. (e) Double logarithmic plot at three different temperatures for BSA-BMEG (solid black line shows the linear fit). (f) Binding constant versus temperature for BSA-BMEG (solid red line shows the linear fit of the data points).	200
32.	Figure 6.2	Representative fluorescence decay traces ( $\lambda_{ex}= 295\text{nm}$ ) of BSA in absence and presence of gradual addition (a) Ethaline and (b) BMEG DESs at 298 K. The instrument response functions (IRF) are shown in solid violet lines and the biexponential fit of the fluorescence decay traces are shown in solid black line. Variation of (c) average lifetime and (d) longer decay component for BSA fluorescence decay in presence of different amount of Ethaline and BMEG. (e) Stern-Volmer plot with respect to lifetime for BSA in presence of BMEG. (f) Variation of amplitude ( $a_2$ ) associated with longer component of BSA fluorescence decay in presence of Ethaline and BMEG.	203
33.	Figure 6.3	Fluorescence emission spectra ( $\lambda_{ex}= 485\text{nm}$ ) of BSA-FITC in absence and presence of gradual addition of (a) ethaline and (b) BMEG (dotted line). (c) Variation of fluorescence intensity of BSA-FITC in presence of different amount of DESs. Fluorescence decays ( $\lambda_{ex}= 485\text{nm}$ ) of BSA-FITC in presence of different quantity of (d) Ethaline and (e) BMEG. The solid navy blue represents the IRF and the solid black line represents the biexponential fits of the fluorescence decay traces. (f) Variation of average lifetime BSA-FITC in presence of different amount of DESs.	212
34.	Figure 6.4	FCS traces of BSA-FITC in presence of (a) Ethaline and (b) BMEG, solid black line shows the fitting of the FCS traces. Normalized fitted FCS traces of BSA-FITC in (c) Ethaline and (d) BMEG. Variation of (e) hydrodynamic radii and (f) conformational time ( $\tau_R$ ) in presence of different quantity of DES.	214
35.	Figure 6.5	Far-UV CD spectra of 2 $\mu\text{M}$ BSA in the absence and presence of different quantity of (a) Ethaline and (b) BMEG.	223

## List of Tables

Sl. No.	Figure No.	Table title	Page No.
1.	Table 1.1	Classification of DESs	10
2.	Table 1.2	Common physical properties of some ILs	13
3.	Table 1.3	Common physical properties of some choline chloride (melting point 576K)-based DESs with different hydrogen bond donor	13
4.	Table 1.4	Some Common differences between ILs and DESs	19
5.	Table 1.5	Molecular volumes ( $V$ ), shape factor ( $f$ ) and slip boundary ( $C_{slip}$ ) condition parameters for some selected probes used in this thesis work	36
6.	Table 2.1	Water content of the solvent systems used in this study	50
7.	Table 2.2	standard error limits for various experimental results	71
8.	Table 3A.1	Absorption and Emission Maxima of C153 in various solvent systems	78
9.	Table 3A.2	The $a_N/G$ value of TEMPO in DESs and HFILs and their estimated $E_T(30)$ values	81
10.	Table 3A.3	Rotational relaxation parameter of different probes in both DES and HFILs	86
11.	Table 3A.4	Rotational relaxation parameter of different probes in both DES and hydroxyl ILs at iso-viscous condition	87
12.	Table 3A.5	Parameters A and p obtain from the fits of $\log \langle \tau_r \rangle$ vs $\log \langle \eta/T \rangle$	90
13.	Table 3A.6	Estimated translational diffusion coefficient ( $D_t$ ) along with $\beta$ value of C153 and MPTS in both DES and HFILs.	94
14.	Table 3A.7	Estimated translational diffusion coefficient ( $D \times 10^{-11}$ m <sup>2</sup> /s) of the cationic species of both DES and hydroxyl ILs as well as HBD of the DES	96
15.	Table 3B.1	Steady state absorption and emission maxima, $\Delta_{solv}G^a$ and $\lambda_{solv}^a$ of C153 in various solvent systems used in this study	109
16.	Table 3B.2	Solvent relaxation parameters of both DESs and HFILs at 298K	114
17.	Table 3B.3	Solvent relaxation parameters and viscosity of both DESs and HFILs at 298K-328K	121
18.	Table 4.1	Absorption and Emission Maxima of C153 in the concerned RTILs	136
19.	Table 4.2	Solvent relaxation parameters of all RTILs utilized in the present study at 298K	140
20.	Table 4.3	Rotational relaxation parameters of perylene and MPTS in all the RTILs at two different temperatures	147
21.	Table 4.4	Rotational relaxation parameters of perylene and MPTS in all the RTILs at iso-viscous condition.	148

22.	Table 4.5	Parameters A and $p$ obtain from the fits of $\log \langle \tau_r \rangle$ vs $\log \langle \eta/T \rangle$	153
23.	Table 4.6	Estimated translational diffusion coefficient ( $D_t$ ) in $\mu m^2/s$ along with their contribution value for perylene and MPTS in all the relevant RTILs	155
24.	Table 4.7	Estimated translational diffusion coefficient ( $D \times 10^{-11} m^2/s$ ) of the cationic species of both non-hydroxyl and hydroxyl ILs.	158
25.	Table 5.1	Absorption and Emission Maxima of C153 in DESs and DES + Li Mixture	170
26.	Table 5.2	The $a_N/G$ value of TEMPO in DESs and molecular solvents and their estimated $E_T(30)$ values	172
27.	Table 5.3	Solvation relaxation parameters of both DESs with varying concentration of LiNTf <sub>2</sub> at 298K	178
28.	Table 5.4	Rotational relaxation parameter of different probes in glyceline.	181
29.	Table 5.5	Rotational relaxation parameter of different probes in ethaline.	182
30.	Table 5.6	Parameters A and $p$ obtain from the fits of $\log \langle \tau_r \rangle$ vs $\log \langle \eta/T \rangle$	185
31.	Table 5.7	Estimated translational diffusion coefficient of DESs with varying mole fraction of LiNTf <sub>2</sub>	188
32.	Table 5.8	Activation energy for viscous flow ( $E_\eta$ ), translational Diffusive flow of choline cation, ( $E_{D,CH^+}$ ) and Rotational diffusive flow ( $E_r$ ) for C153 in DESs and DES + Li Mixture	190
33.	Table 6.1	Fluorescence decay parameters of BSA in the absence and presence of DESs	204
34.	Table 6.2	Binding constant ( $K_B$ ), number of binding sites ( $n$ ), and other relative thermodynamic parameters for the Interaction of BMEG with BSA	208
35.	Table 6.3	Fluorescence decay parameters of FITC-BSA in the absence and presence of DESs.	212
36.	Table 6.4	Estimated fitted parameters of FCS data of BSA-FITC in presence of DESs	214
37.	Table 6.5	Variation in the Secondary Structure ( $\alpha$ -Helical) of BSA in presence of different quantity of DESs	223

## List of Appendices

Sl. No.	Chapter No.		Title	Page No.
1.	3A	Figure APX3A.1	(a) Electronic absorption spectra of Reichardt's dye 30 in all the concerned solvent systems, (b) Normalized electronic absorption spectra of Reichardt's dye 30 showing the shift in $\lambda_{max}^{abs}$ , (c) Normalized electronic absorption spectra of 4-nitroaniline and (d) N,N-dimethyl-4-nitroaniline dye showing the shift in $\lambda_{max}^{abs}$ .	100
2.	3A	Table APX3A.1.	$E_T$ (30) and Kamlet-Taft parameters of concerned solvent systems	100
3.	3A	Figure APX3A.2.	(a) Normalized absorbance spectra of 2-amino-7-nitrofluorene (ANF) in all the concerned solvent systems. (b) Femto-second fluorescence up-conversion decay plot of ANF in all the concerned solvent systems.	101
4.	3A	Figure APX3A.3	Plot of $G(\tau)$ vs time for C153 (a, b) and MPTS (c, d) in ethaline. Plot (a) and (c) are fitted through anomalous diffusion model while plot (b) and (d) fitted through single-component diffusion model.	101
5.	3A	Figure APX3A.4	Plot of $G(\tau)$ vs time for C153 (a, b) and MPTS (c, d) in different HFILs fitted through anomalous diffusion model	102
6.	3A	Table APX3A.2.	Estimated hydrodynamic radii ( $r_H$ in nm) of C153 and MPTS calculated from FCS studies	102
7.	3B	Figure APX3B.1.	Normalized TRES plot at different time interval for (a) [OHEMIM][NTf <sub>2</sub> ] and (b) [OHEMPy][NTf <sub>2</sub> ].	127
8.	3B	Figure APX3B.2	Normalized TRES plot at different time interval for Ethaline at different temperature.	128
9.	3B	Figure APX3B.3	Normalized TRES plot at different time interval for [N <sub>3 1 1 2OH</sub> ][NTf <sub>2</sub> ] at different temperatures	128
10.	4	Figure APX4.1	Normalized TRES plots at different time interval for (a) [N <sub>4 1 1 2OH</sub> ][NTf <sub>2</sub> ] and (b) [N <sub>4 2OH 2OH 2OH</sub> ][NTf <sub>2</sub> ]. Solid line represents the log-normal line shape fitting of the corresponding data and the dotted black line represents the steady-state fluorescence spectra.	162
11.	4	Figure APX4.2	Fluorescence correlation curve for (a,b) Perylene and (c,d) MPTS in [N <sub>4 1 1 1</sub> ][NTf <sub>2</sub> ] along with the fit residual. Left panel curves (a,c) are fitted to single component diffusion model while right panel curves (b,d) are fitted to two component diffusion model	163

12.	4	Figure APX4.3	Fluorescence correlation curve for perylene in HFILs. The solid black curve represents the fit to the points through two component diffusion model.	163
13.	4	Figure APX4.4	Fluorescence correlation curve for MPTS in hydroxyl ILs. The solid black curve represents the fit to the points through two component diffusion model.	164
14.	4	Table APX4.1	Estimated translational diffusion time ( $\tau_D$ ) in millisecond (ms) along with their contribution value for perylene and MPTS in all the relevant RTILs	164
15.	6	Figure APX6.1	Steady-state absorption spectra of BSA-FITC in 10mM phosphate buffer.	229
16.	6	Figure APX6.2	Steady-state absorption spectra of 2 $\mu$ M of BSA in presence of (a) Ethaline and (b) BMEG.	229
17.	6	Figure APX6.3	Steady-state fluorescence spectra of BSA (2 $\mu$ M) in presence of different quantity of BMEG at 303 to 318K.	230
18.	6	Figure APX6.4	Fluorescence decay traces ( $\lambda_{ex}$ = 295nm) of BSA in absence and presence of different quantity of (a) Ethaline and (b) BMEG DESs at 298 K.	230
19.	6	Figure APX6.5	Stern-Volmer plots for quenching of intrinsic BSA fluorescence by BMEG at 298 K. The solid line represents the simulated curve obtained by using equation 6.3.	231
20.	6	Figure APX6.6	Double logarithmic plot at 303K and 313K for BSA-BMEG.	231
21.	6	Figure APX6.7	Steady-state fluorescence spectra of (a) BSA-FITC in presence of GdHCl. Steady-state fluorescence spectra of FITC dye only in presence of (b) Ethaline and (c) BMEG respectively.	231
22.	6	Figure APX6.8	Fitting of the FCS trace of BSA-FITC in 10 mM phosphate buffer through (a) single component diffusion model (equation), and (b) single component diffusion model along with stretched relaxation component (equation). (c) Fitting of FITC dye only in buffer through single component diffusion model.	232
23.	6	Figure APX6.9	(a) FCS traces of BSA-FITC in presence of GdHCl. (b) Normalized fitted FCS traces of BSA-FITC in GdHCl.	232
24.	6	Figure APX6.10	Estimated fitted parameters of FCS data of BSA-FITC in presence of GdHCl	232

## Glossary of Acronyms

ILs	Ionic liquids
RTILs	Room temperature ionic liquids
MILs	Monocationic ionic liquids
DILs	Dicationic ionic liquids
HFILs	Hydroxyl Functionalized Ionic Liquids
TSILs	Task-Specific Ionic Liquids
NTf <sub>2</sub> /Tf <sub>2</sub> N	bis(trifluoromethanesulfonyl)imide
[OHEMIM][NTf <sub>2</sub> ]	1-(2-hydroxyethyl)-3-methylimidazolium bis(trifluoromethanesulfonyl)imide
[OHEMPy][NTf <sub>2</sub> ]	N-(2-hydroxyethyl)-N-methylpyrrolidinium bis(trifluoromethanesulfonyl)imide
[N <sub>3</sub> 112OH][NTf <sub>2</sub> ]	N-(2-hydroxyethyl)-N,N-dimethylpropan-1-aminium bis(trifluoromethanesulfonyl)imide
[N <sub>4</sub> 112OH][NTf <sub>2</sub> ]	N-(2-hydroxyethyl)-N,N-dimethylbutan-1-aminium bis(trifluoromethanesulfonyl)imide
[N <sub>4</sub> 12OH2OH][NTf <sub>2</sub> ]	N,N-bis(2-hydroxyethyl)-N-methylbutan-1-aminium bis(trifluoromethanesulfonyl)imide
[N <sub>4</sub> 2OH2OH2OH][NTf <sub>2</sub> ]	N,N,N-tris(2-hydroxyethyl)butan-1-aminium,
[N <sub>4</sub> 111][NTf <sub>2</sub> ]	N,N,N-trimethylbutan-1-aminium bis(trifluoromethanesulfonyl)imide
Deep Eutectic Solvents	DESs
Choline Chloride	ChCl
Ethylene Glycol	EG
Ethaline/ETH	Choline chloride + Ethylene glycol
Glyceline/Gly	Choline chloride + Glycerol
BMEG	Benzyl trimethylammonium chloride + Ethylene glycol
C153	Coumarin 153
MPTS	sodium 8-methoxypyrene-1,3,6- sulfonate
ANF	2-amino-7-nitro fluorene
TEMPO	(2,2,6,6-Tetramethylpiperidin-1-yl)oxyl
FITC	Fluorescein Isothiocyanate

Rh6G	Rhodamine 6G
REE	Red edge effect
$\lambda_{exc}$	Excitation wavelength
$\lambda_{em}^{max}$	Emission maxima in wavelength
$T_D$	Thermal decomposition temperature
$T_g$	Glass transition temperature
$T_m$	Melting temperature
$\eta$	Viscosity
$\rho$	Density
$a_N/G$	Hyperfine splitting constant in Gauss
$E_T(30)$	Electronic transition energy of Reichardt dye
EPR	Electron Paramagnetic resonance
UV	Ultra-Violet
$S_1$	First excited state
$S_0$	Ground state
TCSPC	Time-Correlated Single Photon Counting
PMT	Photo multiplier tube
CFD	Constant fraction discriminator
TAC	Time-to-amplitude converter
PGA	Programmable gain amplifier
ADC	Analog-to-digital converter
WD	Window discriminator
MCA	Multichannel analyzer
MCP	Microchannel plate
IRF	Instrument response function
FLUPs	Fluorescence Upconversion Spectroscopy
$\phi_f$	Fluorescence quantum yield
$k_{nr}$	Non-radiative rate constant
$k_r$	Radiative rate constant
$\tau_f$	Fluorescence lifetime
$\langle\tau\rangle/\tau_{avg}$	Average lifetime
$\tau_s$	Average solvation time

$\tau_r$	Rotational relaxation time
$\tau_D$	Translational diffusion time
TDDSS	Time-Dependent Dynamic Stokes Shift
TRES	Time resolved emission spectra
CFM	Confocal fluorescence microscope
CCD	Charged coupled device
SPADs	Single or multiple photon avalanche photodiodes
SNR	Signal-to-noise ratio
NLLS	Nonlinear least squares
TTTR	time-tagged time-resolved
FCS	Fluorescence Correlation Spectroscopy
NMR	Nuclear Magnetic Resonance
PFM-NMR	Pulse Field Gradient Nuclear Resonance Resonance
D	Diffusion coefficient
VFT	Vogel-Fulcher-Tammann relationship
SED	Stokes-Einstein-Debye theory
GW	Gierer-Wirtz theory
DKS	Dote-Kivelson-Schwartz theory
SE	Stoke-Einstein theory
BSA	Bovine serum albumin
APX	Appendix

# CHAPTER 1

---

## Introduction

---

## **Abstract**

This chapter provides a brief overview of ionic liquids (ILs) and deep eutectic solvents (DESs), including their different types and physicochemical properties. The chapter also highlights the diverse applications of ILs and DESs in various fields, such as chemical, biological, and material sciences. Recent literature reports are used to discuss the structure and dynamics of ILs and DESs. Additionally, various phenomena that are commonly used to study the microscopic behaviour of these solvents (such as excitation wavelength-dependent emission behaviour, solvation and rotational relaxation dynamics, translational diffusion dynamics, etc.) are explained in detail. Finally, the chapter outlines the current challenges in DESs and ILs research and describes the objectives of the present thesis work.

---

## **1.1. Solvents - a brief introduction**

Solvents are essential components in almost all biological and chemical processes. According to IUPAC, solvents are substances that are capable of dissolving or dispersing other substances, creating homogeneous mixtures or solutions.<sup>1</sup> In biological systems, water is the most common and important solvent.<sup>2</sup> It is essential for many biological processes, such as metabolism, transport of nutrients and waste, and maintenance of cell shape and structure. In chemical processes, solvents play a crucial role in many reactions, including dissolution, precipitation, extraction, and separation.<sup>3</sup> It is worth noting that the choice of solvent can have a significant impact on the outcome of a chemical reaction or biological process.<sup>3-5</sup> The properties of the solvent, such as its polarity, acidity or basicity, and boiling point, can affect the solubility, reaction rates, selectivity, and yield.<sup>4</sup> Therefore, selecting the appropriate solvent is an important consideration in many scientific and industrial applications. In addition, new types of chemical reactions and processes are constantly being developed, and these may require new types of solvents that can meet the specific requirements of the end users. Apart from this,

demand for more sustainable and green solvent systems is constantly increasing, particularly in industries like pharmaceuticals, biotechnology, and materials science.<sup>6</sup> Overall, the development of new solvents with specific properties and characteristics, as well as solvents that are safer, less toxic, and have lower environmental impacts, is an ongoing area of research and development in chemical sciences.<sup>7-11</sup>

The use of solvents can be traced back to ancient times when natural substances such as water, alcohol, and vinegar were used for cleaning, dyeing, and other applications. Over the time, solvent systems have undergone significant progress, with new solvents being developed and existing solvents being improved in terms of their performance and environmental impact.<sup>12</sup> The progress of solvent systems over the time has been influenced by a number of factors, including advances in technology, changes in regulatory requirements, and a growing awareness of the environmental impact of solvents.

- In the 18th-19th century, natural solvents such as water, ethanol, and plant-based oils were commonly used for various applications, including cleaning, extraction, and preservation.<sup>9, 12</sup>
- In the 19<sup>th</sup> century, with the onset of the Industrial Revolution, the demand for more specialized solvents increased. Solvents such as kerosene, benzene, and toluene were developed for use in various industrial applications.<sup>4</sup>
- Later on, the petrochemical industry, which began in the early 20th century, revolutionized the design and development of solvent systems. Solvents such as methanol, ethanol, and acetone were produced on a large scale using petrochemical feedstocks, making them cheaper and more widely available.<sup>3</sup> Moreover, non-aqueous solvents such as dimethyl sulfoxide (DMSO) and N,N-dimethylformamide (DMF) were developed, which have higher solvating power and lower toxicity than many

organic solvents.<sup>13</sup> However, it became clear that these solvents were highly toxic and harmful to human health and the environment

- In the latter part of the 20th century, concerns about the environmental impact of solvents began to grow. This led to the development of "green solvents" that are less toxic and have a lower environmental impact than traditional solvents.<sup>5, 7, 9-11, 14</sup> Examples of green solvents include ILs and supercritical CO<sub>2</sub>.<sup>15</sup> The discovery of liquid ammonia as a solvent for metals and inorganic compounds led to the development of new synthetic materials, such as ammonia-based fertilizers and explosives.
- In the 21st century, there has been a growing interest in green solvents, which are environmentally friendly and sustainable. Examples include ILs, DESs, and bio-based solvents.<sup>9, 16, 17</sup>

Overall, the design and development of solvent systems have progressed from early natural solvents to modern synthetic solvents and, more recently to green and "designer solvents" that are tailored to do specific applications. In this context, both ILs and DESs have come to light as feasible options to serve as sustainable media for various applications ranging from chemical and biological to material chemistry.<sup>18-21</sup>

## 1.2. Ionic Liquids (ILs)

ILs are liquid molten salts that generally consist of large, asymmetrical organic cations and small, inorganic, or organic anions with melting temperatures below 100 °C.<sup>22</sup> In ILs, the cations are typically organic groups such as ammonium, imidazolium, pyrrolidinium, and pyridinium, etc., while the anions can be organic or inorganic, such as chloride, bromide, tetrafluoroborate, and hexafluorophosphate.<sup>23</sup> The constituent ions in ILs have larger sizes than traditional ions, and as a result, their charge is dispersed. This causes the charge density on the constituent ions to be low. The large size of the constituent ions and the low charge density reduce the Coulombic forces between them, which disrupts the lattice packing and prevents the

formation of a regular crystalline structure. As a result, the low charge density on the constituent ions and inefficient packing is responsible for the liquid state of ILs.<sup>24-26</sup> ILs were initially thought to have properties similar to those of conventional molecular liquids, such as water or organic solvents. However, with the advancement of research techniques and a deeper understanding of the structure of ILs, it has become clear that the diverse ordering structures present in ILs are driven by both short-range and long-range interactions among the constituent ions.<sup>26-28</sup> The combination of these interactions leads to the formation of a complex structure in ILs, characterized by the presence of ionic clusters, voids, and channels.<sup>26, 29-31</sup> This unique structure results in a variety of physical and chemical properties, low vapor pressures, high viscosity, low toxicity, high ionic conductivity, extremely high thermal stability, and capability to dissolve a wide range of inorganic, organic compounds making ILs an attractive class of solvents and electrolytes for various industrial applications.<sup>16, 23, 32-37</sup>

The history of ILs dates back to 1914 when the German chemist Paul Walden<sup>38</sup> synthesized an ionic salt, ethylammonium nitrate (EAN), that remained liquid at ambient temperature. EAN was the first documented example of a salt material with a low melting point (12<sup>0</sup>C) and a low viscosity, and it was considered a puzzling for many years. Later, in 1959, Hurley and Wier<sup>39</sup> recognized the potential benefits of mixing aluminium compounds with alkylpyridinium chloride salts to synthesize organic chloroaluminates. This led to the development of the first generation of ILs, which had lower melting points than traditional molten salts and could be synthesized using simpler and less expensive methods.<sup>32</sup> However, these haloaluminate ILs had some drawbacks, including high sensitivity to atmospheric moisture, which could cause their hydrolysis and degradation, and eventually limit their widespread use and commercialization. This problem was overcome when Wilkes and Zaworotko<sup>40</sup>, in 1992, synthesized the air and water-stable 1-ethyl-3-methylimidazolium-based ILs containing tetrafluoroborate, hexafluorophosphate, nitrate, sulphate, and acetate anions.

These ILs are classified as second generation ILs. However, These ILs are very viscous and generate HF acid when hydrolysed in the presence of minute amounts of water.<sup>40</sup> This shortcoming prompted the development of the third generation ILs which are composed of perfluorinated anion containing RTILs such as bis(trifluoromethanesulfonyl)imide (NTf<sub>2</sub>) fluoroalkylphosphate (FAP), etc., and address the problem of second generation RTILs.<sup>41, 42</sup> These ILs have low melting points, low viscosities, and low conductivities and are mostly hydrophobic in nature. However, these anions are more costly and have a larger affinity for attaching Lewis's acid metal ions than other anions in RTILs. Moreover, the disposal of these RTILs is often difficult as they contain fluorine, which is poisonous and dangerous to humans.<sup>41-42</sup> Due to this issue, non-fluorinated orthoborate, carborane anion-containing RTILs that are less expensive and have low coordination are also developed.<sup>43-45</sup>

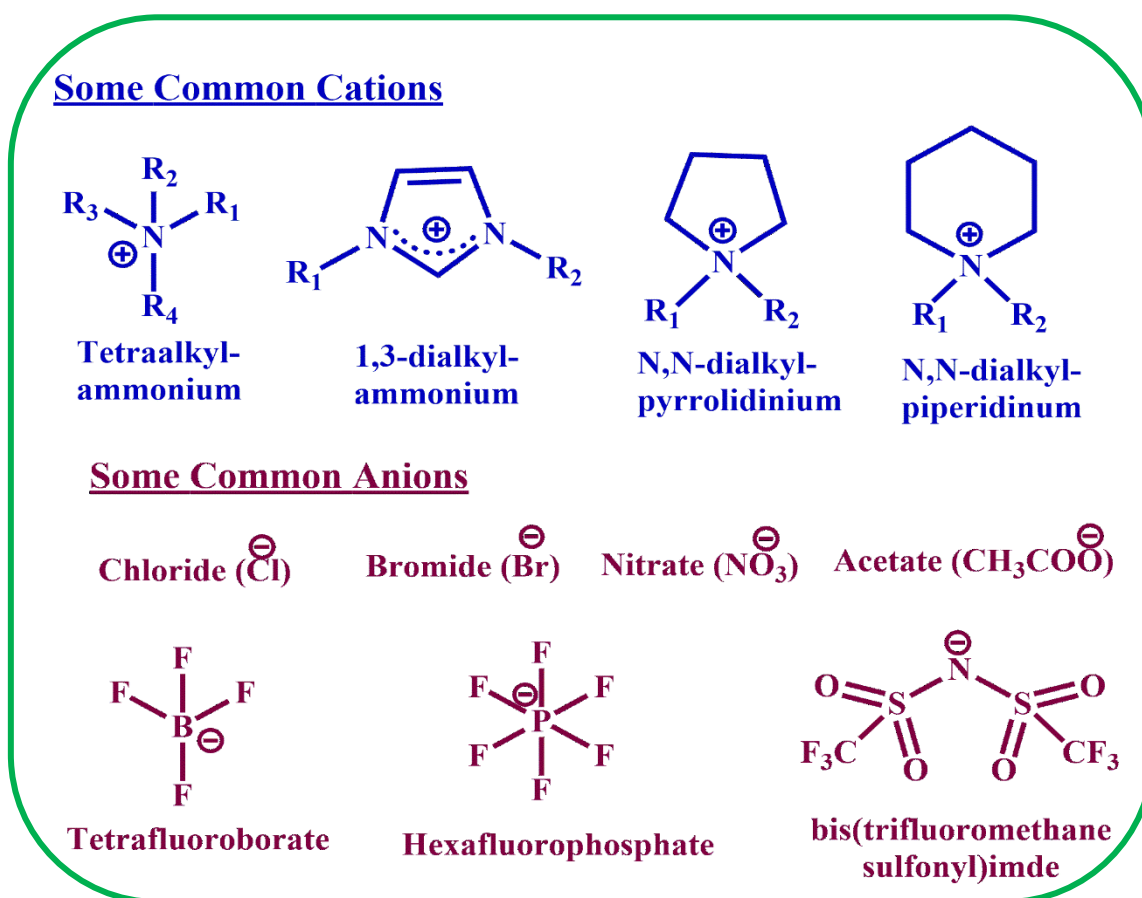


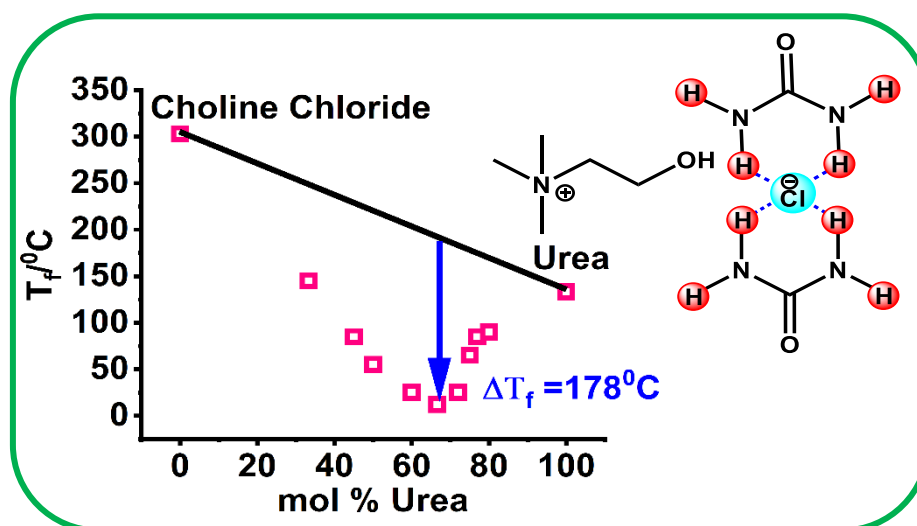
**Chart 1.1.** Molecular diagrams of different cations and anions that are used to synthesize various ILs.

Development of RTILs has expanded significantly in recent years, and many other types of ILs, such as geminal dicationic ILs, functionalized ILs, amino acids-based ILs, etc., have been synthesized.<sup>45-53</sup> Apart from this, task-specific ILs (TSILs) have become more popular as they are specifically designed for a particular application.<sup>54,55</sup> TSILs are synthesized by modifying the cation or anion, or by introducing new functionalities in a conventional ionic liquid to modulate its properties. There are diverse classes of ILs that can be functionalized with various types of functional groups. TSILs having some common functional groups, such as amine, thiol, hydroxyl, carboxylate, etc., have found many applications in diverse areas such as CO<sub>2</sub> capture, asymmetric synthesis, energy storage and conversion, lubricants, etc.<sup>56-62</sup>

### **1.3. Deep eutectic solvents (DESs)**

DESs are eutectic mixtures that are formed by mixing two or more solid or liquid components in a specific ratio that results in a melting point much lower than that of each individual component.<sup>19, 20, 63</sup> The word "DES" refers to liquids that are close to the eutectic composition of the mixture, or the component molar ratio that results in the lowest melting point.<sup>19, 20, 64</sup> DESs are usually composed of large, nonsymmetric ions that have low lattice energy and therefore low melting points. Abbott and co-workers<sup>63</sup> were able to create the first DES in 2003 through the combination of choline chloride and urea in a 1:2 ratio. Although choline chloride and urea have melting points of 303°C and 133°C, respectively, the resulting mixture had a melting point of 12°C and became liquid at room temperature due to a 178°C depression in freezing point temperature. This significant decrease in freezing point led Abbott et al.<sup>63</sup> to coin the term "Deep Eutectic Solvents" to distinguish them from conventional ILs. The researchers have also suggested that DESs are formed through the combination of hydrogen bond donors (HBD), such as quaternary ammonium/phosphonium salts, with hydrogen bond acceptors (HBA), such as acid, amide, or alcohol functionalities.<sup>19,20</sup> The drop in the melting point of the

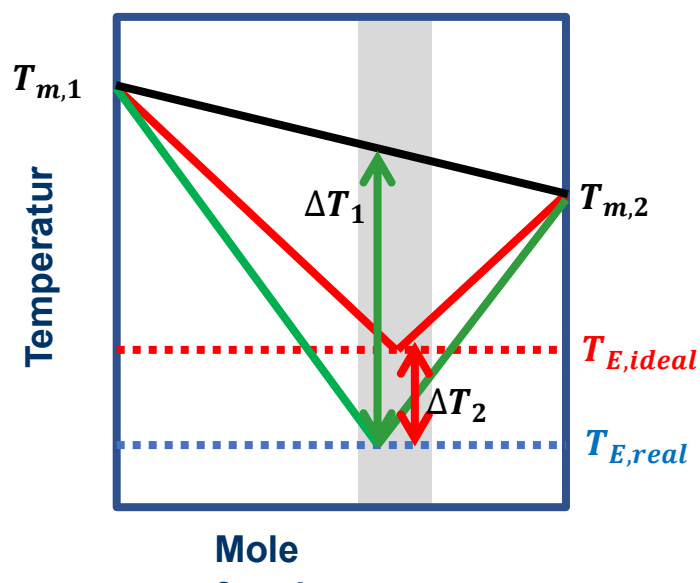
combination in comparison to the melting points of the individual components is brought about by the charge delocalization that takes place through hydrogen bonding between, say, a halide ion and the hydrogen-donor moiety.<sup>63, 64</sup>



**Scheme 1.1.** (a) Phase diagram for the combination of choline chloride with urea at different mol % of urea. (b) Proposed complexation occurring in ChCl:urea DES (1:2 molar ratio) (both figure are adapted from Abbott et al.<sup>63</sup>

It is noteworthy that DESs differ from traditional ILs in two ways: firstly, DESs are not entirely composed of ions, can also include molecular components, and secondly, they can also be formed by combining non-ionic components.<sup>20, 65</sup> It is to be noted that DESs are not pure substances but rather a mixture of two or more pure components. Moreover, DESs are distinct from simple eutectic mixtures in many aspects.<sup>19-20</sup> In 2019, Martin and colleagues<sup>66</sup> proposed a more comprehensive definition of DESs that builds upon the previous understanding of these systems. According to this definition, a DES is a mixture of pure compounds for which the eutectic point temperature is below that of an ideal liquid mixture. This means that the mixture has a lower melting point than what would be expected for a simple eutectic mixture. In order to differentiate a mixture as a DES from other simple eutectic mixtures, the phase diagram should be known. This is because DES systems exhibit strong negative deviations from ideality, meaning that their properties and behaviour differ significantly from what could be

expected for an ideal mixture.<sup>66</sup> However, later on, the definition of DESs provided by Alhadid et al.<sup>67</sup> in 2019 builds on the concept of a simple eutectic mixture with a lower eutectic point temperature than the melting temperatures of the pure constituents, but they added the requirement that the depression in eutectic temperature must be large enough to form a liquid at the operating temperature. In other words, the eutectic mixture should remain in the liquid phase under the operating conditions of interest. Therefore, to identify a mixture as a DES using this definition, knowledge and understanding of solid-liquid equilibria (SLE) are necessary.<sup>67</sup> By studying the SLE of a mixture, researchers can determine the eutectic point and the temperature range in which the mixture will remain in the liquid phase. Overall, it has been mostly accepted by the scientific community that a simple eutectic mixture with a large depression in eutectic temperature relative to the melting temperatures of the pure constituents can be considered a DES if it remains in the liquid phase at the operating temperature.<sup>19-20,63-67</sup>



**Scheme 1.2.** Comparison of the solid-liquid equilibrium (SLE) of a simple ideal eutectic mixture (represented in red) and a deep eutectic mixture (represented in blue). The melting temperatures of the individual components are denoted by  $T_{m,1}$  and  $T_{m,2}$ . The temperature depression is indicated by the difference ( $\Delta T_2$ ) between the ideal eutectic point ( $\Delta T_{E,ideal}$ ) and the real eutectic point ( $\Delta T_E$ ), and not by the difference ( $\Delta T_1$ ) between the linear combination of the melting points of the pure components and the real eutectic point. (This figure has been adapted from Martins et al.<sup>66</sup>)

### 1.3.1 Classification of DESs

With the increasing number of DESs being reported, there is a need to organize and classify these solvent systems based on their constituent components. The general formula that helps to describe DESs is given below<sup>19</sup>,



where Cat<sup>+</sup> is fundamentally any cation containing ammonium, phosphonium, or sulfonium group, and X<sup>-</sup> is a Lewis base, for the most part, a halide anion. When an anion (X<sup>-</sup>) interacts with a Lewis or Brnsted acid (Y), a complex anionic species (Z, where z is the number of Y molecules involved) is formed, which is particularly responsible for the decrease in the freezing point temperature. Smith et al.<sup>19</sup> proposed a classification system that divides DESs into four types (I, II, III, and IV) based on their components. Table 1.1 represents the different classes of DESs.

**Table 1.1.** Classification of DESs

Types		General Formula	Terms
Type I	Quaternary ammonium salt + metal chloride	$\text{Cat}^+ \text{X}^- z\text{MCl}_x$	M = Zn, Sn, Fe, Al, Ga, In
Type II	Quaternary ammonium salt + metal chloride hydrate	$\text{Cat}^+ \text{X}^- z\text{MCl}_x \cdot y\text{H}_2\text{O}$	M= Cr, Co, Cu, Ni, Fe
Type III	Quaternary ammonium salt + hydrogen bond donor	$\text{Cat}^+ \text{X}^- z\text{RZ}$	Z= CONH <sub>2</sub> , COOH, OH
Type IV	Metal chloride hydrate + Hydrogen bond donor	$\text{MCl}_x + \text{RZ} = \text{MCl}_{x-1}^+ \cdot \text{RZ} + \text{MCl}_{x+1}^-$	M= Al, Zn, and Z= CONH <sub>2</sub> , OH

As mentioned above, there are four types of DESs classified according to the nature of the complexing agent and a quaternary ammonium salt. Type I DESs are prepared by the combination of quaternary ammonium salts with metal chlorides. Abbot et al.<sup>68</sup> have synthesized the moisture-stable, Lewis-acidic DESs by mixing appropriate molar ratios of

$MCl_2$  ( $M = Zn$  and/or  $Sn$ ) and quaternary ammonium salts having the general formula  $[Me_3NC_2H_4Y]Cl$  ( $Y = OH, Cl, OC(O)Me, OC(O)Ph$ ). Type II DESs are formed by the complexation of quaternary ammonium salts with metal chlorides. Example includes the dark, viscous liquids formed by the combination of choline chloride with chromium (III) chloride hexahydrate in a 1:2 molar ratio.<sup>69</sup> Type III DESs are also known as organic-organic eutectic mixtures and are becoming increasingly popular due to their metal-free nature, ease of preparation, stability to moisture, and potential for biodegradability. Unlike Type I and II DESs, which contain metal salts, Type III DESs are formed by mixing two or more organic compounds, typically a hydrogen bond donor (HBD) and a hydrogen bond acceptor (HBA).<sup>21, 63, 64</sup> The common HBAs are the quaternary ammonium/phosphonium salts (Chart 1.2), while common HBDs include acid, amides, and alcohol functionalities (Chart 1.3).<sup>19, 20</sup> Since there are numerous HBAs and HBDs are available, large number of Type III DESs can be synthesized. Many review articles have been published signifying the potential of Type III for their industrial scale preparation and use in various fields. Type IV DESs results from the combination of metal chloride hydrate with different HBDs. Examples includes the eutectic mixture of  $ZnCl_2$  with HBDs like urea, acetamide, ethylene glycol.<sup>70</sup> In recent times, apart from these four categories of DESs, another class of DESs have also found growing interest from the research scientific community. These are formally called as Type V DESs or hydrophobic or non-ionic DESs.<sup>71, 72</sup> These types of DESs are phenol or phenolic compound-based DESs where the phenolic OH involves in hydrogen bond formation with another component. Examples include the DES formed by the combination of thymol with menthol.<sup>71-72</sup>

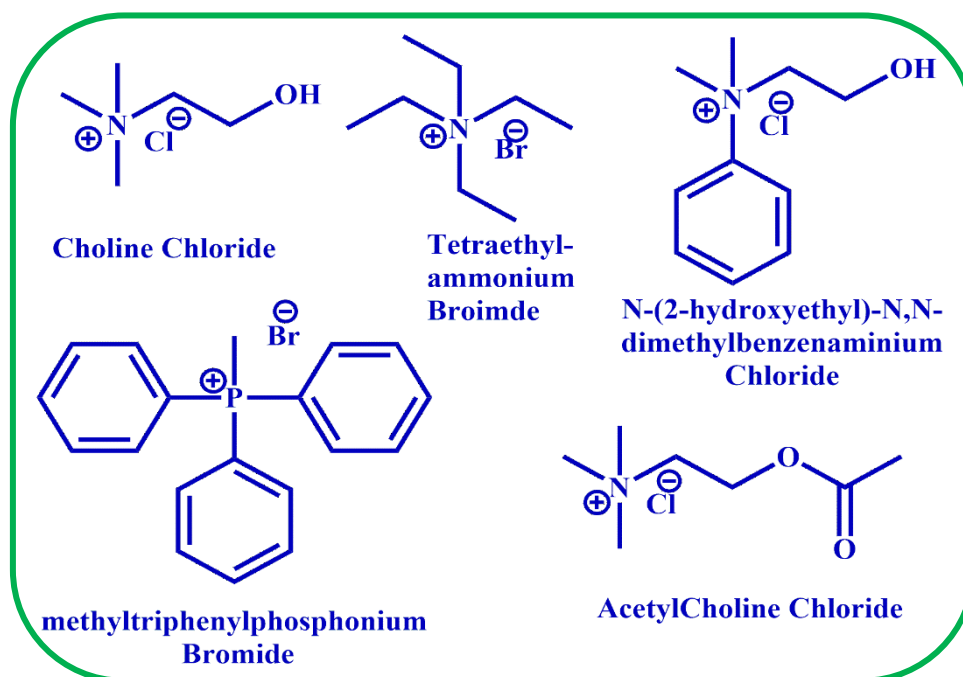


**Chart 1.2.** Some common hydrogen bond acceptors (HBAs)

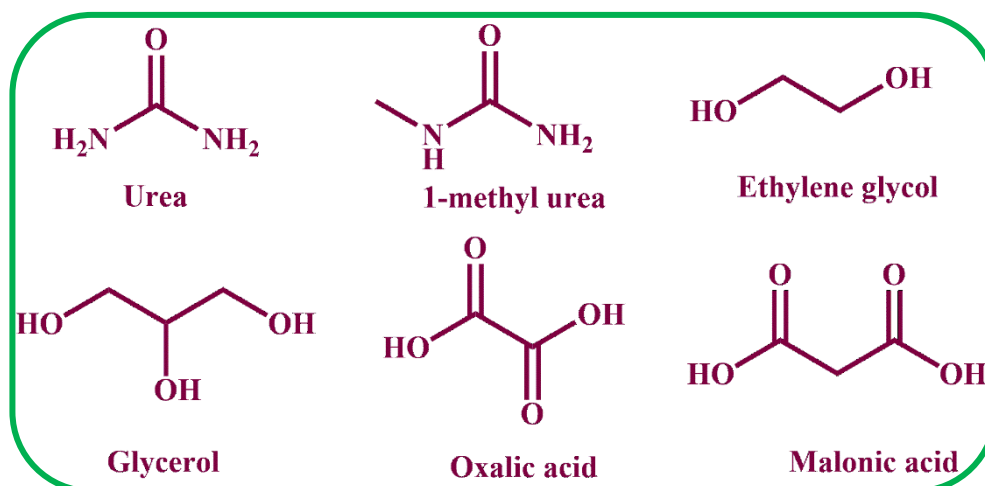


**Chart 1.3.** Some common hydrogen bond donors (HBDs)

#### 1.4. General Physical Properties of RTILs and DESs

Both RTILs and DESs share many interesting physiochemical properties, such as low vapour pressure, non-flammability, high viscosity and density, high thermal and chemical stability, etc.<sup>19, 20, 23, 29, 31, 73</sup> Moreover, these properties can be tuned by varying cations and anions of ILs and the constituents as well as the composition of the components of the DESs. Because of these properties, both DESs and ILs are referred as “designer solvents”.<sup>20, 29, 31</sup> Theoretically,

it is possible to generate  $10^{18}$  combination cations and anions to synthesize different ILs.<sup>29</sup> Similarly,  $10^6 - 10^8$  number DESs can be prepared by different combinations of constituents and by changing the composition of the constituents.<sup>19,20</sup> Some common physical properties of both ILs and DESs are provided in the following tables.

**Table 1.2.** Common physical properties of some ILs<sup>74</sup>

Systems	$T_m$ ( $^{\circ}\text{C}$ )	P (g/cm)	$\eta$ (cP)	$\sigma$ (mS $\text{cm}^{-1}$ )
EMIM Cl	86	solid	solid	solid
BMIM Cl	65	solid	solid	solid
EMIM Tf <sub>2</sub> N	-3	1.52	1.52	34
BMIM Tf <sub>2</sub> N	-4	1.43	1.43	52
OHEMIM Tf <sub>2</sub> N	-9	1.57	1.78	56

**Table 1.3.** Common physical properties of some choline chloride (melting point 576K)-based DESs with different hydrogen bond donor<sup>20</sup>

HBDs ( $T_m$ , K)	$T_m$ (K)	P (g/cm)	$\eta$ (cP)	$\sigma$ (mS $\text{cm}^{-1}$ )
Urea (406)	285	1.25	750	0.199 (313K)
Glycerol (290.8)	233	1.18	376	1.05 (293K)
Ethylene glycol (260.1)	207	1.12	40	7.61 (293K)
Malonic acid (408)	283	1.25	1124	-
2,2,2-Trifluoroacetamide (345)	228	1.342	256	0.39 (313K)

**1.4.1. Melting Point:** Melting is the process by which a solid changes phase to become a liquid. During melting, the crystal lattice of a solid is disrupted, causing the molecules or ions to move more freely and lose their ordered arrangement. Both ILs and DESs

have a wide liquid range due to their low melting point and high decomposition temperature. The lowest melting point for RTILs documented to date is  $-96^{\circ}\text{C}$ .<sup>25</sup> The intermolecular interaction and charge delocalization of the cations and anions significantly influence the melting point of temperature.<sup>75</sup> Similarly, in DESs, the composition and the strength of intermolecular interaction among the constituents of DESs significantly control the melting point.<sup>19-20</sup>

**1.4.2. Thermal Decomposition temperature:** Thermal stability is the ability of a material to resist decomposition or degradation due to exposure to certain high temperatures. The thermal stability of a material is typically characterized by its thermal decomposition temperature, which is the temperature at which the material starts to decompose. Thermal stability of both ILs and DESs depends upon their respective constituents. ILs typically have a thermal stability of up to  $450^{\circ}\text{C}$  and a decomposition temperature of  $300\text{--}500^{\circ}\text{C}$ .<sup>76,77</sup> DESs exhibit thermal behaviour that differs significantly from that of ILs.<sup>78</sup> ILs typically undergo breakdown at higher temperatures, starting with either the anion or cation and ultimately resulting in the degradation of the opposing ion. In contrast, the hydrogen bond connections between DESs often weaken at high temperatures, causing them to initially decompose into hydrogen bond donors (HBDs) and acceptors (HBAs).<sup>79</sup> HBDs with low boiling points or weak stabilities then undergo volatilization or decomposition, whereas the HBAs experience this process at higher temperatures. For instance, choline chloride (ChCl), the most commonly used HBA, begins to degrade at approximately  $250^{\circ}\text{C}$ .<sup>80</sup>

**1.4.3. Density:** Density is defined as the mass per unit volume of a material. It is the measure of how closely packed the particles (atoms, ions, or molecules) in a substance are. The denser a substance is, the more closely packed its particles are. Both RTILs and DESs are much denser than water, with a density between 1.0 to 1.7. For ILs, as the alkyl

chain length of the cation increases, the density of alkylammonium, alkylimidazolium, and alkympyrrolidinium ILs decreases.<sup>81, 82</sup> Additionally, the densities of ILs are influenced by the nature of the cation and anion. When there is a variation in the cationic moiety, the density generally decreases in the order of pyridinium ILs > imidazolium ILs > aliphatic ammonium ILs and piperidinium ILs.<sup>83</sup> In the case of ILs with 1-ethyl-3-methylimidazolium ([EMIM]) cation, the trend of density with respect to the anion follows the order:  $\text{CH}_3\text{SO}_3^- < \text{BF}_4^-$  and  $\text{CF}_3\text{COO}^- < \text{CF}_3\text{SO}_3^- < (\text{CF}_3\text{SO}_2)_2\text{N}^- < (\text{C}_2\text{F}_5\text{SO}_2)_2\text{N}^-$ . The densities of DESs are determined by their composition and constituents. In some DESs, the density is higher than that of the pure components, while the opposite behaviour is also observed. This significant variation in density could be due to the different molecular organization or packing of the DES.<sup>20, 84, 85</sup>

**1.4.4. Viscosity:** Viscosity refers to the resistance of a fluid to flow or deformation caused by internal friction between its molecules or particles. It is a measure of the fluid's thickness or resistance to motion and is typically described as the ratio of the applied shear stress to the resulting shear rate. The higher the viscosity of a fluid, the more resistant it is to flow, while the lower the viscosity, the more easily it can flow. The viscosities of both RTILs and DESs are very high from conventional solvents.<sup>86</sup> Even though for most of the RTILs and DESs, the viscosity is comparable, their viscosity is controlled by respective constituents and the relative interaction between them.<sup>87, 88</sup> Experimental observations indicate that as the chain length of the cation in ILs increases, the viscosity also increases due to strong van der Waals interactions between the cations.<sup>89, 90</sup> Additionally, the ability of the anion to participate in hydrogen bonding is also known to affect the viscosity of the ILs. For instance, ILs with anions such as  $\text{PF}_6^-$  and  $\text{BF}_4^-$  are typically more viscous compared to those with  $\text{Tf}_2\text{N}^-$  ions due to the electronic effect resulting from the presence of a fluoride atom, as well as the

dispersion of the negative charge on the two sulfoxide groups of the  $\text{Tf}_2\text{N}$  anion.<sup>87-90</sup> Similarly, for most DESs, the viscosity is usually greater than 100 cP (except ethylene glycol-based DESs and some non-ionic DESs).<sup>19-20</sup> The high viscosity of DESs is generally attributed to the extensive hydrogen bond network between each component, which restricts the mobility of free species within the DES. The high viscosity may also be due to other factors, such as the large size of the ions and the small void volume of most DESs, as well as other forces, such as electrostatic or van der Waals interactions.<sup>85, 91, 92</sup>

**1.4.5. Conductivity:** Conductivity refers to the ability of a material or substance to conduct electricity. The conductivity of both RTILs and DESs is influenced by several factors, including the nature and concentration of the ions present in the solvent, the temperature, and the viscosity of the solvent. Since ILs are entirely composed of ions, their conductivity is found to be relatively higher as compared to DESs.<sup>93, 94</sup> For example, the ionic conductivity of some ILs can be reached up to  $\sim 10 \text{ mS cm}^{-1}$ .<sup>94, 95</sup> However, for DESs, the ionic conductivity is close to  $2 \text{ mS cm}^{-1}$ .<sup>96, 97</sup> Since the HBAs and the anion of the HBAs of a DES are involved in strong hydrogen bonding interactions, it limits the conduction of the ionic species in the DESs. Nevertheless, the conductivity of DESs is still higher as compared to the common volatile solvents and can still be considered as a potential candidate for electrolytic applications.<sup>19-20</sup>

**1.4.6. Electrochemical Potential Window (EPW):** The EPW refers to the voltage difference between the cathodic and anodic limits of an IL, where the cathodic limit represents the reduction potential and the anodic limit represents the oxidation potential. This voltage range indicates the zone within which the tested substance remains inert, i.e., it does not undergo oxidation or reduction. In certain applications, such as supercapacitors, the EPWs are of primary importance, while in others, such as in lithium-ion batteries, the

cathodic and anodic limits are more critical. ILs generally possess wide electrochemical windows, and their EPWs can exceed 6 V.<sup>98</sup> This feature provides an added advantage when the same is compared with traditional organic solvents containing supporting electrolytes, such as acetonitrile (5.0 V), dichloromethane (3.5 V), and dimethylsulfoxide (4.4 V).<sup>99</sup> Even though the EPWs of DESs are notably narrower than those of ILs, they are still broad enough to cater to various potential applications such as metal processing (for instance, metal deposition and oxidation) and synthetic applications. The EPWs of DESs fall in the range of 1.2 to 4.72. DESs, which are formed by combining choline chloride with urea, methyl urea, and malonic acids, are known to exhibit EPWs that range from 4.3 to 4.72.<sup>99</sup>

**1.4.7. Polarity:** Polarity usually refers to the distribution of electrical charge within the molecule, and it is a very important parameter for predicting the physical and chemical behaviour of a substance in various contexts. The polarity of a solvent can be assessed using the micro-polarity parameter,  $E_T(30)$ , which is determined by measuring the electronic transition energy ( $E_T$ ) of a probe dye, such as Reichardt's Dye 30, in the solvent using absorption spectroscopy techniques like UV-Vis spectroscopy.<sup>100, 101</sup> Although this is a commonly used method, there are several other methods available for determining solvent polarity, including EPR spectroscopy, microwave spectroscopy, FT-IR spectroscopic probe method, FT-IR combined with density functional calculations (DFT), etc.<sup>101</sup> The polarities of many ILs are found to lie close to the polarity of common solvents like acetonitrile, alcohol, etc.<sup>102</sup> However, hydroxyl functionalized ILs having  $\text{NTf}_2$  as anions have shown unusual hyper-polarity with the  $E_T(30)$  value close to water.<sup>103</sup> For DESs that contain alcohol groups as the HBDs (hydrogen bond donors) generally exhibit higher polarity as compared to those containing other HBDs like amide and acid.<sup>104, 105</sup>

### 1.5. ILs versus DESs

Both DESs and RTILs share many similar characteristic features, solvent properties, and unique applications, due to which DESs are often regarded as a sub-class of ILs.<sup>106</sup> However, both ILs and DESs are by far different classes of solvents.<sup>65, 107, 108</sup> One of the major differences between ILs and DESs is their composition and structure. While ILs are entirely consisting of ions, DESs have both ionic as well molecular components. In RTILs, apart from some non-covalent interactions such as van der Waals forces, hydrogen bonding, and dipole-dipole interactions, the Coulombic interaction between the cations and anions is the dominant contributor to the structure and properties of the ILs.<sup>65</sup> On the other hand, in DESs, it is believed that complex hydrogen bonding between the constituent species is the main contributor to the macroscopic physicochemical properties of DESs.<sup>65</sup> The strength of the hydrogen bonding interaction between the hydrogen bond donor and acceptor significantly influences the properties of the DESs. Apart from these differences, DESs are generally known to be more environmentally friendly as compared to the ILs as the former compensate several drawbacks of ILs, including toxicity, biodegradability, biocompatibility, and so on, making them even a superior media for enzymatic reactions, storage, and boosting the stability of various biomacromolecules.<sup>109, 110</sup> As stated before, one of the main drawbacks of RTILs is their potential toxicity, which arises due to the fact that many RTILs contain halogens or other potentially harmful components. In contrast, DESs are often composed of naturally occurring compounds that are less toxic and more biocompatible.<sup>21, 64</sup> Moreover, ILs are generally costly, require complex synthesis and rigorous purifications which prevents their large-scale uses.<sup>106</sup> However, DESs can be simply prepared by mixing and heating the HBAs and the HBDs at a particular composition. Additionally, the starting materials of DESs are readily available and relatively cheaper as compared to ILs. Thus, their simple and energy-efficient preparation coupled with economic viability while retaining many of the desired characteristics of ILs, such

as non-flammability, high thermal stability, high degree of tunability, and good solubilizing power, etc., make them a potential alternative to their counterpart.<sup>19-20</sup>

**Table 1.4.** Some Common differences between ILs and DESs

Ionic liquids (ILs)	DESs
➤ Contain discrete ions	➤ Complex hydrogen bonding between HBA and HBD
➤ Toxic and poor bio-degradability	➤ Relatively Less toxic and biodegradable
➤ Conductivity is high	➤ Conductivity is moderate to high
➤ Complex synthesis and purification	➤ Simple synthesis with no subsequent purification
➤ Expensive and recycling is critical	➤ Cheaper than ILs

## 1.6. Applications of ILs and DESs

The unique properties of DESs and RTILs make them attractive for wide range of applications in chemistry, materials science, energy storage, and biotechnology.<sup>111-115</sup> Both RTILs and DESs have found applications in reaction media, extraction media, gas adsorbates, drug delivery, organic synthesis, electrochemical applications, lubricants, etc.<sup>116-121</sup> Specifically, RTILs find extensive applications in electrochemistry and battery-related research, while DESs are highly applicable in the fields of extraction and bio-transformations.<sup>122-125</sup> Several review articles have been published to recognize and discuss the various applications of both RTILs and DESs.<sup>19-20,126</sup> This section aims to highlight and appreciate the importance of these solvents by discussing some of their selected applications.

*Organic Synthesis:* One of the most significant advantages of both RTILs and DESs is their ability to dissolve a wide range of organic and inorganic compounds, including polar and non-polar compounds, as well as biomolecules. This makes them highly versatile and suitable for a variety of chemical reactions, such as acid-catalysed reactions, metal-catalysed reactions, and enzyme-catalysed reactions.<sup>17, 126</sup> ILs have been employed in several organic reactions, including Diels-Alder, Friedel-Craft, esterification, and Fisher-Indole synthesis.<sup>127</sup> Furthermore, ILs have also been utilized in transition metal catalysed reactions such as the Heck reaction, Suzuki-cross coupling reaction, and ring-closing metathesis reaction, demonstrating excellent stereoselectivity and regioselectivity.<sup>127</sup> Similarly, DESs have been employed in various organic reactions, such as electrophilic substitution, Knoevenagel, and mono-N-alkylation of aromatic amine, along with metal-catalysed reactions like palladium-catalysed coupling reactions (Suzuki, Heck, Sonogashira, and stille coupling reactions).<sup>20</sup> The use of both RTILs and DESs in organic synthesis is rapidly increasing, and more reactions are expected to be conducted in these solvents in the future.

*Nano particle and material synthesis:* DESs and RTILs are promising solvents for the synthesis of metal nanoparticles due to their ability to dissolve a variety of inorganic salts. Lee et al.<sup>128</sup> reported a size-selective synthesis of gold and platinum nanoparticles in thiol-functionalized ILs. Other types of ILs, such as imidazolium and ammonium-based RTILs, have also been used for synthesizing various types of nanoparticles.<sup>129</sup> On the other hand, Sun et al.<sup>130</sup> reported the synthesis of star-shaped gold nanoparticles in reline DESs, and Chirea et al.<sup>131</sup> synthesized gold nanowires through the direct reduction of  $\text{HAuCl}_4$  by  $\text{NaBH}_4$  in DESs. Wong et al. recently developed a method for synthesizing various ZnO nanostructures, including twin cones and nanorods with controllable dimensions, in DESs.<sup>132</sup> DESs and RTILs have also been used to synthesize a variety of zeotypes based on aluminophosphate, borophosphate, zinc phosphates, zirconium phosphates, iron oxalato phosphates, and more.<sup>20</sup>

Additionally, these solvents have been found to have applications in the synthesis of metal-organic frameworks.<sup>20</sup>

*Extraction media:* DESs and RTILs are non-volatile solvents that can dissolve metal ions and form stable complexes with them. This makes them highly effective in metal extraction processes, such as mining and recycling of metals from electronic waste.<sup>19-20</sup> DESs have been shown to be effective in the extraction of metals such as copper, nickel, and zinc from various sources, including ores, tailings, and industrial waste.<sup>19-20</sup> A choline chloride-ethylene glycol-urea hybrid DES was found to be excellent for extracting lead and zinc from electric arc furnace (EAF) dust with selectivity towards only zinc and lead oxides, leaving iron and aluminium oxides insoluble.<sup>133</sup> Similarly, RTILs have been found to be effective in the extraction of various metals, including gold, platinum, and palladium.<sup>134</sup> Rogers et al.<sup>135</sup> demonstrated that the extraction efficiency of  $\text{Hg}^{2+}$  and  $\text{Cd}^{2+}$  was significantly enhanced by utilizing dithizone solubilized in 1-butyl-3-methylimidazolium hexafluorophosphate  $[\text{C}_4\text{Mim}][\text{PF}_6]$ .

*Gas Adsorption:* Both DESs and RTILs are found to be very excellent to act as a gas adsorbate for different gases like  $\text{CO}_2$ ,  $\text{SO}_2$ , etc. Davis et al.<sup>136</sup> synthesized a room temperature ionic liquid by reacting 1-butyl imidazole with 3-bromopropylamine hydrobromide and anion exchange. The resulting ionic liquid contains an amine group and can reversibly capture  $\text{CO}_2$  as a carbamate salt, exhibiting high recyclability. Similarly, Han et al.<sup>137</sup> discovered that a  $\text{ChCl}$ :urea DES supported on molecular sieves is highly efficient as a catalyst for the chemical fixation of  $\text{CO}_2$  to cyclic carbonates. Moreover, it has also been observed that  $\text{ChCl}$ :glycerol readily adsorbs and releases  $\text{SO}_2$ .<sup>138</sup>

*Electrochemical applications:* Both DESs and RTILs have sufficiently large electrochemical windows, making them suitable for use in various electrochemical applications, including batteries, supercapacitors, fuel cells, and more.<sup>99</sup> In particular, RTILs have been extensively studied for their use in solid-state batteries due to their high ionic conductivity, low volatility,

and ability to operate at room temperature. They have been shown to have great potential in improving the performance and safety of various types of batteries, including lithium-ion batteries applications. A solid PEO-LiTf<sub>2</sub>N-[MPPYRRO][Tf<sub>2</sub>N] polymer electrolyte is observed to deliver almost 90% of the theoretical capacity of a Li/electrolyte/LiFePO<sub>4</sub> battery at 40°C.<sup>139</sup> The battery has a charge efficiency of about 99% and capacity retention of 97.6% after 50 cycles. Similarly, Wang et al.<sup>140</sup> combined 1-methyl-3-propylimidazolium iodide and PVDF-HFP to create a polymer gel electrolyte for use in dye-sensitized solar cells (DSSCs) with hydrophobic dye-coated nanocrystalline TiO<sub>2</sub> electrodes sandwiched with counter-electrodes and filled with the ionic liquid-based electrolyte. Moreover, Wanatabe et al.<sup>141</sup> found that certain ILs can serve as the electrolyte for fuel cell reactions, exhibiting electroactivity for H<sub>2</sub> oxidation and O<sub>2</sub> reduction in non-humidifying conditions. On the other hand, a recent study has shown that ChCl/glycerol-based DES can be used as an effective electrolyte in dye-sensitized solar cells.<sup>142</sup> In fact, it was found that 3.88% of sunlight was converted, which is comparable to most IL-based electrolytes. Moreover, DESs are also used to obtain highly conductive natural polymer-based electrolytes, including cellulose acetate, corn starch-based polymers, and p-doped polypyrrole.<sup>20</sup>

*Biological applications:* Both RTILs and DESs have gained significant attention in recent years due to their suitability for a wide range of bio-related applications such as stabilization of protein, inhibition of fibrillation formation, drug delivery, enhancement of enzyme activity, etc.<sup>20, 126</sup> Wu et al.<sup>143</sup> evaluated choline-based ILs for their ability to enhance skin penetration and toxicity via in vitro and in vivo experiments. The results indicated that all ILs improved hyaluronic acid permeability. Banerjee et al.<sup>144</sup> developed an effective oral insulin preparation using CAGE (choline and leucovorin) IL, which interacts with the protein's amino acid residues via hydrophobic and hydrophilic bonds, forming micelles or microemulsions in intestinal fluid. Kim and Lee<sup>145</sup> proposed a simple method to improve enantioselectivity by mixing

*Pseudomonas cepacia* lipase with 1-(3'-phenylpropyl)-3-methylimidazolium hexafluorophosphate ionic liquid. This resulted in higher enantioselectivity compared to commercial lipase of PS-C in toluene, with no significant effect on the reaction rate. Similarly, in 2008, Gorke et al. demonstrated the transesterification of ethyl valerate to butyl valerate, catalysed by hydrolase, in choline chloride/glycerol DESs.<sup>146</sup> Apart from this, many other bio-related applications of DESs have also been reported in the literature.<sup>19-20</sup>

### 1.7. Structure and Dynamics of RTILs and DESs

The study of the organization of molecules in the bulk solvents, specifically in ILs and DESs, is an important area of solvent research, as it has a significant influence on their properties and performance. Specifically, the structure and dynamics of ILs, and supercooled liquids have been extensively investigated previously.<sup>29</sup> Many state-of-the-art experimental techniques such as spectroscopy (2D IR, dielectric relaxation, FT-IR, NMR, OHD-OKE, ultrafast fluorescence, SFG vibrational, neutron diffraction, XPS, XRD, AFM, and theoretical studies based on computer simulations (DFT calculations, ab initio, MD simulations) have been employed to gain insights into the microstructures and dynamics of ILs (a) in bulk liquids, (b) in mixtures of ILs with cosolvents, (c) interfacial regions of ILs and cosolvent mixture, etc.<sup>29, 31</sup> It is to be noted here, as compared to ILs and other common organic solvents, investigation on DESs are rather limited. In recent times, some studies have been conducted on DESs primarily toward understanding the length and time scales of structural organization, interspecies interactions, and structure-properties relationships.

ILs are subjected to intense research, and their structure and dynamics have been investigated by almost all known physical chemistry techniques<sup>29</sup>. The studies conducted so far have indicated that ILs are solvents that can exhibit a range of structural organizations spanning from supramolecular (ion pairs, ion clusters) to mesoscopic (H-bond networks, micelle-like, and bi-continuous morphologies) length scales.<sup>26, 29-31</sup> Ethyl ammonium nitrate

(EAN) is considered as one of the most widely studied IL. The crystal structure EAN is made up of two layers of EA cations in a vertical configuration with  $[\text{NO}_3^-]$  anions interspersed between the ethyl chains.<sup>147</sup> It has also been observed that the lengths of the alkyl side chains of alkylammonium cations have a profound influence on the structural organization of these types of ILs. For example, different structural organizations have been observed in propylammonium nitrate (PAN) and butylammonium nitrate (BAN) ILs<sup>148</sup>. Unlike alkylammonium-based ILs, imidazolium-based ILs exhibit different crystal structures based on the length of the alkyl side chain that is attached to the imidazolium cation. For example, structural studies on ILs through XRD have revealed that ILs that are composed of  $[\text{C}_4\text{Mim}]$  cations and  $\text{Cl}^-$ ,  $\text{Br}^-$ ,  $\text{I}^-$ ,  $[\text{BF}_4]^-$ ,  $[\text{PF}_6]^-$  anions exhibit multiple polymorphs with rotational cation isomers in both crystalline and liquid states.<sup>149</sup> Moreover, it has also been established that imidazolium cations, with longer than  $\text{C}_{14}$  alkyl chains, can form a smectic liquid crystal phase similar to some other protic ILs.<sup>150, 151</sup> Structural studies have also shown that ILs containing halide anions and 1-alkyl-3-methylimidazolium ( $[\text{C}_n\text{Mim}]$ ) cations (where  $n = 12-18$ ) exhibit bilayer crystal lattices, with polar sheets formed by anion species and imidazolium rings, and apolar domains of interdigitated cation alkyl chains.<sup>152</sup>

Apart from this, Multinuclear NMR studies on  $[\text{C}_2\text{Mim}][\text{X}]$  ILs (where  $\text{X} = \text{Cl}^-$ ,  $\text{Br}^-$ , and  $\text{I}^-$ ) have indicated contact ion pair formation in pure ILs, and research works on transport properties of dialkylimidazolium ILs have provided indirect evidence in favour of the ion pair formation.<sup>153</sup> Furthermore, Gebbie et al.<sup>154</sup> have found evidence for a coordinated (cation + anion) network in  $[\text{C}_4\text{Mim}][\text{Tf}_2\text{N}]$ . Later on, the ion cluster model of ILs is also supported by Electrospray ionization mass spectrometry (EI-MS) technique, and describes the bulk structure of ILs in terms of a sea of polydisperse aggregates.<sup>155</sup> Additionally, Wakeham et al., based on X-ray reflectivity (XRR), sum frequency generation spectroscopy (SFG), and neutral impact collision ion scattering spectroscopy (NICISS) data, have suggested the presence of ion clusters

at PIL-air interfaces.<sup>156, 157</sup> The fact that ILs can also exhibit the micellar and reverse micellar structure is supported by XRD as well as small- and wide-angle X-ray scattering studies.<sup>158</sup> In addition to this, Margulis and co-workers<sup>159</sup>, while working on  $[C_n\text{mim}]\text{PF}_6$  (where  $n$  is 6, 8, 10, or 12) based ILs through MD simulation studies, have also reported the micellar-like structure for these ILs. They had shown that in the micellar solution of  $[C_n\text{mim}]\text{PF}_6$ , the spherical anions attracted approximately five cations, causing the imidazolium heads to solvate the negative charge and expel the alkyl chains outward and thereby facilitating the formation of dynamic, near-spherical aggregates with a polar interior and apolar exterior.<sup>159</sup> In another independent study, Schröder et al.<sup>160</sup> proposed the mesoscopic structural features of ILs based on diffusion coefficient measurements of electro-active solutes in aprotic ILs with varying water content (ref).

Similar to ILs, previous reports on the structure and properties of DESs have suggested that the formation of DESs is largely driven by the delocalization of charge between the anion and HBD during the time when they are mixed, as a result of the formation of hydrogen bonds between them. For example, Abbott et al.<sup>63</sup> used HOESY NMR spectroscopy to observe the signals of urea and choline fluoride in a DES mixture and found significant cross-peaks between the two, indicating a correlation between the two components. Additionally, Dai et al.<sup>161, 162</sup>, with the help of NOESY NMR and FT-IR spectroscopy techniques, observed the presence of hydrogen bonds between the components of NADESs. Later, Abbott et al.<sup>21</sup> demonstrated that the conductivity and viscosity trends in choline chloride-glycerol DES can indicate the existence of a 3D intermolecular hydrogen bonding network. D'Agostino et al.<sup>163, 164</sup> used PFG-NMR spectroscopy experiments to suggest the existence of extensive hydrogen-bonded chains of malonic acid molecules in malonic acid-choline chloride DES and inferred that there are complex interactions between different species within DESs. Subsequently, Pandey et al.<sup>105, 165</sup> studied the solvatochromic probe behaviour in various DESs

spectroscopically and estimated their polarity. They also pointed out that the presence of solvent-solvent interactions can be attributed to interspecies hydrogen bonding. Wagle et al.<sup>166</sup> applied quasi-elastic neutron scattering (QENS) to choline chloride-glycerol-based DES to demonstrate that the DES components can have varying localized mobilities due to their different interaction strengths. In a separate work, Edler<sup>167</sup> and his team used wide Q-range neutron diffraction measurements to study ChCl:Urea based DES and through their study, they pointed out that a radially layered sandwich structure could be formed as a result of the interaction between the constituents of reline DES, consisting of strong and weak hydrogen bonding moieties.<sup>167</sup> This sandwich structure could also be seen as a locally stoichiometric cage centered on chloride ions.<sup>167</sup>

Apart from the structural diversity in ILs and DESs, both solvent systems are also found to be dynamically heterogeneous. Samanta and co-workers<sup>168</sup> have observed the heterogeneous nature of ILs through excitation wavelength-dependent fluorescence measurement. Later on, Margulis and co-workers<sup>169</sup>, through MD simulation, have demonstrated that ILs are not only structurally heterogeneous but also, they are dynamically heterogeneous. They have found variations in ion pairing, solvent structure, and dynamics of these ILs. Moreover, time-resolved fluorescence studies by Maroncelli<sup>170</sup> and Bhattacharyya<sup>171</sup> independently have also revealed the dynamic heterogeneity of the ILs. In the same context, very recently, Hunger and co-workers<sup>172</sup>, while working on protic alkylammonium-based ILs through femtosecond IR spectroscopy, have also demonstrated the dynamic heterogeneity of ILs. Their results showed that the ILs could exhibit different relaxation dynamics in different regions of the solvent, indicating the dynamic heterogeneity of the medium. Biswas and colleagues<sup>173-179</sup> have extensively studied the dynamic heterogeneity of both ionic and non-ionic DESs through time-resolved fluorescence experiments and MD simulations. Their investigations have revealed that the solvation and probe rotation times in DESs have a fractional power dependence on the

bulk viscosity of the medium, and they have attributed this behaviour to the presence of dynamic heterogeneity in DESs. Similarly, Sen and co-workers<sup>180-184</sup> have also observed significant decoupling of solvation and translational diffusion time from the medium viscosity in various ionic and non-ionic DESs, suggesting the presence of dynamic heterogeneity in DESs. Saddam et al.<sup>185-187</sup> have also investigated the structural and dynamical behaviour of ChCl and tetraalkylammonium chloride-based DESs and observed the presence of dynamic heterogeneity in the DESs. Recently, Cui et al.<sup>188</sup>, while working on a non-ionic N-methyl acetamide/lauric acid deep eutectic solvent (DES), showed the presence of nano-segregation of polar and nonpolar domains, similar to that of micelles in the concerned medium. Additionally, Kashyap and colleagues<sup>189</sup> used MD simulations to investigate the structures of DESs that are composed of amides and lithium perchlorate. They observed nanoscale spatial heterogeneity caused by the segregated domains of lithium and perchlorate ions. Moreover, Percevault et al.<sup>190</sup> conducted small-angle neutron scattering (SANS) studies on various types of pure and hydrated DESs and confirmed the formation of segregated domains in different DESs and their mixtures with water.

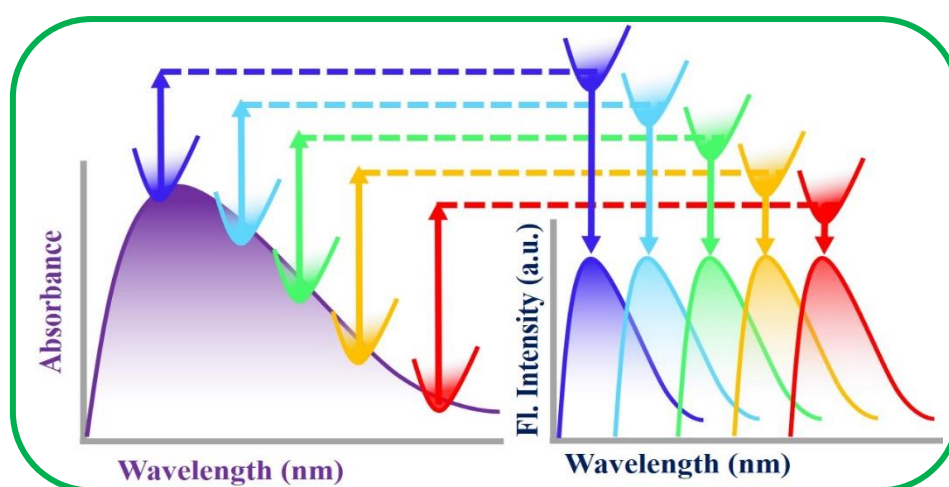
### **1.8. Photophysical Process in RTILs and DESs**

Molecular-level understanding of the intermolecular interaction, structure, and dynamics of new molecular solvents such as RTILs and DESs is essential for their practical applications in various fields. Such knowledge can provide valuable insights into the fundamental mechanisms that govern the behaviour of the concerned solvents, as well as their interactions with other molecules, and thereby, can pave the way for the development of new and improved solvent systems. Various studies based on advanced experimental and computational techniques have been carried out to probe the interactions, structure, and dynamics of the solvents at the molecular level.<sup>150-190</sup> However, probing the microstructural organization and dynamics of these solvent systems through photophysical studies of appropriately chosen fluorescent probe

molecules dissolved in these media are arguably the most suitable methods due to their exceptionally great sensitivity, high selectivity, and simplicity as compared to other available analytical techniques.<sup>180-190</sup> The following sections highlight some of the important photophysical studies in RTILs and DESs that are pertinent to the current thesis work.

***Excitation Wavelength dependence fluorescence study:*** Kasha's rule states that regardless of the excitation wavelength, the fluorescence of a molecule will originate from the lowest vibrational energy level of the lowest electronically excited state of the same spin multiplicity.<sup>191</sup> This means that the emission spectrum of a fluorescent molecule should be independent of the excitation wavelength.<sup>192, 193</sup> However, under some circumstances, it has been observed that the fluorescence spectrum of some organic fluorophores dissolved in confined media shifts towards longer wavelength regions as the excitation wavelengths are increased.<sup>194, 195</sup> This effect is more pronounced when the sample is excited at the red end of the absorption spectrum. Due to this reason, this phenomenon is usually termed as “red edge excitation shift (REES)” or red edge effect (REE).<sup>194-195</sup> REES is generally observed for viscous solvents or glass-forming liquids such as DESs and RTILs, usually at very low temperatures.<sup>168, 196</sup> In viscous media, where the solvation of a solute fluorophore is relatively slow as compared to common solvents such as water, DMSO, ethanol, etc., fluorescence can be observed from different unrelaxed states of the solvent molecules around the fluorophore in these media. Especially, when the fluorescence lifetime ( $\tau_f$ ) of the fluorophore is much shorter than the average solvation time ( $\tau_{solv}$ ) in a particular solvent, fluorophores may exist in a state where it is not fully solvent-equilibrated.<sup>168, 196</sup> Under this condition, the micro-environments around the fluorophores are different, and hence excitation at the red edge of the absorption band excites only those fluorophores with lower transition energy, and since the solvent relaxation is slower than the fluorescence lifetime, the configuration of the solvent molecules remains unchanged within the excited state lifetime, and hence the emission gets red-shifted.

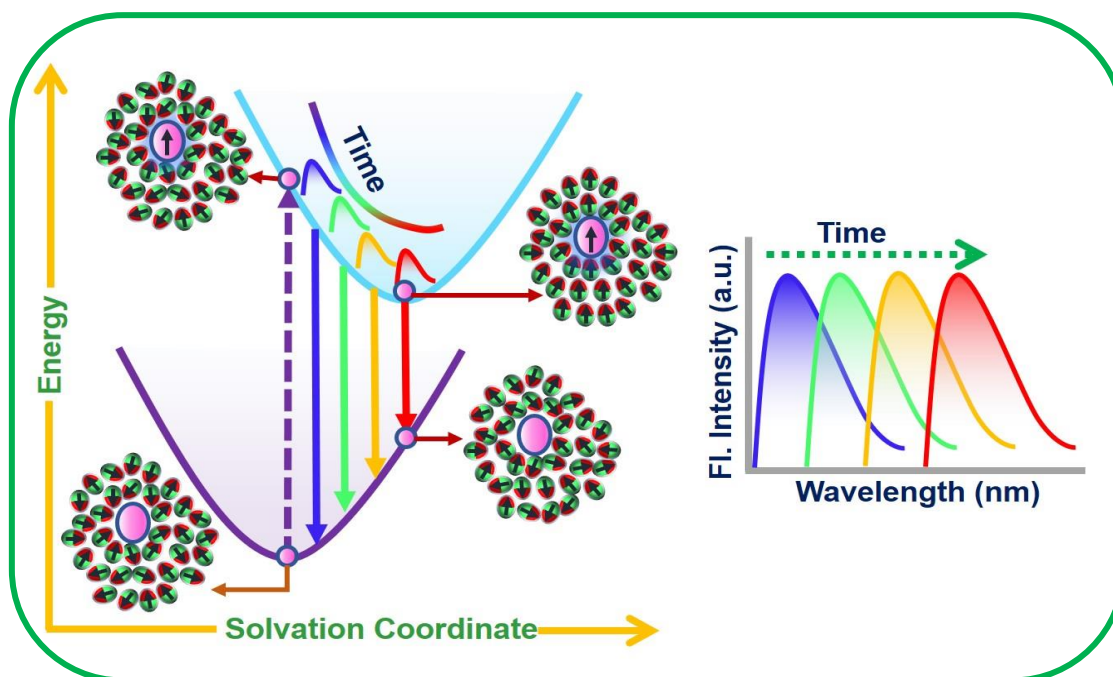
Overall, to see excitation wavelength-dependent emission behaviour, two necessary criteria must be satisfied. Firstly, the ground state must have a distribution of energetically different species, causing an inhomogeneous broadening of the absorption band. Secondly, excited state relaxation rates of these energetically different species should be slower than their fluorescence lifetimes<sup>168</sup>. The first criterion ensures that it is feasible to selectively excite species with varying energies, while the second one makes it possible to monitor emission from each species that has been excited. REES was originally noticed in ILs by Samanta and colleagues<sup>168, 196</sup>, who ascribed it to the spatial heterogeneity in ILs. Later on, Margulis and Co-workers have demonstrated through MD simulation that the origin of REES is due to the dynamic heterogeneity of the medium.<sup>169</sup> They have suggested that while the ground state heterogeneity, which permits photo-selection of the molecules, is present even in ordinary fluid media, the excitation wavelength dependency is only detectable in ILs due to the slow rate of solvation and inefficiency energy transfer among the different energetically excited species in the ILs.<sup>169, 195</sup> Despite the fact that this (REES) study cannot predict the exact length scale of micro-heterogeneity of the medium but this is a quite useful method for qualitative determination of the micro-heterogeneous behaviour of solvent systems such as DESs and RTILs. This phenomenon is pictorially represented in Scheme 1.3.



**Scheme 1.3.** Pictorial Representation of Red-Edge-Excitation Phenomena.

**Solvation Dynamics:** The study of time-dependent solvent response towards a perturbation in the molecular level of a solute dissolved in that solvent is usually termed as solvation dynamics.<sup>197</sup> The dynamics of solvation have a significant impact on a variety of chemical reactions, particularly on charge transfer and photochemical reactions. Studies on solvent relaxation processes are, therefore, crucial because they can fully characterize both the static and dynamic aspects of solute-solvent interactions.<sup>197</sup> Many advanced techniques such as time-dependent fluorescence Stokes shift measurement (TDFSS), dielectric relaxation measurements, FTIR/2DIR, optical Kerr effect (OKE) spectroscopy, transient absorption spectroscopy techniques, molecular dynamics simulation, ab initio calculation, etc., have been exploited to understand the process of solvent dynamics in DESs and RTILs independently.<sup>170, 173-179, 181-184, 198-219</sup> Out of these techniques, TDFSS measurement is the benchmark technique that has been used extensively to investigate the solvation dynamics in RTILs. Scheme 1.4 provides a pictorial representation of the process of solvation.<sup>197-210</sup> Briefly speaking, in this technique, a short laser pulse is used to electronically excite the probe solute, due to which the charge distribution of the solute is altered without changing the molecular geometry of the solute. Immediately after excitation, the solvent molecules reorganized themselves around the solute to stabilize the newly created charge distribution of the solute. This stabilization of the excited state of the solute with time due to solvent reorganization is subsequently reflected in the red shift of the emission spectra, and by estimating the shift in the emission maxima with time, the process of solvent relaxation is monitored.<sup>197-215</sup> During the investigation of solvation dynamics via TDDSS methods, a dye molecule is utilized as a solute probe in a dilute solution. Choosing an appropriate solute is crucial while studying the process of solvation dynamics. If the probe molecule has a shorter lifetime than the solvation time, it would be impossible to observe the entire solvation response. Therefore, the probe molecule used for TDDSS measurements must meet some specific requirements.<sup>197-219</sup> Firstly, the probe molecule should

undergo a significant change in dipole moment or even photoionized upon photoexcitation, leading to a substantial polar stabilization energy in the excited state. Secondly, the excited state lifetime of the probe molecule should be long enough (in the order of nanoseconds) and preferably longer than the solvent reorganization time scale of that particular solvent. Lastly, the probe molecules should not exhibit any other excited state phenomena except for the solvation process.<sup>197-219</sup> Molecular structures of some well-known fluorescent probes are shown in Chart 1.4. Out of all the probes molecules, C153 has been widely used to study the solvation dynamics process. This is because of its rigid structure and appreciable difference in the dipole moment between the ground state ( $\mu = 6\text{D}$ ) and excited state ( $\mu = 10\text{D}$ ).<sup>213</sup> Moreover, its fluorescence is sensitive to the polarity and viscosity of its surroundings, so it can be used to probe changes in the solvation environment around it. Additionally, C153 has a relatively long excited-state lifetime and large Stokes shift (that the emission and absorption maxima are well separated), which allows one to probe solvation dynamics at relatively longer time scales as well as in complex environments.



**Scheme 1.4.** Pictorial representation of the process of dynamics of solvation through time-dependent dynamic Stokes shift measurement.

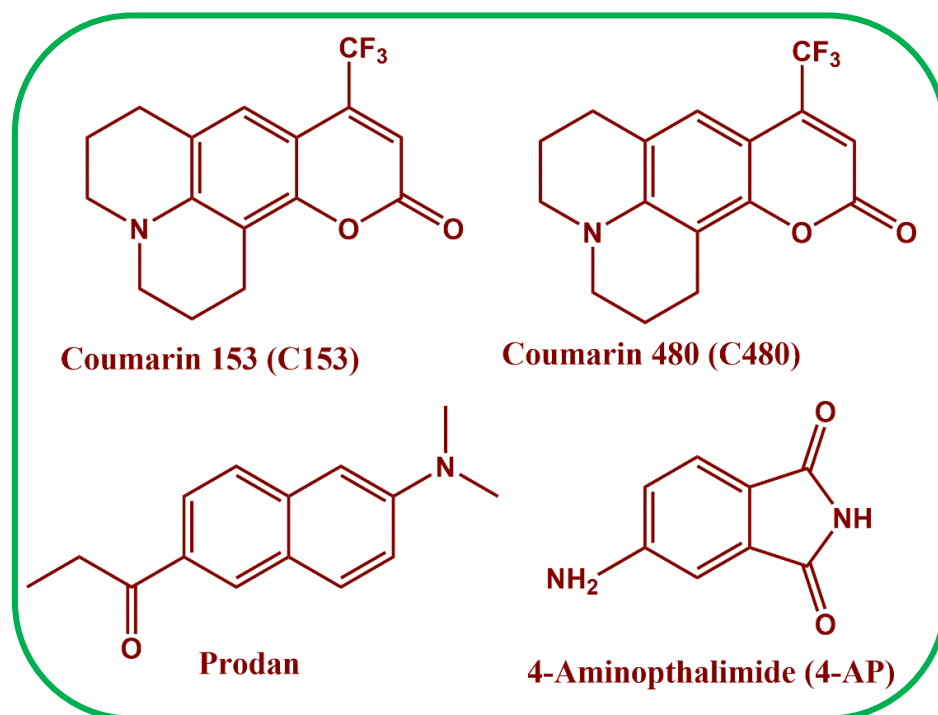


**Chart 1.4.** Representative probes molecules used for the study of solvation dynamics in DESs and RTILs.

Solvation dynamics in conventional dipolar solvents, including water, have been extensively studied starting from the 1980s.<sup>198, 200, 202, 220</sup> The results of such studies provided us with a good understanding of the temporal aspects of solvation in conventional solvents. With the emergence of ILs and their aforementioned potential applications, researchers were curious to understand the dynamics of solvation for this special class of solvent systems. Karmakar and Samanta<sup>206</sup> are the first to examine the solvation dynamics in imidazolium-based ILs through TDDSS measurement. Later on, various groups, including Maroncelli, Petrich, Castner, Bhattacharyya, Biswas, and others, have contributed significantly to understand the solvation dynamics in RTILs through both experimental and theoretical investigations.<sup>197-220</sup> All the studies have demonstrated that solvent relaxations for RTILs take place through multiple time scales, and the slowest component solvation dynamics is directly linked to the bulk viscosity of the medium.<sup>197-220</sup> Interestingly, it is to be noted that Biswas and co-workers<sup>173, 176, 178</sup> have extensively studied the solvation dynamics of acetamide-urea/

acetamide-electrolytes-based DESs through both experimental and theoretical investigations. They have pointed out the decoupling of the average solvation time from the medium viscosity. Later on, Hossain et al.<sup>187</sup> have also studied the solvation dynamics in some alkyl ammonium-based DESs to understand the effect of alkyl chain length on both the ultrafast and slower relaxation time components. Moreover, while some ultrafast solvation dynamics studies on ILs are done by exploiting the broadband fluorescence up-conversion (100 fs resolution) technique, the majority of the studies on solvation dynamics in RTILs are done by using the TCSPC technique.<sup>205-215</sup> While the TCSPC technique is quite effective in understanding the solvent relaxation at the slower time scale, it cannot provide information on the early part (at the faster time scale) of the dynamics due to the limited time resolution of the instrument.<sup>175-179</sup> Moreover, it is to be noted here that while calculating the amplitude of missing solvation components in DESs and RTILs, the estimation of time zero frequency through Fee and Maroncelli<sup>221</sup> method may lead to erroneous outcomes because of the difference in the density that may exist between the reference solvent and the solvent of interest.<sup>182</sup> Thus, to avoid this, it is always better to capture the complete Stokes shift dynamics of the solvent by employing the sub-picosecond time resolution fluorescence up-conversion technique along with picosecond time-resolved fluorescence techniques like the TCSPC technique.

The process of solvation in ILs differs significantly from that in conventional polar solvents.<sup>200-215</sup> While dipolar reorientation of solvent molecules is the primary contributor towards solvent stabilization in dipolar solvents, translational motion of the ionic constituents plays a more significant role in ILs.<sup>198-210</sup> This is due to the change in the dipole moment of the photoexcited probe molecule, which causes the ionic species in ILs to experience a net force and move from their original position, followed by attempts to reorganize themselves around the excited probe molecule. Attempts to understand solvation dynamics in ILs through computer simulation studies have yielded conflicting results. Shim et al.<sup>222</sup> have suggested that

the anions' translational motion is responsible for the fast component of solvation, while Kobrak and Znamenskiy<sup>212</sup> have suggested that collective cation-anion motion is responsible for the fast component. Another study by Shim et al.<sup>223</sup> attributes the ultrafast dynamics to fluctuations in the local ion density around the probe molecule. In this context, Biswas and colleagues<sup>209</sup> have recently shown that the imidazolium cations are polarisable and dipolar rotation of the IL cation is responsible for up to 40% of the ultrafast solvation component. The biphasic nature of solvent relaxation observed in ILs has also provided the clue for understanding solvent dynamics in DESs. Biswas and colleagues<sup>183</sup> studied acetamide-based DESs and found that the initial fast solvent response was due to collective low-frequency modes involving intermolecular vibration and liberation motions of the hydrogen bonding network, while orientational solvent density fluctuation was responsible for the slow components. In a separate study, Sen and colleagues<sup>182, 184</sup> also studied the ultrafast solvation response of ionic and non-ionic DESs and observed that solvation time was significantly decoupled from medium viscosity, indicating the presence of dynamic heterogeneity in these media. Moreover, Kim and Turner<sup>224</sup> investigated the solvent response of choline chloride-based DESs and reported that the local motion of the DES constituents contributed to the faster time scale, while the translational motion of the complex hydrogen bonding network contributed to the slower time scale. In another interesting work, Saddam et al.<sup>187</sup> studied ultrafast solvation dynamics in tetraalkylammonium-based DESs and observed that the cationic size influenced the contribution of the ultrafast solvation time components.

**Rotational Dynamics:** The study of rotational dynamics of fluorescent probes in a given medium has numerous applications in biophysics, biochemistry, and materials science.<sup>193</sup> It can be used to investigate protein conformational changes, molecular interactions, and the properties of complex fluids. Fluorescence anisotropy technique is usually used to study the rotational dynamics of molecules in solution. Both steady-state and time-resolved techniques

can be used to study the fluorescence anisotropy process.<sup>193</sup> However, time-resolved techniques can be more proficient than steady-state measurements for studying complex micro-heterogeneous systems, as the former provides information about the dynamic behaviour of molecules and their interactions within the system. In contrast, steady-state measurements provide information only about the equilibrium state of the system and do not capture the transient behaviour that may be critical in understanding the system's properties and behaviour.<sup>193, 225</sup>

The time-resolved fluorescence anisotropy usually involves the measurements of the dynamics of angular displacement between absorption and subsequent emission of a fluorophore.<sup>193, 225</sup> The basis of time-resolved fluorescence anisotropy is the photo selection of the fluorophore. When a set of fluorophores are illuminated with linearly polarized light, only those fluorophores having their absorption transition moment oriented along the electric field vector of the incident light are preferably excited. This creates an anisotropic polarization in the excited state. However, this polarization is not permanent, and as the excited molecules undergo rotational diffusion in the solution, the orientation of their dipole moment vectors will change over time. This leads to a time-dependent change in the degree of anisotropy of the emitted fluorescence. Hence, by measuring the fluorescence anisotropy, information about the rotational dynamics of the molecules in the given solution can be obtained. This information can be further used to gather information on the size, shape, and mobility of the solute, solute-solvent interactions (hydrogen bonding, electrostatic interactions, etc.) micro-viscosity of the medium.<sup>226-231</sup>

Subsequently, the data obtained from the time-resolved fluorescence measurement can be subjected to further analysis via different existing hydrodynamic models. The Stokes-Einstein-Debye (SED) hydrodynamic model is an example of one such model, which is often used to study the rotational diffusion of solute probes dissolved in a solvent.<sup>232</sup> According to

this theory, the solvent is considered as a structureless continuum, where the rotational relaxation time constant ( $\tau_r$ ) of a medium size solute is related to the bulk of viscosity ( $\eta$ ) of the medium by the following equation<sup>232</sup>

$$\tau_r = \frac{\eta v f c}{k_B T} \quad (1.1)$$

where,  $k_B$  is the Boltzmann constant, T is the absolute temperature, V is the molecular volume of the solute molecule calculated from van der Waals radii, and  $f$  is the shape factor of the solute probe. The shape factor  $f$  indicates how much a molecule deviates from a spherical shape. A perfectly spherical solute has an  $f$  value of one, while an asymmetrical ellipsoid has a higher  $f$  value. The stick and slip limits are the two extreme boundary conditions in SED models. C is the boundary condition parameter having two limiting values, stick ( $C=1$ ) and slip ( $0 < C < 1$ ). The value of C usually signifies the extent of solute-solvent coupling for a given solute and solvent. When solute molecules are larger than solvent molecules, C is one, indicating a stick boundary condition. When the solute molecule is smaller or comparable in size to the solvent molecule, C is less than one, indicating a slip boundary condition. The SED theory assumes solute molecules are either symmetric or asymmetric ellipsoids. It is useful for calculating the rotational coupling constants ( $C_{obs}$ ), which measure the deviation from normal hydrodynamic behaviour. The Solute dimensions, Molecular volumes calculated from the van der Waals radii of the molecule, shape factors, and boundary condition parameters ( $C_{slip}$ ) for different solutes that have been employed in the present thesis work are listed in Table 1.5.

**Table 1.5.** Molecular volumes (V), shape factor (f) and slip boundary ( $C_{slip}$ ) condition parameters for some selected probes used in this thesis work<sup>185, 233</sup>

Solute	Van der Waal's volume (V) ( $\text{\AA}^3$ )	Shape factor (f)	$C_{slip}$
C153	246	1.71	0.24
Perylene	225	1.76	0.085
MPTS	343	1.33	0.11

The SED theory assumes that the hydrodynamic volume of a solute is independent of the solvent continuum, but this assumption is only valid when the solute is much larger than the solvent. In some specific cases where SED theory fails, quasi-hydrodynamic theories, which consider the sizes of both solvent and solute molecules, are used. The Gierer-Wirtz (GW)<sup>234</sup> and Dote-Kivelson-Schwartz (DKS)<sup>235</sup> theories are two such theories that explain the solvent size-dependent rotational behaviour of solute molecules. According to the GW theory<sup>234</sup>, the solvent molecule consists of concentric shells of spherical particles that surround the spherical solute molecules, and the boundary parameter ( $C_{GW}$ ) is estimated by the angular viscosity, which decreases as the number of concentric shells around the solute molecule increases. On the other hand, the DKS theory<sup>235</sup> considers the free space between the solute and the solvent molecule, as well as the size of both molecules. According to this theory, when the size of the solute is compared to the free space of the solvent, a weak coupling between the solute and solvent is observed. In such cases, the solute experiences less friction, leading to a faster rotation in the solvent continuum.

Apart from this, other hydrodynamic models, such as the “Solvent-berg”<sup>236</sup> “Nee Zwanzig”<sup>237</sup>, etc., are also sometimes used by researchers to explain the rotational dynamics of a solute molecule in a given solvent. Typically, the diffusion dynamics of very small ions in a given solvent can satisfactorily be studied through the solvent-berg model. We note here the SED theory entirely fails to explain the rotational behaviour of extremely small ions in the medium. According to the solvent-berg model, the solvent molecules that are just next to the ion are tightly bonded to it.<sup>238</sup> This kinetic unit, known as the “solvent-berg”, moves as a result of the translational movement of the ions. The effective size of the “solvent-berg” is greater than that of the ion; hence its mobility becomes significantly less than that of the naked ion. It has been observed that the relative size of the “solvent-berg” becomes larger with the decrease in the size of the solute ions. However, it is very challenging to quantify this concept due to the

fact that the molecules of the solvent are not always tightly bound to the solvent molecules.<sup>238</sup> On the other hand, the Nee-Zwanzig model<sup>237</sup> considers the rotational diffusion of a solute molecule in a solvent to be a stochastic process based on the assumption that the rotational motion of the solute molecule is coupled to the motion of the surrounding solvent molecules. The rotational motion of the solute is influenced by random thermal fluctuations in the solvent, assuming that the rotational relaxation time of the solute molecule is much shorter than the time scale of solvent fluctuations. The Nee-Zwanzig model is often used in the context of NMR spectroscopy, where it is used to describe the line broadening that occurs due to the rotational motion of a solute molecule in a solvent.

Investigation of rotational dynamics is one of the most powerful techniques to reveal the microscopic structural organization, inter/intra molecular interactions, and dynamics of various complex micro heterogeneous systems such as RTILs and DESs.<sup>233</sup> Keeping this objective in mind, various groups have carried out the investigation on the rotational dynamics of a suitable solute in RTILs through time-resolved fluorescence anisotropy measurements. Fayer and co-workers have investigated the rotational dynamics of a neutral and charged probe in imidazolium-based ILs.<sup>233</sup> Similar to this, Dutt and co-workers have also extensively studied the rotational dynamics of various probes in a variety of ILs.<sup>227-229</sup> Sarkar and co-workers<sup>239-241</sup> have also investigated the rotational dynamics of different solutes in both monocationic and dicationic ILs. All the studies have essentially indicated that the solute rotation not only depends on the medium viscosity but also depends on the specific solute-solvent interactions. The specific solute-solvent interactions in terms of hydrogen bonding can significantly affect the rotational motion of solutes in ILs. Moreover, as ILs are made up of ions, the electrostatic interactions among the charged solutes and ionic constituents of ILs can also influence the rotational dynamics of charged probe molecules. Even though several studies of rotational dynamics on RTILs have been carried out, Similar studies in DESs are very limited. Very

recently, Saddam et al.<sup>185, 186, 242</sup> have studied the rotational dynamics few selected probes in some choline chloride and tetraalkylammonium-based DESs. They have demonstrated that even though some DESs are spatially homogeneous, all DESs are observed to be dynamically heterogeneous.

**Fluorescence Correlation Spectroscopy:** Fluorescence correlation spectroscopy (FCS) is a powerful technique that can be used to study the dynamics and interactions of molecules at the single-molecule level.<sup>193</sup> In FCS, a dilute solution of fluorophores is placed in a small confocal volume, and the fluctuations in fluorescence intensity are measured over time. These fluctuations are caused by the movement of individual molecules in and out of the confocal volume, and can provide information about molecular diffusion, chemical reactions, binding studies, and protein dynamics, among other things. By studying the diffusion of organic fluorophores in confined media, such as RTILs and DESs, FCS can provide insight into the microscopic structural organization of the RTILs.<sup>182, 183</sup> For example, if the fluorophores are observed to diffuse differently in different regions of the RTILs, it may suggest the presence of distinct structural domains within the RTILs. Werner et al.<sup>243</sup> were among the first to study the diffusion behaviour of rhodamine 6G and Atto 532 in imidazolium-based RTILs. Later on, Bhattacharyya and co-workers<sup>244</sup> explored the diffusion of two fluorescent probes (rhodamine 6G and pyrene) in three different RTILs with varying anions. They observed that the diffusion coefficients of the probes were not the same in all regions of the RTILs, indicating the micro heterogeneous nature of these RTILs. They also found that the range of the diffusion coefficients was wider than anticipated, and they concluded that multiple types of microheterogeneities exist in the RTILs. Furthermore, Guo et al.<sup>245</sup> and Patra et al.<sup>246</sup> conducted independent studies investigating the diffusion of selected fluorophores in pyrrolidinium and imidazolium-based ILs using FCS. Their findings, from the FCS data, revealed a bimodal diffusion behaviour of the fluorophore in RTILs, suggesting the existence of two distinct

diffusion rates for the fluorophores, and thereby, indicating a heterogeneous environment where the fluorophore diffuses at two different rates in different domains of the RTILs. Though there are some studies on RTILs involving FCS, the usage of the FCS technique to study the structure and dynamics of DESs is rather limited. Hossain et al.<sup>185, 186, 242</sup> have studied the translational diffusion of some selected probes in two different types of DESs: alcohol-based DESs, and tetraalkylammonium bromide-based DESs, and observed anomalous diffusion behaviour of the fluorophore. They found that the position of the hydroxyl group (OH) in the alcohol-based DESs did not significantly affect the variation of spatial and dynamic heterogeneity. However, they observed that the heterogeneity in the tetraalkylammonium bromide-based DESs became more prominent as the alkyl chain in the cation of the hydrogen bond donor (HBD) increased in length. On the other hand, Sen and co-workers<sup>182, 184</sup> observed the biphasic diffusion behaviour of rhodamine 6G in some DESs, which they attributed to the micro-heterogeneous behaviour of the media. Overall, these findings have highlighted the complex nature of both RTILs and DESs and have demonstrated the importance of FCS in understanding the dynamics and structural heterogeneity of RTILs and DESs.

### **1.9. Nuclear Magnetic Resonance (NMR) Investigations on RTILs and DESs**

NMR spectroscopy is a powerful technique that is widely used in chemistry to characterize molecules and study their interactions. Simple <sup>1</sup>H and <sup>13</sup>C-NMR chemical shift measurements are often used to characterize RTILs and DESs, as these measurements can provide valuable information about the composition and structure of these solvents.<sup>163, 164, 247, 248</sup> Multinuclear NMR techniques are now widely used to study the structure, dynamics, and interactions in DESs and RTILs.<sup>247, 248</sup> Specifically, the pulsed field gradient nuclear magnetic resonance (PFG-NMR) method is becoming increasingly popular in investigating the translational diffusion coefficient, cation-anion interaction, spin-spin relaxation time, and spin-lattice relaxation time of RTILs and DESs.<sup>249</sup> One of the main advantages of the PFG-NMR technique

lies in the fact that it is a non-invasive and non-destructive technique that can provide precise and accurate measurements of diffusion coefficients over a wide range of concentrations and temperatures.<sup>249</sup>

## 1.10. Objective of the Thesis Work

Over the past decade and a half, several photophysical studies have been conducted on ILs and DESs. However, many important issues associated with these solvents still remain unresolved.

Some key issues associated with both RTILs and DESs are mentioned below:

- Although DESs can be categorized (in a macroscopic sense) as a subclass of ILs, it is still not known whether both classes of solvent systems behave similarly at the microscopic level.
- Although hydrogen bonding is believed to be a primary factor contributing to the observed microscopic behaviour of DESs and RTILs, it still remains uncertain how the structure and dynamics of RTILs would be affected if the number of hydroxyl groups on the cationic head is systematically increased.
- DESs are now considered as potential alternatives to both ILs and common volatile organic solvents for their electrochemical applications. However, the structural and dynamical changes in DESs, in the presence of electrolytes, have not been investigated.
- Additionally, DESs are thought to be a more effective medium than ILs for the storage and utilization of biomolecules. However, it's unclear whether all types of DESs or only specific types of DESs are suitable for bio-related applications. Again, the mechanism of protein-DES interaction at a microscopic level has not been investigated properly.

## 1.11. Organization of the thesis

Chapter 1 provides an introduction to ILs and DESs, presenting their different classes and physicochemical properties. The chapter also highlights the applications of ILs and DESs in various fields and discusses the structure and dynamics of these solvents. Various phenomena

used to study and understand the microscopic behaviour of DESs and ILs (excitation wavelength-dependent emission, solute and solvent dynamics, NMR diffusion dynamics, etc.) are also discussed in detail in this chapter. Finally, the chapter outlines the objective of the present thesis work in the context of current challenges in DESs and ILs research.

Chapter 2 covers various methods and instrumental techniques such as steady-state absorption and fluorescence techniques, time-resolved fluorescence spectroscopy methods such as time-correlated single photon counting (TCSPC), fluorescence up-conversion techniques, and single-molecule fluorescence techniques that are used for experimental investigation. This chapter also provides a detailed explanation of the methodologies associated with these techniques and also discusses their error limits.

Chapter 3 is the first working chapter of the current thesis work, which aims to understand the differences in the microscopic behaviour in terms of structure, dynamics, intra- and intermolecular interactions between DESs and RTILs. This study is important in a sense that even though DESs are considered as a subclass of ILs, due to their similar physicochemical properties, they may not necessarily behave similarly at the microscopic level. In view of this, the difference in the microstructural organization and dynamics between a choline chloride-based DES (ethaline) and three hydroxyls functionalized ILs have been investigated by various spectroscopic and analytical techniques. This chapter consists of two parts; the first part of the chapters describes the differences in the solute-solvent dynamics, and translational diffusion dynamics of both DESs and RTILs, while the second part delivers information on the differences with regard to the ultrafast solvation response between DESs and RTILs.

Chapter 4 describes the impact of the increase in the number of hydroxyl groups on the cationic head of ammonium-based room temperature ILs (RTILs) on intermolecular and intramolecular hydrogen bonding interaction, local structural organization, and dynamics of the solvent systems. Three hydroxyl functionalized ammonium-based RTILs (HFILs) with different

numbers of hydroxyl groups on the cationic head and a non-hydroxyl ammonium-based RTIL are investigated using both ensemble-averaged and single-molecule spectroscopy techniques, in order to understand how hydroxyl functionalities, control the structure and dynamics of DESs and RTILs.

The high electrochemical potential windows and low water electrolysis capacity of DESs make them highly attractive candidates for electrochemical applications. However, the impact of electrolytes on the structure, dynamics, and heterogeneity of DESs have not been investigated in detail yet. Chapter 5 focuses on the investigation of the structural organization, dynamics, and intermolecular interactions of DESs in the absence and presence of lithium salt. Specifically, the microscopic behaviour of Ethaline and Glyceline DESs and their mixtures with lithium bis(trifluoromethylsulfonyl) imide (LiNTf<sub>2</sub>) have been investigated using various spectroscopic techniques, such as steady-state and time-resolved fluorescence, EPR, and NMR spectroscopy. It is expected that the outcome of this study will be helpful in realizing the potential of DESs as a suitable electrolytic medium for Li-ion battery-related applications.

While DESs are thought to be highly promising for the storage and processing of biomolecules as they are known to be advantageous over both conventional organic solvents and ILs, it still remains unclear whether all types of DESs are suitable or if only specific types of DESs are appropriate for this purpose. In view of this, chapter 6 seeks to provide a thorough understanding of the mechanism of protein-DES interaction, as well as the structural and conformational stability of a protein (BSA) in the presence of DESs. To achieve this, the chapter examines two DESs, Ethaline (Choline chloride: ethylene glycol) and BMEG (benzyltrimethyl ammonium chloride: ethylene glycol), both having the same hydrogen bond donor but different hydrogen bond acceptors. The selection of the constituents of DESs allows for a deeper understanding of how even a small change in a DES constituent can affect the protein-DES interaction at the molecular level. The investigation of protein-DES interaction is

done by using both ensemble-averaged measurements such as steady-state and time-resolved fluorescence spectroscopy, circular dichroism (CD) spectroscopy, as well as single-molecule measurement techniques like fluorescence correlation spectroscopy (FCS).

The outcome of the present thesis work is expected to advance our fundamental knowledge in understanding the structure, intermolecular interactions, and dynamics of both RTILs and DESs. Some results of the thesis work are also expected to be helpful in realizing the potential of DES-based electrolytes for Li-ion battery applications. Additionally, the investigations of protein-DES interaction studies will also be useful to judge whether DESs can be effectively be used for the storage and handling of biomolecules.

# CHAPTER 2

---

## Materials, Experimental Techniques, and Methods

---

**Abstract**

This chapter describes the synthetic procedure, experimental techniques, and various methodologies employed in the current thesis. Briefly, various chemical sources, preparation of ILs and DESs, and methods of sample preparation for both spectroscopic and microscopic studies have been described. The working principles of a spectrophotometer, spectrofluorometer, time-correlated single photon counting (TCSPC) setup, fluorescence up-conversion spectroscopy, and time-resolved confocal fluorescence microscope (FCS) setup have been discussed. Along with these, different theories and methodologies employed for data analysis have also been discussed. Finally, standard error limits corresponding to different experimental measurements are provided at the end of this chapter.

---

**2.1. Materials**

For this thesis work, variety of different chemicals were purchased from different suppliers and they are used without any subsequent purification for synthesis and studies. Various starting materials, including 1-methylimidazole, N-methylpyrrolidine, N,N-dimethylethanolamine, N-methyldiethanolamine, N-butyldiethanolamine, 1-bromopropane, ethylene glycol, and glycerol, were obtained from Sigma Aldrich. Additionally, probe molecules such as coumarin (153), perylene, 8-Methoxypyrene-1,3,6-trisulfonate trisodium (MPTS), and 2,2,6,6-tetramethylpiperidine-1-oxyl (TEMPO) were purchased from Sigma Aldrich. Deuterated solvents, specifically DMSO-d<sub>6</sub> and D<sub>2</sub>O, were also acquired from Sigma Aldrich. Choline chloride, Benzyl trimethylammonium chloride, butyltrimethylammonium bis(trifluoromethanesulfonyl)imide, 2-bromoethanol, 2-chloroethanol, 1-bromobutane, and lithium Bis(trifluoromethanesulfonyl)imide (LiNTf<sub>2</sub>) were purchased from TCI Chemicals. In addition, 1-(2-hydroxyethyl)-3-imidazolium bis(trifluoromethanesulfonyl)imide was obtained

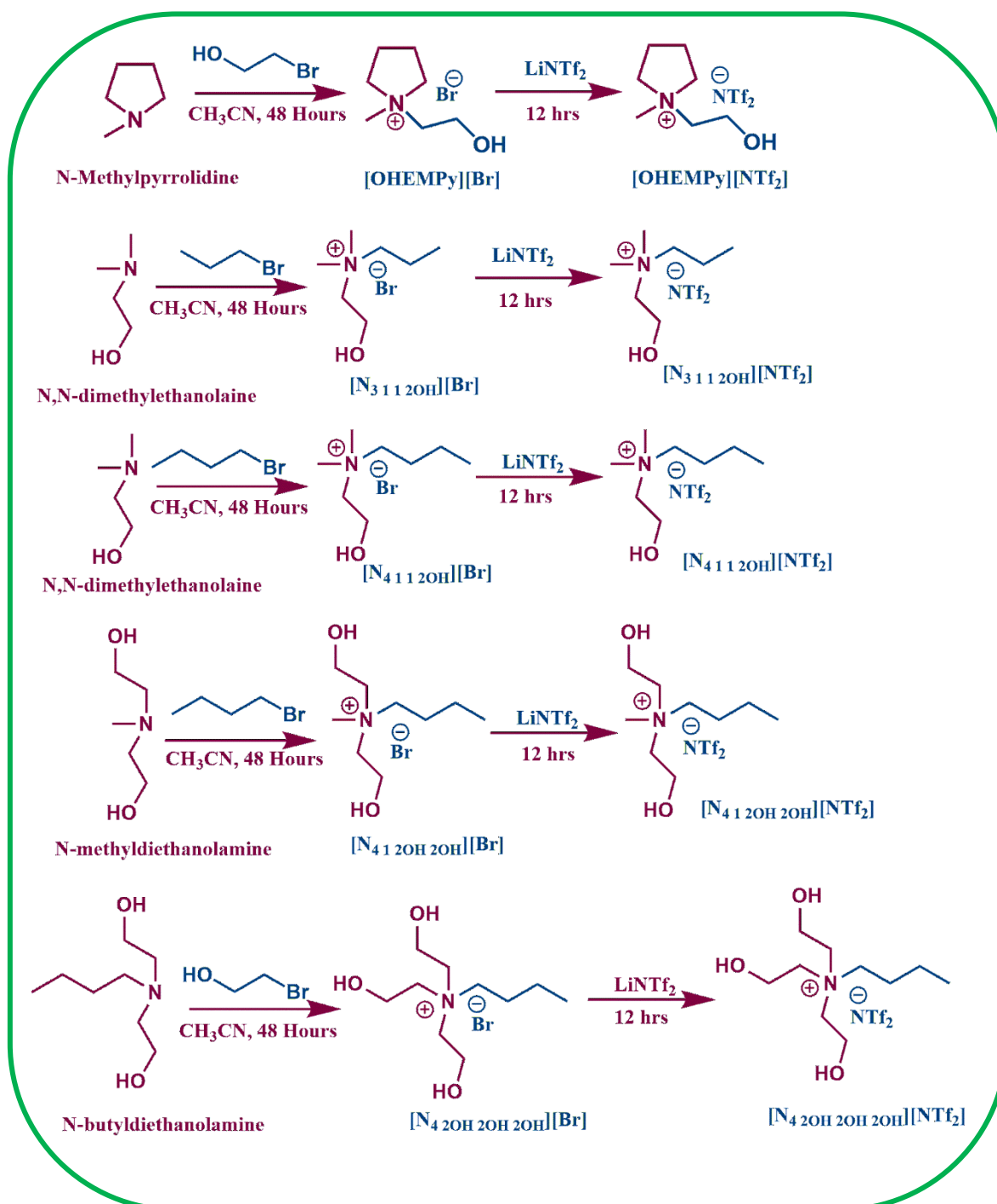
from io-li-tec. For studies related to biology, bovine serum albumin (BSA) and phosphate buffer with a pH of 7.4 were obtained from Sigma Aldrich, while FITC-tagged BSA was purchased from Invitrogen.

## 2.2. Synthesis and Characterization of DESs and RTILs

*2.2.1. General procedure for synthesis of different hydroxyl functionalized ionic liquids (HFILs):* The HFILs have been synthesized following the literature method.<sup>250, 251</sup> A general scheme for the synthesis of different HFILs have been provided in Scheme 2.1. A brief overview of preparation and characterization of these HFILs is as follows.

To 141 mmol of the N-methylpyrrolidinium/ethanolamine (N,N-dimethylaminoethanol, N-methyldiethanolamine and N-butyldiethnaolamine), 30mL of acetonitrile was added in a two-neck round bottom flask equipped with reflux condenser. To the solution, 170 mmol (1:1.2) of respective halo-alkane/halo-ethanol (1-bromopropane/1-bromobutane/ 2-bromoethanol, Scheme 2.1.) was gradually added. The whole solution was stirred and condensed at 353K for 2 days in the same condition. Then the solution was condensed by evaporation in the rotary evaporator. The reaction product was washed several times with diethyl ether and ethyl acetate to obtained the solid product of the bromide salt (for  $[N_4 2OH 2OH 2OH]Br$ , the salt is semi solid). The white solid product was kept under high vacuum at 323K for 12 hours. Then, 65 mmol of lithium bis(trifluoromethanesulfonyl)imide was mixed with 30mL of water and gradually added to an aqueous solution of the 54.3 mmol bromide salt (in 20 mL of water). The solution was stirred for 12 hours. Then two separate layer was formed and the aqueous solution layer was decanted. The ionic liquid layer was dissolved in ethyl acetate and washed with water several times until no precipitation occurs in the washing residue after adding silver nitrate solution. After that, the solvent was evaporated and the viscous residue was mixed with activated charcoal in acetonitrile. The activated charcoal was removed

by filtration to obtain a white solution. Then the solvent was evaporated. The ionic liquid was then dried under high vacuum at 308 K for 3 days. The product was a colorless liquid with 80-85% yield. The compound was characterized by  $^1\text{H-NMR}$  spectrometric studies.



**Scheme 2.1.** Synthesis scheme of HFILs.

**[OHEMPy][NTf<sub>2</sub>]:** <sup>1</sup>H NMR ( $\delta_H$ , ppm): 5.27 t (1H, OH), 3.85 m (2H, N-CH<sub>2</sub>), 3.52 m (4H, CH<sub>2</sub>-N-CH<sub>2</sub>), 3.45 m (2H, O-CH<sub>2</sub>), 3.05 s (3H, N-CH<sub>3</sub>), 2.1 m (4H, CH<sub>2</sub>-CH<sub>2</sub>); ESI-MS (+ve): 130.1244 [OHEMPy]<sup>+</sup>.

**[N<sub>3112OH</sub>][NTf<sub>2</sub>]:** <sup>1</sup>H NMR ( $\delta_H$ , ppm): 5.22 t (1H, OH), 3.80 m (2H, O-CH<sub>2</sub>), 3.44 t (2H, CH<sub>2</sub>-CH<sub>2</sub>-N), 3.36 t (2H, C<sub>2</sub>H<sub>5</sub>-CH<sub>2</sub>-N), 3.12 s (6H, N-(CH<sub>3</sub>)<sub>2</sub>), 1.67 m (2H, CH<sub>2</sub>-CH<sub>3</sub>), 0.84 t (3H, CH<sub>2</sub>-CH<sub>3</sub>); ESI-MS (+ve): 132.1489 [N<sub>3112OH</sub>]<sup>+</sup>.

**[N<sub>4112OH</sub>][NTf<sub>2</sub>]:** <sup>1</sup>H NMR ( $\delta_H$ , ppm): 5.26 t (1H, NCH<sub>2</sub>CH<sub>2</sub>OH), 3.84 m (2H, NCH<sub>2</sub>CH<sub>2</sub>OH), 3.35 m (4H, CH<sub>2</sub>-N-CH<sub>2</sub>CH<sub>2</sub>OH), 3.06 s (6H, N-(CH<sub>3</sub>)<sub>2</sub>), 1.68 m (2H, N-CH<sub>2</sub>CH<sub>2</sub>CH<sub>2</sub>CH<sub>3</sub>), 1.30 m (2H, N-CH<sub>2</sub>CH<sub>2</sub>CH<sub>2</sub>CH<sub>3</sub>), 0.94 s (2H, N-CH<sub>2</sub>CH<sub>2</sub>CH<sub>2</sub>CH<sub>3</sub>); ESI-MS (+ve): 146.1532 [N<sub>4112OH</sub>]<sup>+</sup>.

**[N<sub>412OH2OH</sub>][NTf<sub>2</sub>]:** <sup>1</sup>H NMR ( $\delta_H$ , ppm): 5.23 t (2H, N(CH<sub>2</sub>CH<sub>2</sub>OH)<sub>2</sub>), 3.85 m (4H, N(CH<sub>2</sub>CH<sub>2</sub>OH)<sub>2</sub>), 3.41 m (6H, CH<sub>2</sub>N(CH<sub>2</sub>CH<sub>2</sub>OH)<sub>2</sub>), 3.06 s (3H, N-CH<sub>3</sub>), 1.68 m (2H, N-CH<sub>2</sub>CH<sub>2</sub>CH<sub>2</sub>CH<sub>3</sub>), 1.30 m (2H, N-CH<sub>2</sub>CH<sub>2</sub>CH<sub>2</sub>CH<sub>3</sub>), 0.94 s (2H, N-CH<sub>2</sub>CH<sub>2</sub>CH<sub>2</sub>CH<sub>3</sub>); ESI-MS (+ve): 176.1643 [N<sub>412OH2OH</sub>]<sup>+</sup>.

**[N<sub>42OH2OH2OH</sub>][NTf<sub>2</sub>]:** <sup>1</sup>H NMR ( $\delta_H$ , ppm): 5.20 t (3H, N(CH<sub>2</sub>CH<sub>2</sub>OH)<sub>3</sub>), 3.83 m (6H, N(CH<sub>2</sub>CH<sub>2</sub>OH)<sub>3</sub>), 3.50 t (6H, CH<sub>2</sub>N(CH<sub>2</sub>CH<sub>2</sub>OH)<sub>3</sub>), 3.40 t (CH<sub>2</sub>N(CH<sub>2</sub>CH<sub>2</sub>OH)<sub>3</sub>), 1.68 m (2H, N-CH<sub>2</sub>CH<sub>2</sub>CH<sub>2</sub>CH<sub>3</sub>), 1.30 m (2H, N-CH<sub>2</sub>CH<sub>2</sub>CH<sub>2</sub>CH<sub>3</sub>), 0.94 s (2H, N-CH<sub>2</sub>CH<sub>2</sub>CH<sub>2</sub>CH<sub>3</sub>); ESI-MS (+ve): 206.1835 [N<sub>42OH2OH2OH</sub>]<sup>+</sup>.

**2.2.2. General procedure for the synthesis of DESs:** The DESs used in the current thesis work are synthesized by following a standard procedure as reported in literature.<sup>19-20</sup> Briefly, choline chloride was mixed with ethylene glycol and glycerol separately in 1:2 molar ratio and heated and stirred at 60° C until a homogeneous transparent liquid is formed. Then both the DESs were cool down to room temperature. Both DESs were kept under high vacuum for 24 hours

prior to use.  $^1\text{H}$  NMR was used to characterize the resulting solvents (Supporting information) and found to be consistent with the previously reported data. The viscosity of both DESs have been measured at different temperature and also found to be comparable with the literature report.

$^1\text{H}$  NMR ( $\delta_{ppm}$ ) of Ethaline: 4.75 brs (1H, OH), 4.4 brs (4H, OH), 3.45 m (2H, N-CH<sub>2</sub>), 3.05 m (10H, O-CH<sub>2</sub>), 2.72 s (9H, N-(CH<sub>3</sub>)<sub>3</sub>).

$^1\text{H}$  NMR ( $\delta_{ppm}$ ) of Glyceline: 4.55 brs (1H, CH<sub>2</sub>-OH), 4.3 brs (2H, CH-OH), 4.20 brs (4H, CH<sub>2</sub>-OH), 3.4 m (2H, N-CH<sub>2</sub>) (2H, CH<sub>2</sub>-CH), 3.95m (12H), 2.62 s (9H, N-(CH<sub>3</sub>)<sub>3</sub>).

*2.2.3. Water Content Measurements of DESs and RTILs:* Water content of all the concerned solvents have been measured through Karl Fischer titration after drying several hours. The water content of all the solvent systems have been found to be in accordance with previously reported literature report.<sup>185, 224</sup> We anticipate that water content at this level will not affect the experimental result significantly.

**Table 2.1.** Water content of the solvent systems used in this study.

SI No.	Systems	Water Content (in PPM)
1	[OHEMIM][NTf <sub>2</sub> ]	100
2	[OHEMPy][NTf <sub>2</sub> ]	250
3	[N <sub>3 1 1 2OH</sub> ][NTf <sub>2</sub> ]	570
4	[N <sub>4 1 1 1</sub> ][NTf <sub>2</sub> ]	100
5	[N <sub>4 1 1 2OH</sub> ][NTf <sub>2</sub> ]	250
6	[N <sub>4 1 2OH 2OH</sub> ][NTf <sub>2</sub> ]	570
7	[N <sub>4 2OH 2OH 2OH</sub> ][NTf <sub>2</sub> ]	880
8	Ethaline	800
9	Glyceline	950

## 2.3. Instruments

### 2.3.1. Instrumentations used for characterization of samples

The Bruker Avance 400 MHz NMR spectrometer was used to record the NMR spectra of different samples. ESI-MS (Electrospray ionisation mass spectrometry) spectra were collected using a Bruker micro-TOF-QII mass spectrometer. A cone and plate viscometer was used to measure the viscosity of both DESs and ILs (Brookfield LVDV-III Ultra). Temperature-dependent viscosity measurements were also done using the viscometer and a Julabo water circulator bath.

### 2.3.1. Instrumental Technique for Steady-State Absorption and Fluorescence Measurements

#### 2.3.1.1. Steady-State Absorption Spectroscopy

UV-visible absorption spectroscopy is the commonly employed method to assess the ground electronic state of chromophoric entities. This spectroscopic technique provides information on the electronic energy levels of a system by measuring distinct wavelengths of absorption bands and the molar extinction coefficient. Consequently, this approach enables the identification of various chromophoric groups and their neighbouring environments. Moreover, the absorption profile of an absorbing species is frequently altered by solvent polarity, polarizability, and hydrogen bonding interaction in the ground state.<sup>252</sup> As a result of this, UV-Visible absorption spectroscopy can give more meaningful information on the nature of interactions between chromophoric entities and their surrounding microenvironment in the ground electronic state. The absorption of light by a chromophoric group usually adheres to *Lambert-Beer's law*. According to this law, the absorbance ( $A_\lambda$ ) of a species in a solution at a wavelength  $\lambda$ , is directly proportional to its molar extinction coefficient ( $\epsilon_\lambda$ ) at that wavelength and the concentration ( $C$ ) of the species in the solution, which is given by the following equation<sup>252</sup>,

---

---

$$A_{\lambda} = \log\left(\frac{I_0}{I}\right) = \epsilon_{\lambda}Cl \quad (2.1)$$

where  $I_0$  and  $I$  are the incident and transmitted light intensity at  $\lambda$  wavelength,  $l$  is the path length of the sample in cuvette.

In the current thesis work, the UV-Vis spectroscopy experiments were carried out using a Cary 100 Bio UV-VIS spectrophotometer with a wavelength resolution of 0.15 nm. This apparatus measures absorbance in the UV and Visible regions using a D<sub>2</sub>O lamp and a xenon lamp as excitation sources respectively.

### 2.3.1.2. Steady-State Fluorescence Spectroscopy

The fluorescence spectroscopy is a very sensitive optical techniques for investigating many sorts of photophysical and photochemical processes in the excited state of a fluorophore molecule. A relatively slight change in the energetics or interactions between fluorophore molecules in their excited state can cause a change in the intensity, shape, and emission maximum of the emission spectra of the corresponding species.<sup>193,225,252</sup> Consequently, a better comprehension about the microenvironment of the emitting species can be obtained with the use of this approach.

In the current thesis work, all steady-state fluorescence measurements were carried out using an Agilent Technologies (G9800A) Cary Eclipse fluorescence spectrophotometer using a xenon lamp as the light source. To collect the temperature-dependent fluorescence spectra, the Edinburgh spectrofluorometer FS5 was also employed. In this apparatus, the temperature of the cell was controlled by a North West (TC 125) temperature controller, and it is maintained by circulating water through the cell holder.

## 2.3.2. Instrumental Techniques for Time-Resolved Studies

### 2.3.2.1. Fluorescence Lifetime Measurements

Time-resolved fluorescence spectroscopy measurements are very helpful in revealing the dynamics and kinetics of many photophysical and photochemical processes. This method is more preferable than steady-state fluorescence in a sense that the latter method concentrates more on the equilibrium state of the systems. In this method, a very short laser pulse excites the fluorophore to the excited state, creating an initial population ( $n_o$ ) in the excited state. Now the excited state population decays as time proceeds through both radiative and non-radiative pathways. The rate of population decay of the excited state is given by equation 2.2<sup>193, 225, 252-255</sup>,

$$-\frac{dn(t)}{dt} = (k_r + k_{nr})n(t) \quad (2.2)$$

where  $n(t)$  = number of excited molecules at time  $t$  following the excitation of fluorophore molecule with the very short pulse light. The  $k_r$  and  $k_{nr}$  denotes the radiative and nonradiative rate constant respectively.<sup>252</sup> As emission is considered as a random event, the probability of emission of the fluorophores are same over a given period of time. The excited state population decays in an exponential manner using equation 2.3,

$$n(t) = n_o \exp\left(-\frac{t}{\tau}\right) \quad (2.3)$$

where  $\tau$  is the lifetime of the excited fluorophore. It can be observed that the fluorescence intensity is directly proportional to the number of excited molecules present in the solution. Equation 2.3 can be rewritten in terms of the time-dependent intensity  $I(t)$  and the integration of the final equation 2.3 has been depicted below

$$I(t) = I_o \exp\left(-\frac{t}{\tau_f}\right) \quad (2.4)$$

where  $I_0$  is the intensity at zero time,  $\tau_f$  is the fluorescence lifetime of the fluorophore.  $\tau_f$  is related to the radiative and nonradiative decay rate constants as per equation 2.5, which given as

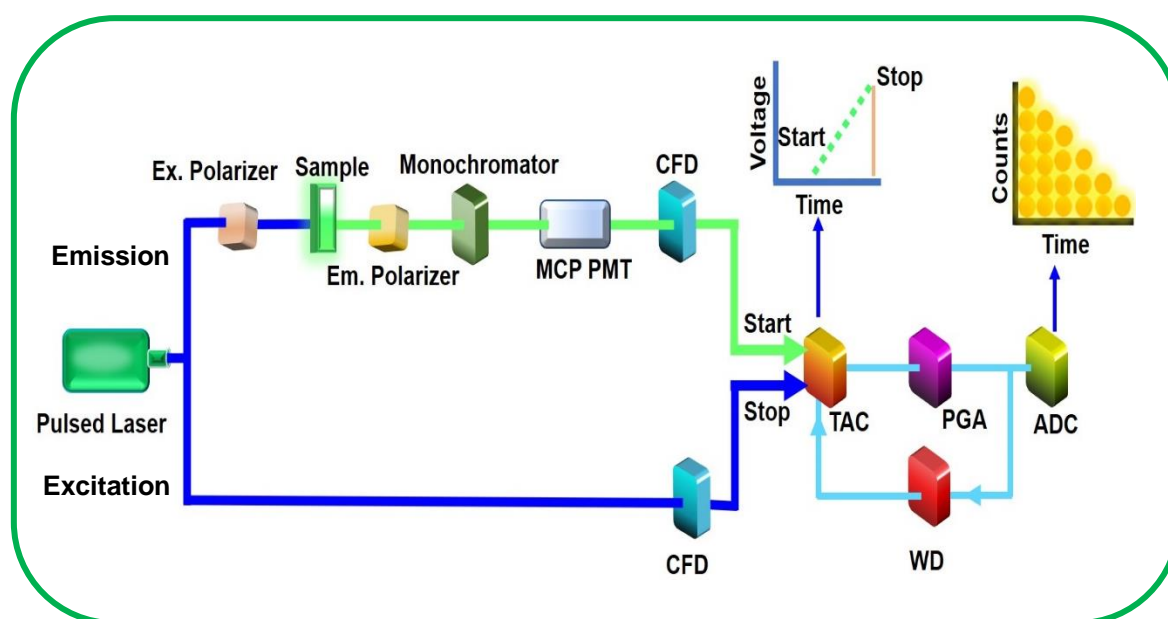
$$\tau_f = \frac{1}{k_r + k_{nr}} \quad (2.5)$$

The time-correlated single photon counting (TCSPC) technique is generally used to estimate the fluorescence lifetime of a fluorophore.<sup>193, 253-255</sup> The observed fluorescence decay of the sample under investigation shows the temporal distribution of these released photons since different molecules spend different amounts of time in the excited state. Thus, the lifetime obtained from the TCSPC instrument is the statistical average of the times the fluorophore molecules reside in the excited state. Although TCSPC is a sophisticated instrument for estimating the excited lifetimes of fluorophores, it has a broad temporal resolution (~80ps), making it unable to capture ultrafast components, if any, present in a fluorophore. Therefore, fluorescence upconversion spectroscopic (FLUPS) techniques are typically used to capture ultrafast lifetime components as they have sub-picosecond time resolution (~300fs). In this thesis work, time-resolved measurements were carried out using Edinburgh Life Spec II and OB920 setups, while a fluorescence upconversion spectrometer was used to measure ultrafast components. The following sections provide an overview of the essential operating principles and key elements of the TCSPC and FLUPS setups.

### **2.3.2.2. Basic Principle of TCSPC Instrument**

The basic operating principle of TCSPC is based on the detection of a single photon upon pulsed excitation of a fluorophore.<sup>193, 253-255</sup> TCSPC usually measures the time gap between the short excitation pulse and the first detected photon. It also represents the time-dependent probability distribution of a single photon emission from an excited fluorophore. The time-dependent fluctuations in fluorescence intensity that occur, when a fluorophore moiety is

excited, are equal to the time-dependent probability distribution of molecules in excited states that may be measured by the device. As TCSPC is a statistical approach, a high repetition rate of the excitation source is necessary in order to detect a significant number of photons in a short amount of time and obtain accuracy in the statistical data. These data stored in the form of a histogram which essentially represents the fluorescence decay profile of the fluorophore. The TCSPC operates similarly to a stopwatch, with the START pulse being produced by a photon either from the excitation source (known as the "forward mode") or from the emission of the sample (known as the "reverse mode").<sup>193</sup> A schematic representation of the working principle of TCSPC setup (in reverse mode) is shown in Scheme 2.2.



**Scheme 2.2.** A schematic diagram for the working principle of TCSPC setup.

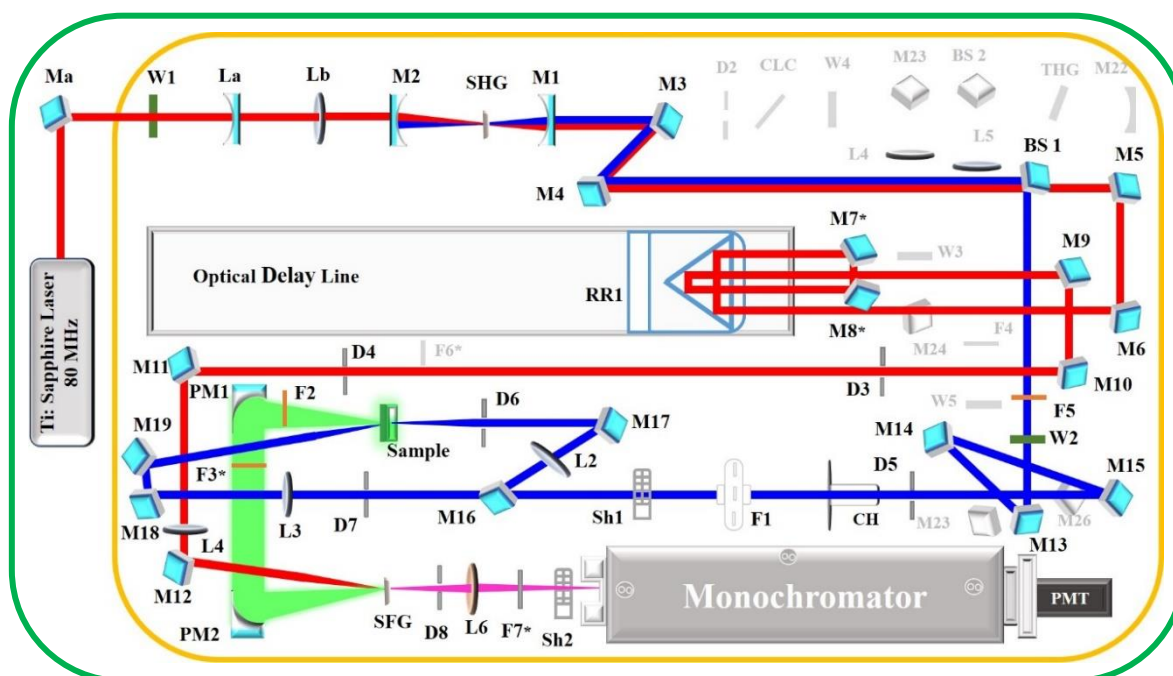
As depicted in Scheme 2.2., one can notice that the excitation pulse is divided into two parts, the first part is used to excite the sample and the second part of the pulse excitation is directed towards the electronics. The optical signal resulting from the emitted photon passes through the PMT to generate an electrical signal that corresponds to START pulse. The START pulse then travels through the Constant Fraction Discriminator (CFD), which precisely measures the actual arrival time of the pulse. The signal then enters the Time to Amplitude

Converter (TAC) through the START input, creating a voltage ramp that rises linearly over time. Now, the second channel, which is composed of excited photons, travels via variable delay line and the CFD before arriving at the TAC unit. These signals are basically the STOP pulses which are used as the STOP input of the same TAC unit. The TAC unit now stop the voltage ramp once it detects the first STOP pulse. In essence, the TAC unit now has a voltage that is proportional to the time interval ( $\Delta t$ ) between the emission (start) and excitation (stop) pulses. The TAC output pulse signals are subsequently passed through PGA (Pulsed Gain Amplifier) to an ADC (Analog-to-Digital Converter). Then a numerical number that is proportionate to the height of the TAC output pulse signal is produced by the ADC and finally the data is stored in the multichannel analyser (MCA). The cyclic procedure described above is repeated several times, producing a collection of histograms of counts in the MCA channels. Generally speaking, this TCSPC working concept is known as "reverse mode" functioning. In present times, almost all TCSPC measurements are done in the "reverse mode".<sup>193</sup> This is because of the high repetition rate of modern pulsed-light-based sources. Before each start pulse, the TAC must be reset and set to zero, which requires a finite amount of time. If the start signals arrive too quickly, the TAC can remain permanently in reset mode to prevent information loss. However, the TCSPC conditions are adjusted so that less than one photon can be detected per hundred laser photons excitation. Thus, these emission pulses are used to initiate the voltage ramp in TAC, and the next laser pulse is utilised to stop the TAC. Present electronics for TCSPC setup only allow the detection of the first arrival photon. Analysis procedure for estimation of fluorescence lifetime and anisotropy from the measured fluorescence decay curves is also discussed in the later part of this chapter. In this thesis work, the fluorescence decays of all samples are recorded using Life Spec II and OB920 TCSPC spectrofluorometer. Appropriate analysis software (F980), provided by Edinburgh company, is used to fit the experimental decay curves and get the fluorescence lifetimes of the samples. The

analysis procedure for estimation of fluorescence lifetime from the measured fluorescence decay curves is also discussed in the later part of this chapter.

### 2.3.2.3. Fluorescence Upconversion Spectroscopy (FLUPS)

Fluorescence Up-Conversion is an ultrafast spectroscopic technique widely used to investigate the ultrafast dynamics or initial dynamics of any fluorophore with a time resolution of 300 fs to 2 ns.<sup>193</sup> As the name implies, this method is based on the sum frequency generated signal (upconverted signal), which is formed by the combination of the emission and gate pulses. The basis for fluorescence up-conversion techniques is the pump-probe process, in which a sample is excited by an ultrafast laser pulse (the pump pulse), and the fluorescence decay is produced by combining the fluorescence from the sample and the laser pulse (the probe pulse). A delay line causes the laser pulse to be time-delayed in relation to the fluorescence of the sample and then both pulses are focused simultaneously on a non-linear optical crystal (in our example, a BBO) to generate the unconverted UV signal.



**Scheme 2.3.** A schematic representation of the up-conversion setup, Fluomax from IB photonics. In the scheme, the red line corresponds to the fundamental laser beam and the blue one frequency-doubled visible beam.

Scheme 2.3 depicts the different components and the operating principle of a fluorescence up-conversion spectrofluorometer. In this technique, the fundamental laser pulse ( $\omega_p$ ) was focus on the  $\beta$ -barium borate (BBO) crystal to generate the second harmonic beam ( $2\omega_p$ ) with the same repetition rate. Then the output light was made to pass through a dichroic mirror (BS1) where both fundamental beam ( $\omega_p$ , gate pulse/probe pulse) and the second harmonic beam ( $2\omega_p$ , excitation pulse/pump pulse) were separated. BS1 transmit the gate beam and reflect the excitation pulse. The excitation pulse was guided through a polarizer W2 ( $35.40^\circ$ ) and focused on the sample for collection of a fluorescence decay at a magic angle. Then the fluorescence from the sample are passes through the filter which only transmit the fluorescence signal. Then the fluorescence signal ( $\omega_f$ ) from the sample are focused on the sum frequency generation (SFG) crystal (BBO crystal) with the help of two parabolic mirror (PR1 and PR2). Now, the gate beam passes through a motorized optical delay line (RR1), which was used to time delayed the gate beam with respect to the fluorescence signal from the sample and also focuses on the same SFG crystal at the same region. As a result, an up-converted signal is generated with frequency equal to the sum of the frequencies of fluorescence and gate pulse ( $\omega_{up} = \omega_f + \omega_p$ ). The upconverted signal is passed through an iris which blocks the fluorescence and the gate beam and up-converted light is focused and guided to a monochromator and finally to the detector (PMT). Spatial and temporal overlap of the two signals is necessary for efficient up-conversion. Fluorescence decay can be obtained from the intensity of the up-converted signal as the delay time is varied for gate pulse if the intensity of the gate pulse remains unaltered during the measurement. To avoid photo degradation, the sample is placed in a rotating cell with a 1 mm path length. The IRF of the instrument was estimated from the Raman scattering of water ( $\sim 250$  fs). In the present thesis work, Femtosecond fluorescence up-conversion data were recorded in a fluorescence up-conversion

spectrometer, FluoMax from IB Photonics Ltd. For excitation of the samples, Ti-sapphire laser (Mai Tai HP, Spectra Physics, 80 MHz, centre wavelength 800nm, 3W @800nm) with a tuneable range from 690 nm to 1040 nm was used.

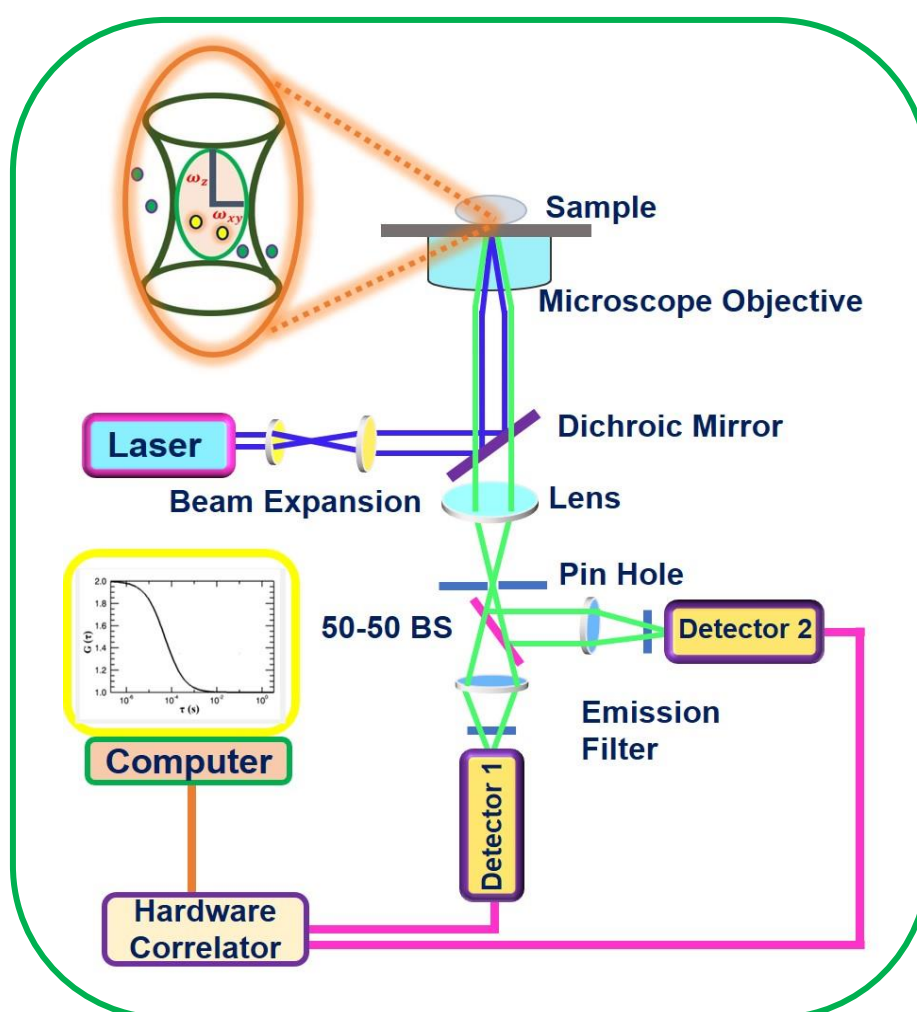
### **2.3.4. Experimental Technique for Single-Molecule Studies**

#### **2.3.4.1. Time-Resolved Confocal Fluorescence Microscopy**

Optical microscopes are a great tool for observing magnified images of small objects. However, to observe micro-objects clearly, the overall resolution of the microscope is crucial. The resolution of a microscope is determined by the excitation wavelength and numerical aperture of the objective lens. It is possible to adjust the resolution of a microscope by changing the excitation source and configuration. Confocal fluorescence microscopy (CFM) has a higher temporal resolution (up to a few nanoseconds) and employs multiple pinholes in the detection path to allow only focused light and obtain measurements in a confocal region. Scheme 2.4 shows a schematic diagram of the time-resolved confocal microscope.

The PicoQuant MicroTime 200 has been used to carry out all the measurements in this thesis. To excite the sample, different pulsed picosecond diode lasers with different wavelengths (403 nm, 444 nm, 483 nm, and 519 nm) have been used along with a continuum laser with an excitation wavelength range from 360 nm to 720 nm. The laser output is transmitted through a polarization-maintaining single-mode optical fiber, guided through a dichroic mirror, and then directed into an inverted microscope (Olympus IX71) with a water immersion objective, UPlansApo NA 1.2, 60X. A sample holder is used to place the sample on a coverslip, and the sample position is adjusted manually using micro-meter screws or automatically using the software-controlled piezo-scanner for precise and repeatable XY scanning and Z-position. The position of the focal point on the sample is monitored by a charged-coupled device detector, and the fluorescence of the sample is collected and passed through a dichroic mirror and filtered using a 430 nm long-pass filter. The fluorescence signal

is allowed to focus into a pinhole with a diameter of 50  $\mu\text{m}$  to remove the out-of-focus signal and is finally directed to the single-photon avalanche photodiodes (SPADs). Depending on the experimental design, single or multiple SPAD detectors can be used. The data is analyzed using SymPhoTime software-controlled PicoHarp 300 TCSPC module in a time-tagged time-resolved (TTTR) mode. Time-resolved confocal fluorescence measurements involve techniques like fluorescence correlation spectroscopy (FCS) and fluorescence lifetime imaging (FLIM), single molecules emission measurements etc.



**Scheme 2.4.** Time-resolved confocal fluorescence microscope setup.

### 2.3.4.2. Fluorescence Correlation Spectroscopy (FCS)

FCS is an elegant and single molecular sensitive technique based on confocal microscopy setup.<sup>256-258</sup> FCS was first introduced by Webb and co-workers<sup>256</sup> while studying the binding

kinetics of ethidium bromide with DNA. FCS techniques usually involves the investigation of the time-dependent fluorescence intensity fluctuation inside a very tiny volume (~ 1fL approximately), The analysis of FCS data provides crucial information on different dynamical processes such as molecular translational diffusion, conformation fluctuations, reaction kinetics, and blinking dynamics of a species in sub microsecond-to-second time scales. Since FCS monitors the sharp fluctuations in fluorescence intensity, the number of fluorophore species inside the confocal volume must be low (only 1 to 3). This can be achieved by using a sample solution of nanomolar concentration. The fluctuations in the fluorescence intensity are then autocorrelated to generate the autocorrelation curves. To improve the temporal resolution and boost the signal to noise ratio, the autocorrelation curves from both detectors are cross-correlated to generate the cross-correlation curves.

## **2.4. Methods**

### **2.4.1. Analysis of the Fluorescence Decay Curves**

#### **2.4.1.1. Data Analysis**

In TCSPC, it is not possible to observe the true intensity decay as the fluorescence decay curve obtained from time-resolved measurements is a convolution or a mixture of the laser pulse and actual fluorescence from the sample. This is because the estimated fluorescence decay time of any fluorophore is higher than the pulse-width of the excitation source. So, the experimental data can be affected by the response time of the photomultiplier tube (PMT), finite decay time of the source pulse, and related electronics.<sup>193</sup> Thus, the overall instrument response function (IRF) depends on the decay time of the laser pulse as well as on the response time of the detector and other associated electronics. Deconvolution of the IRF from the fluorescence decay curves are necessary to obtain the actual fluorescence lifetime of a sample. Therefore, the fluorescence decay profiles were analysed by employing the iterative reconvolution least squares method.<sup>259</sup> This method can be mathematically expressed as the following equation<sup>193, 260, 261</sup>

$$I_m(t) = \int_0^t I_R(t-t')R(t')dt' \quad (2.6)$$

where  $I_m(t)$  = fluorescence intensity at time  $t$ ,  $I_R(t-t')$  = response function of the experimental system,  $R(t')$  = intensity of the exciting pulse at time  $t'$ . IRF was measured using a dilute Ludox solution and deconvolution algorithm is made through iterative reconvolution method.

A nonlinear least squares (NLLS) data processing technique is employed to fit the fluorescence decay curves with an assumed functional form. The least squares approach is useful when the data points meet specific criteria, such as having enough independent data points, having experimental data points with Gaussian distribution of uncertainty, and not having any systematic errors. Both  $I_m(t)$  and  $R(t')$  can be obtained experimentally from the TCSPC setup. During the analysis, a sample-specific decay function  $G(t)$  is first assumed and this function is deconvoluted with the observed  $R(t')$  in accordance to the equation 2.6 to produce a calculated curve  $Y(t)$ . The  $Y(t)$  is then compared with the experimentally observed decay curve  $I_m(t)$ .<sup>193, 260, 261</sup> The variables in the function  $G(t)$  can be changed iteratively until a good fit between the  $Y(t)$  and  $I_m(t)$  is obtained. The function  $G(t)$  is typically assumed to be a sum of exponentials as shown in equation 2.7,

$$G(t) = \sum_i B_i \exp\left(\frac{-t}{\tau_i}\right) \quad (2.7)$$

where  $B_i$  = pre-exponential factor for the  $i^{\text{th}}$  component and  $\tau_i$  = fluorescence lifetime of the corresponding  $i^{\text{th}}$  component. The average lifetime ( $\langle \tau \rangle$ ) of the fluorophore is estimated using equation 2.8,

$$\langle \tau \rangle = \sum_i b_i \tau_i \quad (2.8)$$

where  $b_i$  are the normalized amplitude weighted components and  $\tau_i$  is its corresponding lifetime component. A good fit to the observed decay curves depends on two factors: reduced chi-square values and distribution of weighted residuals.

### 2.4.1.2. Reduced chi-square ( $\chi^2$ ) Values

The reduced  $\chi^2$  is defined by equation 2.9,

$$\chi^2 = \frac{\sum_i W_i (Y_i - I_i)^2}{n-p} \quad (2.9)$$

where  $Y_i$  = count of  $i^{\text{th}}$  channel of the calculated curve,  $I_i$  = count at the  $i^{\text{th}}$  channel of the curve measured experimentally.  $W_i$  [ $W_i = I_i$ ] = weighting factor of the counts in the  $i^{\text{th}}$  channel,  $n$  = number of channels used for the decay to be analysed and  $p$  = number of degrees of freedom in the decay function considered for the analysis which is equal to the number of variables in the function  $G(t)$ . For a good fit, the  $\chi^2$  values must be close to unity. Generally, values of  $\chi^2$  ranging between 1.0 to 1.2 is considered to be a good fit to the data points.

### 2.4.1.3. Distribution of Weighted Residuals

Weighted residual is the difference between the measured decay function and the fitted function. The weighted residuals are considered as one of the important parameters for analysing the TCSPC data set which is defined by equation 2.10,

$$r_i = \sqrt{W_i} (Y_i - I_i) \quad (2.10)$$

The random distribution of the weighted residuals about the zero line over the complete data range is expected to show a good fit. In the present work F980 software provided by Edinburg Instrument has been used for deconvolution of the instrument response function and to fit each decay curve to a suitable mathematical function.

## 2.4.2. Construction and fitting of Time Resolved Emission Spectra (TRES)

TRES usually represents the emission spectra of a fluorophore at particular instant of time after photoexcitation. The energy of the fluorophore in the excited state changes after photoexcitation of the fluorophore to the excited state due to numerous dynamical processes, resulting a change in the fluorescence lifetime of the fluorophore with respect to the emission

wavelength. TRES is created by combining steady-state and time-resolved fluorescence in order to visualise changes in the emission profile immediately following photoexcitation of the fluorophore to the equilibrium state. Maroncelli and Fleming<sup>198</sup> were the first to proposed the method for the construction of TRES plots. According to this method, around 15 to 20 fluorescence decay profiles were collected at magic angle (54.7°) at 5 to 10 nm intervals across the whole range of the steady state emission profile. The decay curves were then fitted using a multiexponential decay function in accordance with equation 2.11 while keeping the  $\chi^2$  value within the range of 1 and 1.2. The random distribution of weighted residuals was also examined during this stage to determine a satisfactory fitting of the decay curves. The fluorescence intensity  $[I(\nu, t)]$  at emission position ( $\nu$ ) and time ( $t$ ) was estimated by the following equation,

$$I(\nu, t) = I_{ss}(\nu) \frac{\sum_j \alpha_j(\nu) e^{-t/\tau_j(\nu)}}{\sum_j \alpha_j(\nu) \tau_j(\nu)} \quad (2.11)$$

where  $I_{ss}(\nu)$  is the steady state fluorescence intensity at  $\nu$ ,  $\tau_j(\nu)$  are the lifetime components and  $\alpha_j(\nu)$  are their corresponding amplitude. The fluorescence spectra for all wavenumber at distinct time have been generated by following this equation. Then, the emission maximum at each time  $\bar{\nu}(t)$  was obtained by fitting the spectrum according to the following log-normal line-shape function which is given by equation 2.12<sup>202</sup>,

$$I = h \exp[-\ln 2 \{ \ln(1 + \alpha) / \gamma \}^2] \quad (2.12)$$

where  $\alpha = 2\gamma(\bar{\nu} - \bar{\nu}_{peak})/\Delta$  and  $\alpha > -1 = 0$  and  $I = 0$  for  $\alpha \leq -1$ ,  $\bar{\nu}_{peak}$  is the wavenumber corresponding to the peak height,  $\Delta$  is the full width at half-maximum (fwhm),  $h$  is the peak maxima and  $\gamma$  is a measure of the asymmetry of the band shape.

### 2.4.3. Solvation Dynamics and Missing Component (MC) Calculation

Peak frequencies obtained from the log-normal fitting of TRES was used for the calculation of solvent correlation function ( $C(t)$ ) which is given below.<sup>202</sup>

$$C(t) = \frac{\bar{\nu}(t) - \bar{\nu}(\infty)}{\bar{\nu}(0) - \bar{\nu}(\infty)} \quad (2.13)$$

where  $\bar{\nu}(\infty)$ ,  $\bar{\nu}(0)$  and  $\bar{\nu}(t)$  are the emission maxima (frequencies) at times infinity ( $\infty$ ), zero ( $t = 0$ ), and  $t$ , respectively. The plot of  $C(t)$  against  $t$  (time) was fitted by a biexponential function as given below,

$$C(t) = \alpha_1 \exp(-t/\tau_1) + \alpha_2 \exp(-t/\tau_2) \quad (2.14)$$

where  $\tau_1$  and  $\tau_2$  are the solvent relaxation time and  $a_1$  and  $a_2$  are normalized pre-exponential factors. Further the  $C(t)$  versus time plot can be fitted by stretched exponential function as follows,

$$C(t) = \exp(-(t/\tau_{solv})^\beta) \quad (2.15)$$

For the fitting of the  $C(t)$  function generated by the combination of both fluorescence up-conversion and TCSPC data, the plot of  $C(t)$  versus  $t$  are fitted to a sum of single exponential as well as a stretched exponential function which is given by the following equation

$$C(t) = f_1 \exp(-t/\tau_1) + f_2 \exp(-t/\tau_2)^\beta \quad (2.16)$$

where  $\beta$  is the stretching exponents, having value between 0 to 1 ( $0 < \beta \leq 1$ ), representing the distribution of the  $\tau_{solv}$  or  $\tau_2$  solvation component. The integral time associated with stretched exponential component is estimated by the following equation

$$\langle \tau_{st} \rangle = \frac{\tau_2}{\beta} \Gamma(\beta^{-1}) \quad (2.17)$$

where  $\Gamma$  is the gamma function and  $\tau_{st}$  is the solvation time associated with stretched exponent time constant  $\tau_2$ .

The boarder temporal resolution of TCSPC setup imposes limitations on the precise estimation of the time-zero spectra and, consequently, the calculation of the dynamic Stokes shift. Therefore, in order to obtain the time-zero spectrum, a semi-empirical approach proposed by Fee and Maroncelli<sup>221</sup> has been applied in the present thesis work. The fundamental premise

of this method is that a particular fluorescent probe should have the same Stokes shift in both polar and nonpolar solvents before solvent relaxation. An approximate time zero frequency ( $\nu(0)$ ), can be calculated by the following relation<sup>221</sup>,

$$\nu_p(0) \cong \nu_p(abs) - \{\nu_{np}(abs) - \nu_{np}(ems)\} \quad (2.18)$$

where the subscripts “p” and “np” represent the polar solvent of interest and a reference nonpolar solvent, respectively. The choice of nonpolar solvent depends on the peak position of absorption of probe molecule in the polar solvent under investigation. Then, the percentage of missing component in dynamics of solvation can be calculated by the following relation<sup>221</sup>,

$$\text{Percentage of missing component, (MC)} = [\{\nu_{cal}(0) - \nu_{obs}(0)\} / \{\nu_{cal}(0) - \nu_{obs}(\infty)\}] \quad (2.19)$$

#### 2.4.4. Time-resolved Fluorescence Anisotropy Measurements

The time-resolved fluorescence anisotropy usually involves the measurements of the dynamics of angular displacement between absorption and subsequent emission of a fluorophore. The basis of time-resolved fluorescence anisotropy is the photo selection of the fluorophore. When a set of fluorophores are illuminated with linearly polarized light, only those fluorophores having their absorption transition moment oriented along the electric field vector of the incident light are preferably excited. This creates an anisotropic polarization in the excited state. However, this polarization is not permanent and various phenomena such as non-parallel absorption emission transition moment, rotational diffusion, torsional vibrations, and energy transfer causes the loss of polarization (depolarization) of the emission. Hence, investigation of the fluorescence anisotropy analysis provides important information regarding the size, shape, and mobility, solute-solvent interaction, micro-viscosity of the medium, etc.<sup>193</sup>

In the time-resolved fluorescence anisotropy measurements, Then the emission intensities corresponding to different excitation and emission polarizer orientation are collected. The ideal anisotropy is expressed by equation 2.20<sup>193</sup>,

$$r(t) = \frac{I_{VV}(t) - GI_{VH}(t)}{I_{VV}(t) + 2GI_{VH}(t)} \quad (2.20)$$

where  $I_{VV}$  is the fluorescence intensity with parallel polarisation, i.e., vertically polarised excitation with vertically polarized emission, and  $I_{VH}$  is the fluorescence intensity with perpendicular polarisation, i.e. vertically polarized excitation with horizontally polarized emission. As the total emission intensity normalises the difference between parallel and perpendicular emission intensities, anisotropy is a dimensionless quantity that is independent of both the fluorophore concentration and the total emission intensity.  $G$  is the instrument correction factor for the detector sensitivity to the polarization of the emission. It is given by the following equation<sup>193</sup>

$$G = \frac{\Sigma I_{VH}(t)}{\Sigma I_{VH}(t)} \quad (2.21)$$

where  $I_{HH}$  is fluorescence intensity with horizontally polarized excitation and horizontally polarized emission and  $I_{HV}$  is the fluorescence intensity with horizontally polarized excitation and vertically polarized emission. This value of  $G$  represents the relative sensitivity of the detection system to the different polarization.  $G$  varies with the emission wavelength and the band pass filter of the monochromator.

In the present thesis work, the time-resolved anisotropy measurements were carried out in a Life Spec II and OB920 Edinburgh setup with 405 and 375 nm laser. For the time-resolved anisotropy measurements, fluorescence intensities at parallel ( $\parallel$ ) and perpendicular ( $\perp$ ) polarization were collected alternatively until a peak difference between parallel ( $\parallel$ ) and perpendicular ( $\perp$ ) decay is  $\sim 5000$  (at  $t = 0$ ) is observed. The same procedure was applied for  $G$ - factor calculation but with horizontal polarization of the exciting laser beam and 5 cycles of repetitions. The temperature of the cell was monitored by circulating water through the cell holder by a Quantum along with a North West (TC 125) temperature controller. Hamamatsu microchannel plate photomultiplier tube (R3809U-50) detector was used to collect the decay

signals of the samples. The decay curves were analysed with the help of F980 decay analysis software. The decay curves were fitted through non-linear least square iteration methods and the quality of the fitting was judge from the chi-square ( $\chi^2$ ) values as well as by verifying the weight deviation. The anisotropy data were fitted to calculate rotational relaxation time by the following equation<sup>193</sup>

$$r(t) = r_0 e^{\left(-\frac{t}{\tau_r}\right)} \quad (2.22)$$

where  $r_0$  is the initial anisotropy and  $\tau_r$  is the rotational relaxation time. It is important to mention here that the  $r_0$  values range from 0.20 to 0.40 for any single-photon excitation. The data corresponding to time-resolved anisotropy decay measurements were further analysed through Stokes-Einstein-Debye (SED) hydrodynamic theory.

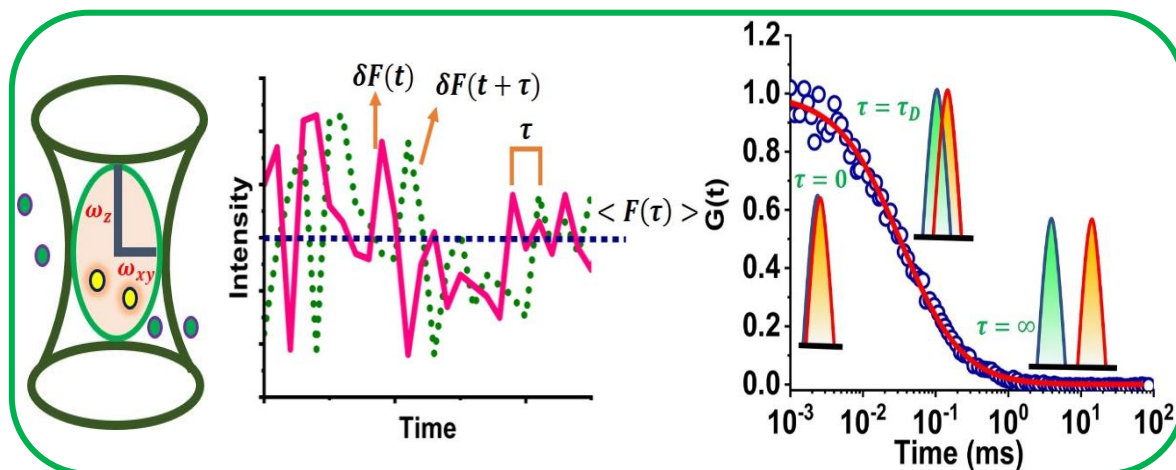
#### 2.4.5. FCS Data Analysis

FCS techniques is a very sensitive and powerful tool for estimating the translational diffusion ( $D$ ) of a probe molecule in a concerned solvent system. This measurement was performed by placing a highly diluted sample (10-20 nM) over a coverslip which in turn placed over the water immersion objective through which the excitation laser was passed. The fluctuation in fluorescence intensities of the sample were measured in very small observation volume ( $\sim 1$  fL) with the help of a pinhole. Now, these fluctuating fluorescence signals were detected by two SPAD detectors and were cross-correlated to generate the correlation curves  $G(\tau)$ . The decay of correlation function with respect to time was used for obtaining the dynamical information on translational diffusion.

The correlation function  $G(\tau)$  for the fluctuation in fluorescence intensity is given by equation 2.23<sup>256-258</sup>

$$G(\tau) = \frac{\langle \delta F(t) \delta F(t+\tau) \rangle}{\langle F(t) \rangle^2} \quad (2.23)$$

where  $\delta F(t)$  and  $\delta F(t + \tau)$  represents the fluctuation in fluorescence intensity around the mean value at time  $t$  and  $(t + \tau)$  respectively and  $\langle F(t) \rangle$  is the average fluorescence intensity.



**Scheme 2.5.** (a) Diffusion of fluorophores through the confocal volume, (b) fluctuations in the relative fluorescence intensities and (c) correlation of the fluctuation in fluorescence intensities at different time interval.

The correlation data can be fitted to both single-component diffusion which is given by the following equation<sup>193, 256-258</sup>,

$$G(\tau) = \frac{1}{N} \left(1 + \frac{\tau}{\tau_D}\right)^{-1} \left(1 + \frac{\tau}{k^2 \tau_D}\right)^{-\frac{1}{2}} \quad (2.24)$$

In equation 2.24,  $N$  represents the average number of fluorescent molecules in the observation volume,  $\tau$  is the delay or lag time, and  $\tau_D$  is the translational diffusion time constant or the time taken for the fluorophore molecule to diffuse through the observation volume.  $k$  represents the aspect ratio of the observation volume which is given by,  $k = z/w_{xy}$ , where  $z$  and  $w_{xy}$  are the longitudinal and transverse radii of the observation volume, respectively. The excitation volume of the FCS setup was calibrated by taking a dilute solution of Rhodamine 6G (R6G) in water whose translational diffusion coefficient ( $D_t$ ) is  $426 \mu\text{m}^2\text{s}^{-1}$ . The estimated excitation volume was  $\sim 0.45\text{fL}$  for 405 nm laser and  $\sim 0.80\text{fL}$  for 483 nm laser sources. The  $D_t$  was calculated by using equation 2.25 which is provided below

$$D_t = \frac{w_{xy}^2}{4\tau_D} \quad (2.25)$$

The single component diffusion model is not always the best choice for fitting autocorrelation data, especially in highly viscous and organized media such as DESs and RTILs. In these cases, alternative models are used to obtain a better fit for the autocorrelation data. One such alternative model is the anomalous diffusion model, which can be expressed using the following equation<sup>185, 186, 262</sup>,

$$G(\tau) = \left[ \frac{1}{N \times [1 + (\tau/\tau_D)^\beta] \times \left[ \sqrt{1 + (\tau/\tau_D)^\beta \left(\frac{1}{k^2}\right)} \right]} \right] \quad (2.26)$$

where  $\beta$  ( $0 < \beta < 1$ ) is the stretching exponent representing the distribution of  $\tau_D$ . Likewise, the two-component diffusion model has also been employed to achieve a better fit for the FCS traces. The corresponding equation for this model is given by equation 2.27<sup>243, 245, 263</sup>,

$$G(\tau) = \frac{1}{N} \left[ \frac{\alpha_1}{\left(1 + \frac{\tau}{\tau_{D1}}\right) \left(1 + \frac{\tau}{K^2 \tau_{D1}}\right)^{1/2}} + \frac{\alpha_2}{\left(1 + \frac{\tau}{\tau_{D2}}\right) \left(1 + \frac{\tau}{K^2 \tau_{D2}}\right)^{1/2}} \right] \quad (2.27)$$

where  $\tau$  is the delay or lag time, and  $\alpha_1$  and  $\alpha_2$  are the corresponding amplitude associated with the translational diffusion time constant  $\tau_{D1}$  and  $\tau_{D2}$  respectively. The average translational diffusion time constant is estimated from the individual amplitude associated with  $\tau_{D1}$  and  $\tau_{D2}$  which is given by

$$\tau_d^{avg} = \alpha_1 \times \tau_{D1} + \alpha_2 \times \tau_{D2} \quad (2.28)$$

#### 2.4.6. Pulsed Field Gradient NMR Techniques

The self-diffusion coefficient of all the samples were determined using pulse field gradient (PFG) NMR techniques. A stimulated echo bipolar pulse-gradient pulse (stebpgp) sequence was applied with maximum gradient pulse strength of 50G/cm. The echo heights were attained

by varying the gradient pulse strength from 2-95 % at 16 equal intervals. The echo heights were fitted using Stejskal–Tanner equation<sup>264</sup> which is given below

$$S(g) = S(0) \exp \left[ -D\gamma^2 \delta^2 g^2 \left( \Delta - \frac{\delta}{3} \right) \right] \quad (2.29)$$

where  $S(g)$  and  $S(0)$  are the echo height at the gradient strength  $g$  and 0, respectively.  $\gamma$  and  $\delta$  are the gyromagnetic ratio of the proton and gradient pulse length, respectively, while  $\Delta$  and  $D$  represents the duration between the two gradient pulses and diffusion coefficient, respectively.

## 2.5. Calculation of Limit of Detection and Limit of Quantification

$$(\text{SD}) = \text{SE} * \sqrt{n} = 9761.73 \quad (2.30)$$

where SD is the standard deviation,  $n$  is the number of data points, SE is the standard error.

Limit of detection =  $(3 * \text{SD})/\text{slope}$

Limit of quantification =  $(10 * \text{SD})/\text{slope}$

Here slope is the ratio of relative fluorescence intensity versus quencher concentration.

## 2.6. Standard Error Limits

**Table 2.2.** standard error limits for various experimental results

Experimental Parameter	Error
$\lambda_{\text{max}}$ (abs./flu.)	$\pm 1-2$ nm
Viscosity	$\pm 2$
$\tau_f$ (> 1ns)	$\pm 5\%$
Rotational Relaxation time	$\pm 5\%$
Average solvation time	$\pm 5\%$
Diffusion coefficient (through NMR)	$\pm 5\%$
Diffusion coefficient (through FCS)	$\pm 5-10\%$

# CHAPTER 3A

---

## Understanding the Differences in the Microscopic Behaviour between Deep Eutectic Solvents and Room Temperature Ionic Liquids

---

---

Barik, S.; Chakraborty, M.; Mahapatra, A.; Sarkar, M.; *Phys. Chem. Chem. Phys.*, 2022,24, 7093-7106.

**Abstract**

In the first part of this chapter, the differences in the microscopic behaviours in terms of structural organization, intra- and inter-molecular interactions, and dynamics of the solvent systems between DESs and RTILs containing similar functionalities (hydroxyl) have been investigated. For this purpose, we have employed three hydroxyl-functionalized ILs (HFILs) and one choline chloride-based DES (ethaline), and their microscopic behavior has been investigated by exploiting various spectroscopic techniques such as EPR, time-resolved fluorescence, NMR, and FCS studies. Estimation of polarity through EPR spectroscopy has revealed that the HFILs employed in these studies are hyper-polar (close to water) in nature, whereas the polarity of the DES is found to be close to aliphatic polyhydroxy-alcohol. Interestingly, both time-resolved fluorescence anisotropy and FCS studies on these systems have suggested that HFILs are dynamically more heterogeneous than the DES. More interestingly, PFG-NMR measurements have indicated that the fluid structure of ethaline is relatively more associated as compared to that of HFILs despite the fact that all the cations have the same hydroxyl functionalities. All these investigations have essentially demonstrated that despite having similar functionalities, the microscopic behaviour of both DES and HFILs employed in the present study are significantly different from each other, indicating the interplay of various intermolecular interactions within the constituent species in governing the behaviours of these solvent systems.

---

**3A.1. Introduction**

The recent upsurge interest in RTILs towards both industry and academia stems from their many desirable physicochemical properties.<sup>24, 29</sup> However, non-biodegradability and toxicity are some of the challenging issues which are often encountered with RTILs.<sup>107-108</sup> In contrast to this, DESs have emerged as a potential substitute for both RTILs and common volatile

organic solvents owing to their biodegradability, biocompatibility, relatively less toxicity and environment-friendly nature.<sup>19-20</sup> As both RTILs and DESs share many characteristic physicochemical properties, DESs are often regarded as a subclass of ILs.<sup>19-20, 106</sup> However, researchers have pointed out that despite their similarities, both DESs and RTILs are by far different groups of substances.<sup>106-108</sup> In RTILs, apart from some non-covalent interaction (Van der Waal's interaction, dipole-dipole interaction, etc.), columbic interaction between the cations and anions is the dominant contributor to the structure and property of ILs.<sup>65</sup> However, in case of DESs, it is believed that complex hydrogen bonding between the constituent species is responsible for governing the macroscopic physicochemical properties of DESs.<sup>19-20</sup> Due to this, it has also been pointed out that there are much more differences than similarities between these two classes of systems.<sup>106-108</sup> In this scenario, it would be interesting to know the comparative behavior of DES and ILs having similar functionalities (hydroxyl group) so as to understand whether the microscopic behaviour of these classes of solvent systems is dictated by hydrogen bonding interaction or other types of intermolecular interaction.

As stated earlier many advance experimental and theoretical techniques have been undertaken to explore the microscopic structural organization and dynamics of DESs and RTILs independently.<sup>147-167</sup> Atkins and co-workers<sup>29</sup> have suggested that ILs have huge structural diversity depending on the nature of ions as well as their self-organization into ion pairs, ion crystal lattice, H-bonding network, and micellar domains. Fayer and co-workers<sup>31</sup> have also reported that the intra and intermolecular interactions in ILs have a significant impact on the heterogeneous microstructural organization and liquid morphology, which contribute to the dynamic heterogeneity of ILs. Moreover, the complex solvation process of ILs has also been reported by many groups, and it has been demonstrated that the multiple time scale of solvent relaxation phenomena is significantly affected by the heterogeneity of the medium.<sup>205-</sup>

<sup>225</sup> However, for DESs, assessment about the medium heterogeneity is not straightforward. For example, Biswas and co-workers<sup>176-178</sup> have reported that the non-ionic DES form between the combination of acetamide and urea is not heterogeneous, whereas the combination of choline chloride /urea or acetamide/electrolyte mixtures are both spatially and dynamically heterogeneous. Furthermore, the DES ethaline, a mixture of choline chloride and ethylene glycol, is reported to be spatially homogeneous but dynamically heterogeneous.<sup>185, 265</sup> Though there are few studies that describe the structural organization of some neat ILs and DESs, understanding of the differences in the microscopic structural organization between these two classes of substances still remains hazy. Therefore, it would be interesting to probe the differences in the microscopic behaviour between DESs and ILs in terms of the nature of solute-solvent interaction, intermolecular interactions, and dynamics of the solvents systems in a comparative manner by employing substances having similar functional moieties for both DESs and ILs. Studies on this aspect are expected to be helpful in understanding the structure-property relationship for this class of substances.

In light of the foregoing discussion, the current study focuses on understanding the differences in the microscopic behaviour between DES and ILs. For this purpose, a DES, namely ethaline (choline chloride + ethylene glycol 1:2 ratio) and three other hydroxyl group containing RTILs, are employed for the study. The hydroxyl functionalized ILs (HFILs) have been chosen purposefully so that apart from the role of the hydroxyl group, various other factors which account for the microscopic behaviour of both DES and ILs can be clearly understood. Furthermore, for a fair comparison between the DES and ILs, a cholinium ionic liquid ( $[N_{311}][NTf_2]$ ) (Chart 3A.1) consisting of propyl chain length has also been used for this study. The differences in the microscopic behaviour between the DES and HFILs have been investigated with the help of different spectroscopic techniques such as steady-state and time-

resolved fluorescence, FCS, EPR, and NMR so that information regarding the local environment, solute-solvent interactions, and the dynamic of the solvent systems can be obtained. Especially, rotational and translational diffusion dynamics of some selected probes through time-resolved fluorescence anisotropy measurement and FCS techniques, respectively, have been used to differentiate the local environment and nature of solute-solvents interaction between DES and ILs. Moreover, the polarities and self-diffusion coefficients of the concerned solvent systems have been estimated by exploiting EPR and NMR techniques, respectively. All these investigations have revealed a significant difference in the microscopic behaviours between the HFILs and DES despite the fact that they have the same (hydroxyl) functionalities. This observation indicates that in addition to intermolecular hydrogen bonding interaction, the interplay of various other types of intermolecular interactions within the constituent species can also have a significant impact on governing the behaviours of these solvent systems.

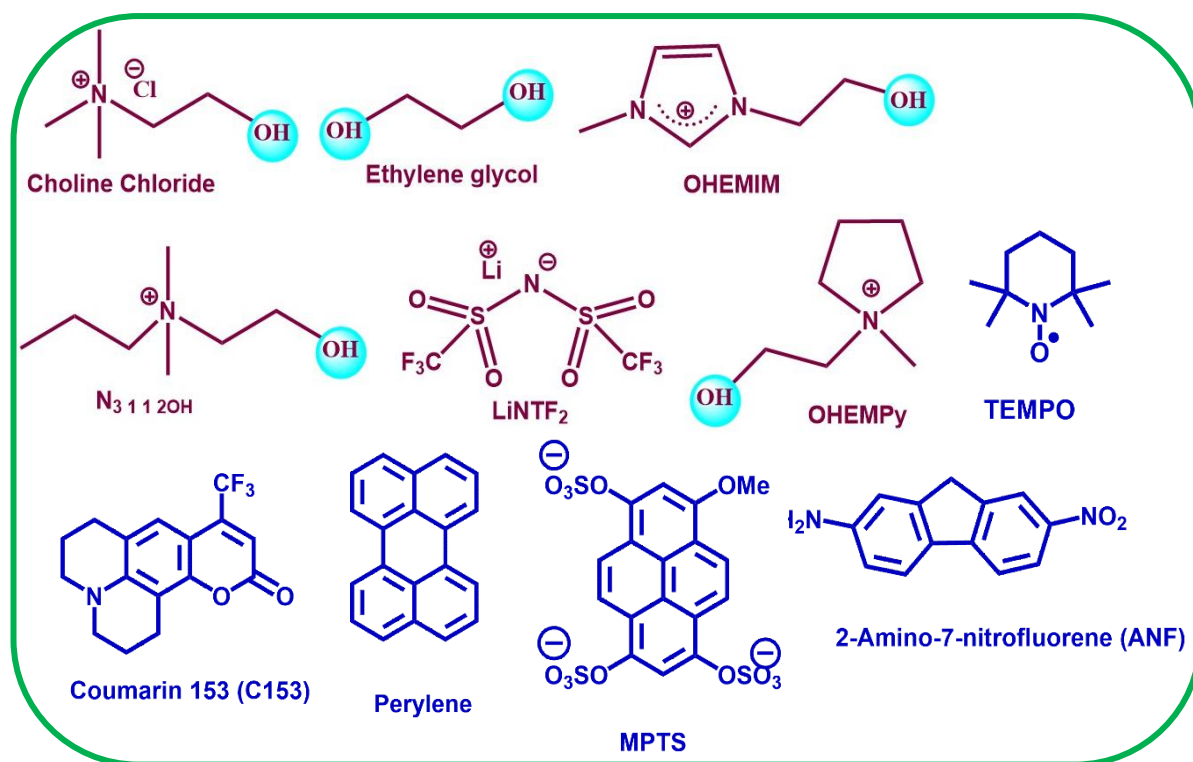


**Chart 3A.1.** Chemical Structure of the DES, HFILs and the probes used in this work.

### 3A.2. Experimental Sections

The detail about the synthesis of different HFILs and the DES have been provided in chapter 2. Both DES and HFILs are dried in the vacuum at 323K for 2 days so as to reduce the moisture contain before use. The viscosity values of all the solvents systems are almost comparable with previously reported literature values. The dried solvents were transferred into 2cm quartz cuvette and requisite amount of probe was added to prepare the solution (keeping absorbance below 0.3). The probes (C153, Perylene and MPTS) concentration was 5-7  $\mu\text{M}$  (keeping the absorbance below 0.3) for steady-state and time-resolved fluorescence studies, whereas for FCS studies the probe concentration was 10-20 nM. All the cuvette were thoroughly sealed with septum and parafilm to avoid moisture intake. The details about different instrumental techniques (i.e., steady-state and time-resolved fluorescence, FCS, EPR, and NMR) and procedure for data analysis have been discussed in chapter 2.

### 3A.3. Results and Discussions

#### 3A.3.1. Steady-State Spectral Measurements

The steady-state absorption and emission spectra of a dipolar probe C153 in both DES and HFILs are provided in Figure 3A.1 The absorption and emission maxima of C153 in all the concerned solvents are collected in Table 3A.1. From Figure 3A.1, one can observe that there are hardly any differences observed in the emission or absorption spectra of C153 in DES and HFILs. From Table 3A.1 also, no noticeable changes in absorption or emission maxima of C153 are observed in all the solvent systems. So, in the current experimental condition and looking only at the steady state spectra, both DES and HFILs seem to be indistinguishable from each other, indicating a similar polar environment for both DES and HFILs.

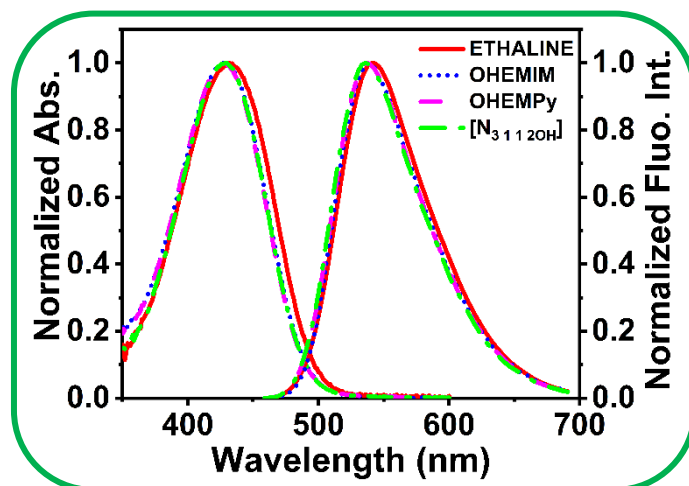


**Figure 3A.1.** Normalized absorption (left side) and emission spectra (right side) of C153 in Ethaline and HFILs.  $\lambda_{ex} = 405 \text{ nm}$ .

**Table 3A.1.** Absorption and Emission Maxima of C153 in various solvent systems

System	$\lambda_{\text{max}}(\text{abs})$ (nm)	$\lambda_{\text{max}}(\text{ems})$ (nm)
Ethaline	431	539
[OHEMIM][NTf <sub>2</sub> ]	429	538
[OHEMPy][NTf <sub>2</sub> ]	428	536
[N <sub>3 1 1 20H</sub> ][NTf <sub>2</sub> ]	428	537

However, just by monitoring the absorption and emission spectra of C153 in a concerned solvent, it is often difficult to comprehend the medium polarity accurately. This is because the difference in the ground state and excited state dipole moment is not very high for C153 (~ 6 Debye).<sup>105, 213</sup> Moreover, effect such as solute-solvent hydrogen bonding interaction is not well accounted for C153 when the polarity of a solvent is estimated through the steady-state spectral shift of C153.<sup>105, 213</sup> Here, we would also like to note that many previous studies on DESs and ILs also fail to distinguish the medium polarity completely only by observing the steady-state spectral properties of C153.<sup>186, 213, 242, 266</sup> Since the polarity of the medium is often estimated spectroscopically by measuring the transition energy of Reichardt's dye 30 in that solvent, we have also made an attempt to estimate the polarity of the media that are used in this

study through this method.<sup>100, 101</sup> The absorption spectra of Reichardt's dye 30 for the current solvent systems (DES and HFILs) have been provided in Figure APX3A.1. From Figure APX3A.1, it can be seen that the long wavelength CT band in [OHEMIM][NTf<sub>2</sub>] and [OHEMPy][NTf<sub>2</sub>] is missing due to which it is not possible to estimate the solvent polarity parameter ( $E_T(30)$ ) and Kamlet-Taft parameter for all the solvents (Table APX3A.1). It is not surprising as the Reichardt's dye 30 is found to be insoluble in many molecular liquids and more importantly the long wavelength CT band also remain absent in many molecular solvents.<sup>103</sup> The absence of the long wavelength CT band of Reichardt's dye 30 can be explained by considering the protonation of phenolate oxygen atom arising from the acidity of these HFILs.<sup>103</sup>

Considering the above discussion, we have explored the utility of EPR spectroscopy as a valuable method to accurately measure small changes in medium polarity. This approach is an alternative to the methods mentioned earlier, and involves monitoring the EPR spectra of a free radical probe, such as 2,2,6,6-tetramethylpiperidine-1-oxyl (TEMPO), in media such as ILs.<sup>267-269</sup> The nitroxide radical of TEMPO usually exists in a charge transfer (CT) structure and shows a triplet hyperfine structure with unequal intensities in the EPR spectra.<sup>266-268</sup> The ( $a_N/G$ ) value, which describes the nitrogen isotropic hyperfine coupling constant in Gauss, indicates the perturbations of the spin-density distribution of TEMPO in solution caused by electrostatic interactions and hydrogen bonding with the solvent. It has also been reported that the value of ( $a_N/G$ ) depends on the spin density around the nitrogen atom. As the medium polarity increases, the stabilization of the ground state CT structure of the nitroxide radical increases the spin density around the nitrogen atom, resulting in an increase in ( $a_N/G$ ) for TEMPO. Therefore, by estimating the ( $a_N/G$ ) value of TEMPO in the solvents, one can obtain a quantitative idea of the difference in polarity between DES and HFILs. Figure 3A.2 shows the EPR spectra of TEMPO, along with corresponding simulated spectra, in both DES and

HFILs. The line shape of the EPR spectra reflects the spin relaxation process due to the tumbling motion of TEMPO radical, and differences in the line shape indicate variations in the rotational behaviour of TEMPO in these solvents.<sup>266-268</sup> The rotational motion of TEMPO in a particular solvent is significantly affected by its viscosity, intermolecular hydrogen bonding interaction with the solvent molecule, and extent of microheterogeneity of the solvent.<sup>266-268</sup> Since the aforementioned properties of the concerned solvent systems are different for each solvent, it is reasonable to observe a difference in the line shape of the EPR spectral signal due to a change in the microenvironment of these solvent systems.

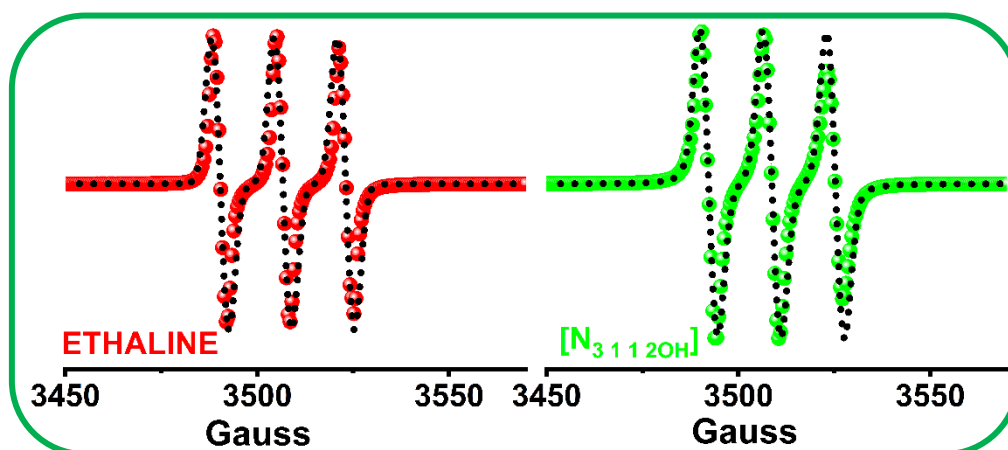


**Figure 3A.2.** EPR spectra of TEMPO (Blue sphere) in DES and HFILs. Red line represents the corresponding simulated spectra.

Here we note that for viscous and confined media like DESs and RTILs, assessment of  $a_N/G$  value from the maxima of two successive hyperfine lines may lead to imprecise estimation of the  $a_N/G$  value because of spectral broadening.<sup>268</sup> In such a scenario, the  $a_N/G$  values have been estimated from the centre point of two consecutive hyperfine lines. The EPR spectra of TEMPO dissolved in a series of known solvents of varying polarities have also been recorded, and their corresponding  $a_N/G$  values have been estimated with the help of spectral data. In addition to this, the solvent polarity parameter ( $E_T(30)$ ) values of these known solvents are collected from the literature.<sup>270</sup> Then, a calibration curve is generated by plotting the  $a_N/G$  values (Y-axis) of TEMPO in these known organic solvents against their corresponding  $E_T(30)$

values (X-axis). The  $E_T(30)$  values for various known solvents are provided in Table 3A.2. Figure 3A.3 represents the plot of  $a_N/G$  versus  $E_T(30)$  for various solvent systems. Now by estimating the  $a_N/G$  values for the unknown solvent systems and then by using the calibration curve,  $E_T(30)$  values of the unknown solvent system are determined.

**Table 3A.2.** The  $a_N/G$  value of TEMPO in DESs and HFILs and their estimated  $E_T(30)$  values

Solvents	$a_N/G$	$E_T(30)/\text{kcal mol}^{-1}$
Ethaline	$16.31 \pm 0.012$	$58.6 \pm 0.015$
[OHEMIM][NTf <sub>2</sub> ]	$16.57 \pm 0.011$	$61.8 \pm 0.017$
[OHEMPy][NTf <sub>2</sub> ]	$16.49 \pm 0.012$	$60.4 \pm 0.015$
[N <sub>3</sub> 112OH][NTf <sub>2</sub> ]	$16.52 \pm 0.018$	$60.8 \pm 0.017$
[BMIM][NTF <sub>2</sub> ] <sup>a</sup>	$16.03 \pm 0.019$	$52.5 \pm 0.02$
Ethylene glycol	$16.24 \pm 0.017$	$56.3 \pm 0.015$
Chloroform	$14.87 \pm 0.016$	$39.1 \pm 0.018$
Acetone	$15.04 \pm 0.018$	$42.2 \pm 0.015$
Ethyl alcohol	$15.82 \pm 0.017$	$51.9 \pm 0.016$

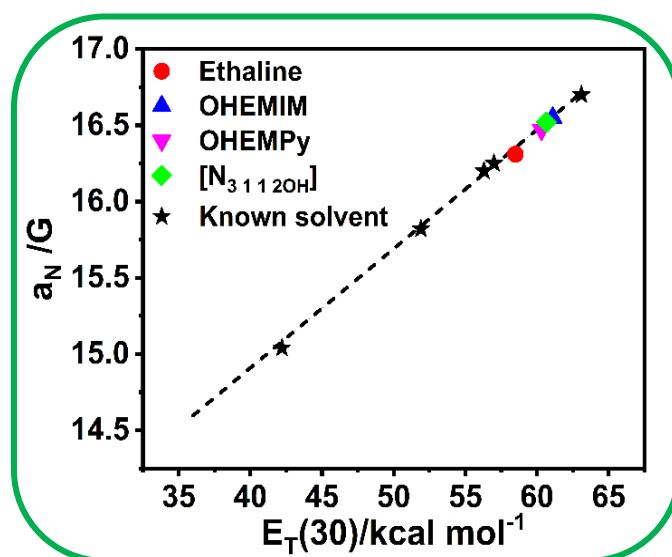


**Figure 3A.3.** Plot of  $a_N/G$  vs.  $E_T(30)$  values of TEMPO in both DES and HFILs. The black square indicates the  $E_T(30)$  values corresponding to known solvents.

From Table 3A.2, it can be noticed that the  $E_T(30)$  values of HFILs are found to be higher than that of ethaline, indicating that the micro-polarities of the HFILs are relatively higher than that of ethaline. Interestingly, the  $E_T(30)$  values of all the HFILs are found to be close to that of water ( $E_T(30) = 63.1 \text{ kcal mol}^{-1}$ ).<sup>270</sup> Deng and co-workers<sup>103</sup>, while determining the polarity of some non-hydroxyl and hydroxyl functionalized ILs through solvatochromic studies of Recharadt's dye, have also found the unusual hyper-polarity of HFILs. Through computational studies, they have demonstrated that the intramolecular synergistic effect that exists between the hydroxyl group of the cation and the corresponding anion is primarily responsible for the unusual hyper-polarity of HFILs. Furthermore, Shibuya and co-workers<sup>267</sup> have suggested that the oxygen of ATEMPO (4-amino-2,2,6,6-tetramethylpiperidine-1-oxyl) can interact with the C2 hydrogen of 1-butyl-3-methylimidazolium bis(trifluoromethanesulfonyl)imide through hydrogen bonding interaction and thereby increase the value of  $a_N/G$  and polarity of the medium. In light of these findings, in the present study, we can infer that in [OHEMIM][NTf<sub>2</sub>], both C2 hydrogen and the hydroxyl group can form H-bonding interaction with anion as well as with the oxygen of nitroxide radical and thereby enhance the polarity of the medium to a greater extent as compared to that of other two HFILs. Here we would like to mention that the hyper-polarity of HFILs is one of the interesting findings as these functionalized ILs can be potential candidates for high polar non-acidic and non-aqueous media, which can be used as a substitute for water and high polar organic solvents in synthesis and catalysis.<sup>103</sup>

As DES and HFILs are highly viscous media, solvation of a solute fluorophore occurs relatively slowly compared to common solvents such as water, DMSO, or ethanol. As a result, fluorescence can be observed from different unrelaxed states of the solvent around the fluorophore in these media. This is particularly true when the fluorescence lifetime of the

fluorophore is much shorter than the average solvation time in a specific solvent, allowing the fluorophores to exist in a state where they are not fully solvent-equilibrated.<sup>168, 196, 271</sup> Under these conditions, the microenvironments around the fluorophores differ, resulting in a shift in the emission maxima as the wavelength of the excitation source varies. This is a very well-known method for determining the micro-heterogeneous behaviour of a given heterogeneous solvent.<sup>168, 195, 196, 271</sup> In the current studies, we have tried to explore the difference in the micro-heterogeneous behaviour of DES and HFILs by employing excitation wavelength ( $\lambda_{ex}$ )-dependent shift in fluorescence maxima ( $\lambda_{em}^{max}$ ) of 2-amino-7-nitrofluorene (ANF). ANF has a lifetime of nearly 50 picoseconds, and it is known to exhibit a shift in  $\lambda_{em}^{max}$  by increasing the  $\lambda_{ex}$  towards longer wavelength.<sup>168, 196</sup> Upon looking at Figure 3A.4, a shift of 8 nm of  $\lambda_{em}^{max}$  is observed in case of ethaline by increasing the  $\lambda_{ex}$  from 390 to 510 nm. However, the shift in  $\lambda_{em}^{max}$  is found to be more than double in case of [OHEMPy] [NTf<sub>2</sub>], indicating more spatial heterogeneity in the medium as compared to ethaline. Furthermore, by comparing ethaline with its IL analogous ([N<sub>3112</sub>OH] [NTf<sub>2</sub>]), the observed shift in  $\lambda_{em}^{max}$  is also found to be greater (15 nm) for the latter than the former. This observation indicates that the DES under current studies is spatially less heterogeneous as compared to the HFILs. Here we would like to mention that ANF also shows a shift of 8 nm of the absorption maxima upon going from [OHEMIM][NTf<sub>2</sub>] to ethaline (Figure APX3A.2(a)), which is because of the difference in the medium polarity. However, it has been reported earlier that the extent of shift in the  $\lambda_{em}^{max}$  with increase in  $\lambda_{ex}$  is not because of the shift in the  $\lambda_{max}^{abs}$  but arises because of the inhomogeneous broadening of the absorption spectra due to a distribution of the solute-solvent interaction energy in these confined media which is found to be more for the HFILs (FWHM=112 nm) as compared to the DES (FWHM= 101 nm).<sup>169, 213</sup> Moreover, the average lifetime ( $\tau_{avg}$ ) for ANF in both ethaline and HFILs are found to be comparable ( $\tau_{avg} \leq 40$  ps) (Figure APX3A.2(b)). But the average

solvation time ( $\tau_{solv}$ ) in these media, as reported earlier (e.g.  $\tau_{solv}$  = 160 ps for ethaline and 560 ps for OHEMIM)<sup>224, 272</sup> are found to be much higher than the  $\tau_{solv}$  of ANF. Therefore, it is possible to observe fluorescence from the excited species which are not fully solvent equilibrated.<sup>169, 213</sup> As shown before, the  $\tau_{solv}$  is estimated to be different for different solvents. Hence, as the average solvation time (as well as viscosity) in HFILs are much higher as compared to that of ethaline, it is reasonable to expect a more shift in the  $\lambda_{em}^{max}$  with increase in the  $\lambda_{ex}$  for the former than the latter. Though the investigation of  $\lambda_{ex}$  dependence shift in  $\lambda_{em}^{max}$  cannot provide the exact length scale at which the particles are correlated, it only provides a qualitative idea about the medium heterogeneity.

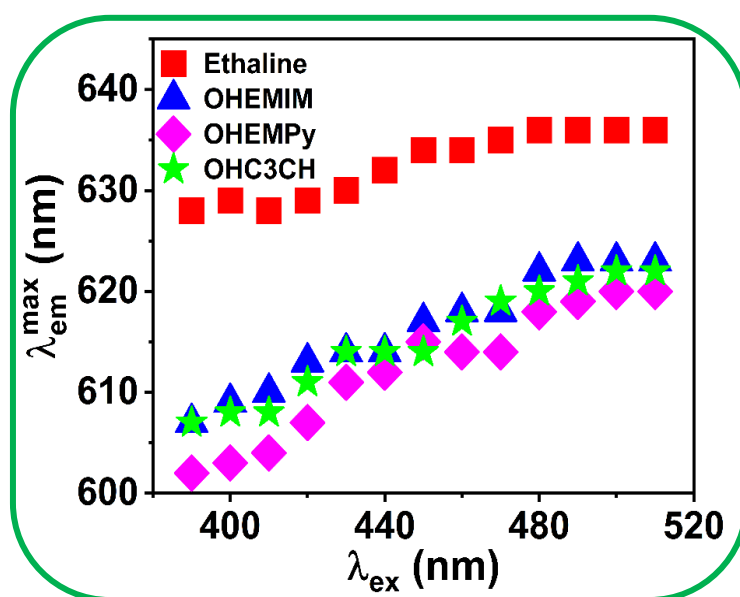


**Figure 3A.4.** Plots of  $\lambda_{em}^{max}$  versus  $\lambda_{ex}$  of ANF at 298 K of DES and HFILs. (Experimental error =  $\pm 2$  nm).

### 3A.3.2. Rotational Relaxation Dynamics

Since DESs also differ from ILs based on their constituent materials and preparation method, the local structure organization of DESs could be different from that of ILs. So, to know more about the difference in the microscopic behaviour in terms of solute-solvent interactions in given micro-heterogeneous systems like DES and HFILs, rotational dynamics

for three probe molecules of different chemical characteristic have been investigated through time-resolved fluorescence anisotropy measurement.

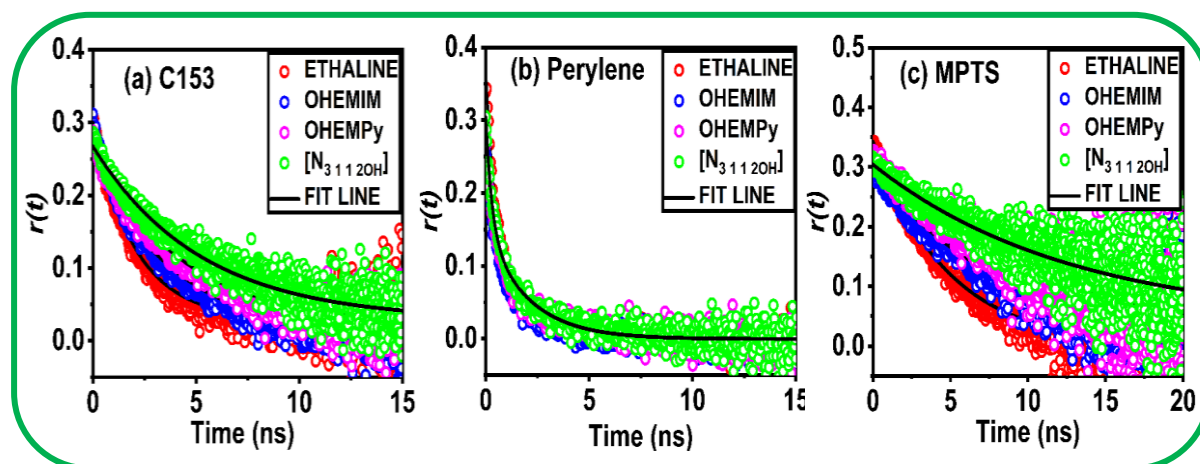


**Figure 3A.5.** Time-resolved fluorescence anisotropy decay for (a) C153, (b) perylene and (c) MPTS in DES and HFILs at 298 K.

**3A.3.2.1. C153:** Figure 3A.5(a) represents the plot of time-resolved fluorescence anisotropy decay for C153 in both DES and HFILs at 298K. The data have been fitted to a single exponential decay function to obtain the rotational reorientation time ( $\tau_r$ ) of C153 in both DES and HFILs. The measured  $\tau_r$  values along with viscosity at 298K to 328K are collected in Table 3A.3. From Figure 3A.5(a), a faster anisotropy decay of C153 in ethaline as compared to the HFILs is observed, owing to the lower bulk viscosity of the former than the latter. From Table 3A.3 also, one can find that the experimentally observed  $\tau_r$  value of C153 in ethaline is relatively lower than that in the HFILs. As the temperature increases, there is a consistent decrease in the  $\tau_r$  values across all solvent systems. This trend corresponds to the overall reduction in the bulk viscosity of the concerned medium as temperature increases (Table 3A.3). However, when the data is compared for ethaline and its ILs analogous, i.e.  $[N_{31120H}][NTf_2]$ , it can be noticed that the  $\tau_r$  value does not vary proportionately with the increase in the value of the viscosity of concerned medium.

**Table 3A.3.** Rotational relaxation parameter of different probes in both DES and HFILs

System	$\eta$ (cP)/T (K)	C153		Perylene		MPTS	
		$\tau_r$ (ns)	$C_{obs}$ (avg.)	$\tau_r$ (ns)	$C_{obs}$ (avg.)	$\tau_r$ (ns)	$C_{obs}$ (avg.)
Ethaline	38.5/(298)	2.44		0.95		4.79	
	30.6/(303)	1.90		0.80		4.02	
	24.7/(308)	1.55	0.65	0.68	0.30	3.3	1.27
	20.5/(313)	1.27		0.57		2.84	
	16.9/(318)	1.1		0.51		2.41	
	14.7/(323)	0.95		0.44		2.11	
[OHEMIM][NTf <sub>2</sub> ]	72.7/(298)	4.02		1.53		7.12	
	57.6/(303)	3.42		1.3		5.92	
	45.5/(308)	2.85	0.61	1.07	0.25	4.95	1.06
	37.2/(313)	2.34		0.92		4.40	
	30.6/(318)	1.98		0.81		3.82	
	26.5/(323)	1.75		0.72		3.39	
[OHEMPy][NTf <sub>2</sub> ]	92.4/(298)	4.30		1.69		7.64	
	71.8/(303)	3.60		1.39		6.45	
	58.4/(308)	3.15	0.55	1.18	0.22	5.69	0.95
	47.3/(313)	2.62		0.98		5.12	
	39.1/(318)	2.23		0.83		4.52	
	31.4/(323)	1.83		0.76		3.72	
[N <sub>3112</sub> OH][NTf <sub>2</sub> ]	98.5/(298)	4.76		1.81		8.91	
	77.5/(303)	3.92		1.43		7.88	
	63.4/(308)	3.4	0.55	1.2	0.21	7.19	1.07
	52.1/(313)	2.85		1.02		6.3	
	42.3/(318)	2.32		0.9		5.28	
	34.2/(323)	2.03		0.77		4.48	

**Table 3A.4.** Rotational relaxation parameter of different probes in both DES and hydroxyl ILs at iso-viscous condition.

System	C153	Perylene	MPTS
Ethaline	2.44	0.95	4.79
[OHEMIM][NTf <sub>2</sub> ]	2.36	0.94	4.45
[OHEMPy][NTf <sub>2</sub> ]	2.20	0.81	4.47
[OHC3CH][NTf <sub>2</sub> ]	2.19	0.82	4.57

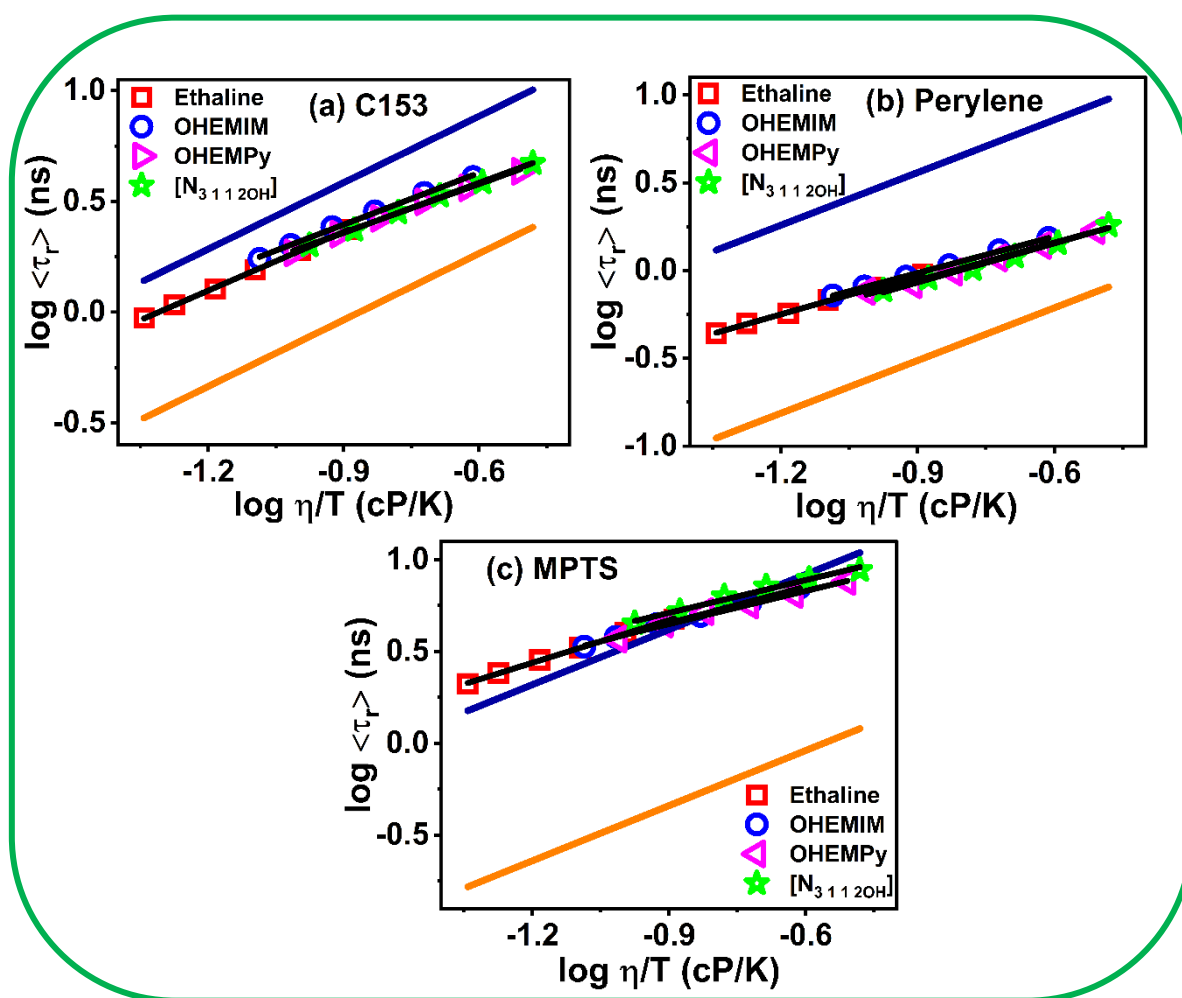


**Figure 3A.6.** log-log plot of  $\tau_r$  versus  $\eta/T$  of C153 (a), perylene (b) and MPTS (c) in both DES and HFILs. Solid orange and blue line represent the slip and stick boundary condition respectively. Solid black line represents linear fit to the data points.

For example, upon going from ethaline to  $[\text{N}_{3112\text{OH}}][\text{NTf}_2]$ , the viscosity increases by nearly 2.5 times, whereas the increase in  $\tau_r$  value is estimated to be almost 2 times. Additionally, we have also measured the  $\tau_r$  value of C153 in all concerned media at iso-viscous condition (Table 3A.4). From Table 3A.4, one can also notice that the rotational diffusion of C153 in HFILs are found to be faster than that of ethaline. All these observations essentially indicate that C153 experiences different friction in ethaline and  $[\text{N}_{3112\text{OH}}][\text{NTf}_2]$ , and micro-viscosity felt by C153 is different in the two media.

To shed more light about the solute-solvent interaction in the media under study, the  $\tau_r$  values are analyzed by the Stokes-Einstein-Debye equation (equation 1.1)<sup>193, 232</sup>. Figure 3A.6(a) shows the SED plot of C153 in both DES and HFILs, revealing that the  $\tau_r$  values for C153 in all relevant solvent systems lie between the stick and slip boundary line predicted by hydrodynamic theory. A more detailed understanding about the interaction of C153 with both DES and HFILs can be obtained by considering the friction coefficient,  $C_{obs}$  value (ratio between the experimentally measured  $\tau_r$  value and theoretically calculated  $\tau_r$  value).<sup>229, 233</sup> Since the  $C_{obs}$  value is obtained by the aforementioned ratio, the value of  $C_{obs}$  usually depicts the extent of solute-solvent interaction. It is important to note that changes in temperature can also alter hydrogen bonding and therefore change the structure of the medium, which would also affect the  $C_{obs}$  value. Table 3A.3 indicates that the average  $C_{obs}$  value of C153 in ethaline is relatively higher than in the HFILs, suggesting that C153 experiences more friction in ethaline than in HFILs. Additionally, data from Table 3A.3 reveals that among the HFILs, C153 experiences more hindered rotation in  $[\text{OHEMIM}][\text{NTf}_2]$  compared to the other two HFILs. Thus, in the present study, the observation of different friction coefficient for the probe solute in different media that are employed in the study, indicates that micro-viscosity felt by

the solute is different and all these results evidently reveals that the microscopic structural organisation of HFILs are different from each other as well as different from ethaline.

To corroborate the above outcomes, we have fitted the  $\tau_r$  value of C153 in all solvents with the temperature reduced viscosity ( $\eta/T$ ) through a power-law relationship<sup>226-229</sup> given by

$$\tau_r = A(\eta/T)^p \quad (3A.1)$$

where  $A$  and  $p$  are two constants. While this relationship is purely empirical, it is still commonly used in the investigation of the rotational diffusion of fluorophores in DESs and ILs. This is because it provides a straightforward and clear way to gain insight into the microscopic structural organization of a solvent system. For homogeneous solvent, the value of the exponent  $p$  is considered to be close to one, and its deviation from unity reflects the departure from SED hydrodynamic behaviour (breakdown of SED hydrodynamic theory).<sup>273, 274</sup> It is worth noting that Biswas and colleagues have demonstrated that the decoupling of rotational diffusion of a solute from the viscosity of the medium is due to the dynamic heterogeneity of the medium.<sup>175, 176, 273</sup> They have also suggested that the greater the deviation of  $p$  from unity, the greater the viscosity-diffusion decoupling and the more dynamic heterogeneity there is in the medium. Previous studies have shown that the distribution of relaxation rates for molecules residing in different local environments in organized media, such as ILs, is responsible for dynamic heterogeneity within the medium.<sup>175-179, 203, 275</sup> The value of  $A$  and  $p$  obtained from the empirical fitting have been collected in Table 3A.5. From the Table 3A.5, it can be noticed that for both the DES and HFILs the value of  $p$  deviates significantly from unity indicating dynamic heterogeneity in these classes of systems. Previously, it has been demonstrated for ILs that the fractional viscosity dependence of  $\tau_r$  arises because of non-Brownian motions such as orientational jumps and hydrogen bond fluctuation.<sup>175-179, 203, 274, 229-231, 274</sup> Furthermore, for DESs also hydrogen bond fluctuation and consequent motion of the constituent particles have

been considered as the primary cause for the observed fractional viscosity dependence of  $\tau_r$  in DESs.<sup>185, 186, 242, 273</sup> In light of this, the fractional viscosity dependence of  $\tau_r$  for the current solvent systems can also be rationalized by considering the fluctuation of hydrogen bonding network and the inertia-driven motion which is different from normal Brownian motions.

**Table 3A.5.** Parameters  $A$  and  $p$  obtain from the fits of  $\log \langle \tau_r \rangle$  vs  $\log \langle \eta/T \rangle$

System	C153		Perylene		MPTS	
	$A$	$p$	$A$	$p$	$A$	$p$
Ethaline	$14.4 \pm 0.81$	$0.88 \pm 0.01$	$4.37 \pm 0.38$	$0.74 \pm 0.04$	$23.4 \pm 1.15$	$0.78 \pm 0.02$
[OHEMIM][NTf <sub>2</sub> ]	$12.5 \pm 0.79$	$0.77 \pm 0.02$	$4.07 \pm 0.42$	$0.70 \pm 0.02$	$17.8 \pm 1.03$	$0.66 \pm 0.03$
[OHEMPy][NTf <sub>2</sub> ]	$10.2 \pm 0.69$	$0.73 \pm 0.01$	$3.89 \pm 0.36$	$0.71 \pm 0.01$	$15.5 \pm 0.97$	$0.60 \pm 0.02$
[N <sub>3112</sub> OH][NTf <sub>2</sub> ]	$10.8 \pm 0.73$	$0.75 \pm 0.01$	$3.98 \pm 0.31$	$0.73 \pm 0.02$	$17.8 \pm 1.02$	$0.60 \pm 0.03$

**3A.3.2.2. Perylene:** As stated earlier, perylene being apolar, tends to locate itself in the apolar region of a medium and become helpful in probing the apolar domain of the medium.<sup>233</sup> The time-resolved anisotropy decay of perylene (Figure 3A.5(b)) in all the solvents under study is found to be much faster as compared to the other two probes (C153 and MPTS). This indicates that perylene does not experience any strong solute-solvent interaction like MPTS (*vide infra*). From Table 3A.3, we can see that at any particular temperature,  $\tau_r$  value of perylene in ethaline is smaller than that in HFILs because of the low viscosity of the former than the latter. Using SED theory and analyzing the log-log plot of  $\tau_r$  versus  $(\eta/T)$  (Figure 3A. 6(b)), one can notice that the  $\tau_r$  values of [N<sub>3112</sub>OH][NTf<sub>2</sub>] lie more close to the slip line, indicating relatively faster rotation of the solute in the HFILs. This observation is also evident from the estimated  $C_{obs}$  value for perylene, where the  $C_{obs}$  value of perylene are found to be low for HFILs (0.19) than

that found in DES (0.26). Moreover, the  $p$  values (Table 3A.5) obtained from the empirical relation (equation 3A.1) for perylene in both DES and ILs are found to be almost comparable (0.75-0.70). This is because of the fact that perylene does not involve itself in any strong solute-solvent interaction or specific hydrogen bonding interaction with the concerned solvents, and hence similar extent of dynamic heterogeneity is experienced by perylene in these two classes of solvent systems.<sup>233, 276</sup>

**3A.3.2.3. MPTS:** The polar ionic region of the medium is monitored by using MPTS as the probe solute as it locates itself in the polar ionic region of a given medium.<sup>233</sup> The time-resolved fluorescence anisotropy decay of MPTS (Figure 3A.5(c)) is found to be much slower than that of the other two solute probes (perylene and C153). This indicates that MPTS moves to the compact region, which is the ionic region of the medium.<sup>233</sup> Moreover, it has been shown previously for ILs that since MPTS has hydrogen bond acceptors such as the sulphite group ( $\text{SO}_3^-$ ), it can participate in hydrogen bonding interaction with the acidic hydrogen of the ILs. Similarly, in the present study also, it can be expected that sulphite group of MPTS can involve in hydrogen bonding interaction with the hydroxyl group of both DES and HFILs as well as with the HBD of the ethaline. From Table 3A.3, we can see that at 298 K the  $\tau_r$  value for MPTS is nearly 5 times higher as compared to the same for perylene in DES and HFILs. This hindered rotation of MPTS in these media indicates that solute-solvent interaction is significantly strong for MPTS in all these media than that for perylene. Analysis of the data in light of SED theory also reveals that the  $\tau_r$  value of MPTS in both DES and HFILs lies close to the stick line and thereby indicating hindered rotation of MPTS in these media. Interestingly, upon a closer look at the log-log plot of  $\tau_r$  versus  $(\eta/T)$  (Figure 3A.6(c)), one can see that the rotational motion of MPTS in DES is the slowest as compared to that in HFILs, and thus the  $\tau_r$  values for MPTS in DES found to lie completely above the stick line. This behaviour is

generally called as super-stick behaviour in hydrodynamic terminology.<sup>230, 233</sup> This super-stick behaviour can also visualize by looking at the  $C_{obs}$  value (Table 3A.3) of MPTS in these media. Previously, the super-stick behaviour of MPTS in self-organized media like ILs have been rationalized by considering the solute-solvent specific hydrogen bonding interaction.<sup>185, 230, 233</sup> Furthermore, it has also been reported that the hindered rotation of charged solutes in DESs is caused due to the hydrogen bonding interaction between the charged solute and the constituent of DESs.<sup>185, 186</sup> Considering these facts, it can be concluded that the hydrogen bonding interaction of MPTS with the DES and HFILs is primarily responsible for the hindered rotation of the solute in the respective media. Furthermore, the  $p$  value (Table 3A.5) obtained from the empirical relation (equation 3A.1) is found to be much lower for the DES (0.78) as compared to the HFILs (0.60). This observation indicates that HFILs are dynamically more heterogeneous as compared to the DES. The difference in the extent of dynamic heterogeneity between DES and HFILs in the present study perhaps also indicates the different rates of relaxation of the hydrogen bond fluctuation for the solute-solvent or solvent-solvent intermolecular interactions.<sup>203, 239</sup>

### 3A.3.3. FCS Studies

FCS is a highly sensitive single molecule detection techniques which is employed for the studies of different dynamical processes such as molecular translational diffusion, conformation fluctuations, reaction kinetics, blinking dynamics, etc.<sup>257, 258</sup> In the present investigation, FCS studies have also been performed to get a better understanding of probes diffusion dynamics and intermolecular solute-solvent interaction at a single molecular level. Figure 3A.7 represents the fluorescence correlation decay curves ( $G(\tau)$ ) of C153 and MPTS in ethaline medium. The data have been fitted through both single component diffusion model (equation 2.24) as well as anomalous diffusion model<sup>262</sup> (equation 2.26). However, looking at

the fit residual (as well as reduced  $\chi^2$ ), the anomalous diffusion model was found to fit the data (Figure 3A.7(a)) in a much better way as compared to single component diffusion model (Figure APX3A.3). The normalized FCS decay curve of C153 and MPTS have been provided in Figure 3A.7(c) & 8(f) respectively. The anomalous diffusion model fitting for C153 and MPTS in other HFILs are provided in the Figure APX 3A.3. The stretching exponent  $\beta$ , obtained from the anomalous diffusion model represents the extent of deviation from single component diffusion model and gives the broad distribution of diffusion time ( $\tau_D$ ) of the probe molecules. The translational diffusion coefficients ( $D_t$ ) as well as the stretching exponent  $\beta$  of the probes in their respective solvent system estimated from equation 2.25 & 2.26 are collected in Table 3A.6.

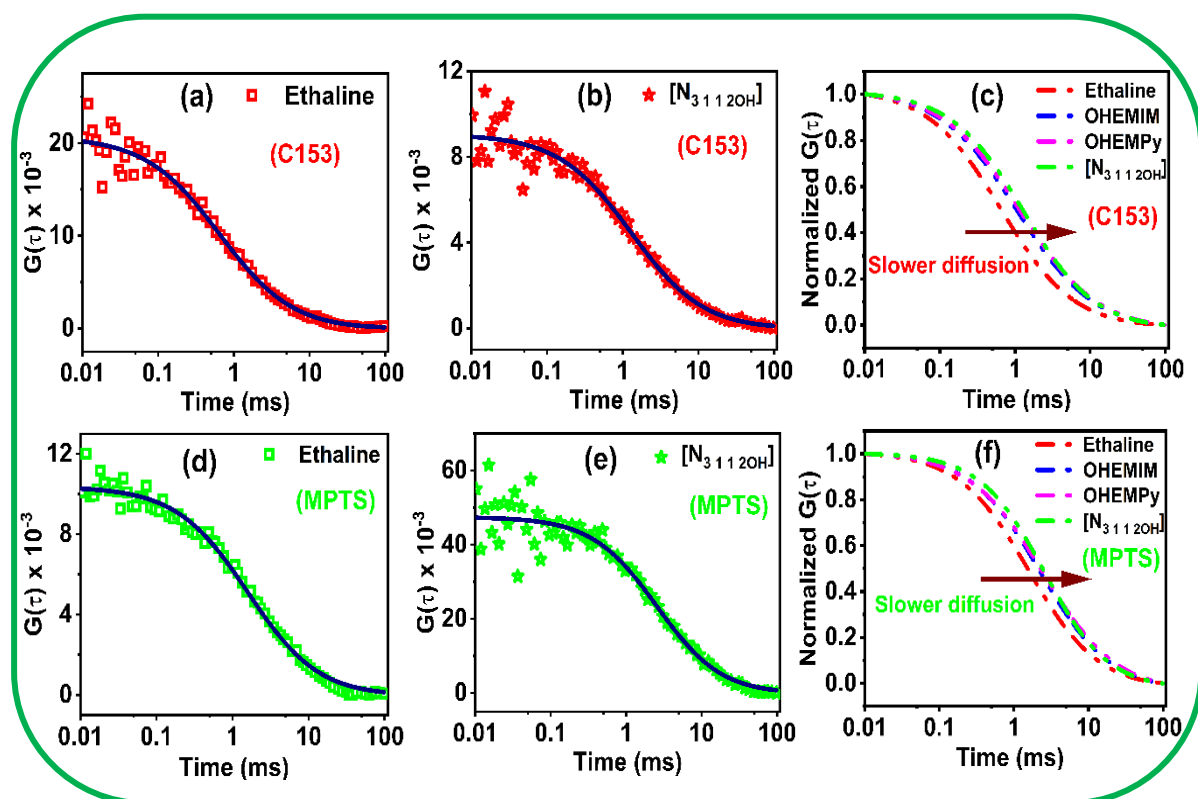


**Figure 3A.7.** Plot of  $G(\tau)$  vs time for C153 (a, b) and MPTS (d, e) in ethaline fitted through anomalous diffusion model. (c) and (f) are the normalized FCS decay curve for C153 and MPTS respectively in both DES and HFILs.

**Table 3A.6.** Estimated translational diffusion coefficient ( $D_t$ ) along with  $\beta$  value of C153 and MPTS in both DES and HFILs.

Systems	C153		MPTS	
	$D_t$ ( $\mu\text{m}^2/\text{s}$ )	$\beta$	$D_t$ ( $\mu\text{m}^2/\text{s}$ )	$\beta$
Ethaline	$24.8 \pm 2.7$	$0.88 \pm 0.02$	$10.0 \pm 1.2$	$0.90 \pm 0.03$
[OHEMIM] [NTf <sub>2</sub> ]	$15.0 \pm 1.8$	$0.84 \pm 0.03$	$7.07 \pm 0.9$	$0.85 \pm 0.04$
[OHEMPy] [NTf <sub>2</sub> ]	$13.4 \pm 1.6$	$0.83 \pm 0.03$	$6.48 \pm 0.8$	$0.85 \pm 0.03$
[N <sub>3 1 1 2OH</sub> ] [NTf <sub>2</sub> ]	$12.3 \pm 1.7$	$0.85 \pm 0.02$	$6.23 \pm 0.8$	$0.86 \pm 0.02$

From Table 3A.6, one can notice that the diffusion coefficient ( $D_t$ ) of C153 is found to be much faster in ethaline as compared to that in [N<sub>3 1 1 2OH</sub>] [NTf<sub>2</sub>] due to the fact that the medium viscosity of the former is lower than the later. Furthermore, the  $D_t$  value of the neutral solute C153 in a particular medium is found to be much faster than that of the ionic solute MPTS (Table 3A.6). For example, the  $D_t$  value of C153 ( $24.8 \mu\text{m}^2/\text{s}$ ) in [N<sub>3 1 1 2OH</sub>] [NTf<sub>2</sub>] is estimated to be nearly 2 times larger than the same for MPTS ( $6.23 \mu\text{m}^2/\text{s}$ ) in [N<sub>3 1 1 2OH</sub>] [NTf<sub>2</sub>]. This suggests that MPTS (with its sulphite group) can interact more strongly with the HFILs as compared to the same that can be observed for neutral C153. More interestingly, for the DES Ethaline,  $D_t$  value of C153 is found to be  $\sim 2.5$  times higher than that for MPTS. This indicates that frictional resistance to the translational diffusion of MPTS in ethaline is relatively more than the same for MPTS in HFILs. Moreover, among the HFILs, negligible differences in the  $D_t$  value of both probe molecules are observed in case of both [OHEMPy][NTf<sub>2</sub>] and [N<sub>3 1 1 2OH</sub>][NTf<sub>2</sub>]. However, for [OHEMIM][NTf<sub>2</sub>], even though the viscosity is found to be lower as compared to the other two HFILs, the  $D_t$  value of MPTS remains almost same in all the HFILs. This is further evident from the hydrodynamic radius (Table APX3A.2.) estimated for the solutes through FCS studies. This observation is also suggestive of the fact that the

extent of solute-solvent interaction in [OHEMIM][NTf<sub>2</sub>] is relatively stronger as compared to that in the other two HFILs. Essentially all these results that are obtained from the translational diffusion dynamics of probe solutes in both DES and HFILs nicely corroborate with the results obtained from time-resolved anisotropy studies.

Apart from the translational diffusion coefficient, another parameter obtained from the fitting of FCS traces is the stretching exponent  $\beta$ , whose values are found to lie between 0.9 to 0.85 for both probes in all the solvent systems under study. The  $\beta$  value (which is well below unity) indicates that the diffusion dynamics of the solute molecule in these media are diverse in nature in terms of their translational diffusion time.<sup>185, 262</sup> It has been well documented that for viscous heterogeneous media like DES and RTILs, the mean square displacement (MSD) of the solute molecule does not follow the normal Brownian diffusion ( $\beta = 1$ ), instead follows a sub-diffusive behaviour,  $\langle r(\tau)^2 \rangle \propto \tau^\beta$  (where  $\beta < 1$ ).<sup>262</sup> As for conventional homogeneous solvents, the diffusion of these solute molecules follows a single component diffusion model ( $\beta = 1$ ), the deviation of  $\beta$  value from unity indicates the presence of dynamic heterogeneity in all these media.<sup>185-187, 262</sup> In the current study, as can be seen, the value of  $\beta$  deviates more for HFILs (e.g.,  $\beta = 0.83$  for C153 in [OHEMPy][NTf<sub>2</sub>]) as compared to the DES ( $\beta = 0.88$  for C153 in ethaline) indicating more dynamic heterogeneity in the HFILs as compared to the DES, which is also consistent with the result obtained from the time-resolved anisotropy measurements.

#### 3A.3.4. PFG-NMR Studies

The differences in the microstructural organisation between DES and HFILs are further investigated by the PFG-NMR technique. In the present study, the value of translational diffusion coefficient ( $D$ ) for both DES and HFILs have been estimated in the temperature range 298 K-323 K. The cationic part of both DES and HFILs have been monitored exclusively

during the measurement and the measured  $D$  values of both DES and ILs have been collected in Table 3A.7. From

**Table 3A.7.** Estimated translational diffusion coefficient ( $D \times 10^{-11} \text{ m}^2/\text{s}$ ) of the cationic species of both DES and hydroxyl ILs as well as HBD of the DES

Temperature (K)	[Choline <sup>+</sup> ]/EG <sup>a</sup>	[OHEMIM <sup>+</sup> ]	[OHEMPy <sup>+</sup> ]	[OHC3CH <sup>+</sup> ]
298	2.32/3.43	1.72	1.34	1.43
303	2.94/4.24	2.26	1.73	1.83
308	3.57/5.32	2.88	2.16	2.3
313	4.36/6.44	3.6	2.64	2.84
318	5.12/7.80	4.42	3.23	3.53
323	6.3/8.92	5.32	3.83	4.35

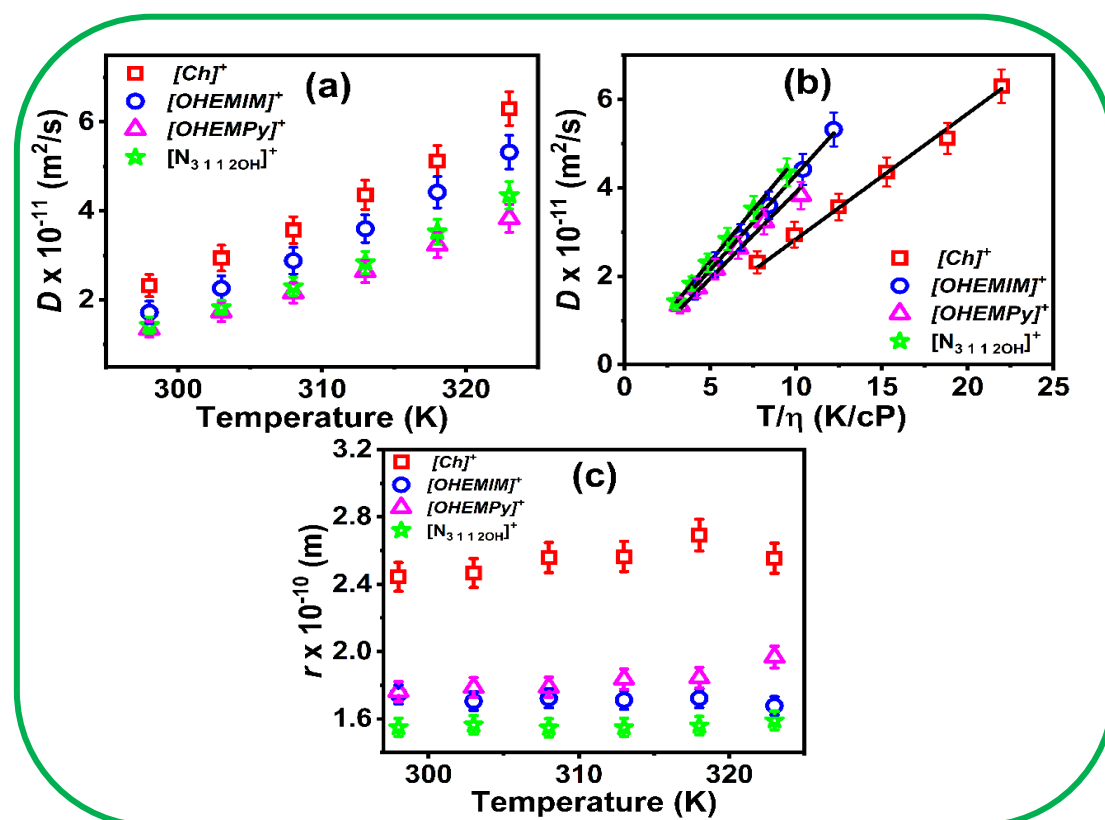


**Figure 3A.8.** (a) Temperature dependent variation of the self-diffusion coefficients of DES and HFILs, (b)  $D$  vs  $T/\eta$  plot of DES and HFILs. The value of slope (in  $\text{JK}^{-1}\text{m}^{-1}$ ) for different solvents have been shown in the legends, (c) hydrodynamic radii of cationic species calculated through SE equation.

From Figure 3A.8(a), a gradual increase in the  $D$  value with rise in temperature for all concerned systems can be observed. This observation can be attributed to the lowering of the viscosity of the medium upon increase in temperature. Moreover, one can observe from Table 3A.7 that the mobility of the choline cation of the DES at any particular temperature is the fastest compared to the same for the cationic component of all the HFILs. This behaviour is also consistent with the viscosity of these medium (Table 3A.3). In ethaline, one can also noticed that the  $D$  value of the HBD (i.e., ethylene glycol) is more as compared the choline cation indicating its higher mobility. This is because of the smaller size of the former than the latter. However, upon careful inspection it can be noticed that, upon going from ethaline to its ILs analogues  $[N_{3,1,1,2OH}][NTf_2]$ , the increase in viscosity is observed to be more than two times (~2.5 times), whereas the decrease in  $D$  value is estimated to be less than two times (~1.75 times). This dipropionate change of  $D$  value with bulk viscosity clearly reveals that bulk viscosity is not the sole factor in governing the mobility of cation of both DES and HFILs.

To have a deeper insight into this behaviour, the NMR data have been analysed in light of famous Stokes-Einstein equation by following equation<sup>277</sup>

$$D = \frac{kT}{6\pi\eta r} \quad (3A.2)$$

where  $k$  is the Boltzmann constant,  $T$  is the absolute temperature,  $\eta$  is the viscosity of the medium and  $r$  is the hydrodynamic radius. By plotting  $D$  against  $T/\eta$ , the slope for  $(= k/6\pi r)$  for both DES and HFILs is calculated. The slope being inversely proportional to hydrodynamic radii of the cations, a steeper slope represents larger hydrodynamic radius. From Figure 3A.8(b), the order of slopes for various diffusing species are estimated to be  $(\text{Ch}^+) > [\text{OHEMPy}^+] > [\text{OHEMIM}^+] > [N_{3,1,1,2OH}^+]$ . The steepest slope for choline cation of the DES suggest that the hydrodynamic radius of DES is larger as compared to HFILs. Further, to support our observation, we have also calculated the hydrodynamic radii ( $r$ ) of the cationic

species of all the concerned solvents through the SE equation at different temperature and the data have been provided in Figure 3A.8(c). From Figure 3A.8(c), one can also noticed the larger hydrodynamic radius of Choline cation (2.44 Å) as compared to that of the cationic species of HFILs (1.75-1.55 Å). It is pertinent to mention in this context that D'Agostino et al.<sup>164</sup> while working on choline chloride based DESs reported a larger hydrodynamic radius for choline cation in ethaline medium. Moreover, in a separate work, they have also reported significant association between the HBD and the hydroxyl group of choline cation in anhydrous condition.<sup>163</sup> Later on, Ludwig and coworkers<sup>278</sup> have also reported that significant cation-cation interaction takes place in hydroxyl containing ILs as compared to that in non-HFILs despite of the cation-cation repulsion. Moreover, the effect of cation-cation interaction on the hydrodynamic radii of hydroxyl containing ILs have also been studied by different group<sup>279</sup> as well as by Sarkar and co-workers<sup>280</sup> independently. It is interesting to note that in the present study despite of the fact that the HFILs can involve in intermolecular cation-cation H-bonding interaction, their hydrodynamic radii are found to be smaller as compared to that of ethaline. This observation probably indicates that because of the cation-cation repulsion, the intermolecular cation-cation interaction mediated by H-bonding interaction is somewhat weaker as compared to that of the intermolecular H-bonding interaction between the constituents of ethaline DES. As a result, the structure of ethaline is more associated in nature compared to that of hydroxyl-functionalized ILs, which makes the hydrodynamic radii of the former relatively larger than that of the latter.

#### **3A.4. Conclusion**

The present study has been undertaken basically to understand the differences in the behaviour in terms of intermolecular interactions, dynamics and structures between DES and RTILs. For this purpose, a choline chloride-based DES (ethaline) and three hydroxyl functionalized ionic

liquid have been employed so that apart from the hydrogen bonding interactions, role of various other type of intermolecular interaction among the constituent species of the solvent systems in governing their behaviours are understood. All these investigations have unravelled several interesting findings. Excitation wavelength-dependent emission have indicated that the HFILs employed in these studies are spatially more heterogeneous as compared to ethaline. EPR spectral measurements have revealed that the polarity of HFILs employed in this study are significantly high, whereas polarity of ethaline is found to be close to that of aliphatic polyhydroxy alcohols. This hyper-polarity of HFILs has been rationalized by considering the intramolecular synergistic effect that exist between the hydroxyl group of cations and the corresponding anion. Investigation of rotational and translational diffusion dynamics of selected probes have indicated that the extent of solute-solvent interaction is relatively higher in DES in comparison to that in HFILs. Interestingly, diffusions studies have revealed that decoupling of solute dynamics from the medium viscosity is found to be more for HFILs than that for ethaline, indicating the extent of dynamic heterogeneity is more in HFILs as compared to that for ethaline. Measurements and analysis of self-diffusion coefficient through NMR have suggested that ethaline have larger hydrodynamic radius as compared to the HFILs indicating more associated structure in ethaline. Essentially, all the results obtained from these investigations have demonstrated that despite having similar functional moieties, different intra/intermolecular interaction (such as solute-solvent interaction, specific hydrogen bonding interaction, coulombic interaction etc.) operating at microscopic level are considerably different between DES and HFILs. This further highlight that all these interactions and energetics lead to a distribution of relaxation rate as well as spatial rearrangement which are different for DES and HFILs and are primarily responsible for observing the difference in the micro-heterogeneous behaviour between DES and HFILs. These differences in intermolecular interactions and micro-heterogeneous behaviour are manifested on the structure-property

relationship for these solvent systems. Hence, outcomes of the present study have revealed that consideration of DESs as a subclass of ILs may not be appropriate and DESs should be treated as a special class of solvent systems having its own identity.

### 3A.5. Appendix

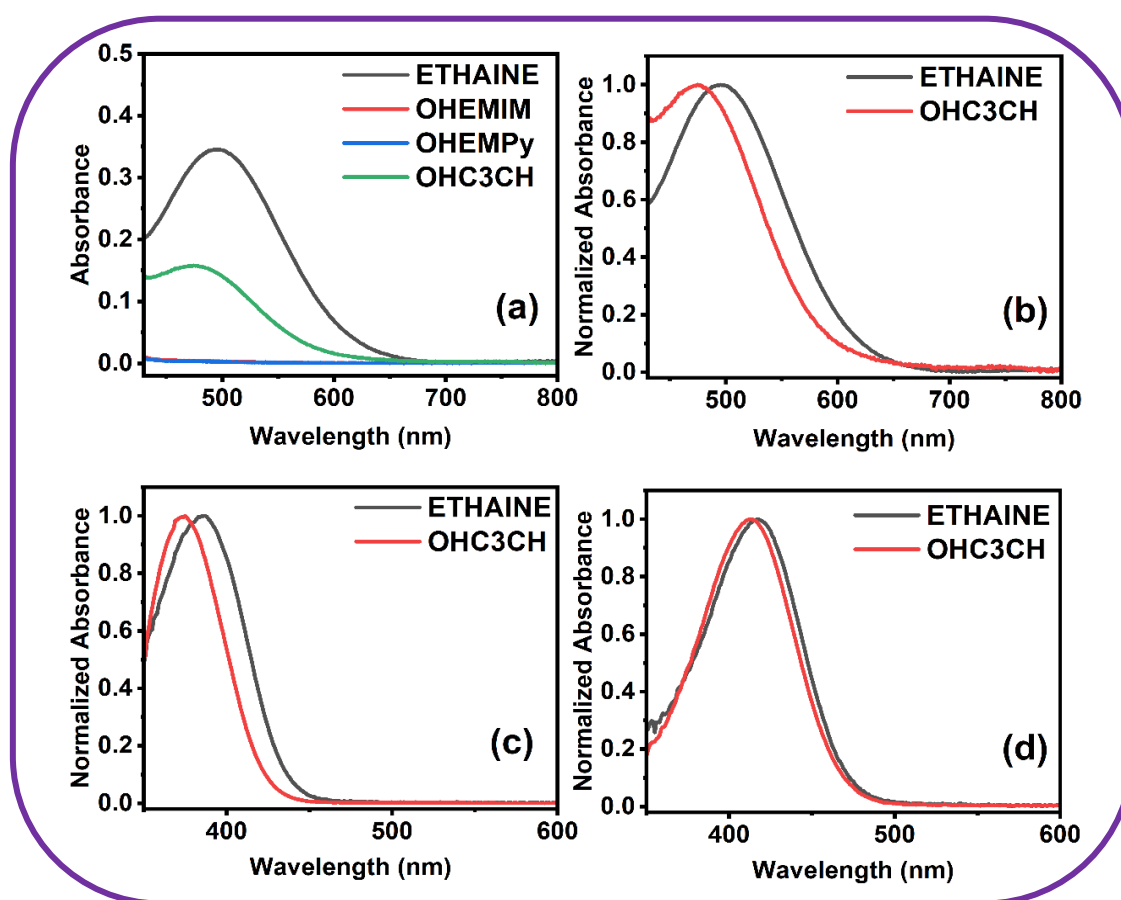


**Figure APX3A.1.** (a) Electronic absorption spectra of Reichardt's dye 30 in all the concerned solvent systems, (b) Normalized electronic absorption spectra of Reichardt's dye 30 showing the shift in  $\lambda_{max}^{abs}$ , (c) Normalized electronic absorption spectra of 4-nitroaniline and (d) N,N-dimethyl-4-nitroaniline dye showing the shift in  $\lambda_{max}^{abs}$ .

**Table APX3A.1.**  $E_T$  (30) and Kamlet-Taft parameters of concerned solvent systems

Systems	$E_T$ (30)/ kcal mol <sup>-1</sup>	$\pi^*$	$\alpha$	$\beta$
[N <sub>4111</sub> ][NTf <sub>2</sub> ]	57.78	1.19	0.84	0.45
[N <sub>4112OH</sub> ][NTf <sub>2</sub> ]	60.19	1.13	1.05	0.25

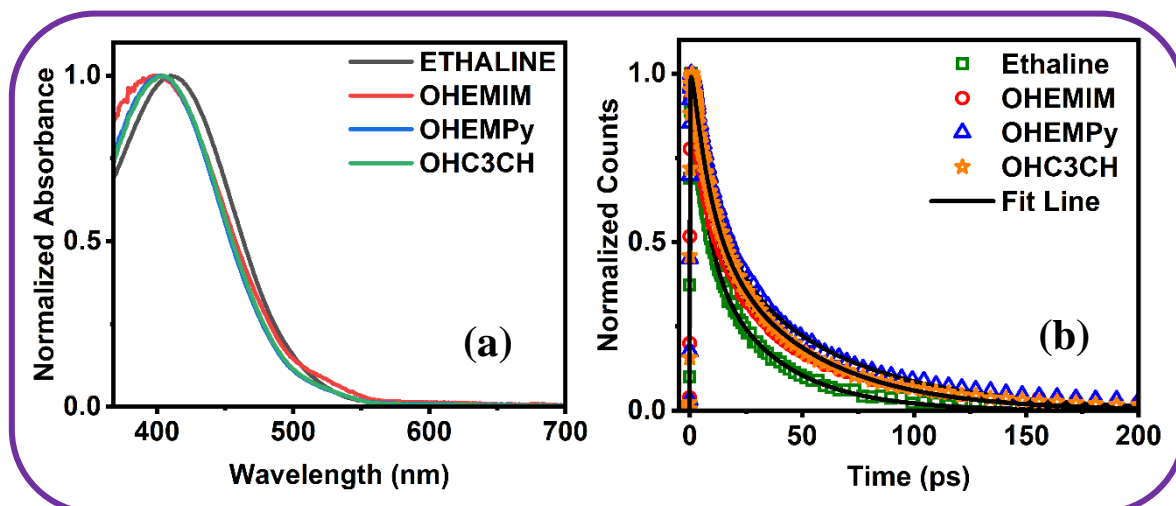


**Figure APX3A.2.** (a) Normalized absorbance spectra of 2-amino-7-nitrofluorene (ANF) in all the concerned solvent systems. (b) Femto-second fluorescence up-conversion decay plot of ANF in all the concerned solvent systems.

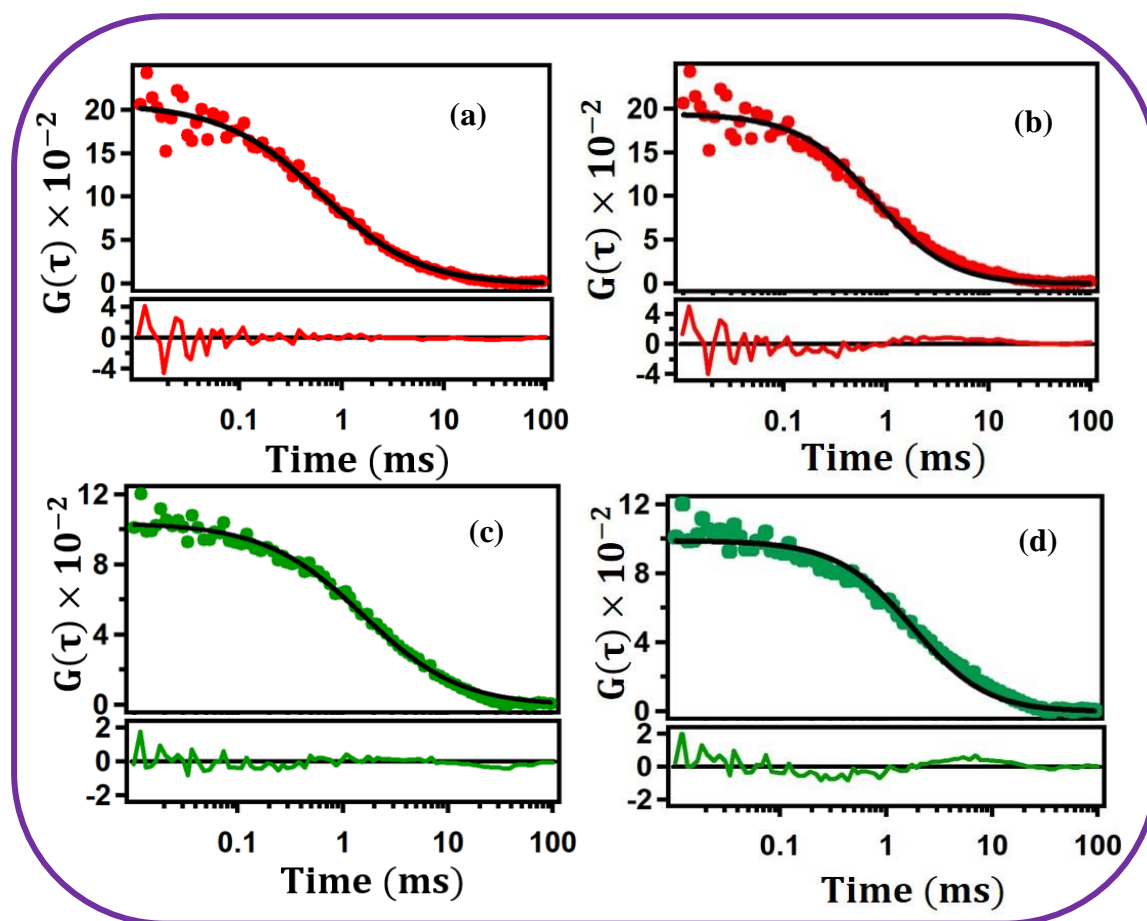


**Figure APX3A.3.** Plot of  $G(\tau)$  vs time for C153 (a, b) and MPTS (c, d) in ethaline. Plot (a) and (c) are fitted through anomalous diffusion model while plot (b) and (d) fitted through single-component diffusion model.

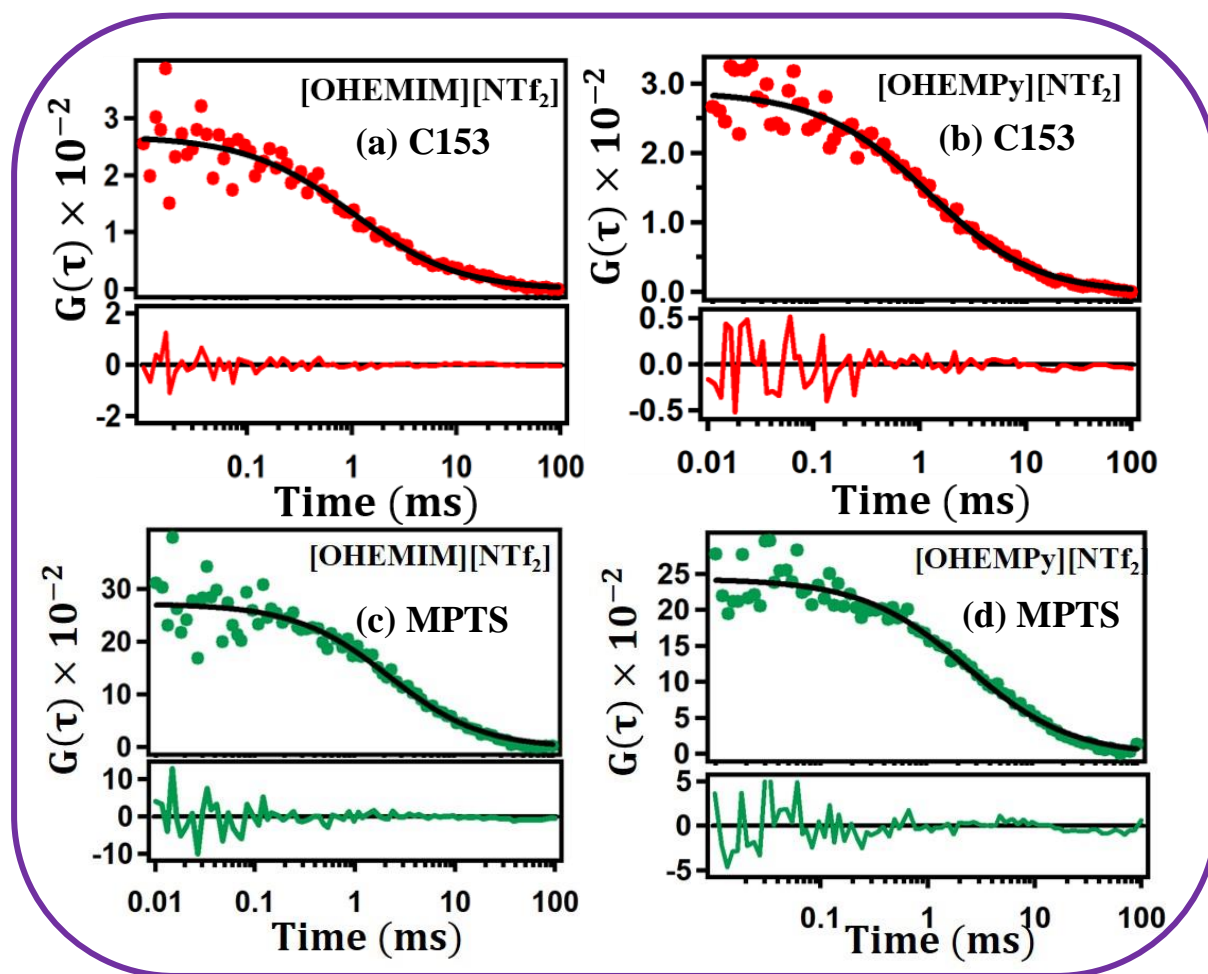


**Figure APX3A.4.** Plot of  $G(\tau)$  vs time for C153 (a, b) and MPTS (c, d) in different HFILs fitted through anomalous diffusion model.

**Table APX3A.2.** Estimated hydrodynamic radii ( $r_H$  in nm) of C153 and MPTS calculated from FCS studies

Systems	C153	MPTS
Ethaline	$0.23 \pm 0.02$	$0.57 \pm 0.04$
[OHEMIM][NTf <sub>2</sub> ]	$0.20 \pm 0.02$	$0.43 \pm 0.03$
[OHEMPy][NTf <sub>2</sub> ]	$0.18 \pm 0.02$	$0.37 \pm 0.03$
[N <sub>3</sub> 112OH][NTf <sub>2</sub> ]	$0.18 \pm 0.03$	$0.36 \pm 0.03$

## CHAPTER 3B

---

### **Studies on the Temperature-Dependent Ultrafast Solvation Dynamics in Deep Eutectic Solvents and Room Temperature Ionic Liquids**

---

---

**Barik, S.; Preeyanka, N.; Chakraborty, M.; Mahapatra, A.; Sarkar, M.; J.**  
*Mol. Liq.*, 2022, 367, 120545.

**Abstract**

The second part of the chapter aims to provide a comprehensive understanding of the differences in solvent relaxation behavior between DESs and RTILs. For this purpose, the dynamics of solvation have been investigated with the same sets of DESs and HFILs as used in the previous part of the chapter. The FLUPS technique, coupled with the TCSPC technique, has been employed to study the complete Stokes shift dynamics of a dipolar probe, coumarin 153 (C153), dissolved in these media. The solvent response functions generated from the dynamic Stokes shift data have revealed a bimodal solvent relaxation behavior, with a very fast sub-picosecond and a relatively slower picosecond to sub-nanosecond solvation time component for both DES and HFILs. The relatively slower solvation time component, which correlates with the bulk viscosity of the concerned medium, is found to arise due to the diffusional motion of the constituents of both DES and HFILs. Interestingly, temperature-dependent solvent relaxation measurements have revealed that at iso-viscous conditions, the solvent relaxation is much faster in the DES as compared to that in HFILs, indicating differences in solvent relaxation behavior at the later part of the solvent response. More interestingly, when the early part of the dynamics was monitored, the amplitude associated with the ultrafast component for the DES increased significantly with an increase in temperature, whereas it remained almost unchanged for the HFIL. This indicates that even at shorter timescales, the process of solvent relaxation is considerably different for both DES and HFILs. Overall, these investigations have demonstrated that despite having similar functionalities, the different motions related to the solvent relaxations, operating at the microscopic level, in both these classes of solvents are significantly different from each other.

---

### 3B.1. Introduction

In the past decade, both deep eutectic solvents (DESs) and room temperature ionic liquids (RTILs) have gathered considerable attention from the research communities because of their potential use in diverse fields such as chemical, biological, and material science.<sup>16, 19-20, 126-145</sup> Both DESs and RTILs share many appealing features, such as high chemical and thermal stability, nonflammability, high conductivity, wide liquid range, and a good solubilizing capacity of a number of organic and inorganic compounds.<sup>19-20,16,29</sup> These unique properties of both DESs and RTILs make them attractive for a range of applications, including as solvents and reaction media.<sup>126-146</sup> Specifically, both DESs and RTILs have found applications as alternative reaction media to traditional organic solvents in various chemical reactions, including catalytic reactions, oxidation reactions, and enzymatic reactions, among others.<sup>126-135</sup> They have been found to offer many advantages, such as higher product yields, better selectivity, and the ability to carry out reactions under mild conditions. It is well known that the chemical reactivity of a solute/reactant in a particular medium is intricately related to the dynamics of solvation of the medium where the solute is dissolved.<sup>197, 198</sup> Therefore, understanding the dynamics of solvation of DESs and RTILs becomes very critical for assessing their suitability as reaction media for various chemical reactions.

Solvation dynamics is a fundamental characteristic of liquid-phase dynamics, and it refers to the time-dependent response of solvent molecules towards the perturbation in the solute at a molecular level.<sup>197-200</sup> Particularly, dynamics of solvation has profound influence on charge transfer reaction such as electron and proton transfer reactions and other photochemical reactions. Apart from this, studies of solvation dynamics can provide valuable information about the fluid characteristics of these systems, such as hydrogen bonding, polarity, dielectric response, polarizability, molecular shape and size, etc.<sup>197-215</sup> Therefore, understanding solvent

dynamics is crucial for obtaining information about the kinetics and inter-relationship between the rates of various reactions, such as electron transfer reactions and photochemical reactions, and the rate of solvation in the solvent medium.<sup>197-200</sup> It is important to note that while DESs are often considered a subtype of ILs due to their similar physicochemical properties, they have different constituents with distinct chemical natures that can influence the chemical reactivity of solutes in different ways. Additionally, the intra and intermolecular interactions in DESs and RTILs are significantly different. For example, electrostatic interactions between an organic cation and inorganic/organic anion primarily govern the behaviour of ILs, while a complex hydrogen bonding network between the hydrogen bond acceptor and donor controls the structure-property relationships in DESs.<sup>19-20,16,29</sup> Therefore, even though DESs and RTILs may behave somewhat similarly, their molecular-level dynamics and solvation behaviours can differ significantly from each other. Therefore, to better understand the relationship between solvation dynamics and the prevailing intra/intermolecular interactions in these media, it would be worthwhile to investigate the solvent relaxation behaviour of both DESs and ILs containing similar functionalities, such as hydroxyl groups.

Though the dynamic of solvation is extensively studied in RTILs, very little is known about the issue in DESs despite their significant usage in various synthetic applications.<sup>205-215, 175, 177, 179, 182-184</sup> In fact, dynamically, DESs and RTILs may not necessarily behave in a similar fashion even though both classes of solvents have many common physicochemical properties. Moreover, apart from several studies where broadband fluorescence up-conversion (100 fs resolution) technique has been used to study the ultrafast solvation dynamics in RTILs, most of these studies of solvation dynamics are primarily based on TCSPC techniques, where the early part of the solvent dynamics was missed due to the limited time resolution of the instrument.<sup>20-215</sup> Besides this, ultrafast solvation dynamics studies in DESs are elusive. It is

also worth noting that while calculating the amplitude of missing components in DESs and RTILs, the estimation of time zero frequency through Fee and Maroncelli<sup>221</sup> method may lead to erroneous outcomes because of the difference in the density between the reference solvent and the solvent of particular interest. Thus, to avoid this, it is always better to capture the complete Stokes shift dynamics of the solvent by employing a sub-picosecond time resolution fluorescence up-conversion technique along with pico-second time-resolved fluorescence measurement. Additionally, we note here that the dependence of the ultrafast solvation component on temperature has not been studied extensively. Considering all these discussions, it is expected that studies on sub-picosecond solvation dynamics on DESs and RTILs having similar chemical functionalities will not only help to understand the difference in their dynamical behavior, if any, but also be useful to explore these media for carrying out various chemical reactions.

Keeping in mind the above issues, the present work aims to provide a comprehensive understanding about the difference in the solvation behaviour of DESs and RTILs. To address this issue, a DES, namely ethaline and three other HFILs (Chart 3A.1.) are employed for the study. The hydroxyl group based ILs have been selected decisively so that apart from the role of hydroxyl group, various other factor which account for the solvent relaxation process can be gleaned. To investigate the difference in solvent response between these two classes of substances, TDDSS of a dipolar probe C153 is measured by combining the TCSPC technique (85 ps resolution) with the FLUPs (250 fs resolution) technique. Additionally, we have also investigated the temperature-dependent solvation relaxation behaviours in both DES and HFILs through combination of both these techniques. All these investigations have revealed a significant difference in the solvent relaxation behaviour between these two classes of media despite the fact that they have same (hydroxyl) functionalities. The outcomes of this

investigation are expected to advance our understanding of the mechanism of solvation dynamics in both DESs and RTILs, which can aid in the development of new reaction media with customized properties.

### 3B.2. Experimental Sections

The detail about the synthesis of different HFILs and the DES have been provided in chapter 2. The dried solvents were transferred into 2cm quartz cuvette and requisite amount of probe was added to prepare the solution (keeping absorbance below 0.3 for TCSPC measurements and 1.5 for FLUPS measurements). All the cuvette were thoroughly sealed with septum and parafilm to avoid moisture intake. The details about different instrumental techniques such as steady-state absorption and fluorescence, time-resolved fluorescence (TCSPC and FLUPS), and the procedure for data analysis have been discussed in chapter 2.

### 3B.3. Results and Discussions

#### 3B.3.1. Steady-State Measurements and Solvation Energy

Prior to the investigation of the difference in solvent response between DES and HFILs to the excited state of the dipolar probe C153, the energy difference between the  $S_0 \leftrightarrow S_1$  states of C153 in both classes of solvents was estimated using steady-state absorption and emission spectra (Figure 3A.1). Two static solvation characteristics such as the solvation free energy difference ( $\Delta_{solv}G$ ) which provides an idea about the difference in the solvation free energy of the  $S_0$  and  $S_1$  state of C153 while the solvent reorganization energy ( $\lambda_{solv}$ ) which depict the solvent contribution to the nuclear reorganization energy accompanying the  $S_0 \leftrightarrow S_1$  transition have been estimated by following equations<sup>199</sup>

$$\Delta_{solv}G = \frac{1}{2}h[\nu_{abs} + \nu_{\infty}] - \Delta G_0 \quad (3B.1)$$

$$\lambda_{solv} = \frac{1}{2}h[\nu_0 - \nu_{\infty}] \quad (3B.2)$$

where  $\nu_{abs}$ ,  $\nu_0$  and  $\nu_\infty$  represents the frequency (in  $\text{cm}^{-1}$ ) of the absorption maxima, “time zero” emission maxima, and emission maxima of solvent equilibrated state of C153, respectively. The time zero emission peak frequency ( $\nu_0$ ) represents the emission immediately after excitation, before any solvent relaxation takes place, and this is calculated by following the procedure given by Fee and Maroncelli<sup>221</sup>, whereas the  $\nu_\infty$  value has been estimated from the time-resolved fluorescence measurements (*vide infra*). The gas phase free energy difference ( $\Delta G_0$ ) for C153, which is close to  $296 \text{ kJ mol}^{-1}$ , has been taken from the literature report.<sup>199, 217</sup>

**Table 3B.1.** Steady state absorption and emission maxima,  $\Delta_{solv}G^a$  and  $\lambda_{solv}^a$  of C153 in various solvent systems used in this study

System	$\nu_{abs}$ ( $10^3 \text{ cm}^{-1}$ )	$\nu_{ems}$ ( $10^3 \text{ cm}^{-1}$ )	$\nu_0$ ( $10^3 \text{ cm}^{-1}$ )	$\nu_\infty$ ( $10^3 \text{ cm}^{-1}$ )	$-\Delta_{solv}G$ $\text{kJ mol}^{-1}$	$\lambda_{solv}$ $\text{kJ mol}^{-1}$
Ethaline	23.20	18.55	20.20	18.39	47.24	10.82
[OHEMIM][NTf <sub>2</sub> ]	23.31	18.59	20.29	18.45	46.22	11.01
[OHEMPy][NTf <sub>2</sub> ]	23.35	18.66	20.33	18.46	45.92	11.19
[N <sub>3112</sub> OH][NTf <sub>2</sub> ]	23.36	18.62	20.34	18.47	45.81	11.19

<sup>a</sup>Experimental error =  $\pm 5\%$

The estimated  $\Delta_{solv}G$  and  $\lambda_{solv}$  for C153 in all the concerned solvent systems are collected in Table 3B.1. From Table 3B.1, it can be observed that both  $\Delta_{solv}G$  and  $\lambda_{solv}$  for C153 in both DES and HFILs are found to be comparable with previously reported values in DESs and RTILs.<sup>187, 199, 217</sup> Additionally, both of these parameters are found to lie within the narrow range of  $47.2\text{-}45.8 \text{ kJ mol}^{-1}$  and  $10.66\text{-}9.98 \text{ kJ mol}^{-1}$ , respectively, indicating a similar kind of solvation energetics in both DES and HFILs. This observation is also supported by the fact that the steady-state spectral properties of C153 are almost similar in both DES and HFILs. Moreover, it has also been reported by Jin et al.<sup>199</sup> that the  $S_0 \leftrightarrow S_1$  transition of C153 is more sensitive to the nonspecific polar interaction while it is very less sensitive to the specific

hydrogen bonding interaction. In view of all these arguments, it can be rationalized that by considering the energetics of solvation of the  $S_0 \leftrightarrow S_1$  transition of C153, it is difficult to distinguish the difference in the solvent response of both DES and HFILs towards the excited state of C153.

### 3B.3.2. Ultrafast Solvation Dynamics

To study the ultrafast solvation response of both DES and HFILs, the TDDSS of C153 in all the concerned solvents are recorded at several wavelengths at 10 nm intervals across the entire fluorescence spectrum of C153.<sup>198</sup> Representative fluorescence decay curves for C153 at three different wavelength in ethaline and  $[N_{3112OH}][NTf_2]$  measured through both FLUPS and TCSPC techniques are provided in Figure 3B.1. From Figure 3B.1, one can notice the wavelength-dependent change in fluorescence intensity decay for C153 in these solvents, where a faster monotonous decay at shorter wavelength and a slow rise followed by decay at longer wavelength have been observed which also indicates the process of solvation.<sup>197-210</sup> These fluorescence decay curves are then fitted to a multiexponential decay function (equation 2.7) independently to extract the time constant and their respective contribution.

After this, TRES plots are constructed with the help of the steady-state emission intensity and the fitting parameters obtained from the fluorescence decay curves by following a standard protocol.<sup>198-200</sup> The details about the construction of TRES plots are provided in chapter 2. The TRES plots up to 100 pico-second are reconstructed from the FLUPS data, while the rest are constructed from the TCSPC data. Here, we note that similar procedure has also been used by other researchers while constructing the TRES plots for RTILs and DESs.<sup>187, 217</sup> Figure 3B.2 display the TRES plots of C153 in ethaline and  $[N_{3112OH}][NTf_2]$  at 298 K at 7-8 distinct time intervals (for the rest of the solvent, the TRES plots are provided in the Appendix, Figure APX3B.1). From Figure 3B.2, a time-dependent red shift of the emission maxima of

C153 in both classes of solvent systems has been observed. This observation essentially indicates the solvent-mediated relaxation around the excited state of the solute molecule, which ultimately lowers the energy of the emitting state of C153.<sup>198-210</sup>

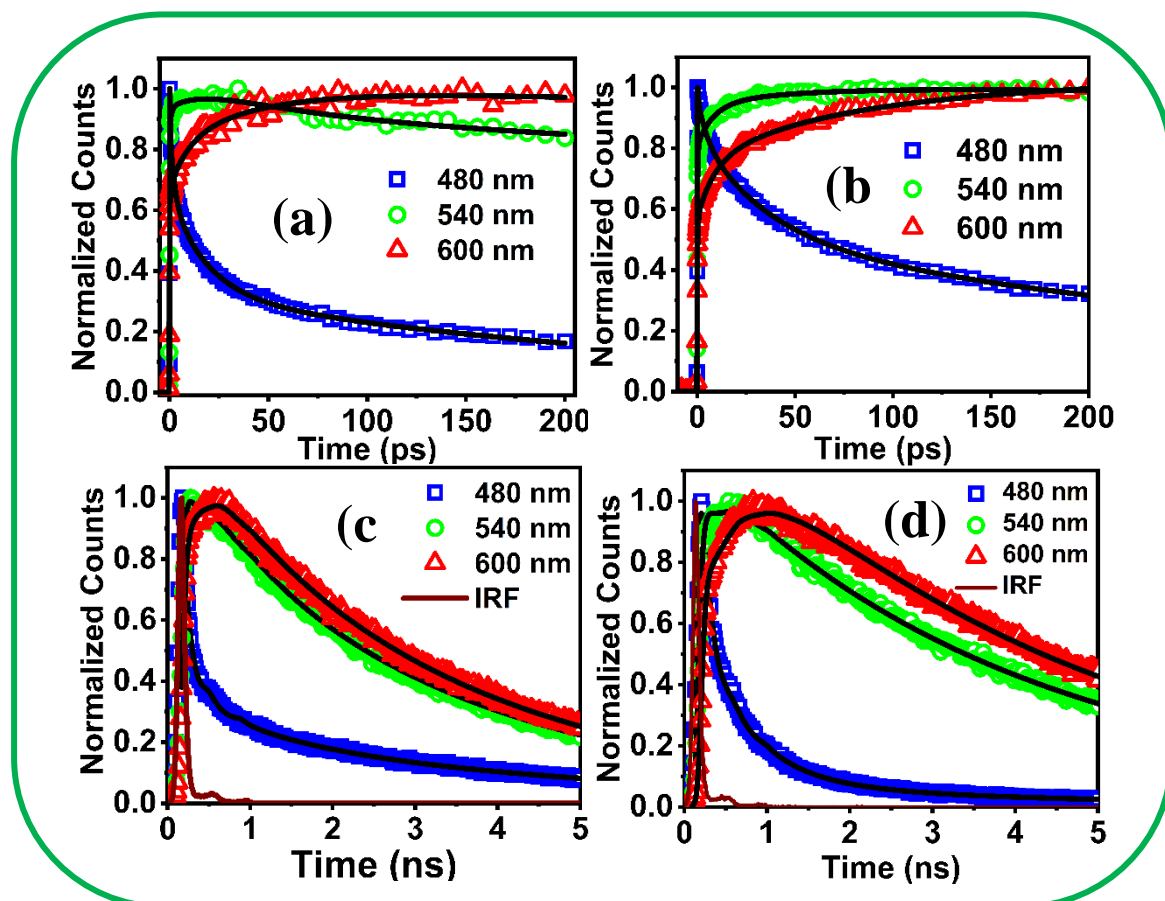


**Figure 3B.1.** Fluorescence decay profiles of C153 ( $\lambda_{ex} = 405$  nm) at 298 K in Ethaline (a, c) and N<sub>3</sub> 1 1 2OH (b, d) measured through FLUPS (upper panel) and TCSPC (lower panel) techniques respectively. The inset values show the monitoring wavelength. The solid black line represents the multiexponential fit to the data points.

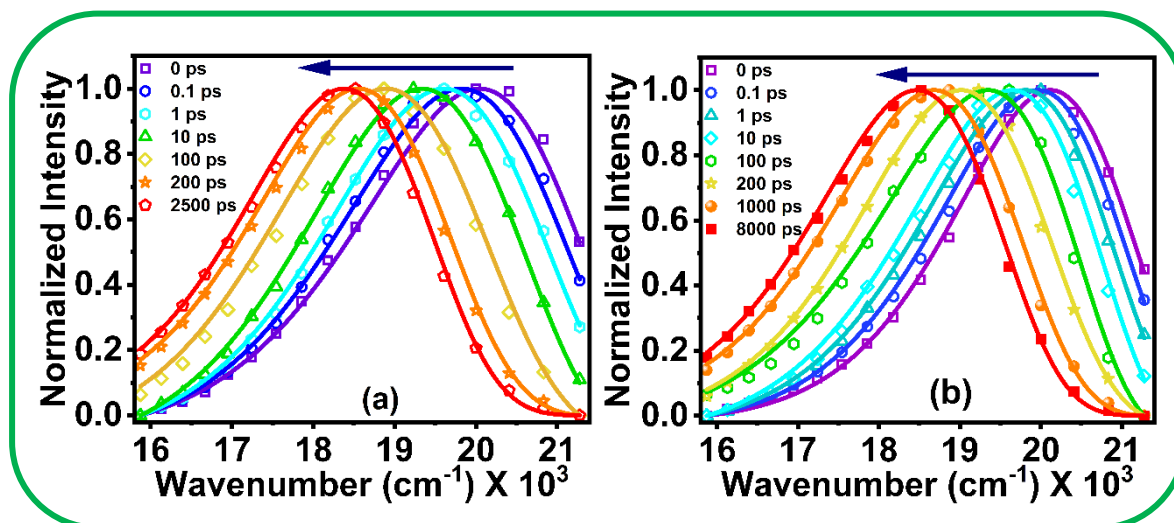


**Figure 3B.2.** Normalized TRES plot at different time interval for (a) ethaline and (b)  $[N_{311}][NTf_2]$ . Solid line represents the log-normal line shape fitting of the corresponding data.

Following this, the time evolution of the peak frequencies  $\nu(t)$  has been obtained by fitting the TRES plots at various time intervals through a log-normal line shape function (equation 2.12). The estimated peak frequencies at “time zero” ( $\nu_0^{obs}$ ) and the fully solvent equilibrated frequencies ( $\nu_{\infty}^{est}$ ) of C153 in all the concerned solvent systems obtained from the fitting have been collected in Table 3B.2. Apart from the peak frequencies, a marginal increase in the  $\gamma$  value (-0.32 to -0.22) with the increase in time has been observed which indicates that the TRES plots are becoming more symmetric with time.<sup>23-25</sup> Similarly, the other parameter  $\Delta$  (fwhm) shows a steady decrease with the increase in time. Previous reports have demonstrated that the time-dependent change in spectral width reflects a combination of effects due to both changes in solvation state as well as to vibrational relaxation.<sup>23-25</sup> However, to monitor the solvent response, we have primarily focused on the time evolution of peak frequencies, as done in the earlier literature reports. The observed  $\nu_0^{obs}$  as well as  $\nu_{\infty}^{est}$  values of C153 are found to be almost identical (Table 3B.2) in all the HFILs, whereas the same value is found to be a little less for ethaline medium. However, the total magnitude of dynamic Stokes shifts ( $\Delta\nu = \nu_0^{obs} - \nu_{\infty}^{est}$ ) are found to be almost comparable in both DES and HFILs. It is also

pertinent to mention here that the total observed dynamics Stokes shifts estimated for both DES and HFILs through the combination of FLUPS and TCSPC techniques are closely parallel to the previously reported values for DESs and ionic liquids.<sup>182-184, 187, 217</sup> Another important aspect of the time-dependent solvent response of both classes of solvent systems that need to be addressed is the amount of missing component. Here, it is important to note that the values of  $\Delta\nu$  in ethaline and HFILs measured by the TCSPC technique alone are found to be nearly 900-1000  $\text{cm}^{-1}$ , and the amplitude of the missing component is estimated to be nearly 40-50 % of the total dynamics. Kim and co-workers<sup>224</sup> while working on the solvation response of choline chloride-based DESs, have also reported less than 1000  $\text{cm}^{-1}$  of total dynamic Stokes shift. It is to be noted here that the missing solvation component is estimated by following Fee and Maroncelli method.<sup>221</sup> In this method, the time zero frequency (i.e., solute emission frequency immediately after laser excitation) is usually calculated by subtracting the steady states Stokes shift of the dipolar probe in a reference non-polar solvent from the steady state absorption spectrum of the same probe in the desired polar solvent under investigation. However, this method becomes less accurate when the densities of both polar and non-polar reference solvents differ appreciably from each other.<sup>183, 221</sup> In the present study, the difference in density between the reference non-polar solvent (say cyclohexane, density = 0.79  $\text{g}/\text{cm}^3$ ) and DESs/RTILs (say [OHEMIM][NTf<sub>2</sub>], density = 1.58  $\text{g}/\text{cm}^3$ ) is significantly high. Thus, it is expected that the estimation of time zero frequency, as well as the missing components through this method, becomes more erroneous. Therefore, with the help of the FLUPS technique having sub-picosecond temporal resolution, almost entire solvent response can be fully characterized. This is supported by the fact that estimated  $\Delta\nu$  values, in the present study, for both the DES and HFILs are found to be much larger (1770- 1680  $\text{cm}^{-1}$ ) with almost negligible missing components (1-2%) as compared to that estimated through only TCSPC techniques. Here, we would like to point out that the amount of total dynamical Stokes shift obtained in the current

investigation is consistent with earlier literature findings that recorded the entire solvent response for DESs and RTILs. All these observations essentially indicate that almost complete solvent response of both DES and HFILs to the excited state of C153 have been captured in the present study with the help of both these techniques.

**Table 3B.2.** Solvent relaxation parameters of both DESs and HFILs at 298K

Systems	$\eta$ (cP)	$\alpha_1$	$\tau_1$ (ps)	$\alpha_2$	$\tau_2$ (ps)	$\beta$	$\tau_{st}$ (ps)	$\nu_0^{obs}$ ( $10^3$ $\text{cm}^{-1}$ )	$\nu_\infty^{est}$ ( $10^3$ $\text{cm}^{-1}$ )	$\Delta\nu$ ( $10^3$ $\text{cm}^{-1}$ )	% Missed
Ethaline	38.8	0.23	0.36	0.77	112	0.64	158	20.07	18.39	1.68	2.00
OHEMIM	72.7	0.18	0.44	0.82	273	0.56	439	20.17	18.45	1.72	2.00
OHEMPy	92.4	0.17	0.48	0.83	321	0.52	556	20.23	18.46	1.77	1.00
[N <sub>3112</sub> OH]	98.5	0.19	0.50	0.81	360	0.56	579	20.20	18.47	1.73	1.00

Hereafter, the peak frequencies obtained from the log-normal fitting of TRES are used for the calculation of the normalized spectral shift correlation function ( $C(t)$ ) by following equation 2.13. The plots of  $C(t)$  against  $t$  (time) for all the solvent systems at 298 K are provided in Figure 3B.3. Here, it is important to mention that while constructing the plots of  $C(t)$  against  $t$  (time), there is a mismatch of peak frequencies between the time range 100-600 ps calculated by FLUPS and TCSPC methods. However, this observation is not unusual, and similar kind of discrepancy between these two techniques has also been reported by various research groups while working on the solvation dynamics of C153 in RTILs and DESs.<sup>187, 217</sup> In the present study, the mismatch between these two techniques is resolved by applying a literature method as suggested by Maroncelli and coworkers.<sup>217</sup> From Figure 3B.3, one can notice that almost 20-25 % solvent relaxation have been completed within 500fs for both DES and HFILs. In this context, we note that Zhang et al.,<sup>217</sup> as well as Chowdhury et al.,<sup>201</sup> while working on RTILs

independently, have also reported almost 30% solvent relaxation within 300 fs. These observations essentially indicate the presence of a very fast (ultrafast) solvation component in the solvent-mediated relaxation process of C153 in the excited state.

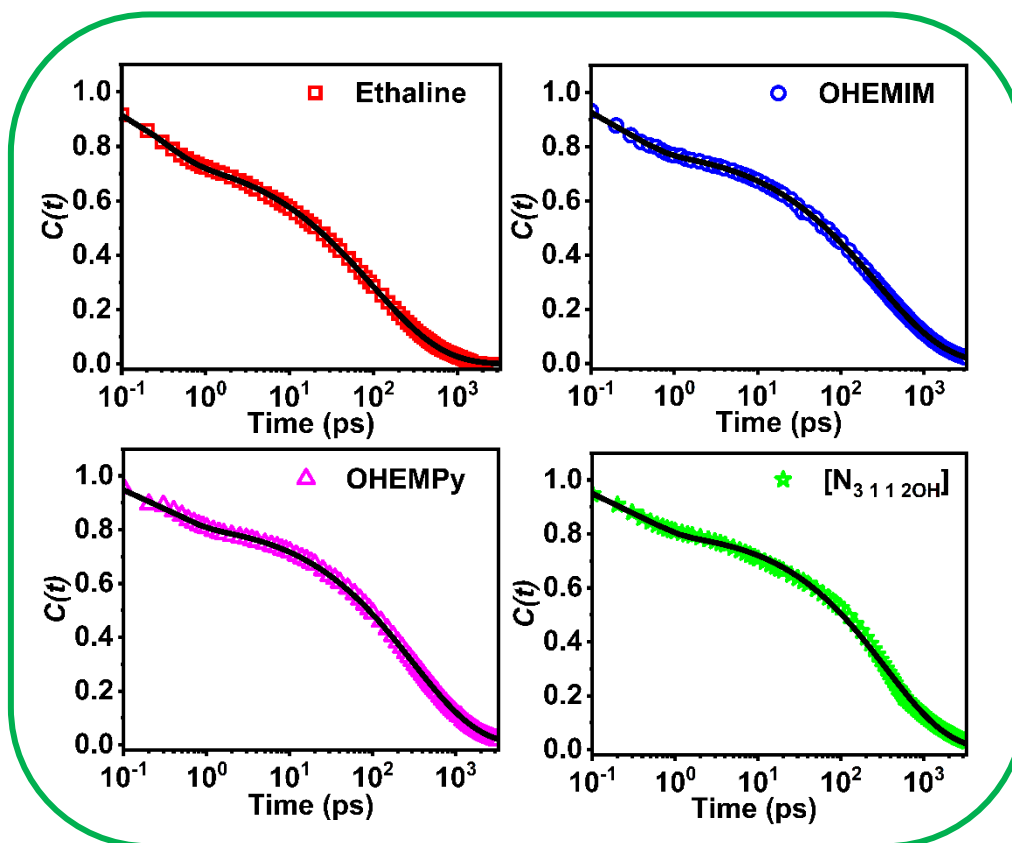


**Figure 3B.3.** Spectral shift correlation function  $C(t)$  decay with time for C153 in (a) ethaline (b)[OHEMIM][NTf<sub>2</sub>] (c) [OHEMPy][NTf<sub>2</sub>] (d) [N<sub>3 1 1 2OH</sub>][NTf<sub>2</sub>] at 298K. The solid line represents fit to the data point.

To get further information regarding the solvent relaxation phenomena as well as to quantitatively characterized the time evolving peak frequencies, the plots of  $C(t)$  versus  $t$  are fitted to a sum of single exponential as well as a stretched exponential function by following equation 2.16. Moreover, the integral time associated with the stretched solvation time component is also estimated by following equation 2.15. Here it is worth mentioning that the plot of  $C(t)$  versus  $t$  for both DES and HFILs measured through TCSPC techniques only shows a biphasic solvation characteristic with an ultrafast component of picosecond time scale and a

---

---

relatively slow component of sub-nano to nanosecond time scale.<sup>224, 281, 282</sup> Kim and co-workers<sup>224</sup> have also reported similar biphasic solvation behaviour in choline chloride-based DESs. However, the  $C(t)$  versus *time* plots generated by the data obtained from combined TCSPC and FLUPS measurements do not provide a reasonable biexponential fit to the data, whereas it gives a better fit when the data is fitted by equation 2.16. While different reasons for the physical origin of this behaviour have been provided by different research groups, the fitting of the solvent relaxation data by equation 2.16 is found to be suitable in almost all cases.<sup>187, 217, 283</sup> This issue has been rationalized by considering the fact that the early part of the solvent response, which is missed due to the broader temporal resolution of the TCSPC setup, is well accounted by equation 2.16.<sup>187, 217, 282</sup>

The fit parameters obtained from the fitting of the  $C(t)$  versus *time* plots through equation 2.16 have been summarized in Table 3B.2. From Table 3B.2, one can notice that for both DES and HFILs, there are two distinct solvation time components, a small amplitude ultrafast time component of sub-picosecond time scale (0.33-0.52 ps) and a relatively slower time component (110-360 ps) associated with a larger amplitude. Similar kind of values for the ultrafast component as well as for the slower component have been reported by different groups while studying the complete solvent response in different types of DESs and RTILs of comparable viscosity.<sup>182, 183, 187, 217</sup> Here, one can notice that the relatively longer time component is associated with a stretched exponent ( $\beta$ ) whose values lie below unity (0.64-0.52) for both DES and HFILs indicating the broad distribution of the slower relaxation time component. Previously it has been suggested that for heterogeneous media like DESs and RTILs, the deviation of the value of  $\beta$  from unity arises because of the heterogeneous diffusional motions, which is different from the classical hydrodynamic motions of the constituent ions and the extent of deviation of  $\beta$  value from unity correlates with the extent of medium heterogeneity.<sup>187, 217</sup> In light of the above discussions, in the present scenario also, the

observation of the deviation of  $\beta$  value from unity for both DES and HFILs can be rationalized by considering the micro-heterogeneous nature of these media. Furthermore, the departure of  $\beta$  value from unity is found to be almost similar for all the HFILs ( $\beta = 0.52-0.56$ ) while the same is found to deviate less from unity ( $\beta = 0.64$ ) for the DES, indicating a larger distribution of the slower time component for the HFILs as compared to that for DES. This observation essentially indicates that the HFILs are relatively more micro-heterogeneous in nature than that of the DES (ethaline). In this context, we would like to note that the observation of larger micro-heterogeneous nature of HFILs is consistent with our previous observations<sup>284</sup>, where microheterogeneity of these concerned media are probed by rotational dynamics, FCS and PFG-NMR studies (Chapter 3A).

Another important feature of solvent relaxation behaviour that needs to be understood is the dependence of the integral time of the slower component ( $\tau_{st}$ ) on the solvent viscosity. Previous studies of solvation dynamics on DESs and RTILs have suggested that the value of  $\tau_{st}$  represents the average solvation time of the concerned medium, and the values strongly correlate with the viscosity of the medium.<sup>187, 217</sup> From the plot of  $\tau_{st}$  versus viscosity (Figure 3B.4), it can be seen that the values of  $\tau_{st}$  is directly proportional to the bulk viscosities of the media. Therefore, this observation suggests that the slower component of the solvent relaxation process is associated with diffusional motion of the constituents of the concerned solvent. Keeping in mind the outcome of the solvent dynamics in supercooled liquid, the slower component of the solvent response can be linked to bulk structural reorganization.<sup>175-177, 182, 183, 187, 217</sup> Interestingly, it has been found that upon going from ethaline to  $[N_{311}2OH][NTf_2]$ , even though the change in bulk viscosity is nearly 2.5 times, the change in  $\tau_{st}$  value is found to be more than 3.5 times. This observation indicates that the solvent relaxation is much faster in ethaline as compared to that in HFILs. This difference in the solvent response occurring at a slower time scale essentially indicates that the mechanism of solvent relaxations operating at

the microscopic level are significantly different for DES and HFILs despite the fact that both these systems contain similar hydroxyl functional groups. Now when we consider the initial rapid solvent relaxation, it can be seen that the time constants of the ultrafast component as well as the amplitude (Table 3B.2 and Figure 3B.4 (b)) associated with it are almost comparable in both DES and HFILs. Therefore, just by looking at the ultrafast solvation time component values, at this stage, it is difficult to conjecture any difference in the initial solvent response between DES and RTILs, and thus further studies are required to throw more light on these issues.

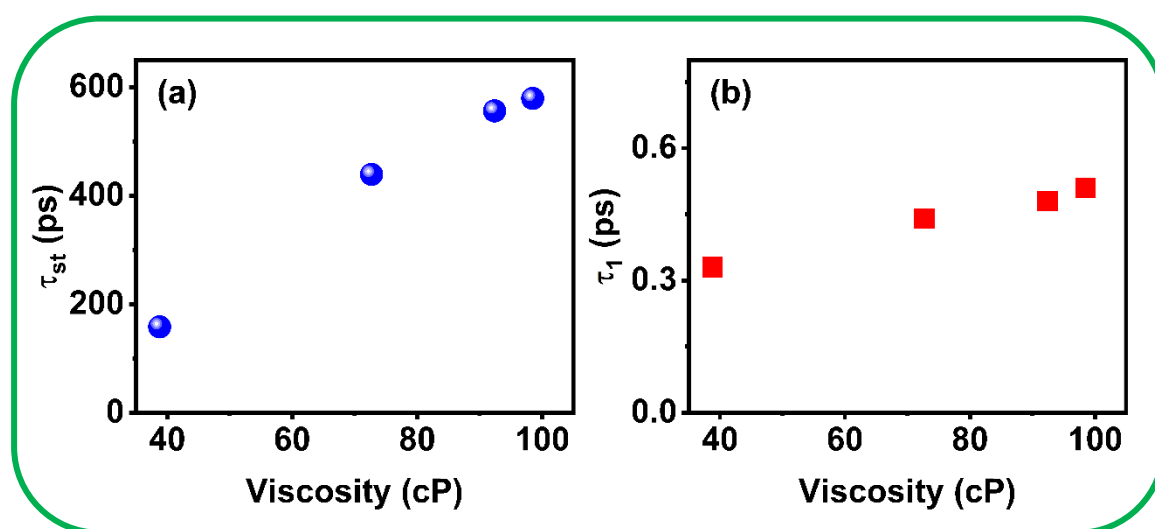


**Figure 3B.4.** Variation of (a) long time and (b) short time component against the bulk viscosity of the solvents at 298 K.

Before hypothesizing about the origin of the ultrafast as well as the multiple solvation time components in confined media like DESs and RTILs, we would like to note that the solvent responses of these media are much more complex and are fundamentally different from conventional polar solvents.<sup>197-210</sup> In case of ordinary polar solvents, reorientation of the solvent's dipoles around the excited state of solute molecules is primarily responsible for the solvent relaxation process, whereas for RTILs the individual motions of ions, as well as collective motions of the constituent ions, are responsible for the solvent relaxation behaviour.

Maroncelli and co-workers<sup>203-205</sup>, through fluorescence up-conversion measurements, have demonstrated that for imidazolium-based ILs, the small amplitude motion of the planar imidazolium cation in the close vicinity of the probe is responsible for the ultrafast solvation component, whereas the slow component is strongly related to the bulk viscosity the solvent. However, later on, the author pointed out that the inertial motion of the cation and/or anion is primarily responsible for the ultrafast solvent response.<sup>217</sup> On the other hand, Petrich and Co-workers<sup>201, 285</sup>, through both experimental and theoretical calculation, have demonstrated that for imidazolium-based RTILs, the polarizability of the cationic moiety close to the solute probe leads to the initial rapid solvation relaxation. Furthermore, Biswas and co-workers<sup>208, 209</sup>, through both dielectric relaxation measurement and theoretical calculation, have also suggested that the imidazolium cation is polarizable and dipolar rotation of the imidazolium cation can also contribute significantly to the early parts of the solvent response. Contrary to the above arguments, Kobark<sup>210, 211</sup>, with the help of molecular dynamics simulation, has suggested that the speculation of cation or anion dynamics to the initial solvent response is oversimplified and collective motion of cation and anion contributes significantly as cation-anion correlation begins to occur within 200fs. Samanta and co-workers<sup>214, 281</sup>, through experimental studies, have also provided a similar kind of explanation for the initial rapid solvent relaxation process. The biphasic nature of solvent relaxations, as observed in RTILs, forms the basis of the mechanism to describe the solvent response in DESs. Biswas and co-workers<sup>177, 178</sup>, while working on acetamide-based DESs, reported that the collective low-frequency modes involving intermolecular vibration and liberation motions of the hydrogen bonding network led to the initial fast solvent response, while the orientational solvent density fluctuation is responsible for the observed slow components. Moreover, Cui et al.,<sup>286</sup> through molecular dynamics simulation and ab initio calculations, have suggested that the in-place motion of the choline cation, such as rotations and/or translation motion without involving any centre of the

mass movement, contributes significantly to the initial ultrafast solvation component. Additionally, Reuter et al.,<sup>287</sup> through dielectric relaxation measurement, have shown that the solvation relaxation of the choline chloride-based DESs involves significant dipolar reorientational motions, which may contribute to the initial solvent response. Considering all the above discussions, one can realize that the solvent reorganization in DES and RTILs is quite complex, and assigning a particular molecular motion to the time component corresponding to initial rapid solvent response for both DES and HFILs is rather a challenging task. Thus, further studies based on dielectric relaxation measurements, temperature-dependent ultrafast solvation dynamics etc., are expected to help in understanding the difference of the solvent response corresponding to the initial part of the solvent relaxation in both classes of the solvent systems.

### 3B.3.3. Temperature-Dependent Ultrafast Solvation Dynamics

To get further information about the differences in the ultrafast as well as the total solvation response between DES and HFILs, temperature-dependent solvation dynamics of C153 in ethaline and  $[\text{N}_{3112\text{OH}}][\text{NTf}_2]$  have been carried out in the temperature range of 298 K-328 K. The corresponding TRES plot of C153 in ethaline and  $[\text{N}_{3112\text{OH}}][\text{NTf}_2]$  at different temperatures are provided in the Appendix (Figure APX3B.2 and Figure APX3B.3). The  $C(t)$  versus time plots generated after fitting the TRES plots of C153 in both media are shown in Figure 3B.5. From Figure 3B.5, it can be seen that with the increase in temperature, the solvent relaxation process becomes faster in both media. Interestingly, upon a closer look at Figure 3B.5, it can be noticed that with the increase in temperature, the solvent relaxation for ethaline is found to be much faster as compared to the same for  $[\text{N}_{3112\text{OH}}][\text{NTf}_2]$ . For example, for ethaline at 298 K, nearly 20% of the total solvation response is found to be completed within 400 fs, whereas at a relatively higher temperature (328K), nearly 40% of the total solvent response is found to be completed. On the contrary, for  $[\text{N}_{3112\text{OH}}][\text{NTf}_2]$ , the total solvation

response that is completed within 400 fs is found to be almost similar (~20%) at lower (298K) as well as at elevated temperature (328K). These observations are indicative of the fact that the process of solvent relaxation events in both of these media are significantly different from each other.

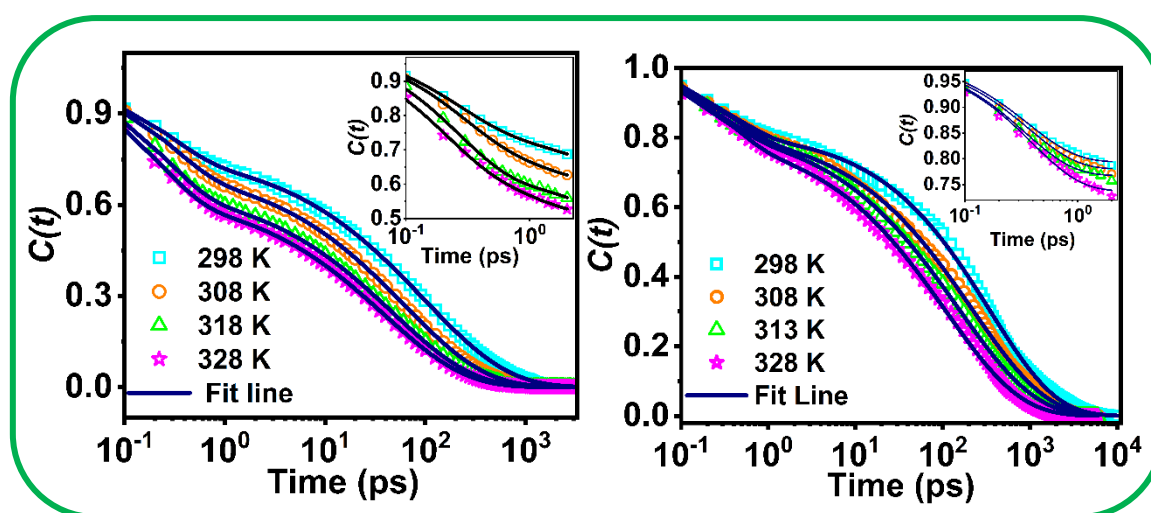


**Figure 3B.5.** Spectral shift correlation function  $C(t)$  decay with time for C153 in ethaline and  $[N_{3112OH}][NTf_2]$  at different temperature. The solid line represents fit to the data point.

**Table 3B.3.** Solvent relaxation parameters and viscosity of both DESs and HFILs at 298K-328K

Systems	Temperature (K)	$\eta$ (cP)	$\alpha_1$	$\tau_1$ (ps)	$\alpha_2$	$\tau_2$ (ps)	$\beta$	$\tau_{st}$ (ps)
Ethaline	298	38.8	0.23	0.36	0.77	112	0.64	158
	308	24.7	0.29	0.34	0.71	74	0.67	98
	318	16.7	0.36	0.35	0.64	53	0.69	74
	328	12.3	0.41	0.34	0.59	40	0.72	49
$[N_{3112OH}]$	298	98.5	0.19	0.50	0.81	360	0.56	579
	308	63.4	0.21	0.50	0.79	255	0.56	410
	318	42.7	0.21	0.48	0.79	195	0.57	310
	328	29.3	0.22	0.49	0.78	141	0.59	217

To get more in-depth information about the mechanism solvation in DES and HFILs, the data corresponding to  $C(t)$  versus time plots at several temperatures are fitted through equation 2.16 and the fitted parameter are collected in Table 3B.3. From Table 3B.3, it can be observed that for both the media, the integral time associated with the slower components ( $\tau_{st}$ ) decrease considerably with increase in temperature indicating a faster solvent relaxation event in both classes of solvents. This decrease in the values of  $\tau_{st}$  are consistent with the decrease in the bulk viscosity of the medium. This observation further supports the fact that the slower component of the solvent response, which represents the bulk structural reorganization, is directly related to the medium viscosity. Interestingly, upon a careful inspection of the data, one can notice that at 318 K, the viscosity (42.7 cP) of  $[N_{311}2OH][NTf_2]$  medium is almost comparable with the viscosity of ethaline medium (38.8 cP) at 298 K. However, the  $\tau_{st}$  value of  $[N_{311}2OH][NTf_2]$  medium is estimated to be almost twice the value of  $\tau_{st}$  in ethaline medium. This finding further corroborates with our earlier observation, where a faster solvent response for the DES as compared to the HFILs has been observed. Furthermore, from Table 3B.3, it can be found that the  $\tau_{st}$  value does not vary proportionately with the solvent viscosity of  $[N_{311}2OH][NTf_2]$ , whereas the  $\tau_{st}$  values more or less follow with the solvent viscosity of ethaline. For example, upon going from 298 K to 328 K, the lowering of viscosity of  $[N_{311}2OH][NTf_2]$  is more than 3 times, while the value of  $\tau_{st}$  decrease only by  $\sim 2.5$  times. To understand the dependence of  $\tau_{st}$  value with the medium viscosity, the  $\tau_{st}$  values for both ethaline and  $[N_{311}2OH][NTf_2]$  are fitted with an empirical relation which is given by<sup>175-182</sup>

$$\tau_{st} \propto (\eta/T)^p \quad (3B.3)$$

where  $p$  is a constant whose value is close to one for ordinary homogeneous solvents. However, deviation of  $p$  value from unity indicates the departure of the diffusional motion from the classical hydrodynamic motion. This may be due to the non-hydrodynamic centre of

mass movement of the constituents of the solvent, such as orientational jumps, angle jumps etc.<sup>175-185</sup> Biswas and co-workers<sup>175-179</sup> have previously demonstrated that deviation of  $p$  value from unity essentially indicates the dynamic heterogeneity of a medium. The log-log plots of  $\tau_{st}$  versus  $\eta/T$  are provided in Figure 3B.6. The fitting of the data shows that  $p$  value is less than one in both DES and HFILs. This fractional dependence of  $\tau_{st}$  with viscosity shows that both these media are dynamically heterogeneous. Furthermore, a larger departure of  $p$  value from unity in  $[\text{N}_{3112}\text{OH}][\text{NTf}_2]$  ( $p = 0.75$ ) as compared to the same for ethaline medium ( $p = 0.91$ ) has also been observed, which essentially indicates that though both the media are dynamically heterogeneous, the extent of dynamic heterogeneity is more for the HFILs as compared to the DES. Here it is also important to note that though the value  $p$  is found to be relatively higher as compared to the  $\beta$  value, nevertheless both these exponents exhibit a similar trend upon going from ethaline to the HFILs, indicating larger dynamic heterogeneity in the latter than the former.

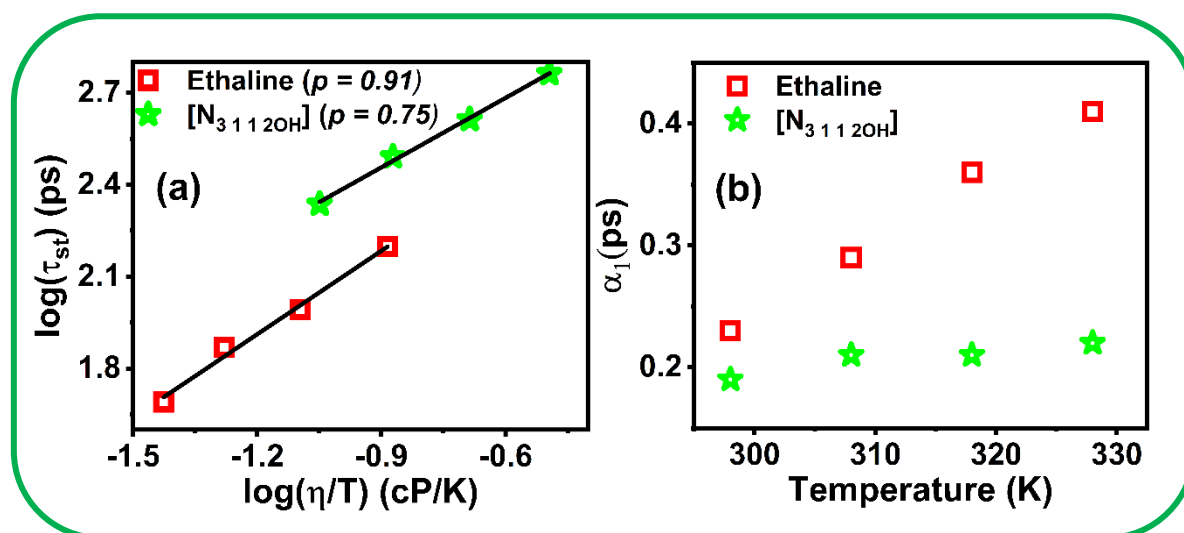


**Figure 3B.6.** (a) log-log plot of  $\tau_{st}$  versus  $\eta/T$ . The solid line represents fit to the data point. (b) amplitude associated with the sub-picosecond component versus temperature.

Now when we focus on the initial part of ultrafast solvent relaxation for both media, it can be seen that with the increase in temperature, the ultrafast time component remains constant

(with uncertainties of 6-8%) even though the viscosities of both the media change significantly. This observation clearly indicates that the ultrafast time components of these media are independent of the bulk viscosity of the medium. It is to be noted here that Sen and co-workers<sup>184</sup>, in a separate work, have also found similar behaviour in acetamide-urea-based DES. Through transient absorption spectroscopy and femtosecond optical Kerr effect (OKE) spectroscopy, they have suggested that the ultrafast time component is totally independent of the solvent viscosity and the low-frequency collective modes of the solvent involving intermolecular vibration and liberation motion are responsible for the observed ultrafast solvent relaxation. Another important aspect of the ultrafast solvation component is the amplitude associated with the sub-picosecond time constants. Here it is pertinent to mention here that Maroncelli and co-workers<sup>217</sup> while working on RTILs, have suggested that for imidazolium and pyrrolidinium-based RTILs, the amplitude of the ultrafast component is inversely related to the alkyl chain length of the cationic moiety. Later on, taking a similar path, Saddam et al.<sup>187</sup> while working on alkylammonium-based DESs, have reported that with the increase in the alkyl chain length of the HBA, the amplitude of the ultrafast component decreases considerably. Thus, these studies have pointed out that the length of the alkyl chain of the cation of both DESs and RTILs is an important factor in controlling the amplitude of the ultrafast solvation component. Since the alkyl chain length, as well as the cationic radii (0.3-0.33 nm)<sup>284</sup> of both DES and HFILs, are approximately the same, the amplitudes associated with the ultrafast solvation components (Table 3B.2) at 298 K are found to be almost comparable for all the concerned media. Interestingly, with the increase in temperature from 298 K to 328 K, the amplitude of the ultrafast component for ethaline medium is found to increase by nearly two times (Figure 3B.6), whereas the same is found to be nearly independent of temperature for  $[N_{3,1,1,2OH}][NTf_2]$ . This observation undoubtedly indicates that even at ultrafast time scales, different motions related to the relaxation process in DES and HFILs are

considerably different from each other. Since numerous experimental and simulation studies<sup>208-210, 214, 217, 286</sup> have suggested that various fast local motions, without involving the movement of the centre of mass of the constituents of DESs and RTILs, such as dipolar rotation, vibration, libration, translation, etc., are responsible for the observed ultrafast relaxation process, it is really a challenging task to assign which particular motion is accountable for the observed difference in the ultrafast relaxation behaviour. Nevertheless, the presence of extensive hydrogen bonding network in ethaline medium, which is highly temperature dependent<sup>173, 174, 176, 184, 185</sup> might have caused a larger change in the amplitude associated with the ultrafast relaxation component for ethaline as compared to the same for [N<sub>3</sub> 1 1 2OH][NTf<sub>2</sub>]. Considering this, various collective modes involving the intermolecular hydrogen bonding network, position, and orientations of the constituent of the DES present in the close vicinity of the solute contribute to the initial solvent response in DES, whereas the local motion of the cation and anion of the HFILs in the first solvation shell contributes to the initial solvent response in HFILs. However, this observation which ascertained some difference in the ultrafast relaxation behaviour between DES and HFILs warrants further rigorous validation by both experimental and theoretical methods.

### 3B.4. Conclusion

In the present work, we have tried to understand the difference in the solvent relaxation behaviour between DES and RTILs, if any, by employing TDDSS measurement technique at both picosecond and femtosecond time resolution. For this purpose, FLUPS (fs) technique have been combined with TCSPC spectroscopy (ps) technique in order to capture the complete solvent dynamics of a choline chloride-based DES and three hydroxyls functionalized RTILs, so that role of various intra/intermolecular interaction on the solvent relaxation behaviour can be understood. All these investigations have revealed several interesting findings. The

estimations of static solvation energetics for the  $S_0 \leftrightarrow S_1$  transition of C153 have indicated a similar polar environment experienced by C153 in both DES and HFILs. Interestingly, the solvent response functions generated from the complete Stokes shift dynamics measurements have revealed a bimodal solvent relaxation behaviour, consisting of a very fast sub-picosecond solvation time component and a broadly distributed relatively slower pico- second to sub-nanosecond solvation time component for both DESs and RTILs. The broadly distributed slower time component, which correlates with the medium viscosity, is found to arise due to the heterogeneous diffusional motion of the constituents of DES and RTILs. However, studies of temperature-dependent solvation dynamics have suggested that at nearly iso-viscous conditions, the solvent relaxation for ethaline is much faster as compared to the same for  $[N_{3,1,1,2OH}][NTf_2]$ . This observation indicates that various non-hydrodynamics diffusional motions responsible for solvent relaxation at a slower time scale are significantly different for both DES and HFILs. Additionally, pronounced fractional viscosity dependence of slower solvation time component for  $[N_{3,1,1,2OH}][NTf_2]$  as compared to the same for ethaline has also indicated the appreciable difference in the solvent relaxation behaviour between DES and HFILs at slower solvation time scale. More interestingly, while monitoring the initial solvation response, even though the sub-picosecond solvation time component is observed to remain same for both ethaline and  $[N_{3,1,1,2OH}][NTf_2]$ . However, the amplitude associated with the sub-picosecond solvation time component for ethaline was found to change significantly at elevated temperatures, whereas the same for  $[N_{3,1,1,2OH}][NTf_2]$  was found to be unchanged. This observation indicates that even at sub-picosecond time scales, various fast local motions (such as rotation, vibration, libration, translation, etc., without involving the movement of centre of mass of the constituents) at the immediate vicinity of the solute, responsible for initial solvent relaxation, are considerably different for DES and HFILs. Essentially, all the results obtained from these investigations have demonstrated that despite having similar functional moieties,

different motions related to the solvent relaxations for DES and HFILs are significantly different from each other. This further highlight that various inter/intramolecular interactions, including hydrogen bonding interaction, greatly influence the dynamical behaviour in DESs and RTILs. The outcome of the present study is expected to be helpful not only for understanding the solute reactivity in these media but also for utilizing both DESs and RTILs as potential media for carrying out targeted chemical reactions, in particular electron transfer reactions.

### 3B.5. Appendix

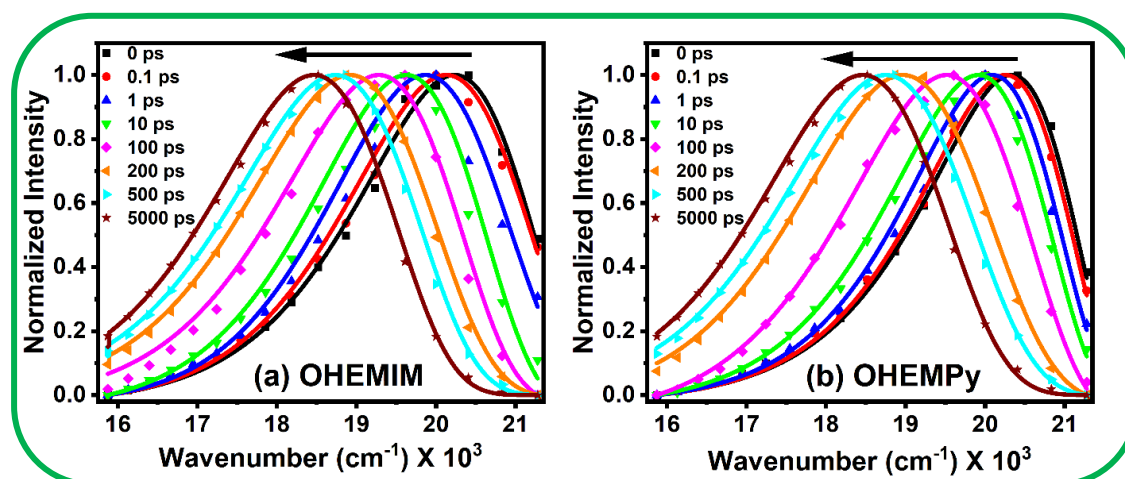


**Figure APX3B.1.** Normalized TRES plot at different time interval for (a) [OHEMIM][NTf<sub>2</sub>] and (b) [OHEMPy][NTf<sub>2</sub>].

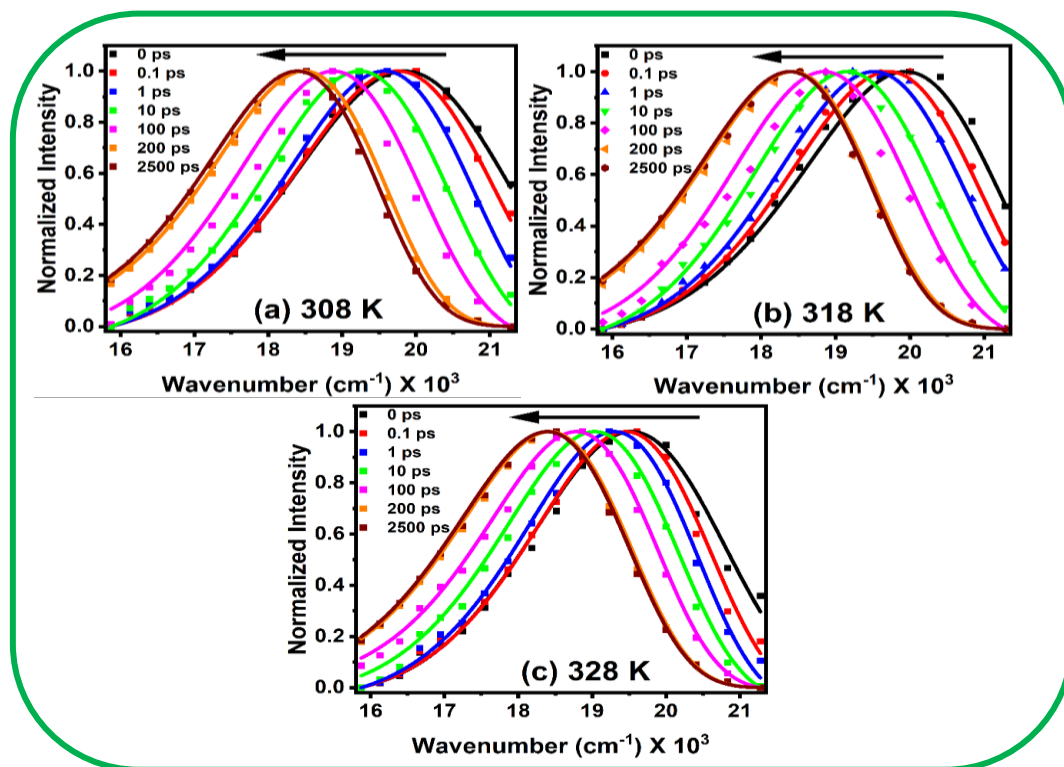


**Figure APX3B.2.** Normalized TRES plot at different time interval for Ethaline at different temperature.

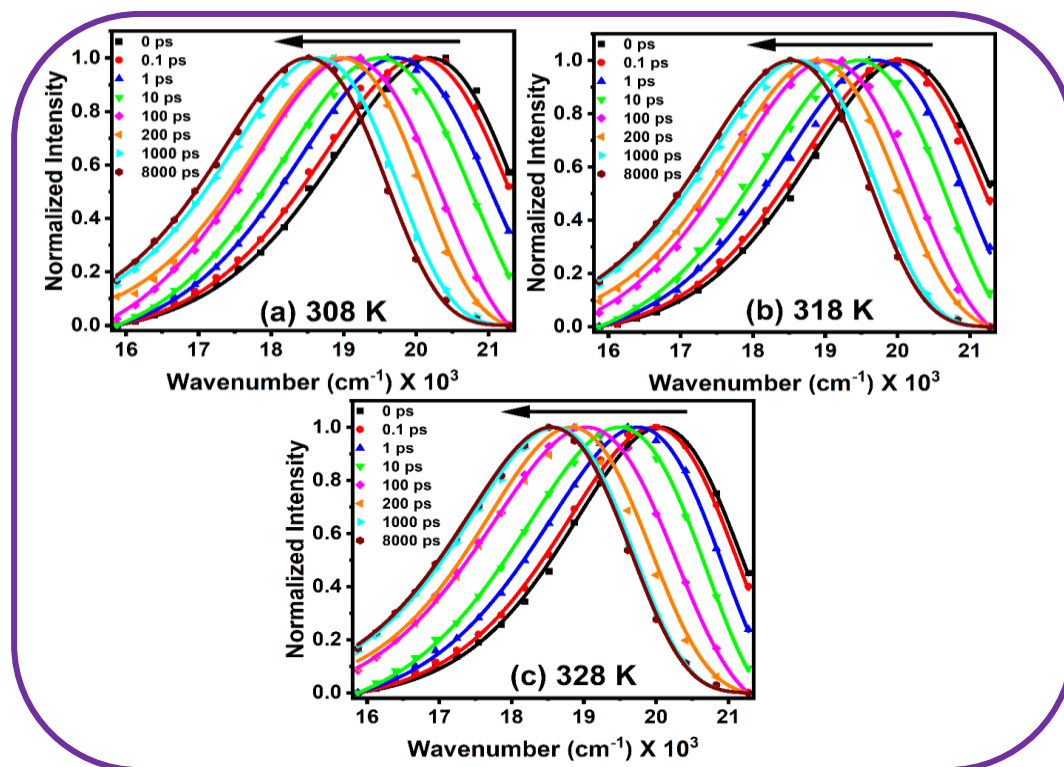


**Figure APX3B.3.** Normalized TRES plot at different time interval for  $[\text{N}_{3112}\text{OH}][\text{NTf}_2]$  at different temperatures

# CHAPTER 4

---

## Probing the Impact of Increase in the Number of Hydroxyl Groups on the Structure and Dynamics of Ammonium-Based Room Temperature Ionic Liquids

---

---

**Barik, S.; Mahapatra, A.; Jena, D.; Sarkar, M.; *J. Photochem. Photobiol. A Chem.*, 2023, 437, 114505**

**Abstract**

This chapter aims to understand how the number of hydroxyl groups on the cationic head of ammonium-based room temperature ionic liquids (RTILs) affects the inter- and intra-molecular hydrogen bonding interaction, local structural organization, and dynamics of the solvent systems. For this purpose, three hydroxyl functionalized ammonium-based RTILs (HFILs) bearing different numbers of hydroxyl groups on the cationic head, as well as a non-hydroxyl ammonium-based RTIL, have been examined using both ensemble average and single-molecule spectroscopy techniques. Investigation of solvent relaxation dynamics of all the concerned RTILs by the combination of FLUPS and TCSPC techniques have revealed a bimodal solvent relaxation behaviour having a very fast sub-picosecond and a relatively slower picosecond to nanosecond solvation time component for all the RTILs. Interestingly, analysis of the rotational and translational diffusion dynamics of a few particular solutes have indicated that the solvent–solvent interaction in the poly-hydroxyl-based HFILs is substantially stronger than the solute–solvent interaction. Additionally, analysis of the rotational diffusion data has also suggested that all RTILs exhibit significant dynamic heterogeneity, which increases with increase in the number of hydroxyl groups on the cationic head of HFILs. Moreover, PFG-NMR study has shown that the HFILs have considerably greater hydrodynamic radii than the non-hydroxyl RTILs, which is likely due to the result of stronger hydrogen bonding interaction between the hydroxyl groups and the constituent of the HFILs. The outcomes of all these investigations have essentially demonstrated that the subsequent addition of hydroxyl functionalities to the cationic head of the RTILs significantly alters the intra/intermolecular interactions, local structural organization, and heterogeneity of the medium.

---

#### 4.1. Introduction

In recent years, the development of room-temperature ionic liquids (RTILs) has gained momentum as their properties can be customized to aid chemical processes ranging from chemical synthesis to material and biological sciences.<sup>126-127,29, 31, 126</sup> The tunability of RTILs has become a focus of intense research for the design and development of various task-specific ILs as per the need of the end users.<sup>31, 48, 90</sup> In general, task-specific ILs can be fine-tuned in two ways, either by using alkyl side chains of varying length as nonpolar moieties attached to the ionic core of a given molecular ion or by adding various functional groups to the side chains and/or to the ionic cores.<sup>48, 251, 288, 289</sup> The latter approach, in particular, has been proposed to be a game changer for the development and application of functionalized ILs as an alternative media to conventional organic solvents.<sup>23, 28, 29, 31, 48, 90</sup> Additionally, by adding a hydroxyl group to the cationic head of an RTIL, it is possible to create ILs with an expanded electrochemical window, improved hydrophilicity and enzyme activity, higher viscosities, and thermal stability and superior media for solubilizing inorganic and organic salts.<sup>103, 251</sup> These aforementioned properties can be tailored further by changing the position and number of hydroxyl functionalities on the cationic head of the RTILs.<sup>251</sup> However, the molecular origin of such attractive properties of hydroxyl functionalized ionic liquids (HFILs) is still unclear due to limited literature reports on the same issue. Therefore, understanding the intra/inter molecular hydrogen bonding interaction, local structural organization and dynamics of the solvent systems at the molecular level, and their role in governing structure-property relations, is very important and a prerequisite to the design of a suitable ionic liquid for a given application.

Despite the fact that HFILs have rose to prominence more than a decade ago, most of these studies are basically devoted to the applications of these media in various fields.<sup>126, 290,</sup>

<sup>291</sup> However, relatively few investigations are conducted to comprehend the microscopic behaviour of HFILs. Samanta and co-workers<sup>281</sup> have investigated the solvation and rotational dynamics of some selected solutes in hydroxyl functionalized imidazolium-based RTILs and observed that the solute-solvent interaction in the HFILs hindered the rotation of the ionic solute. In a separate study, Dutt et al.<sup>227</sup> have examined the rotational dynamics of a neutral and a charged probe in methylimidazolium-based ILs with and without hydroxyl functionalization, and they have observed that both probes rotated more slowly in the former than the latter. Recently, Deng and colleagues<sup>103</sup> have looked into the polarity of several HFILs, and they have demonstrated that HFILs have an unusually high degree of polarity. Besides this, some theoretical works on HFILs have also been reported by some other researchers.<sup>292-297</sup> In their study of the self-assembly of cations in aqueous solutions of HFILs, Palchowdhury and Bhargava have reported that the cation self-aggregates from quasispherical aggregates to intercalated aggregates as the alkyl chain length on the cation increases.<sup>293</sup> Furthermore, Ludwig and Co-workers have done extensive theoretical investigations on HFILs to understand the impact of intermolecular hydrogen bonding on the structure-property relationship.<sup>294-297</sup> Through neutron scattering, infrared spectroscopic techniques, and MD simulation studies, they have reported that cation-cation intermolecular hydrogen bonding interaction can lead to cationic cluster formation, which in turn influences the glass formation and crystallization of these ILs.<sup>294-297</sup>

From the above discussion, it can be understood that not much is known about the microscopic behaviour of HFILs. Moreover, the local structural organization and solvent dynamics of HFILs bearing two or more hydroxyl groups (poly-hydroxyl ILs) are rather unexplored. It is to be noted here that the interplay of various intra/intermolecular interactions, such as columbic interaction, hydrogen bonding interaction, and dispersion forces between

alkyl chains, have a strong bearing on the local structure organization and dynamics of the RTILs.<sup>29, 31</sup> It is also commonly accepted that this local structural organization has a considerable influence on the heterogeneity of the medium.<sup>31</sup> Therefore, studies on the influence of intermolecular hydrogen bonding interaction on the medium heterogeneity and local structure organisation of homologous sequences of HFILs with varying numbers of hydroxyl groups could prove to be vital. Considering this, studies on the dynamics of the solute and solvent in HFILs can be very helpful in identifying correlations between the structure and dynamics of these media. In addition to this, it is necessary to comprehend the impact of interionic interaction on the timescale of solvent organization in such reaction media when developing a solvent to carry out a certain reaction and produce the required product.

Keeping the above discussion in mind, the current study focuses on the understanding of the microscopic behaviour in terms of nature of intra/intermolecular interaction, microscopic structural organisation and dynamics of some hydroxyl functionalized ammonium-based RTILs. In order to accomplish this, ammonium-based RTILs bearing different number (1 to 3) of hydroxyl groups (N-(2-hydroxyethyl)-N,N-dimethylbutan-1-aminium bis(trifluoromethanesulfonyl)imide,  $[N_4 1 1 2OH][NTf_2]$ ; N,N-bis(2-hydroxyethyl)-N-methylbutan-1-aminium bis(trifluoromethanesulfonyl)imide,  $[N_4 1 2OH 2OH][NTf_2]$  and N,N,N-tris(2-hydroxyethyl)butan-1-aminium bis(trifluoromethanesulfonyl)imide,  $[N_4 2OH 2OH 2OH][NTf_2]$ , Chart 4.1) on the cationic head of the RTILs are synthesized and employed in the study. Additionally, a non-hydroxyl ammonium-based RTIL, N,N,N-trimethylbutan-1-aminium bis(trifluoromethanesulfonyl)imide,  $[N_4 1 1 1][NTf_2]$ , Chart 4.1) has also been used in the experiment to gain a better understanding of the impact hydroxyl groups on the microscopic behaviour of the HFILs. Different spectroscopic methods, including steady-state and time-resolved fluorescence, FCS, and NMR have been used to investigate the microscopic behaviour

of both non-hydroxyl and hydroxyl ILs so that a clearer picture on the local environment, solute-solvent interaction, and dynamic of the solvent systems can be obtained. Especially, ultrafast solvent relaxation process of all the concerned RTILs to the excited state of C153 has been investigated with the help of TCSPC and FLUPS techniques. The differences in the local environment and the nature of solute-solvent interaction among the concerned RTILs have also been identified using rotational and translational diffusion dynamics of some chosen probes by time-resolved fluorescence anisotropy measurement and FCS methods, respectively. Furthermore, by utilising NMR methods, the self-diffusion coefficients of the relevant solvent systems have been determined. All the present investigations have demonstrated that presence of hydroxyl group significantly influence the structure and dynamics of the HFILs.

#### **4.2. Experimental Sections**

The detail about the synthesis of different HFILs (Chart 4.1) used in this study have been provided in chapter 2. All the RTILs are dried in the vacuum at 323K for 2 days so as to reduce the moisture contain before use. The dried solvents were transferred into 2cm quartz cuvette and requisite amount of probe was added to prepare the solution. For solvation dynamics study the concentration of the probe (C153) was kept at  $\sim 7 \mu\text{M}$  (keeping absorbance below 0.3) for both steady-state and TCSPC measurement and  $60\text{-}65 \mu\text{M}$  (keeping absorbance below 1.5) for femtosecond up-conversion measurement. Moreover, the probes (Perylene and MPTS) concentration were  $5\text{-}7 \mu\text{M}$  (keeping the absorbance below 0.3) for rotational dynamics studies, whereas for FCS studies the probe (Perylene, MPTS) concentration was  $10\text{-}20 \text{ nM}$ . All the cuvette were thoroughly sealed with septum and parafilm to avoid moisture intake.

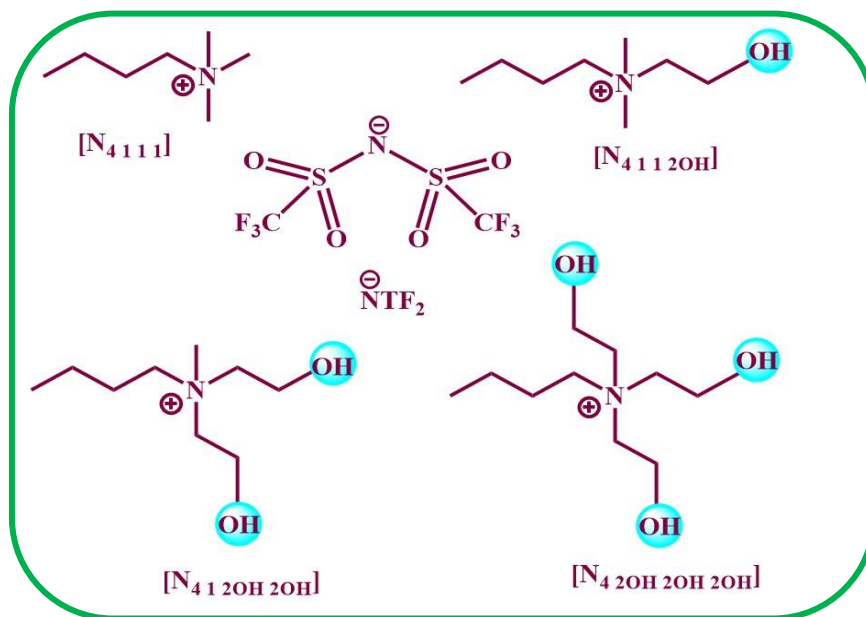


**Chart 4.1.** Chemical structure of different RTILs used in this study.

### 4.3. Results and Discussions

#### 4.3.1. Steady-State Spectral Measurements

Before studying the difference in the microscopic behaviour of the non-hydroxyl and hydroxyl ILs, the steady-state absorption and emission spectra of C153 have been recorded in all the concerned RTILs. Figure 4.1 display the steady-state absorption and emission spectra of C153 in the desired solvents, while the corresponding maxima are collected in Table 4.1. From Figure 4.1, it can be noticed that with the increase in the number of hydroxyl groups in the cationic head, a continuous shift in the absorption maxima has been observed in the concerned RTILs. For example, a 12 nm (Table 4.1) of shift in absorption maxima have been observed upon going from  $[N_{4111}][NTf_2]$  to  $[N_{4112OH}][NTf_2]$ . Similarly, there is also a 13 nm of shift in the emission maxima upon going from  $[N_{4111}][NTf_2]$  to  $[N_{4112OH}][NTf_2]$ . This red shift in absorption and emission maxima of C153 in the HFILs indicates that the HFILs are more polar as compared to the non-hydroxyl ILs. Here, we also note that Deng and co-worker<sup>103</sup> have also observed higher polarity for the hydroxyl functionalized ILs, which they have assigned to the synergistic

hydrogen bonding interaction between the hydroxyl groups of the cation and the corresponding anions of the HFILs. Considering this, in the present study also, the higher polarity of the HFILs is due to the hydrogen bonding interaction between the hydroxyl groups and the  $\text{NTf}_2^-$  anions. Furthermore, with the increase in the number of hydroxyl groups, no change in the fluorescence maxima is observed though one could expect an increase in the polarity of these media. Here, it is important to note that for viscous media like ionic liquids, where the solvation of a solute fluorophore is relatively slow as compared to common solvent, fluorescence can be observed from different unrelaxed states of the solvent around the fluorophore in these media.<sup>168, 169, 196</sup> In the present case, with the increase in the number of hydroxyl groups on the cationic head of the ILs, the viscosity of the medium increases significantly. For example, there is an almost 7-fold increase in viscosity upon going from  $[\text{N}_{4.1.1.1}][\text{NTf}_2]$  to  $[\text{N}_{4.2\text{OH}2\text{OH}2\text{OH}}][\text{NTf}_2]$  (Table 4.3, *vide infra*). Moreover, there is also a 5-time increase (*vide infra*) in the average solvation time upon going from  $[\text{N}_{4.1.1.1}][\text{NTf}_2]$  to  $[\text{N}_{4.2\text{OH}2\text{OH}2\text{OH}}][\text{NTf}_2]$ . Due to this, the observed fluorescence may not necessarily originate from the fully solvent-equilibrated excited state of C153 in the HFILs. Therefore, no significant change in the steady-state fluorescence spectra has been observed with the increase in the number of hydroxyl groups on the cationic head of the ILs, even though one could expect an increase in the polarity of the medium.

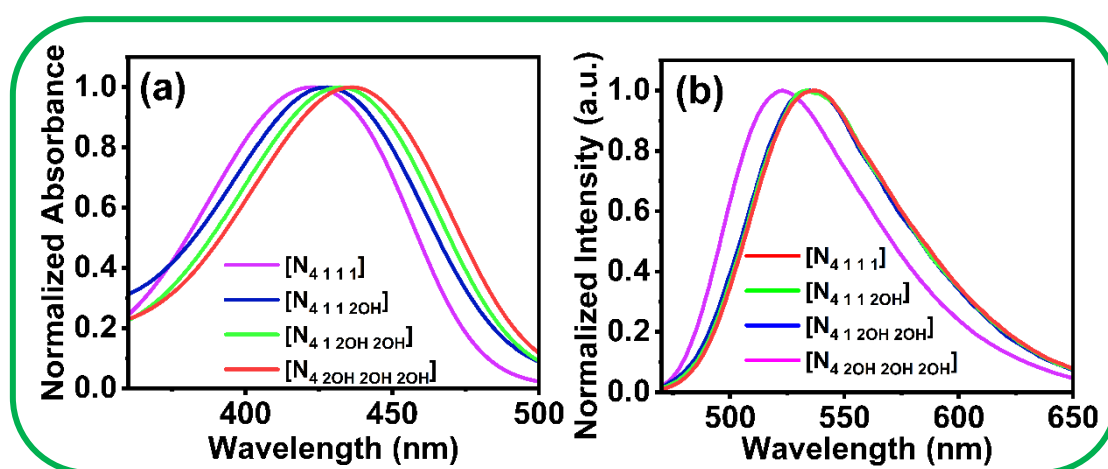


**Figure 4.1.** (a) Normalized absorption and (b) emission spectra of C153 in both non-hydroxyl and hydroxyl ILs.  $\lambda_{ex} = 405 \text{ nm}$ .

**Table 4.1.** Absorption and Emission Maxima of C153 in the concerned RTILs

System	$\lambda_{\max}(\text{abs})$ (nm)	$\lambda_{\max}(\text{ems})$ (nm)
[N <sub>4 1 1 1</sub> ][NTf <sub>2</sub> ]	423	523
[N <sub>4 1 1 2OH</sub> ][NTf <sub>2</sub> ]	428	535
[N <sub>4 1 2OH 2OH</sub> ][NTf <sub>2</sub> ]	432	535
[N <sub>4 2OH 2OH 2OH</sub> ][NTf <sub>2</sub> ]	435	536

### 4.3.2. Ultrafast Solvation Dynamics

In order to explore the complete solvation phenomena in both non-hydroxyl and hydroxyl ILs, the TCSPC technique and the FLUPS technique have been used in combination in the current study. To do this, initially, the time-dependent dynamic Stokes shift (TDDSS) of C153 in each of the relevant solvents is measured at various wavelengths at 10-nanometer intervals. Figure 4.2 shows typical FLUPS and TCSPC measurements of C153 fluorescence decay curves in [N<sub>4 1 1 1</sub>][NTf<sub>2</sub>] and [N<sub>4 1 2OH 2OH</sub>][NTf<sub>2</sub>] at three distinct wavelengths. As can be seen in Figure 4.2, the fluorescence intensity decay for C153 in both solvents exhibits a wavelength-dependent variation, with shorter wavelengths exhibiting a rapid monotonous decay and longer wavelengths exhibiting a steady rise followed by decay, both of which are indicative of the solvation process.<sup>198-205</sup> The time constant and their corresponding individual contribution are then extracted by fitting each fluorescence decay curve separately to a multiexponential decay function (equation 2.7).

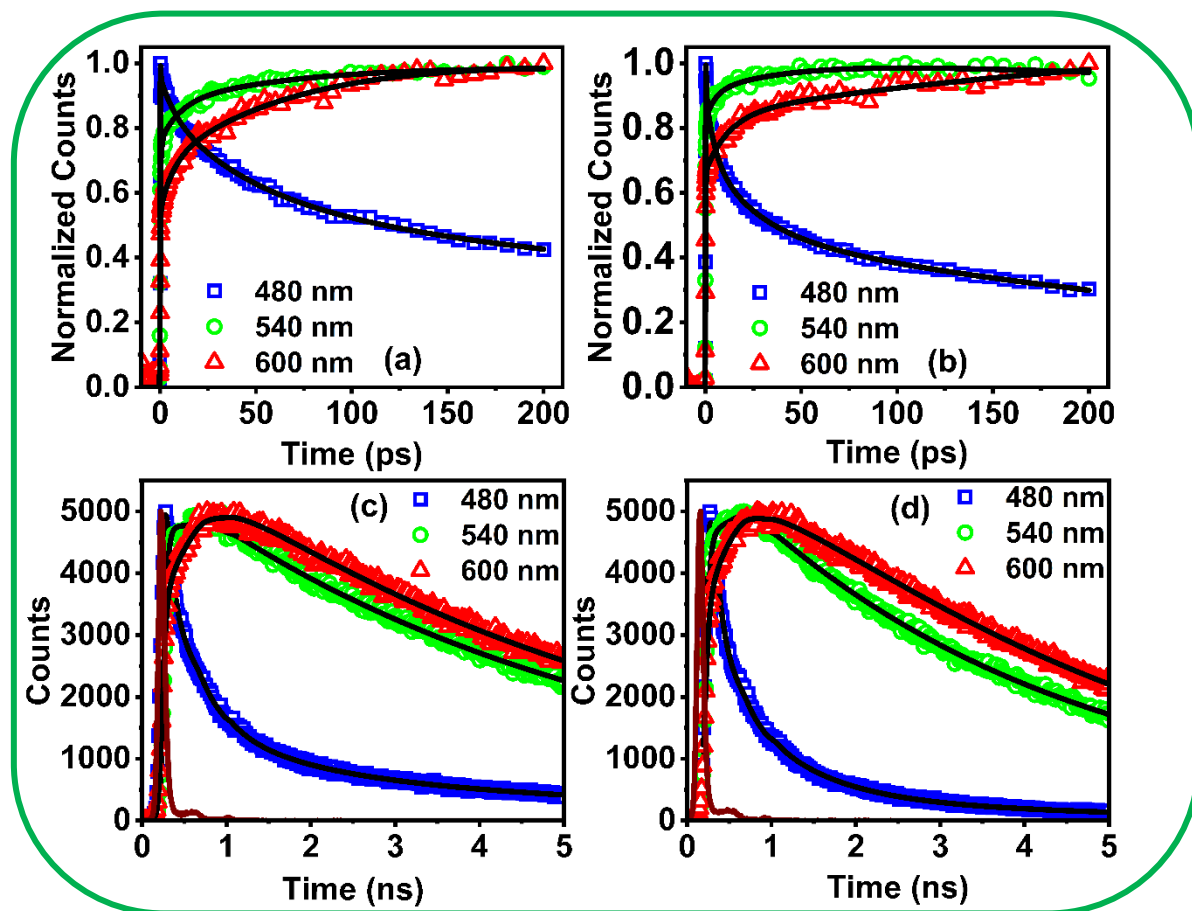


**Figure 4.2.** Fluorescence decay profiles of C153 ( $\lambda_{ex} = 405$  nm) at 298 K in  $[N_{4111}][NTf_2]$  (a, c) and  $[N_{4120H20H}][NTf_2]$  (b, d) measured through FLUPS (upper panel) and TCSPC (lower panel) techniques respectively. The solid black line represents the multiexponential fit to the data points while the solid brown line is the instrument response function (IRF).

Following this, time-resolved emission spectra (TRES) are constructed using the steady-state emission intensity and fitting parameters derived from fluorescence decay curves according to a predetermined procedure.<sup>197-200</sup> The FLUPS data are used to rebuild the TRES plots up to 100 picoseconds, while the TCSPC data are used to recreate the rest. A similar approach has also been used by other researchers to create the TRES plots in RTILs.<sup>187, 217</sup> Representative TRES plots of C153 in  $[N_{4111}][NTf_2]$  and  $[N_{4120H20H}][NTf_2]$  at eight separate time intervals are shown in Figure 4.3. (while for the rest of the solvent, the TRES plots are provided in the Appendix, Figure APX4.1). A time-dependent red shift of the emission maxima of C153 in both classes of solvent systems has been seen in Figure 4.3. This finding effectively

suggests that the excited state of the solute molecule is relaxed by the solvent, lowering the energy of the emission state of C153.<sup>198-207</sup> Following that, the temporal evolution of the peak frequencies  $\nu(t)$  was produced by fitting the TRES plots at different time intervals with a log-normal line shape function (equation 2.12). Here we would like to mention that the peak frequencies  $\nu(t)$  obtained from the log-normal fitting of the TRES plots represent the wavelength corresponding to the highest intensity and have been frequently used by many researchers to generate the solvent correlation function.<sup>202-207</sup>

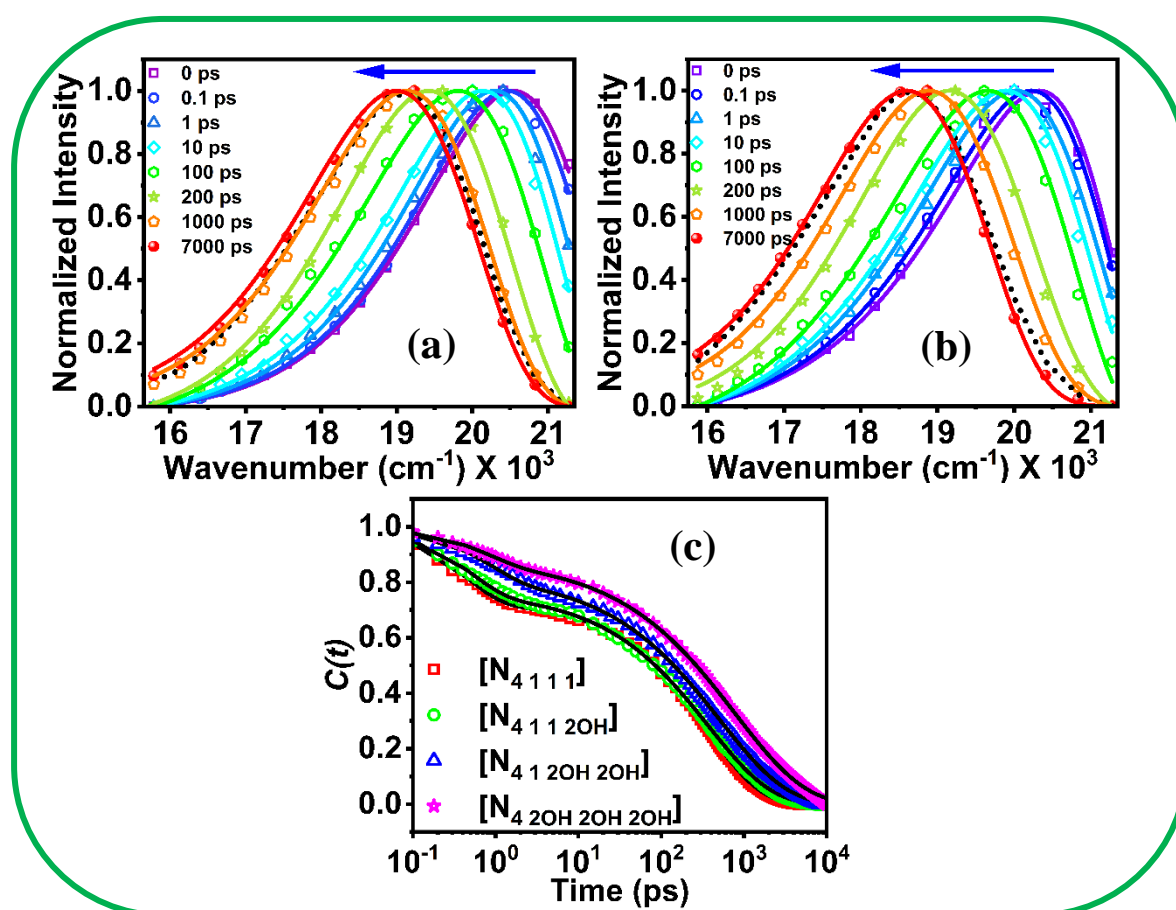


**Figure 4.3.** Normalized TRES plots at different time interval for (a)  $[N_{4111}][NTf_2]$  and (b)  $[N_{412OH2OH}][NTf_2]$ . Solid line represents the log-normal line shape fitting of the corresponding data and the dotted line represents the steady-state fluorescence spectrum of C153 in the corresponding HFILs. (c) Spectral shift correlation function  $C(t)$  decay with time at 298K for C153 in all the RTILs utilized in the study. The solid line represents fit to the data point.

In Table 4.2, the estimated peak frequencies of C153 at "time zero" ( $\nu_0^{obs}$ ) and the totally solvent equilibrated frequencies ( $\nu_\infty^{est}$ ) obtained from the fitting have been compiled.

The overall magnitudes of the dynamic Stokes shifts ( $\Delta\nu = \nu_0^{obs} - \nu_\infty^{est}$ ) for all the RTILs employed in this work are also estimated from the relevant data. Here, we note that the values of  $\Delta\nu$  in the RTILs, as determined by the TCSPC approach alone, are found to be close to 760-1250  $\text{cm}^{-1}$ . In fact, for  $[\text{N}_4\text{2OH}_2\text{OH}][\text{NTf}_2]$  with such a high viscosity value (642 cP), almost 30% of the total dynamic fluorescence Stokes shifts, as estimated through Fee and Maroncelli<sup>221</sup> method, have been missed due to the broader temporal resolution of the TCSPC instrument. The same is also found to be true for the non-hydroxyl ILs, where it has been observed that more than 50% of the total dynamic shifts were missed due to very fast relaxation. However, the entire solvent response of these RTILs can be fully realized with the aid of the FLUPS technique, which has sub-picosecond temporal resolution.<sup>217</sup> This is found to be true as the estimated  $\Delta\nu$  values using the combined TCSPC and FLUPS approaches are observed to be substantially larger (1670 - 1848  $\text{cm}^{-1}$ ) than those obtained through the TCSPC measurements. It is also crucial to note that the total dynamic fluorescence Stokes shifts for the RTILs calculated using the FLUPS and TCSPC techniques are pretty close to those reported earlier.<sup>201, 202, 217</sup> All of these findings essentially show that practically full solvent response of the RTILs to the excited state of C153 has been captured in the current investigation with the aid of both of these methods.

**Table 4.2.** Solvent relaxation parameters of all RTILs utilized in the present study at 298K

Systems	$\alpha_1$	$\tau_1$ (ps)	$\alpha_2$	$\tau_2$ (ps)	$\beta$	$\tau_{st}$ (ps)	$\vartheta_0^{obs}$ ( $10^3$ $\text{cm}^{-1}$ )	$\vartheta_\infty^{est}$ ( $10^3$ $\text{cm}^{-1}$ )	$\Delta\vartheta$ ( $10^3$ $\text{cm}^{-1}$ )
$[\text{N}_{4111}][\text{NTf}_2]$	0.27	0.45	0.73	360	0.67	478	20.45	18.78	1.67
$[\text{N}_{4112\text{OH}}][\text{NTf}_2]$	0.23	0.49	0.77	374	0.58	588	20.32	18.54	1.78
$[\text{N}_{412\text{OH}2\text{OH}}][\text{NTf}_2]$	0.17	0.72	0.83	511	0.53	890	20.33	18.50	1.83
$[\text{N}_{42\text{OH}2\text{OH}2\text{OH}}][\text{NTf}_2]$	0.12	0.76	0.88	789	0.51	1516	20.32	18.48	1.84

Thereafter, the normalized spectral shift correlation function ( $C(t)$ ) is generated from the peak frequencies obtained from the log-normal fitting of TRES using equation 2.13. Figure 4.3(c) represents the  $C(t)$  versus time plot for all the concerned RTILs. Here we would like to mention that there is a discrepancy in peak frequencies between the time range 100-600 ps, computed by FLUPS and TCSPC methods when building the plots of  $C(t)$  against  $t$  (time). This observation is not unusual since other research groups<sup>187, 217</sup> studying the solvation dynamics of C153 in RTILs and DESs have also noted a similar type of disparity between these two approaches, and the mismatch between these two approaches is addressed by using a literature strategy as recommended by Maroncelli and co-workers.<sup>217</sup> According to Figure 4.3(c), roughly 20% of the total solvent response for  $[N_{4.1.1.1}][NTf_2]$  and  $[N_{4.1.1.2OH}][NTf_2]$  is observed to be completed within 500 fs, compared to about 10% for  $[N_{4.1.2OH.2OH}][NTf_2]$  and  $[N_{4.2OH.2OH.2OH}][NTf_2]$ . These findings essentially show that the solvent-mediated relaxation of C153 in the excited state includes a very fast (ultrafast) initial solvation component. Moreover, the rise in the cationic size of the HFILs with subsequent additions of hydroxyl functionality to the cationic head may also cause a decrease in the contribution of the ultrafast component. While examining the ultrafast solvation dynamics of alkyl-imidazolium and pyrrolidinium-based RTILs with different chain lengths on the cationic head, Zhang et al.<sup>217</sup> have also offered a similar argument to rationalize the observation.

In order to gain additional insight into the solvent relaxation phenomena and quantitatively characterize the time evolution of peak frequencies,  $C(t)$  versus  $t$  plot has been fitted to a sum of single exponential as well as a stretched exponential function (equation 2.16), while equation 2.17 estimates the integral time associated with the stretched exponential component. Table 4.2 provides a summary of the relevant fit parameters that are derived by fitting the  $C(t)$  versus *time* plots using equation 2.16. From Table 4.2, it can be noticed that

there are two separate solvation time components for all the RTILs, a small amplitude ultrafast time component with a sub-picosecond time scale (0.4-0.8 ps) and a somewhat slower time component (478-1516 ps) linked to a greater amplitude. While analyzing the entire solvent response in various types of RTILs of comparable viscosity, many groups reported similar kinds of values for the ultrafast component as well as for the slower component.<sup>202-207</sup> As can be seen from Table 4.2, the substantially longer time component is associated with a stretched exponent ( $\beta$ ) whose values (0.67-0.51) are less than unity for the RTILs, demonstrating that the slower relaxation time component has a broader distribution. Previously, it was proposed that for heterogeneous media such as DESs and RTILs, the deviation of the value of  $\beta$  from unity arises due to heterogeneous diffusional motion that differs from the classical hydrodynamic motion of the constituent ions, and the extent of the deviation of the  $\beta$  value from unity also appears to be correlated with the degree of the medium's heterogeneity.<sup>187, 217</sup> In light of the aforementioned arguments, the current observation of the deviation of the  $\beta$  value from unity for The RTILs can be explained by taking into account of the micro-heterogeneous nature of these media. Furthermore, it is clear from Table 4.2 that the more hydroxyl groups that are added to the cationic head of the RTILs, the greater the deviation of  $\beta$  value from unity. This result basically indicates that the heterogeneity of the medium increases with an increase in the number of hydroxyl groups at the cationic head. Now coming to the integral time associated with the slower component, one can notice a substantial change in  $\tau_{st}$  values with consecutive addition of the hydroxyl group to the cationic head. This increase in  $\tau_{st}$  values is in accordance with the increase in the bulk viscosity of the medium. It has been suggested in earlier studies of solvation dynamics on RTILs that the value of  $\tau_{st}$  denotes the average solvation time of a concerned medium and that the values closely correspond to the bulk viscosity of the given medium. Both experimental and computer simulation studies have pointed out that the slower component of the solvent relaxation process is associated with the

diffusional motions of the constituents of the concerned solvent.<sup>202-215</sup> Thus, this relationship between the slow solvation time component and viscosity likely reflects the fact that the slower solvation time component is linked to the bulk structural relaxation of the solvents. However, upon a more careful look at Table 4.2, one can notice that upon going from  $[N_{4\ 1\ 1\ 1}][NTf_2]$  to  $[N_{4\ 2OH\ 2OH\ 2OH}][NTf_2]$ , the increase in viscosity is almost 7 times, whereas the increase in  $\tau_{st}$  values is nearly 3 times. This disproportionate change in  $\tau_{st}$  values with the medium viscosity indicates the decoupling of the solvation times from the viscosity of the medium. Similar decoupling of average solvation time from medium viscosity has already been reported by various research groups.<sup>175-183</sup> This decoupling of the long solvation time component from medium viscosity essentially indicates that the long solvation time component is associated with the heterogenous diffusional motion of the constituent of the HFILs outside the first solvation shell.<sup>202-220</sup>

Now when we consider the initial rapid solvent relaxation, it can be noticed that for  $[N_{4\ 1\ 1\ 1}][NTf_2]$  and  $[N_{4\ 1\ 1\ 2OH}][NTf_2]$ , the ultrafast solvation time component is almost identical. Additionally, with further addition of hydroxyl groups to the cationic head, a marginal change in the ultrafast solvation time component has been observed in  $[N_{4\ 1\ 2OH\ 2OH}][NTf_2]$  and  $[N_{4\ 2OH\ 2OH\ 2OH}][NTf_2]$ . However, a closer look at the data (Table 4.2) indicates that the estimated ultrafast solvation time component is almost independent of the viscosity of the medium. Previous works by various researchers on ultrafast solvation dynamics in confined media like RTILs and DESs have also pointed out that the ultrafast time component is independent of the medium viscosity.<sup>202-220</sup> This observation essentially suggests that the motion related to the ultrafast solvation relaxation does not involve any centre of mass diffusion of the constituents of the solvents. Several experimental and simulation studies have suggested that the observed ultrafast relaxation process is caused by different fast local motions such as dipolar rotation,

vibration, libration, translation, and so on.<sup>175-182, 215-220</sup> Thus, in the present case also, without assigning any particular solvation mechanism, the observed sub-picosecond solvation components can be assigned to various fast local motions of the solvent at the immediate vicinity of the excited state of the solute. Another important parameter of the ultrafast solvation relaxation is amplitude associated with the sub-picosecond time constant. Upon going from [N<sub>4</sub> 1 1 1][NTf<sub>2</sub>] to [N<sub>4</sub> 1 1 2OH][NTf<sub>2</sub>], a gradual decrease in the amplitude of the sub-picosecond component has also been observed in all the concerned RTILs. Here we would like to note that Maroncelli and co-workers<sup>217</sup> have demonstrated that the amplitude of the ultrafast component decreases with an increase in the alkyl chain length on imidazolium and pyrrolidinium-based RTILs. Moreover, Samanta and co-workers<sup>187</sup>, while working on tetraalkylammonium-based DESs, have also observed that the amplitude of the ultrafast component is inversely related to the cationic size of the DESs [45]. Considering the above arguments, in the present study, it would be reasonable to deduce that the decrease in amplitude of the ultrafast component in this scenario might have happened due to a rise in the cationic size of the RTILs with the subsequent addition of hydroxyl groups to the cationic head.

### 4.3.3. Rotational Relaxation Dynamics

To get a more comprehensive understanding of the nature of solute-solvent interaction and microscopic structural organization of the given liquid system, we have investigated the rotational dynamics of some selected probes in concerned RTILs through time-resolved fluorescence anisotropy measurement. Figure 4.4 displays representative time-resolved fluorescence anisotropy decays for Perylene and MPTS at 298 in both the non-hydroxyl and hydroxyl functionalized ILs. The rotational reorientation time ( $\tau_r$ ) at various temperatures has been estimated by fitting the anisotropy decay data of perylene and MPTS to single and bi-exponential functions, respectively. The bulk viscosity of the relevant media and the estimated

$\tau_r$  values for perylene and MPTS at different temperatures (298K to 323K) have been tabulated in Table 4.3.

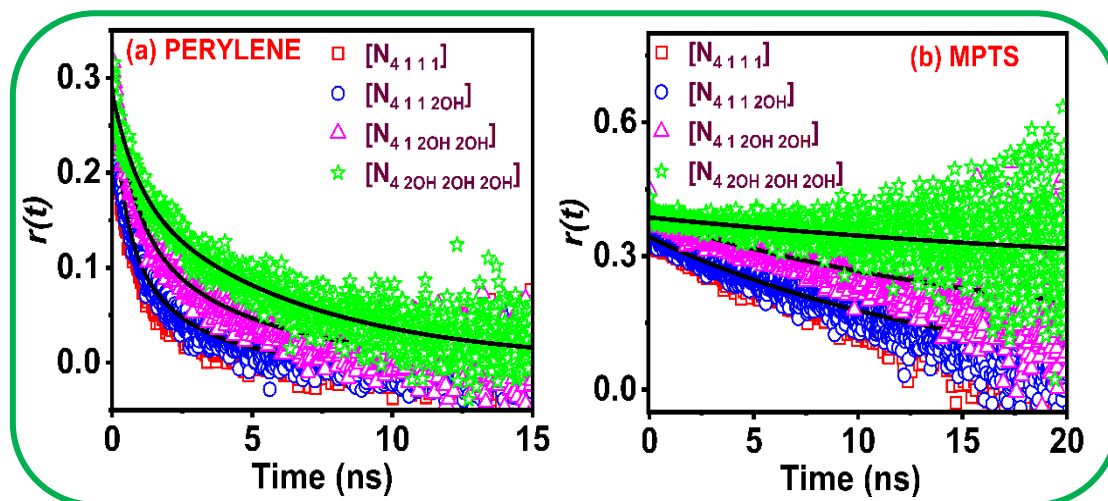


**Figure 4.4.** Time-resolved fluorescence anisotropy decay for (a) perylene and (b) MPTS in all the RTILs at 298 K.

From Figure 4.4, one can notice that for a given probe molecule, the anisotropy decay is found to be much faster in the non-hydroxyl IL than the hydroxyl ILs due to the relatively lower viscosity of the former than the latter. Moreover, the anisotropy decays of both perylene and MPTS are found to be slowest in  $[N_4 2OH 2OH 2OH][NTf_2]$ . This is because of its very high viscosity owing to the extensive intra/intermolecular hydrogen bonding interaction in the IL. Similarly, for a given set of IL, one can notice that the rotational diffusion of perylene is found to be much faster than that of MPTS. This observation is further supported by the fact that the estimated  $\tau_r$  values of MPTS (Table 4.3) for a given RTIL at a particular temperature are found to be  $\sim 8$  to 14 times higher than the same for perylene. This data essentially shows that the solvent molecules significantly impede the rotational diffusion of MPTS, possibly as a result of strong solute-solvent intermolecular interactions. However, upon a careful inspection of the data, one can notice that the  $\tau_r$  value does not vary proportionately with the increase in the value of the bulk viscosity of the concerned medium. For example, upon going from  $[N_4 1 1 1][NTf_2]$  to  $[N_4 2OH 2OH 2OH][NTf_2]$  though there is a  $\sim 7$ -fold increase in the bulk viscosity of

---

---

the medium, the estimated increase in  $\tau_r$  value is only  $\sim 5$  and  $2$  times for perylene and MPTS respectively. This preliminary analysis shows that the frictions experienced by both the probes in the hydroxyl and non-hydroxyl ILs are significantly different from each other.

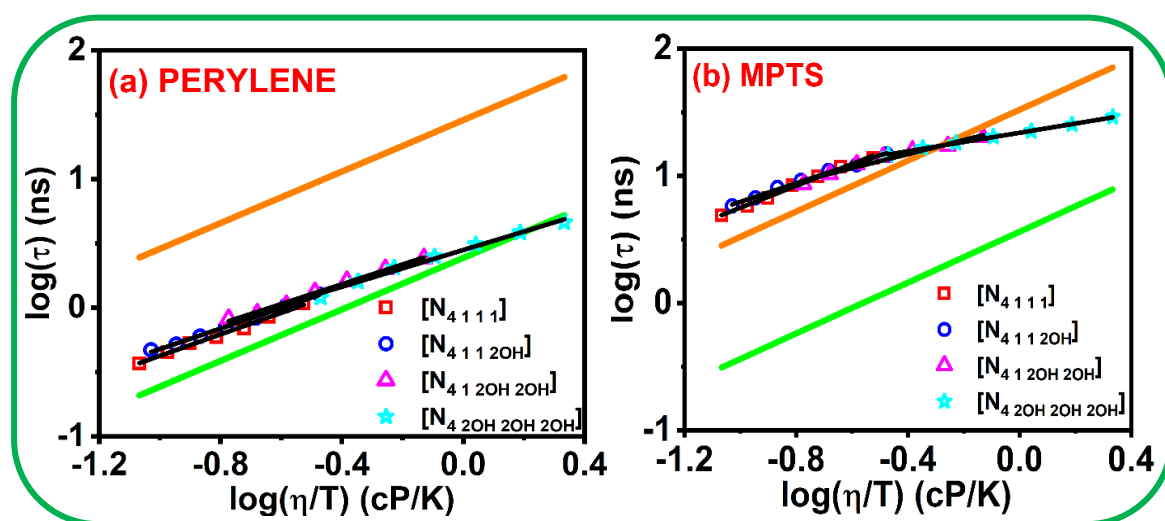
In order to throw more light on the above findings, the anisotropy decay of both perylene and MPTS have also been investigated at iso-viscous conditions by adjusting the temperatures of the concerned media so that apart from viscosity, the role of various intra/intermolecular interactions between solute and the ILs in governing the rotational diffusion of the probe solute can be understood. From Table 4.4, one can also notice that at iso-viscous conditions, the estimated  $\tau_r$  values for perylene are found to be almost comparable in all the ILs under investigation. This observation essentially suggests that perylene, which locates itself in the non-polar alkyl region of these ILs, experiences a similar micro-environment in both non-hydroxyl and hydroxyl ILs, and the introduction of hydroxyl groups in the ILs does not alter the alkyl region of the ILs significantly. Interestingly, appreciable change in the experimentally observed  $\tau_r$  values for MPTS under the same condition have been observed upon going from  $[\text{N}_{4,1,1,1}][\text{NTf}_2]$  to  $[\text{N}_{4,2\text{OH},2\text{OH},2\text{OH}}][\text{NTf}_2]$ , indicating a significant changes in the structural organization and intra/intermolecular interaction in the polar region of the ILs with the introduction of hydroxyl functionalities in the cation head of the ILs. This is a very interesting observation, and to get more detailed information regarding the solute-solvent/solvent-solvent interaction and microstructural organization of both non-hydroxyl and hydroxyl ILs, the rotational relaxation data have been analyzed in light of the Stokes-Einstein-Debye (SED) equation (equation 1.1).<sup>193, 277</sup>

**Table 4.3.** Rotational relaxation parameters of perylene and MPTS in all the RTILs at two different temperatures.

System	$\eta$ (cP)/T (K)	Perylene		MPTS	
		$\tau_r$ (ns)	$C_{obs}$ (avg.)	$\tau_r$ (ns)	$C_{obs}$ (avg.)
[N <sub>4111</sub> ][NTf <sub>2</sub> ]	88.9/(298)	1.08		13.8 ± 0.2	
	69.3/(303)	0.85		11.8 ± 0.21	
	58.5/(308)	0.69	0.14 ± 0.01	9.9 ± 0.2	1.59 ± 0.06
	48.1/(313)	0.59		8.4 ± 0.2	
	39.9/(318)	0.53		6.7 ± 0.19	
	34.3/(323)	0.45		5.8 ± 0.19	
	28.1/(328)	0.37		4.9 ± 0.19	
[N <sub>4112OH</sub> ][NTf <sub>2</sub> ]	99.7/(298)	1.28		14.9 ± 0.27	
	79.1/(303)	1.04		12.2 ± 0.26	
	63.8/(308)	0.83	0.15 ± 0.01	11 ± 0.26	1.65 ± 0.05
	51.7/(313)	0.71		9.2 ± 0.24	
	43.2/(318)	0.60		8.1 ± 0.22	
	36.6/(323)	0.52		6.7 ± 0.22	
	30.7/(328)	0.47		5.8 ± 0.22	
[N <sub>412OH2OH</sub> ][NTf <sub>2</sub> ]	221.1/(298)	2.42		20.1 ± 0.29	
	167.8/(303)	2.0		17.2 ± 0.27	
	127.5/(308)	1.61	0.14 ± 0.01	15.8 ± 0.28	0.95 ± 0.05
	101.7/(313)	1.32		14.1 ± 0.27	
	83.1/(318)	1.05 ± 0.02		12.3 ± 0.24	
	67.7/(323)	0.9 ± 0.03		10.3 ± 0.24	
	55.3/(328)	0.82 ± 0.03		8.6 ± 0.24	
[N <sub>42OH2OH2OH</sub> ][NTf <sub>2</sub> ]	642.2/(298)	4.6 ± 0.06		29 ± 0.32	
	467/(303)	3.84 ± 0.06		25.3 ± 0.33	
	338.8/(308)	3.1 ± 0.05	0.11 ± 0.01	22.4 ± 0.32	0.80 ± 0.05
	252.4/(313)	2.5 ± 0.04		20.3 ± 0.28	
	188.4/(318)	2.05 ± 0.03		18.1 ± 0.26	
	145.2/(323)	1.6 ± 0.03		16.6 ± 0.24	
	111.2/(328)	1.2 ± 0.03		14.5 ± 0.24	

**Table 4.4.** Rotational relaxation parameters of perylene and MPTS in all the RTILs at iso-viscous condition.

Systems	$\eta$ (cP)	$\tau_r$ (ns) (perylene)	$\tau_r$ (ns) (MPTS)
[N <sub>4</sub> 1 1 1][NTf <sub>2</sub> ]		1.08	13.8
[N <sub>4</sub> 1 1 2OH][NTf <sub>2</sub> ]	88.9	1.13	13.3
[N <sub>4</sub> 1 2OH 2OH][NTf <sub>2</sub> ]		1.11	12.6
[N <sub>4</sub> 2OH 2OH 2OH][NTf <sub>2</sub> ]		1.09	12.2

**Figure 4.5.** log- log plot of  $\tau_r$  versus  $\eta/T$  of (a) perylene and (b) MPTS in all the RTILs. Solid orange and green line represent the stick and slip boundary condition respectively. Solid black line represents linear fit to the data points.

The SED plots of both perylene and MPTS in all the RTILs are provided in Figure 4.5. Inspection of the SED plot of perylene (Figure 4.5 (a)) reveals that the rotational diffusion of perylene follows slip hydrodynamic behaviour in all the RTILs. We note here that Dutt and co-workers have reported a comparable slip hydrodynamic behaviour for 9-phenylanthracene while examining the rotational diffusion of the nonpolar probe in several RTILs.<sup>226-231</sup> Additionally, in imidazolium-based ionic liquids, Fayer and co-workers have also stated the slip hydrodynamic behaviour of perylene.<sup>233</sup> It has been well documented that in the absence of any specific solute-solvent interaction, the rotational motion of a medium-sized solute (e.g.

perylene, 9-phenylanthracene, etc.) usually follows slip hydrodynamic behaviour. This finding suggests that perylene, which is located in the hydrophobic region, does not suffer any particular solute-solvent interaction and hence follows slip hydrodynamic behaviour in all the RTILs. This observation is further supported when the solute-solvent coupling constant ( $C_{obs}$ ) values for perylene are analyzed. The  $C_{obs}$  value is expressed as the ratio between the experimentally measured  $\tau_r$  value and theoretically calculated  $\tau_r$  value, and represents the extent of solute-solvent interaction. Because  $C_{obs}$  value is calculated using the aforementioned ratio, the value of  $C_{obs}$  usually indicates the degree of solute-solvent interaction by removing the effects of viscosity and temperature. From Table 4.3, it can be noticed that the  $C_{obs}$  values (0.15-0.11) for perylene are found to be almost identical in all the RTILs used in this study. This essentially indicates that perylene experiences a similar microenvironment in all the RTILs. This further indicates that the introduction of successive hydroxyl groups to the cationic head does not alter the hydrocarbon (apolar) dominated molecular region of these RTILs significantly.

Now to see what happens in the polar region (ionic region) of the concerned RTILs, the rotational relaxation behaviour of MPTS is monitored in these media. From the log-log plot of  $\tau_r$  versus  $\eta/T$  (Figure 4.5 (b)), it can be seen that the rotational motions of MPTS in all the RTILs are close to the stick hydrodynamic prediction indicating hindered solute rotation in these media. A close examination of the SED plot of MPTS reveals that the rotational behaviour of MPTS in  $[N_{4111}][NTf_2]$  and  $[N_{4112OH}][NTf_2]$  lies beyond the stick line. This type of behaviour, as per hydrodynamic terminology, is known as super-stick behaviour.<sup>229, 233</sup> Here, it is important to mention that observation of super-stick behaviour is not uncommon, and previously, it has been observed by many researchers while investigating the rotational dynamics of ionic solutes in RTILs and DESs.<sup>185-187, 226-231</sup> Dutt and co-workers have reported similar super-stick behaviour of rhodamine 110 in imidazolium-based ionic liquids.<sup>229</sup>

Likewise, Fayer and co-workers have also observed similar super-stick behaviour of MPTS in imidazolium-based ILs.<sup>233</sup> They have ascribed this super-stick behaviour of MPTS to the hydrogen bonding interaction between the acidic C2 hydrogen of the imidazolium cation and MPTS, as well as the electrostatic interaction between the probe and the cation of the RTILs. Based on the information thus far, it can be reasonable to infer that MPTS, being negatively charged, are mostly involved in electrostatic interactions with the cation of the RTILs, although they can also be involved in specific hydrogen bonding interactions in the presence of acidic hydrogen in the cationic moiety of the RTILs. Taking this into account, the super-stick behaviour for  $[\text{N}_{4111}][\text{NTf}_2]$  is predominantly due to electrostatic interaction, but that for  $[\text{N}_{4112\text{OH}}][\text{NTf}_2]$  is due to both electrostatic and solute-solvent specific hydrogen bonding interaction. Additionally, a comparable or even larger extent of super-stick behaviour for  $[\text{N}_{412\text{OH}2\text{OH}}][\text{NTf}_2]$  and  $[\text{N}_{42\text{OH}2\text{OH}2\text{OH}}][\text{NTf}_2]$  might be anticipated with an increase in the number of hydroxyl groups on the cationic head due to availability of more number of solute-solvent specific hydrogen bonding interaction sites. In contrast, the rotational behaviour of MPTS in both the above mention solvent lies somewhat below the stick line. This observation can be more clearly understood by looking at the estimated  $C_{obs}$  values for MPTS in these solvents. As can be seen from Table 4.3, the average  $C_{obs}$  value (1.6-1.65) of MPTS is almost similar in  $[\text{N}_{4111}][\text{NTf}_2]$  and  $[\text{N}_{4112\text{OH}}][\text{NTf}_2]$ . However, successive addition of hydroxyl group to the cationic head gradually decreases the average  $C_{obs}$  values (Table 4.3) for MPTS as observed in  $[\text{N}_{412\text{OH}2\text{OH}}][\text{NTf}_2]$  and  $[\text{N}_{42\text{OH}2\text{OH}2\text{OH}}][\text{NTf}_2]$ . In fact, the  $C_{obs}$  values for MPTS are found to decrease by 50% upon going from  $[\text{N}_{4111}][\text{NTf}_2]$  to  $[\text{N}_{42\text{OH}2\text{OH}2\text{OH}}][\text{NTf}_2]$ . This clearly indicates that the specific solute-solvent interaction is relatively weaker in the RTILs having greater number of hydroxyl groups. Here we would like to emphasize that the extent of the solute-solvent specific hydrogen bonding interaction has a considerable influence on the  $\tau_r$  value of a rotating solute.<sup>226-231</sup> If the specific hydrogen bonding interaction is sufficiently

strong and persists throughout the molecular rotation, the rotation of the solute becomes slower. However, if there is any flexibility in the hydrogen bonding interaction between solute and solvent in relation to the angular rotation of the solute, there will be no impact on the rotation of molecules. In this context, works by Ludwig and co-workers are worth mentioning.<sup>294-297</sup> Through molecular dynamic simulation and neutron diffraction techniques, they have shown that cooperative hydrogen bonding interaction in hydroxyl functionalized ionic liquids can overcome the columbic interaction and can result in hydrogen-bonded cation clusters, which ultimately influence the structure and property of these ILs. Furthermore, they have also noted that the cation-cation hydrogen bonding interaction for hydroxyl functionalized pyridinium-based ionic liquids is 0.96 to 3.96 kJ/mol stronger than the corresponding cation-anion hydrogen bonding interaction.<sup>295</sup> Previously, it has also been suggested that short alkyl moieties surrounding the positively charged core organized themselves in a roughly spherical geometry and subsequently shield the positive charge, which also results in dynamic ion cluster formation.<sup>29</sup> Both experimentally and theoretically, similar ion cluster formations in RTILs have been demonstrated in previous literature reports.<sup>155-157, 294-297</sup> Considering this, a similar ions cluster formation and shielding of the positive charge of the cation can also be expected in the present case with the increase in the number of hydroxyl functionality around the cationic head which may further reduce the extent of solute-solvent interaction. In view of this, in the present scenario, the faster rotational diffusion of MPTS in  $[N_{4.1}2OH_{2OH}][NTf_2]$  and  $[N_{4.2OH_{2OH}2OH}][NTf_2]$  can be rationalized by considering a combined effect of reduced solute-solvent interaction due to cationic cluster formation and shielding of the positive charge on the cationic head as well as stronger solvent-solvent hydrogen bonding interaction than solute-solvent interaction.

To get further information about the nature and extent of solute-solvent/solvent-solvent interaction, we have fitted the  $\tau_r$  value of perylene and MPTS against temperature-reduced viscosity ( $\eta/T$ ) in all solvents using a power-law relationship ( $\tau_r = A(\eta/T)^p$ , equation 3A.1). Table 4.5 contains the values of  $A$  and  $p$  that were determined from the empirical fitting of the rotational relaxation data. As can be seen from Table 4.5, the value of  $A$  ( $=vfc/k$ ) remains almost same for perylene, whereas a substantial decrease (almost 50%) in  $A$  value is observed for MPTS upon increase in the number of hydroxyl groups on the cationic head of the RTILs. This decrease in the  $A$  value essentially indicates the decrease in the boundary condition parameter.<sup>228-231, 274, 276</sup> Furthermore, Table 4.5 shows that for all of the RTILs utilized in the study, the value of  $p$  considerably deviates from unity for both perylene and MPTS. Here it is pertinent to mention that similar fractional viscosity dependence of  $\tau_r$  have been observed by different researchers, including us, in confined media like DESs and RTILs.<sup>173, 228-231, 273, 274, 276, 282, 284</sup> Additionally, it has also been reported that the viscosity-diffusion decoupling and dynamic heterogeneity of the medium increase in proportion to the departure of  $p$  from unity.<sup>176, 273</sup> All the prior reports have essentially shown that the distribution of relaxation rates for molecules residing in various local environments in organized media, such as ILs, is what causes the dynamic heterogeneity in that medium.<sup>181-183, 229, 231, 274</sup> Moreover, it has already been shown for hydroxyl ILs that non-Brownian motions, such as orientational leaps and hydrogen bond fluctuations, are the origin of decoupling of  $\tau_r$  value from medium viscosity<sup>181-183, 185, 186, 242</sup>. Taking into account of the foregoing explanation, the divergence of  $p$  from unity in the present scenario as well indicates the dynamic heterogeneity of the medium because of the fluctuation of the hydrogen bonding network and the inertia-driven motion, which differs from typical Brownian motions.

**Table 4.5.** Parameters  $A$  and  $p$  obtain from the fits of  $\log \langle \tau_r \rangle$  vs  $\log \langle \eta/T \rangle$ 

System	Perylene		MPTS	
	$A$	$p$	$A$	$p$
[N <sub>4 1 1 1</sub> ][NTf <sub>2</sub> ]	2.95 ± 0.16	0.84 ± 0.05	40.74 ± 1.60	0.86 ± 0.03
[N <sub>4 1 1 2OH</sub> ][NTf <sub>2</sub> ]	3.02 ± 0.18	0.80 ± 0.04	33.88 ± 1.47	0.73 ± 0.02
[N <sub>4 1 2OH 2OH</sub> ][NTf <sub>2</sub> ]	2.88 ± 0.16	0.77 ± 0.03	24.55 ± 1.25	0.55 ± 0.02
[N <sub>4 2OH 2OH 2OH</sub> ][NTf <sub>2</sub> ]	2.75 ± 0.13	0.72 ± 0.03	21.88 ± 1.21	0.36 ± 0.02

As can be seen from Table 4.5, there is a marginal decrease in the  $p$  value (0.84-0.72) upon going from [N<sub>4 1 1 1</sub>][NTf<sub>2</sub>] to [N<sub>4 2OH 2OH 2OH</sub>][NTf<sub>2</sub>]. This observation indicates that in the absence of any specific solute-solvent interaction, the relaxation rates of perylene in the hydrocarbon-dominated region do not alter significantly upon successive addition of hydroxyl group to the cationic head. This further suggests that dynamic heterogeneity felt by perylene in the molecular region is more or less similar in all the RTILs. Now focusing on the polar/ionic region, a marginal change in  $p$  values for MPTS has been observed upon going from [N<sub>4 1 1 1</sub>][NTf<sub>2</sub>] to [N<sub>4 1 1 2OH</sub>][NTf<sub>2</sub>]. However, with further addition of hydroxyl functionality to the cationic head, a drastic decrease in  $p$  value can be observed. In fact, a ~45% decrease in  $p$  value upon going from [N<sub>4 1 1 1</sub>][NTf<sub>2</sub>] to [N<sub>4 2OH 2OH 2OH</sub>][NTf<sub>2</sub>] is observed. This larger deviation of  $p$  value from unity for MPTS indicates a larger distribution of the relaxation rates in the poly-hydroxyl ILs as compared to the non-hydroxy IL. This further point out that with successive addition of hydroxyl functionality to the cationic head, there is a significant increase in dynamic heterogeneity of the medium.

## 4.3.4. FCS Studies

To get further insight into the probe diffusion dynamics in the respective solvents and intermolecular solute-solvent interaction at the single molecular level, FCS studies are also employed in the current investigations. The fluorescence correlation decay curves ( $G(\tau)$ ) of perylene and MPTS in  $[N_{4111}][NTf_2]$  are depicted in Figure 4.6(a) and (b) as representative examples. The FCS decay curves are fitted through a two-component diffusion model as the single-component diffusion model does not give a reasonable fit (Appendix, Figure APX4.2). The fitted FCS decay curves for both the probe solute in the rest of the RTILs are provided in the Appendix (Figure APX4.3 and Figure APX4.4), while the normalized FCS decay curve of both probes in all the relevant RTILs are provided in Figure 4.6 (c) and (d).

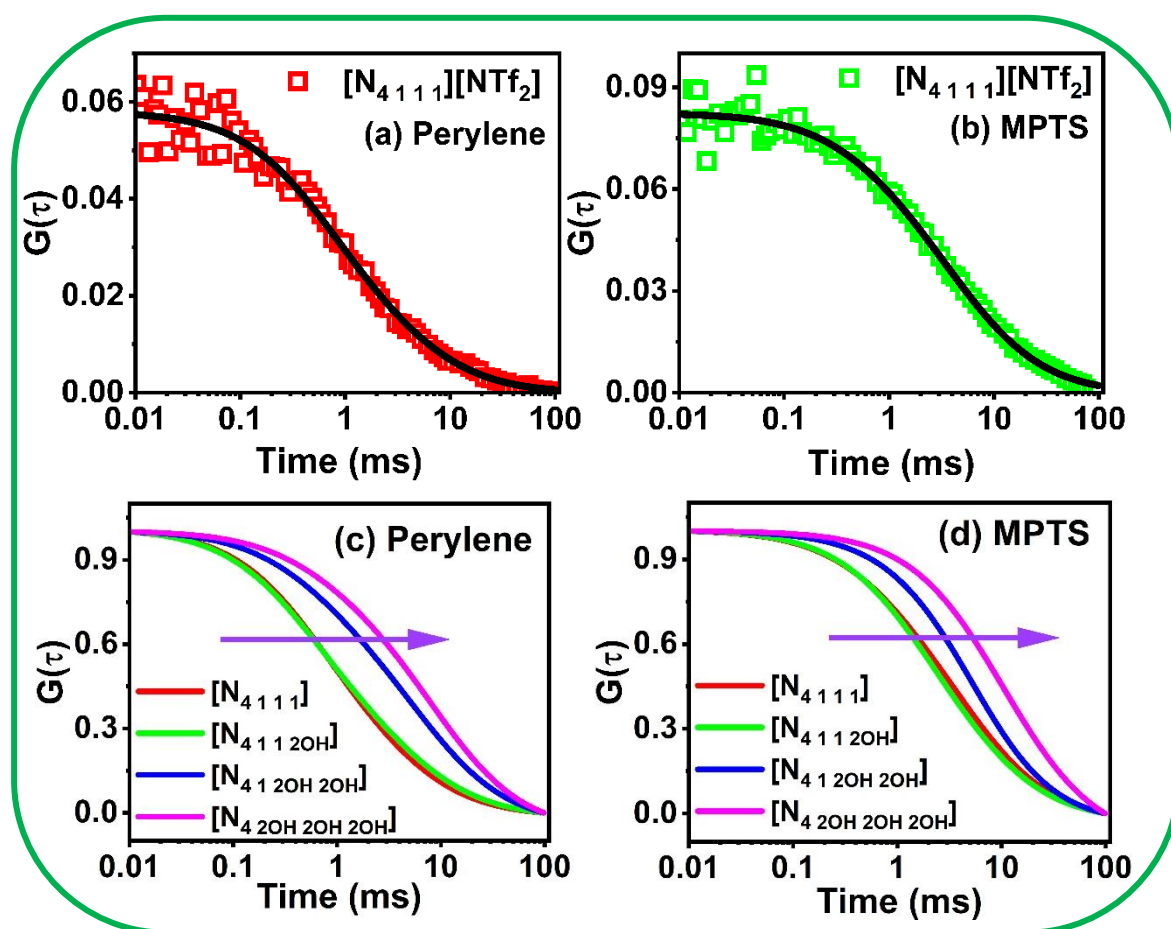


**Figure 4.6.** Plot of  $G(\tau)$  vs time for (a) Perylene and (b) MPTS in  $[N_{4111}][NTf_2]$ . (c) and (d) are the normalized FCS decay curve for perylene and MPTS respectively in the relevant RTILs.

**Table 4.6.** Estimated translational diffusion coefficient ( $D_t$ ) in  $\mu\text{m}^2/\text{s}$  along with their contribution value for perylene and MPTS in all the relevant RTILs

Systems	Perylene				MPTS			
	$\alpha_1$	$D_1$	$D_2$	$D_{avg}$	$\alpha_1$	$D_1$	$D_2$	$D_{avg}$
[N <sub>4</sub> 111][NTf <sub>2</sub> ]	0.62	26.7	2.9	17.7	0.44	10.0	2.5	5.8
[N <sub>4</sub> 112OH][NTf <sub>2</sub> ]	0.6	23	2.8	15	0.68	7.2	1.8	5.5
[N <sub>4</sub> 12OH2OH][NTf <sub>2</sub> ]	0.34	19.7	1.9	7.9	0.71	2.3	1.2	2.8
[N <sub>4</sub> 2OH2OH2OH][NTf <sub>2</sub> ]	0.29	9.3	1.3	3.7	0.7	1.5	0.8	1.6

Table 4.6 contains all of the pertinent fitting parameters that are derived from the bimodal fit of the FCS Traces. In this context, it is worth noting that Guo et al.<sup>245</sup> have observed a similar bimodal diffusion behaviour of rhodamine 6G in a series of pyrrolidinium ionic liquids. In addition, Samanta and co-workers<sup>246</sup> have also reported the suitability of the bimodal diffusion model for some selected fluorophores in several RTILs. Many other researchers working on confined media, such as DESs and RTILs, have also documented similar bimodal diffusion of ionic solutes.<sup>182-184, 243, 244</sup> All of these results effectively show that the bimodal diffusion of fluorophores arises due to the spatial heterogeneity of RTILs, and due to which molecular translational motions occur in two separate regions, namely apolar (domain created by alkyl tails of the ILs) and polar (domain form by ionic constituents) regions with a continuity in the domain structure of the RTILs whose length scale is more than the confocal dimension.<sup>245</sup> However, it has also been previously demonstrated that the FCS analysis may disclose a bimodal diffusion behaviour of a solute in less viscous ILs and DESs, despite the fact that no excitation wavelength dependence of steady-state fluorescence emission was seen.<sup>185, 246</sup> This suggests that bimodality in diffusion is not necessarily totally determined by solution's spatial heterogeneity and may result from the inherent temporally heterogeneous dynamics of the

medium.<sup>181-184</sup> Moreover, when the two translational diffusion time constants are not particularly comparable, as in the present case, even if molecules switch between the domains in the observation volume, two diffusion values should be obtained. Because of this, the concept of several solutes diffusing in various microscopic domains with divergent relaxation periods may no longer be required to explain anomalous or multiexponential relaxation kinetics at long times.<sup>181</sup> Therefore, in such cases, the heterogeneous translational diffusion motion of the solutes is most preferably described by the average translational diffusion relaxation rates. Considering this, as done previously, in the present study also, we have particularly focused on the average translational diffusion coefficient of the solute molecules to understand the solute-solvent interaction at single molecular level.<sup>181-184</sup>

One can see from Table 4.6 that the translational diffusion of perylene is found to be substantially faster (by around two to three times) than that of MPTS in any given solvent. This is due to the fact that perylene does not encounter any particular solute-solvent interaction in RTILs, which causes its diffusion to be much faster in that solvent. In contrast, MPTS is well known to engage in strong electrostatic and solute-solvent specific hydrogen bonding interactions (in the presence of acidic hydrogen), which eventually restrict its mobility. As hydroxyl groups are subsequently added to the cationic head, the bulk viscosity of the medium progressively rises, resulting in a continuous decrease in the  $D_{avg}$  values for both fluorophores. Additionally, the  $D_{avg}$  value for any particular probe is found to be highest in  $[N_{4111}][NTf_2]$  and lowest in  $[N_{42OH2OH2OH}][NTf_2]$ . This is due to the lower viscosity of the former than the latter. Upon a careful look at the data in Table 4.6, one can notice that there is almost 5-fold decrease in  $D_{avg}$  for perylene upon going from  $[N_{4111}][NTf_2]$  to  $[N_{42OH2OH2OH}][NTf_2]$ , whereas the increase in the bulk viscosity is estimated to be more than 7-fold (Table 4.3). On the other hand, for MPTS decrease in  $D_{avg}$  is found to be  $\sim 3.5$  fold upon going from  $[N_{4111}$

$_{1}][\text{NTf}_2]$  to  $[\text{N}_{4,2\text{OH},2\text{OH},2\text{OH}}][\text{NTf}_2]$ . This disproportionate change in  $D_{avg}$  with viscosity upon going from  $[\text{N}_{4,1,1,1}][\text{NTf}_2]$  to  $[\text{N}_{4,2\text{OH},2\text{OH},2\text{OH}}][\text{NTf}_2]$  certainly indicates that the probe solutes experience different extents of solute-solvent interaction in different RTILs used in this study. This is further supported by the estimated hydrodynamic radii (Table APX4.1.) of both solutes in the respective ionic liquids. As mentioned previously, the constituents of the hydroxyl ILs can participate in strong intra- and intermolecular hydrogen bonding interactions, and due to this, the hydroxyl groups of the cations in these ILs are expected not to be readily available for making solute-solvent hydrogen bonding interactions with the probe solutes. Therefore, the diffusion of MPTS becomes relatively faster in the hydroxyl ILs as compared to the non-hydroxyl ILs. Here, we note that upon going from  $[\text{N}_{4,1,1,1}][\text{NTf}_2]$  to  $[\text{N}_{4,2\text{OH},2\text{OH},2\text{OH}}][\text{NTf}_2]$ , the change in  $\tau_{st}$  values ( $\sim 3.2$  times, Table 4.2) is almost similar to the change in the  $\tau_d^{avg}$  values (Table APX4.1, 3.2-3.8 times for MPTS and perylene). This observation essentially indicates that the extent of decoupling of the longer solvation time component and  $\tau_d^{avg}$  value from the medium viscosity is almost similar. In this context, it is important to mention that Sen and co-workers<sup>182</sup>, while working on lauric acid/menthol-based DES, have estimated the extent of decoupling of the longer solvation time component and the translational diffusion time component from the medium viscosity and have found that the extent of decoupling is large, suggesting a larger heterogeneity at longer time scale. Moreover, they have also reported that the extent of decoupling is almost similar for both dynamical events, which essentially indicates the correlation between these two dynamical events occurring outside the first solvation shell. In the present scenario also, similar extent of decoupling of the longer solvation time component and  $\tau_d^{avg}$  value from the medium viscosity indicates the correlation between the two dynamical processes and greater temporal heterogeneity at the larger time scale. All these results essentially indicate that, in addition to viscosity, the mobility of the fluorophores

in these media is greatly influenced by the intermolecular interactions between the solute and solvent as well as the heterogeneity of the medium.

#### 4.3.5. PFG-NMR Studies

In order to gain a deeper understanding of the cation-cation/cation-anion interaction within the solvent, which can significantly affect the microstructural organization of ILs, the self-diffusion coefficient of both non-hydroxyl and hydroxyl ILs are estimated by exploring pulse field gradient NMR (PFG-NMR) technique. Since PFG-NMR is a non-invasive and chemically selective technique, it is proved to be excellent for simultaneously estimating the self-diffusion coefficients of several species in a given mixture and can offer details on the size, shape, and intermolecular interactions of the concerned species.<sup>247, 249, 277</sup> Specifically, in the current study, translational diffusion coefficient ( $D$ ) values for both hydroxyl and non-hydroxyl ILs are estimated from the slope by fitting the NMR data using the Stejskal–Tanner equation (equation 2.29).<sup>264</sup> During the measurement, the cationic component of RTILs is monitored exclusively, and the measured  $D$  values for relevant RTILs are tabulated in Table 4.7.

**Table 4.7.** Estimated translational diffusion coefficient ( $D \times 10^{-11} \text{ m}^2/\text{s}$ ) of the cationic species of both non-hydroxyl and hydroxyl ILs.

Temperature (K)	$[\text{N}_{4111}]^+$	$[\text{N}_{4112\text{OH}}]^+$	$[\text{N}_{412\text{OH}2\text{OH}}]^+$	$[\text{N}_{42\text{OH}2\text{OH}2\text{OH}}]^+$
298	1.95	1.05	0.43	0.13
303	2.80	1.32	0.59	0.18
308	3.60	1.75	0.79	0.26
313	4.70	2.22	1.05	0.38
318	5.95	2.8	1.35	0.54
323	7.20	3.5	1.75	0.73
328	8.80	4.3	2.2	0.98

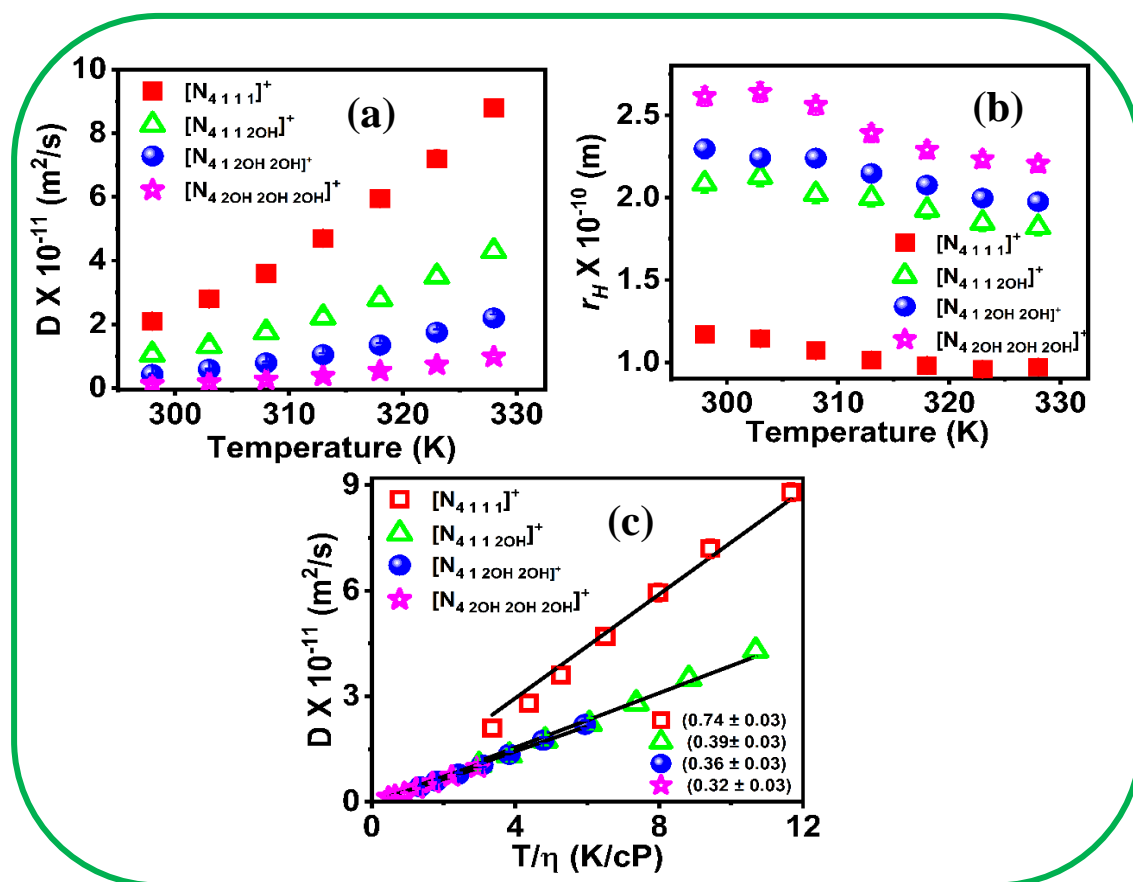


**Figure 4.7.** (a) Temperature dependent variation of the self-diffusion coefficients of the RTILs (b), hydrodynamic radii of cationic species calculated through SE equation, (c)  $D$  vs  $T/\eta$  plot of RTILs.

As can be seen from Table 4.7, at any particular temperature, the  $D$  value for the non-hydroxyl ILs is found to be the highest among all the concerned ILs. This indicates that the mobility of the non-hydroxyl IL is faster than the hydroxyl ILs because of the lower viscosity of the former than the latter. Additionally, with the increase in the number of hydroxyl groups on the cationic head, a gradual decrease in the  $D$  values can also be seen. This observation also correlates with the viscosity of the medium. It is also well known that increase in the size of the diffusing species (here, cation) and magnitude of cation-anion/cation-anion intermolecular interaction can also slow the diffusion process. Therefore, using the Stokes-Einstein equation ( $D = kT/6\pi\eta r$ ), we have calculated the hydrodynamic radius ( $r_H$ ) of all the RTILs in the temperature range of 298 K to 328 K in order to learn more about the impact of viscosity, size,

and intra/inter molecule interaction inside the ILs on the mobility of the RTILs. The estimated  $r_H$  values of the relevant RTILs are shown in Figure 4.7(b). As can be seen from Figure 4.7(b),  $[\text{N}_{4\ 1\ 1\ 1}]^+$  has the smallest hydrodynamic radius among the concerned RTILs at any given temperature. However, when hydroxyl functionalities are added to the cationic head, a significant rise in the  $r_H$  values has been observed, with  $[\text{N}_{4\ 2\text{OH}\ 2\text{OH}\ 2\text{OH}}]^+$  having the largest hydrodynamic radius. Here we would like to note that when the  $r_H$  values of the cations of the relevant RTILs are calculated from their theoretical van der Waal's volume (through the Edward increment method)<sup>277</sup>, a marginal increase (~15%) in the hydrodynamic radii have been observed upon going from  $[\text{N}_{4\ 1\ 1\ 1}]^+$  to  $[\text{N}_{4\ 2\text{OH}\ 2\text{OH}\ 2\text{OH}}]^+$ . However, the hydrodynamic radii, estimated through PFG-NMR, shows a 125% increase upon going from  $[\text{N}_{4\ 1\ 1\ 1}]^+$  to  $[\text{N}_{4\ 2\text{OH}\ 2\text{OH}\ 2\text{OH}}]^+$ . This clearly indicates that the increase in the hydrodynamic radii of the hydroxyl ILs is because of the strong intermolecular interaction between the constituents of the ILs (cation-anion/cation-anion), which effectively increases the size of the hydroxyl ILs and thereby slow down the diffusion of the cationic component of the hydroxyl ILs. To further support this observation, the NMR data have been analyzed by plotting  $D$  against  $T/\eta$ . Given that the slope and the hydrodynamic radii are inversely related, a steeper slope corresponds to a higher hydrodynamic radius. From Figure 4.7(c), it can be seen that  $[\text{N}_{4\ 1\ 1\ 1}]^+$  has the largest slope values, which essentially indicates that the non-hydroxyl-based IL has the smallest hydrodynamic radii among the concerned RTILs. With the addition of hydroxyl functionalities, a sharp decrease in the slope value has been observed, with  $[\text{N}_{4\ 2\text{OH}\ 2\text{OH}\ 2\text{OH}}]^+$  having the steepest slope. In fact, more than 55% decrease in the slope value has been observed upon going from  $[\text{N}_{4\ 1\ 1\ 1}]^+$  to  $[\text{N}_{4\ 2\text{OH}\ 2\text{OH}\ 2\text{OH}}]^+$ . It is also important to mention that Fujita et al.<sup>279</sup> have reported relatively slower diffusion of hydroxyl ammonium-based RTILs as compared to their non-hydroxyl counterpart. Similarly, Ludwig and co-workers<sup>278</sup> have also reported slower diffusion of hydroxyl functionalized imidazolium-based RTILs, and this slower diffusion of the cationic

---

---

moiety has been rationalized by considering significant hydrogen bonding mediated cation-cation interactions. Considering this, in the present scenario also, one can expect similar cation-cation hydrogen bonding interaction in the hydroxyl functionalized ILs. Moreover, extensive cation-cation hydrogen bonding interaction can also be expected for  $[\text{N}_4\text{ 2OH 2OH 2OH}][\text{NTf}_2]$  containing three hydroxyl groups which will effectively increase the hydrodynamic radius of the cationic component.

#### 4.4. Conclusion

In the present study, we have investigated the microscopic behaviours, in terms of intermolecular interactions, local structural organisation and solvent dynamics of some ammonium-based RTILs as a function of hydroxyl group on the cationic moiety using various spectroscopic techniques. For this purpose, three hydroxyl functionalized ammonium based RTILs (HFILs) bearing different numbers of hydroxyl groups on the cationic head as well as a non-hydroxyl ammonium based RTIL have been employed in the present study. All these investigations have uncovered a number of interesting findings. The solvent response functions generated from the complete Stokes shift dynamics measurements have revealed a bimodal solvent relaxation behaviour, consisting of a very fast sub-picosecond solvation time component and a broadly distributed relatively slower pico-second to nanosecond solvation time component for all the RTILs. The broadly distributed slower time component which correlates with the medium viscosity is found to arise due to the heterogeneous diffusional motion of the cations and anions while the sub-picosecond component arises due to fast local motions of the constituents of the RTILs. Interestingly, investigation of rotational and translational diffusion dynamics of selected probes have indicated that the extent of solute-solvent interaction is relatively weaker in the poly-hydroxyl ILs as compared to the same in the non-hydroxyl ILs. This is due to the stronger solvent-solvent inter/intra molecular hydrogen

bonding interaction between the hydroxyl groups and the constituent of the poly-hydroxyl ILs. More interestingly, analysis of rotational diffusions data has revealed that, decoupling of solute dynamics with medium viscosity is found to be more for poly-hydroxyl ILs than that for non-hydroxyl ILs, indicating a larger extent of dynamic heterogeneity in the former than the later. Additionally, study of the self-diffusion coefficient through NMR have revealed that HFILs have significantly larger hydrodynamic radii than non-hydroxyl ILs do due to stronger intermolecular hydrogen bonding interaction in the former than the later. Essentially, all the results obtained from these investigations have demonstrated that addition of hydroxyl functionality to the cationic head of the RTILs considerably alter the local structural organisation ad dynamics of the solvent systems. Furthermore, the extensive hydrogen bonding interaction among the solvent molecule in the poly-hydroxyl ILs significantly influence the macroscopic physicochemical properties of the HFILs.

#### 4.5. Appendix

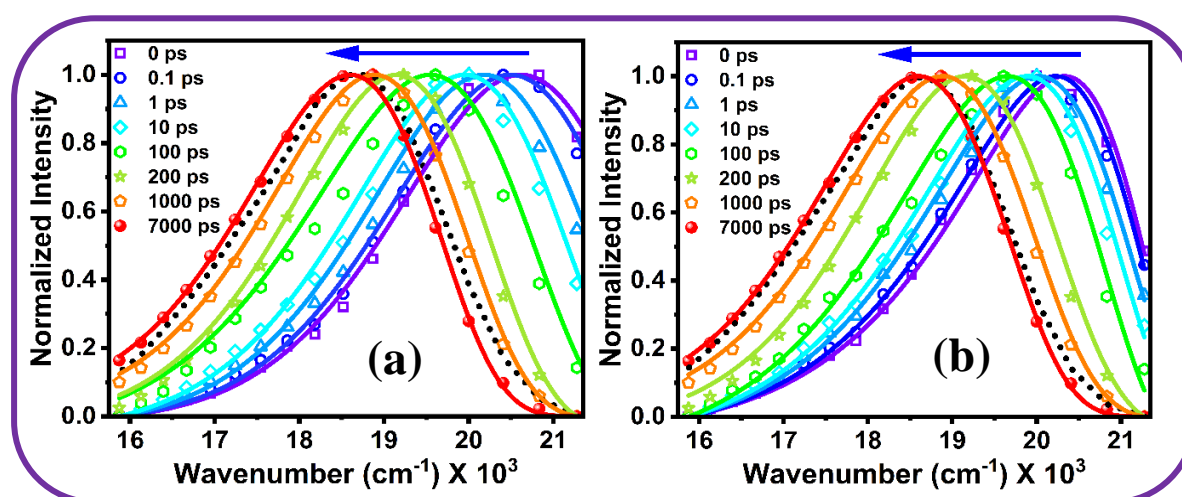


**Figure APX4.1.** Normalized TRES plots at different time interval for (a)  $[N_{4.1.1.2OH}][NTf_2]$  and (b)  $[N_{4.2OH.2OH.2OH}][NTf_2]$ . Solid line represents the log-normal line shape fitting of the corresponding data and the dotted black line represents the steady-state fluorescence spectra.

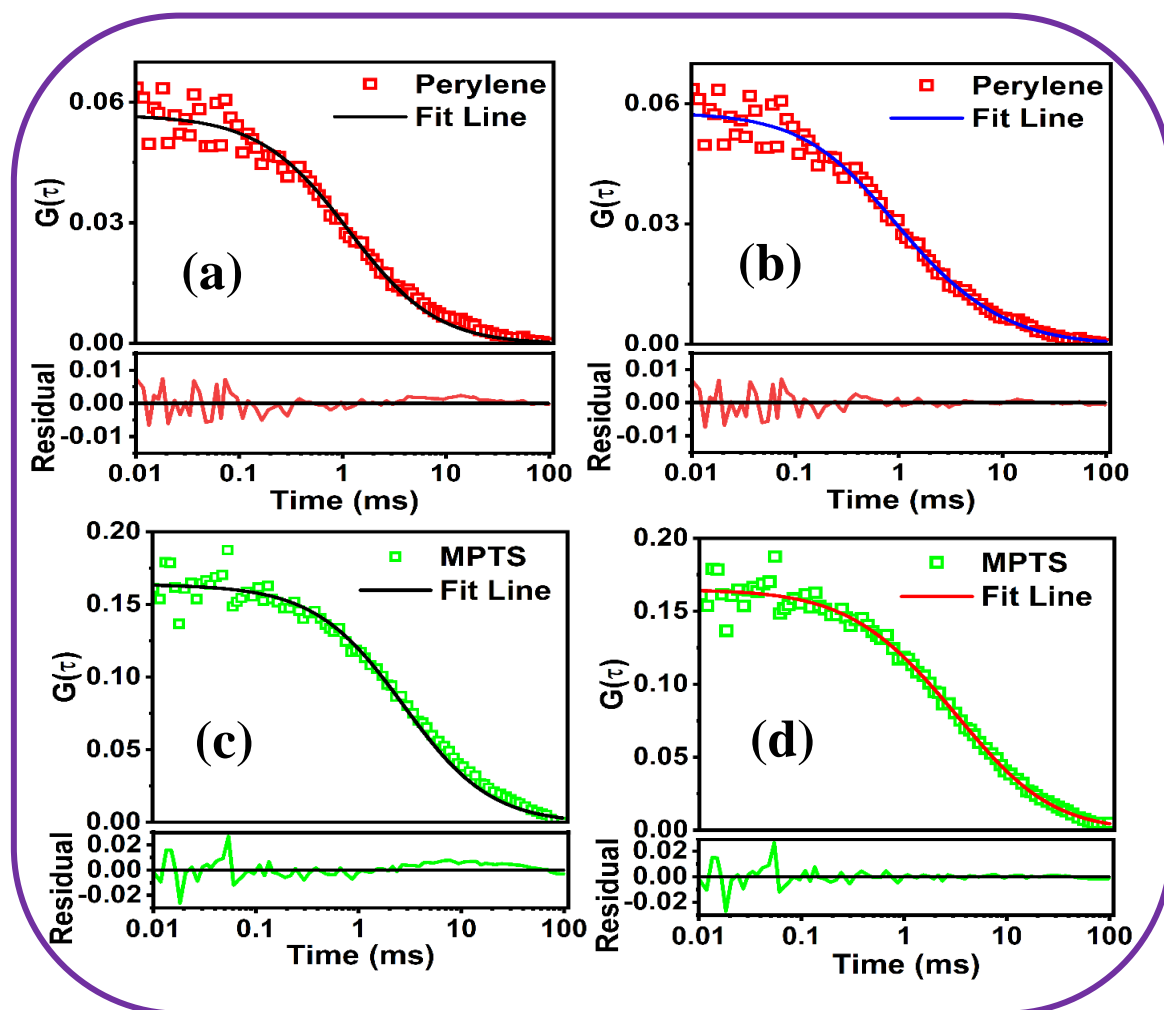


**Figure APX4.2.** Fluorescence correlation curve for (a,b) Perylene and (c,d) MPTS in  $[N_{4,1,1}][NTf_2]$  along with the fit residual. Left panel curves (a,c) are fitted to single component diffusion model while right panel curves (b,d) are fitted to two component diffusion model.

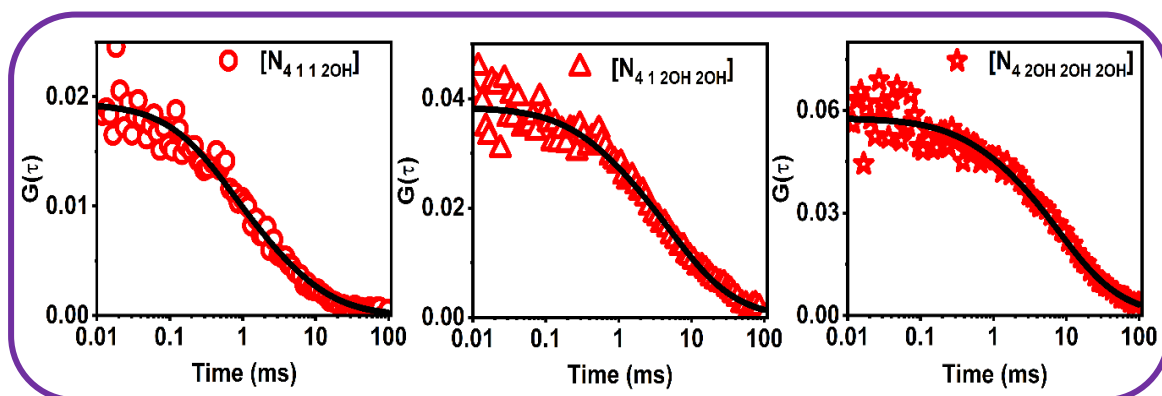


**Figure APX4.3.** Fluorescence correlation curve for perylene in HFILs. The solid black curve represents the fit to the points through two component diffusion model.

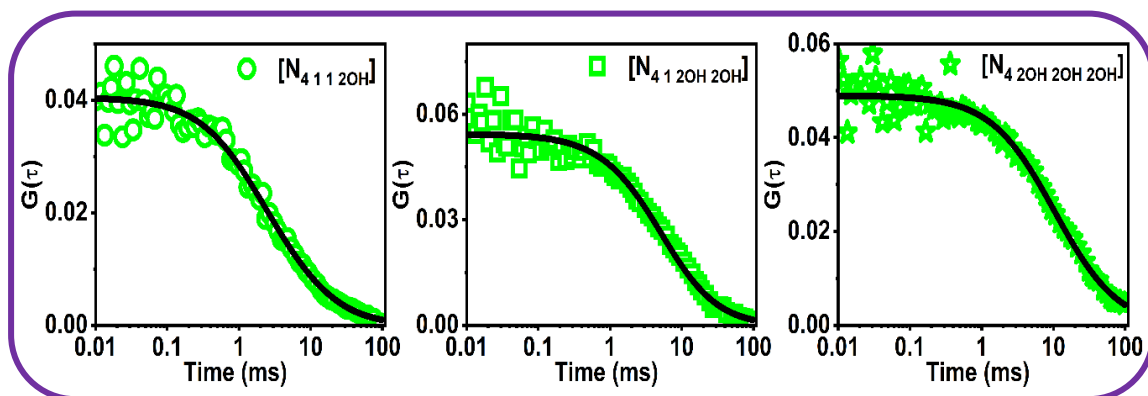


**Figure APX4.4.** Fluorescence correlation curve for MPTS in hydroxyl ILs. The solid black curve represents the fit to the points through two component diffusion model.

**Table APX4.1.** Estimated translational diffusion time ( $\tau_D$ ) in millisecond (ms) along with their contribution value and hydrodynamic radii ( $r_H$  in nm) for perylene and MPTS in all the relevant RTILs

Systems	Perylene					MPTS				
	$\alpha_1$	$\tau_{D_1}$	$\tau_{D_2}$	$\tau_{avg}$	$r_H$	$\alpha_1$	$\tau_{D_1}$	$\tau_{D_2}$	$\tau_{avg}$	$r_H$
[N <sub>4</sub> 1 1 1]	0.62	0.52	4.76	2.13	0.42	0.44	1.38	5.52	3.70	0.14
[N <sub>4</sub> 1 1 2OH]	0.60	0.60	4.93	2.33	0.40	0.68	1.92	7.67	3.75	0.15
[N <sub>4</sub> 1 2OH 2OH]	0.34	0.70	7.27	5.03	0.35	0.71	6.00	11.50	7.59	0.13
[N <sub>4</sub> 2OH 2OH 2OH]	0.29	1.48	10.62	7.97	0.22	0.7	9.20	17.26	11.62	0.10

Experimental Error =  $\pm 5\%$

# CHAPTER 5

---

## Influence of Lithium Salt on the Structure and Dynamics of Deep Eutectic Solvents

---

---

Barik, S.; Chakraborty, M.; Sarkar, M.; *J. Phys. Chem. B*, 2020, 124, 14, 2864–2878.

**Abstract**

The work of this chapter has been undertaken with an objective to understand the intermolecular interaction, structural organization, and dynamics of two DES systems in the absence and presence of lithium salt so that the potential of these mixtures in electrochemical application can be realized. For this purpose, the steady-state and time-resolved fluorescence, EPR, and NMR behaviour of two DESs (ethaline and glyceline) and their mixture with lithium bis(trifluoromethylsulfonyl) imide (LiNTf<sub>2</sub>) has been investigated. Measurements of polarity through EPR technique have revealed that the polarities of DESs are close to aliphatic polyhydroxy alcohol and the polarities of the medium increase with the increase in lithium salt concentration. Studies on solvation dynamics have indicated that there is an increase in average solvation time with the increase in lithium salt concentration. Investigation of rotational dynamics of some selected fluorophore in these media has shown that addition of lithium salt significantly alters the nano/microstructural organization of both DESs. Further, measurements of the self-diffusion coefficient through NMR have also supported the perturbation of the nanostructural organization of the solvent systems by addition of lithium salts. Essentially, all of these investigations have suggested that addition of lithium salt significantly alters the microscopic behaviour of DESs. The outcome of this study is expected to be helpful in realizing the potential of these media for various electrochemical applications including application in lithium-ion battery.

---

**5.1. Introduction**

In recent times, deep eutectic solvents (DESs) have emerged as an alternative to both common organic solvents and ionic liquids (ILs).<sup>19, 20, 63, 64</sup> DESs are similar to ILs in terms of characteristic physicochemical properties such as low vapor pressure, high viscosity, high thermal stability, etc.<sup>19, 20</sup> However, DESs are found to be more advantageous over ILs due to

their low toxicity, biodegradability, availability of cheaper raw materials, and energy-efficient preparation.<sup>17, 21, 109, 110</sup> Due to its environment-friendly nature, large electrochemical potential windows, and negligible water electrolysis capacity, they are expected to be very attractive candidates for electrochemical applications.<sup>142, 298</sup> However, knowledge about the medium in terms of their structural organization, intermolecular interaction, and dynamics is very limited as compared to ILs, perhaps due to availability of very less number of literature for DES on the same issue. Hence, studies on DESs in the absence and presence of lithium salts are expected to provide valuable knowledge regarding the structural organization of DESs and their mixture with lithium salts, which will eventually be helpful in realizing the potential of these media toward electrochemical application including application in lithium-ion battery.

Some experimental studies by exploiting fluorescence, small angle neutron scattering, NMR diffusion, and theoretical studies based on molecular dynamics (MD) simulation have been carried out to understand the structure and dynamics of DESs.<sup>161-167</sup> Hossain and Samanta<sup>185</sup> have employed steady-state and time-resolved fluorescence as well as fluorescence correlation spectroscopy to get insight into the microscopic structural organization of ethaline. In a separate work, they have also proposed the increase in both static and dynamic heterogeneity of the DESs with increase in chain length of the HBD.<sup>186</sup> Furthermore, Kim and co-workers<sup>224</sup> have also demonstrated similar type of medium heterogeneity for choline chloride-based deep eutectic solvent through photophysical studies. Biswas and co-workers<sup>173, 176</sup>, while working on DESs (alkyl amide + electrolyte), have figured out the presence of both spatial and dynamic heterogeneity in the medium. In a different work, Anouti and co-workers<sup>299</sup> have studied the electrochemical behaviour of N-methylacetamide and lithium salts mixture with an objective to find out the suitability of these media for application in lithium battery. In a separate work on reline (urea + choline chloride) DES, Pandey and co-workers<sup>300</sup> have observed a decrease in lifetime of pyrene in the presence of lithium chloride.

The above discussions depict that, even though some studies have provided some information regarding the microscopic behaviour of neat DES media, the studies on the effect of lithium salt on the structural organization of DESs are inadequate. However, on the similar objective, structure breaking of ILs upon addition of Li salts has already been investigated, anticipating that the outcome of these studies can be very useful for using ILs in electrochemical application.<sup>301-303</sup>

Considering all the above facts, we have made an attempt to understand the intermolecular interaction, microscopic structural organization, and solvent dynamics of two choline chloride-based deep eutectic solvents, namely, ethaline (choline chloride + ethylene glycol) and glyceline (choline chloride + glycerol), in the absence and presence of lithium bis(trifluoromethylsulfonyl) imide (LiNTf<sub>2</sub>) salt by exploiting steady-state and time-resolved fluorescence measurements. Additionally, EPR and NMR techniques have also been used to understand the behaviour of concerned media. The lithium salt (LiNTf<sub>2</sub>) has been chosen purposefully because of its good conductivity, large electrochemical windows, high solubility, high thermal stability, low toxicity, and low production cost as compared to other common lithium salts (LiPF<sub>6</sub>, LiClO<sub>4</sub>, LiBF<sub>4</sub>, LiAsF<sub>6</sub>, etc.) used for lithium-ion battery applications.<sup>304</sup> Steady-state spectral properties and EPR technique have been employed to estimate the polarity of the medium. Solvent dynamics of the (DES + Li salt) mixture have been investigated by TDDSS measurements. Time-resolved fluorescence anisotropy measurements have also been carried out to get an idea about the rotational dynamics and solute–solvent interaction of the concerned (DES + Li salt) mixture system. Self-diffusion coefficients of the constituents of DESs in the absence and presence of Li salts have also been determined employing the NMR technique. All the studies have indicated a significant change in the structural organization of both DES systems in the presence of lithium salt. The outcome of the present study is expected to help in understanding the kinship among the structure, intermolecular interaction, and

dynamics of these solvents, which would eventually facilitate the design and development of various such solvent systems for many electrochemical applications.

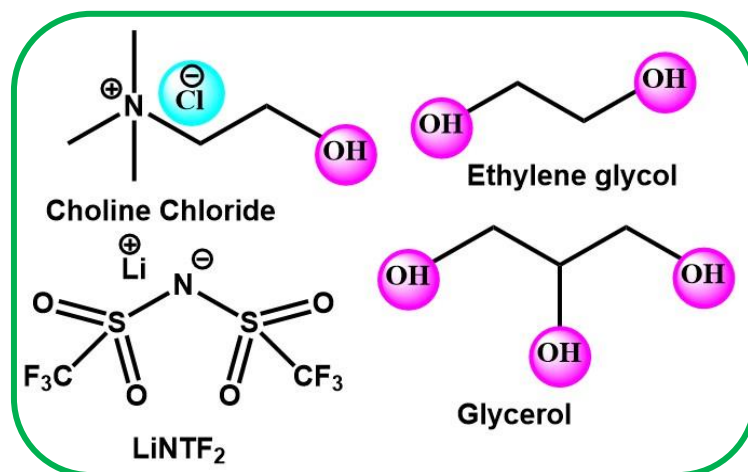


**Chart 5.1.** Molecular structure of the components of DESs and the lithium salt used in the present study.

## 5.2. Experimental Sections

The detail about the synthesis of DESs have been provided in chapter 2. LiNTf<sub>2</sub> was added to both synthesized DESs (up to 0.3 mole fraction in ethaline and up to 0.08 mole fraction in Glyceline, after the solution become saturated) keeping at least one mole fraction (0.05 mole fraction) common in both DESs and stirred for some time to completely mix them. Then the solvents were transferred into 2cm quartz cuvette and requisite amount of probe was added to prepare the solution (keeping absorbance below 0.3). All the cuvette were thoroughly sealed with septum and parafilm to avoid moisture intake. The details about different instrumental techniques (i.e., steady-state and time-resolved fluorescence, and NMR) and procedure for data analysis have been discussed in chapter 2.

## 5.3. Results and Discussions

### 5.3.1. Steady-State Spectral Measurements

Figure 5.1 displays the steady-state absorption and emission spectra of a dipolar probe C153 in both ethaline and glyceline along with their mixture with lithium salt. Table 5.1

summarizes the absorption and emission maxima of C153 in the solvent systems. From Table 5.1, it can be observed that there are no considerable changes in the absorption and emission maxima of C153 in both DESs in the neat condition and in the presence of lithium salts, indicating that the polarities of both DES are similar, and under the experimental condition, addition of lithium salt does not alter the polarity of DES media.<sup>105</sup>

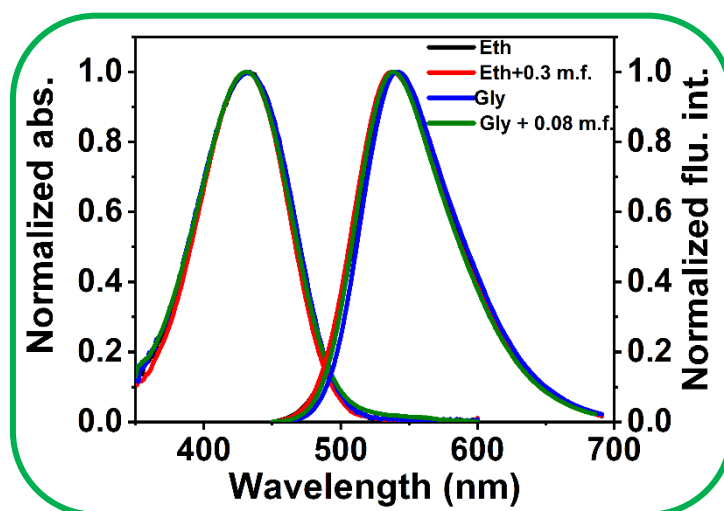


**Figure 5.1.** Normalized absorption (left side) and emission spectra (right side) of C153 in both DESs containing different mole fraction of lithium salt.

**Table 5.1.** Absorption and Emission Maxima of C153 in DESs and DES + Li Mixture

System	$\lambda_{\max}(\text{abs})$ (nm)	$\lambda_{\max}(\text{ems})$ (nm)
Neat ethaline	429	540
Ethaline + 0.05 m.f. LiNTf <sub>2</sub>	430	540
Ethaline + 0.1 m.f. LiNTf <sub>2</sub>	430	541
Ethaline + 0.2 m.f. LiNTf <sub>2</sub>	430	542
Ethaline + 0.3 m.f. LiNTf <sub>2</sub>	431	542
Neat Glyceline	431	539
Glyceline + 0.05 m.f. LiNTf <sub>2</sub>	432	540
Glyceline + 0.08 m.f. LiNTf <sub>2</sub>	432	540

In this context, we would like to note that it is not always possible to find out the small change in the micropolarity of a given medium by monitoring only the steady-state spectral

properties of C153.<sup>213</sup> For example, it has been found previously that for ionic liquids, the change in steady-state spectral properties of C153 could not distinguish the polarity of the given media.<sup>213</sup> Subsequently, it has also been demonstrated for ILs and its mixture with organic cosolvents that a very small change in polarity of a given medium can be estimated quantitatively by monitoring the EPR spectra of the EPR active probe, TEMPO, in the concerned solvent systems.<sup>267</sup> Therefore, the estimation of aN/G value of TEMPO in neat DES and (DES + Li salt) mixture is also expected to provide an idea about the polarity of the corresponding medium. Figure 5.2 represents the EPR spectra of TEMPO, along with the corresponding simulated spectra, in both DESs and DESs with different mole fractions of LiNTf<sub>2</sub> salt. From Figure 5.2, we can notice that significant line broadening of the EPR signal has taken place upon addition of LiNTf<sub>2</sub> salt to both DESs. The change in line shape of the EPR spectra clearly indicates the perturbation of the solvent upon addition of lithium salt. It has been demonstrated previously by Mladenova et al.<sup>269</sup>, and Akdogan et al.<sup>268</sup>, independently, that inhomogeneity of a medium is primarily responsible for the EPR line shape broadening. Therefore, in the present scenario, also the EPR line shape change in both DESs due to addition of LiNTf<sub>2</sub> salt indicates the inhomogeneous nature of the medium.

The  $E_T(30)$  values for various known solvents<sup>270</sup> are provided in Table 5.2, and the  $E_T(30)$  values of the DESs and (DES + Li) mixture are estimated according to the procedure illustrated in chapter 3A (Section 3A.3.1). Figure 5.3 represents the plot of aN/G versus  $E_T(30)$  for various solvent systems. From Table 5.2, it can be noticed that the polarity of glyceline is greater as compared to that of ethaline. This is quite in accordance with the higher polarity of glycerol as compared to ethylene glycol. Furthermore, with addition of lithium salt to both the DESs, an increase in  $E_T(30)$  values has been observed, which indicates the increase in polarity of the medium. Essentially, the present EPR data demonstrate that the polarities of both the solvents (DESs) are closed to aliphatic polyhydroxy alcohol.

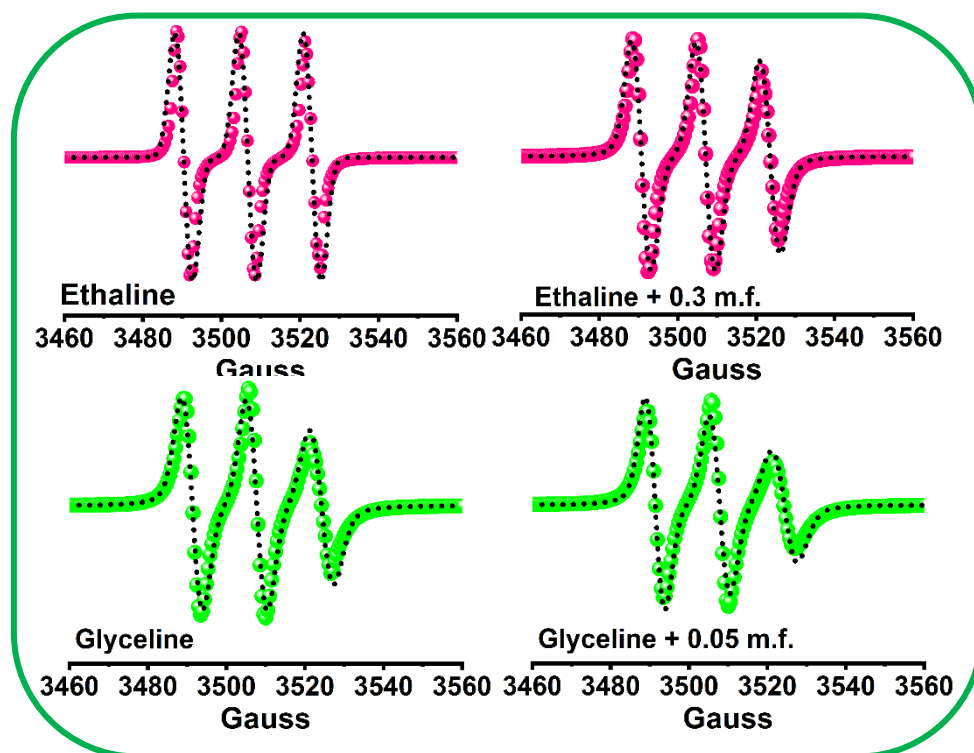


**Figure 5.2.** EPR spectra of TEMPO in both DESs in the absence and presence of LiNTf<sub>2</sub>.

**Table 5.2.** The  $a_N/G$  value of TEMPO in DESs and molecular solvents and their estimated  $E_T(30)$  values

Solvents	$a_N/G$	$E_T(30)/\text{kcalmol}^{-1}$
Ethaline	$16.31 \pm 0.012$	$58.6 \pm 0.015$
Ethaline + 0.05 m.f.LiNTf <sub>2</sub>	$16.33 \pm 0.011$	$58.8 \pm 0.017$
Ethaline + 0.1 m.f.LiNTf <sub>2</sub>	$16.37 \pm 0.012$	$59.3 \pm 0.015$
Ethaline + 0.2 m.f.LiNTf <sub>2</sub>	$16.41 \pm 0.018$	$59.8 \pm 0.017$
Ethaline + 0.3 m.f.LiNTf <sub>2</sub>	$16.47 \pm 0.012$	$60.6 \pm 0.012$
Glyceline	$16.46 \pm 0.015$	$60.5 \pm 0.015$
Glyceline + 0.05 m.f.LiNTf <sub>2</sub>	$16.49 \pm 0.010$	$60.9 \pm 0.014$
Glyceline + 0.08 m.f.LiNTf <sub>2</sub>	$16.50 \pm 0.014$	$61.0 \pm 0.017$
[OHEMIM][NTf <sub>2</sub> ]	$16.56 \pm 0.016$	$62.2 \pm 0.018$
[BMIM][NTF <sub>2</sub> ]	$16.03 \pm 0.019$	$52.5 \pm 0.02$
Ethylene glycol	$16.24 \pm 0.017$	$56.3 \pm 0.015$

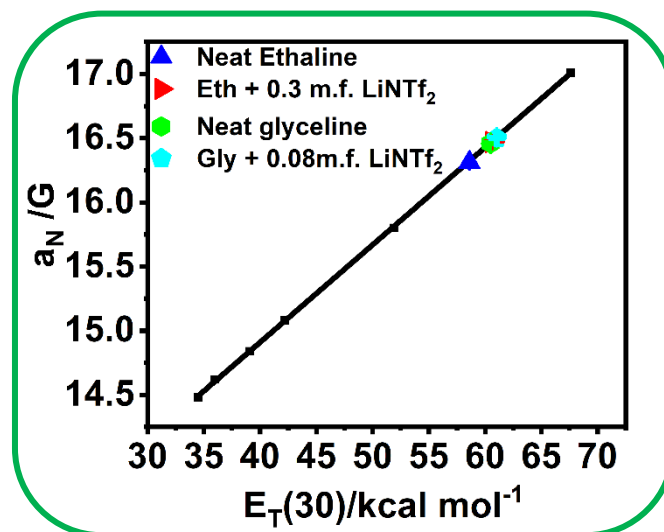


**Figure 5.3.** Plot of  $a_N/G$  vs.  $E_T(30)$  values of TEMPO in both DES and HFILs vs.  $E_T(30)$  values of TEMPO in both DESs in absence and presence of LiNTf<sub>2</sub>. The black square indicates the values corresponding to known solvents.

Like polarity, microheterogeneous behavior is also an important physical attribute of the medium as physicochemical properties and the microheterogeneous nature of the given media are intricately related to each other.<sup>168, 196, 213</sup> Therefore, it is important to understand the microheterogeneous behavior of the different solvent systems employed in the study. Particularly, it is essential to know whether the Li<sup>+</sup> ion can influence the microheterogeneous nature of DESs. To achieve this, excitation wavelength ( $\lambda_{ex}$ ) dependence of fluorescence maxima ( $\lambda_{em}^{max}$ ) of a suitable fluorescent solute molecule in those media is investigated. We would also like to note here that studies on excitation wavelength-dependent fluorescence measurements are a simple but useful method to qualitatively demonstrate the presence of spatial heterogeneity in a given liquid system.<sup>168</sup> It is well known that, if the medium is microheterogeneous, the molecule with shorter lifetime shows a progressive red shift of the  $\lambda_{em}^{max}$  with an increase in the  $\lambda_{ex}$ , and by estimating the total shift in the emission maxima, one would be able to qualitatively assess the medium heterogeneity. In the current study, to know the microheterogeneous behavior of DES solvent systems and the effect of Li<sup>+</sup> salt on the microheterogeneity of the medium, the  $\lambda_{ex}$  dependence of fluorescence behavior of 2-amino-

7-nitrofluorene (ANF) ( $\tau_f < 50$  ps)<sup>168</sup> is carried out in both the DES media in the absence and presence of lithium salt. The solute ANF is chosen decisively because of its very short excited-state lifetime as compared to C153 ( $\tau_f \approx 4.2$  ns in ethanol) so as to observe the emission from different unrelaxed states of the solute molecule and get more insight into the microheterogeneity of the solvent systems. From Figure 5.4, it can be observed that, for all the solvent systems upon gradual increase in  $\lambda_{ex}$ , the  $\lambda_{em}^{max}$  of ANF is increased, but total shift in the  $\lambda_{em}^{max}$  is estimated to be different for different systems. For example, in neat ethaline, upon going from  $\lambda_{ex} = 380$  to 520 nm, the total shift in emission maximum is estimated to be only 9 nm, whereas the same in the (ethaline + 0.2 mole fraction of lithium salt) mixture is found to be 15 nm. On the other hand, in the glyceline medium, the total shift in emission maximum is observed to be 20 nm. This observation indicates that the neat DESs and (DESs + Li) salt mixture, used in the current study, are spatially heterogeneous and the heterogeneity is greater for the glyceline medium. Therefore, though this study cannot provide an exact length scale of spatial heterogeneity of the sample, but it certainly gives a qualitative idea about the medium heterogeneity.

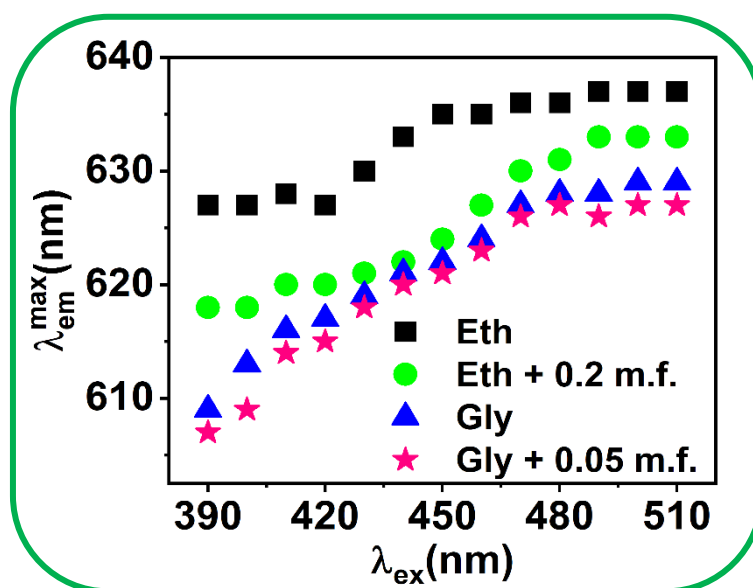


**Figure 5.4.** Plots of  $\lambda_{ex}$  versus  $\lambda_{em}^{max}$  of ANF at 298 K of both DESs medium in the absence as well as in presence of LiNTf<sub>2</sub>.

### 5.3.2. Solvation Dynamics

Since the study of dynamics of solvation provides information regarding the dynamical behaviour of a solvent system, which, in turn, relates to chemical reactivity of a solute molecule, it is important to understand the solvent relaxation dynamics of both DESs in the neat condition and in the presence of lithium salt. For this purpose, the TDDSS of the fluorescence spectra of C153 in the concerned solvent systems has been monitored extensively.<sup>197-207</sup> To study this phenomenon, wavelength-dependent fluorescence intensity decays of C153 in the concerned solvent systems have been collected. A faster decay at shorter wavelength and growth followed by decay at longer wavelength signifies the process of solvation (Figure 5.5).<sup>197-207</sup>

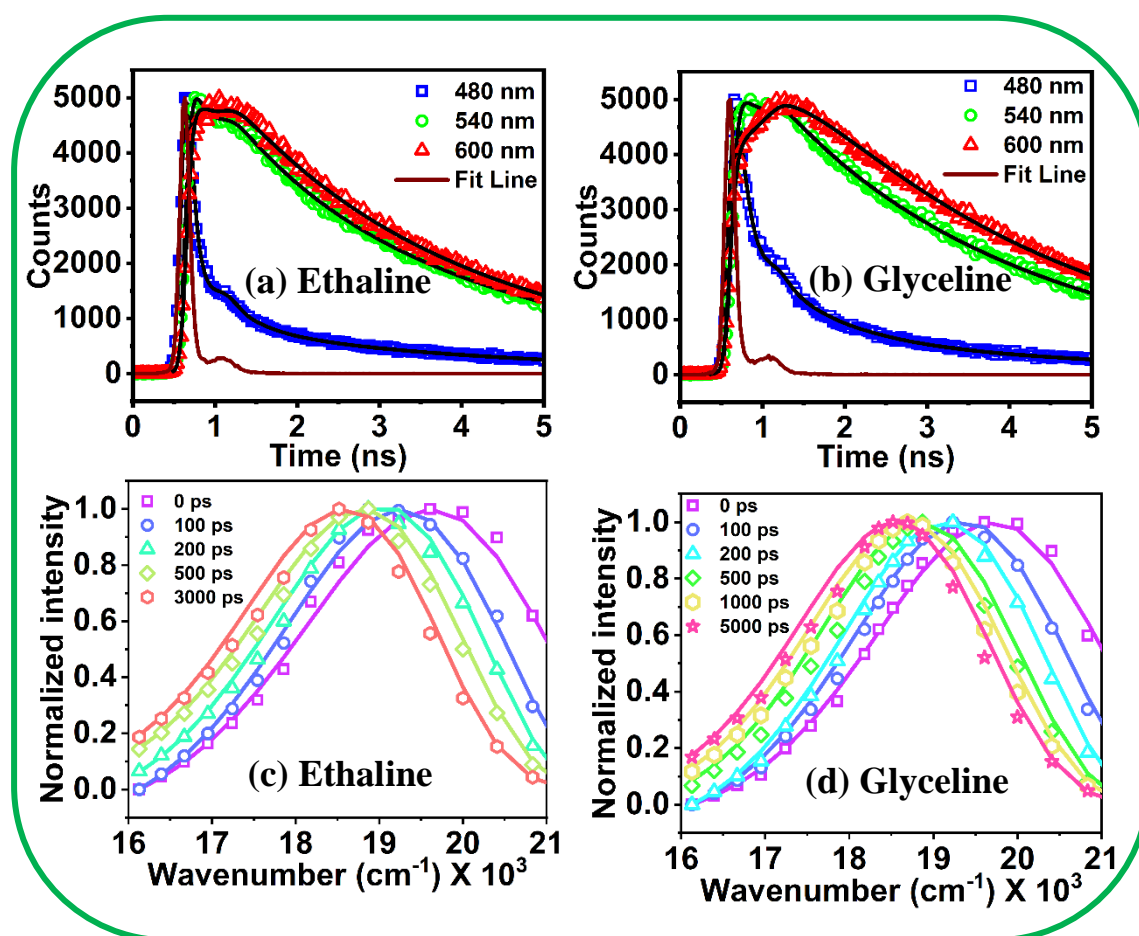


**Figure 5.5.** (a), (b) Fluorescence decay of C153 at three different wavelengths in both DESs and (c), (d) TRES plots for both DESs in neat condition.

After this, the TRES plots are constructed by following the standard protocol as mentioned in Chapter 2.<sup>198-200</sup> Representative TRES plots for both DESs in the neat condition are provided in Figure 5.5 (c & d). The gradual red shift of the emission maxima with time has indicated the process of solvent relaxation. Furthermore, a continuous decrease in the fwhm of the TRES plots with time has been observed for both DESs in the absence and presence of lithium salt, which evidently advocated the stabilizing effect of the solvent systems on the excited state of the dipolar solute molecule.<sup>198-200</sup> This time-dependent change in spectral width reflects the change in the solvent environment. Moreover, due to the solute-solvent interaction, the shape of the potential energy surface changes, leading to the narrowing of the spectral width, which is a common feature of solvent relaxation.<sup>198-207, 212-218</sup>

Now, the peak frequencies (emission maxima) obtained from the log-normal fitting (equation 2.12) of the TRES plot are used for the calculation of solvent correlation function ( $C(t)$ ) (equation 2.13). Figure 5.6 represents the plot of spectral shift correlation function  $C(t)$  versus time for both DESs in the neat condition as well as with various (DES + Li salt) mixtures. The  $C(t)$  versus time plot can provide a qualitative idea about the time-dependent Stoke shift of C153. The relevant solvent relaxation parameters obtained from both the biexponential fit (equation 2.14) and stretched exponential fit (equation 2.15) of the  $C(t)$  versus time plot are collected in Table 5.3. From Table 5.3, we can see that the  $\langle\tau_s\rangle$  value obtained from biexponential fits and stretched exponential fits are very similar for the ethaline medium, but for the glyceline medium, a little difference is observed. In the case of ionic liquids, previously, it has been shown by Samanta<sup>214, 281</sup> and by our group<sup>240, 280</sup> independently, that ionic liquids also exhibit a similar kind of biphasic solvation behaviour, having faster and slower components. Das and Biswas<sup>175</sup>, while working on choline chloride urea-based DES, have also observed biphasic solvation behaviour of the dipolar probe C153. Here, it is worth

mentioning that due to finite resolution (40 ps) of the experimental setup (TCSPC), a considerable portion of the solvation component, which is very fast (ultrafast), cannot be observed.<sup>221</sup> It may be noted that, for ILs, also an ultrafast solvation component has been observed. In the present study, for the ethaline medium, the missing solvation component is estimated to be nearly 30–40% (equation 2.19), whereas the same for the glyceline medium is 10%. The lowering of the ultrafast solvation component for the highly viscous glyceline medium indicates that the dipolar rotation of solvent molecules plays an important role in the ultrafast component of solvation.<sup>209</sup> Sarkar and co-workers<sup>239</sup> have previously shown through NMR and fluorescence studies that the ultrafast component can be linked to dipolar rotation of the solvent molecule. For ionic liquids, it has also been suggested that the fast component is due to the immediate response of the ions, and this motion is independent of another. The slow component, which is viscosity-dependent, represents the complex dynamical process involving structural reorganization and deformation as supported by simulation studies. Since the present DESs resemble ionic liquids physicochemically, a similar kind of relaxation process is believed to be occurring in DES.

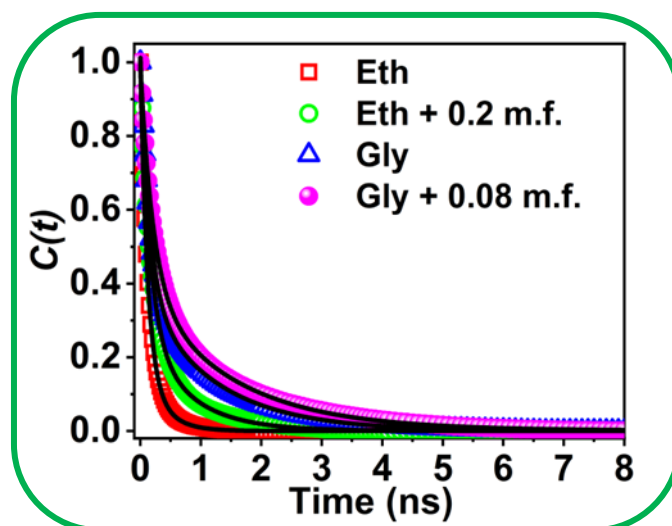


**Figure 5.6.** Spectral shift correlation function  $C(t)$  decay with time for C153 in ethaline and glyceline in absence and presence of LiNTf<sub>2</sub> at 298K. The solid line represents biexponential fit to the data point.

**Table 5.3.** Solvation relaxation parameters of both DESs with varying concentration of LiNTf<sub>2</sub> at 298K

System/(viscosity in cP)	bi-exponential fit				Stretched exponential fit			
	$a_1$	$\tau_1$ (ns)	$a_2$	$\tau_2$ (ns)	$\langle\tau_s\rangle$ (ns)	$\beta$	$\tau_{solv}$ (ns)	$\langle\tau_{st}\rangle$ (ns)
Ethaline/ (38.8)	0.82	0.11	0.18	0.34	0.16	0.90	0.14	0.16
Ethaline + 0.05 m.f. LiNTf <sub>2</sub> /(51)	0.78	0.12	0.22	0.38	0.18	0.86	0.17	0.18
Ethaline + 0.2 m.f. LiNTf <sub>2</sub> /(116)	0.70	0.15	0.30	0.73	0.32	0.77	0.27	0.32
Glyceline/ (345.7)	0.63	0.15	0.37	1.20	0.54	0.69	0.36	0.46
Glyceline + 0.05 m.f. LiNTf <sub>2</sub> /(377.8)	0.61	0.18	0.39	1.26	0.60	0.67	0.45	0.58
Glyceline + 0.08 m.f. LiNTf <sub>2</sub> /(409.9)	0.60	0.27	0.40	1.46	0.68	0.67	0.56	0.74

While analyzing the observable dynamics, we have found that the  $\langle\tau_s\rangle$  value of the ethaline medium is significantly less as compared to that in the glyceline medium (Table 5.3). This has happened due to higher bulk viscosity of the glyceline medium. Interestingly, upon addition of lithium salt, a gradual increase in  $\langle\tau_s\rangle$  for both DESs has been observed, which is also in accordance with the increase in bulk viscosities of these media. More interestingly, upon careful look, we can see from Table 5.3 that the contribution of the slower component increases gradually with an increase in the concentration of lithium salt. Here, we would like to note that, previously, it has been suggested that the fast component is associated with the relaxation of the local DES structure (nonhydrodynamic movement), whereas the slower component can be linked to the relaxation of the bulk hydrogen bonding network.<sup>224</sup> In view of this, we can infer that the reason for the increase in the contribution of the slower component can be attributed

to the formation of the hydrogen bonding network through the involvement of the  $\text{NTf}_2^-$  anion of  $\text{LiNTf}_2$  salt.

For the electrolytic application of a medium, the conductivity of the medium plays a pivotal role which in turn depends upon the diffusion coefficient of the cation and anion. From the well-known Nernst-Einstein equation, conductivity ( $\sigma$ ) and diffusion coefficient ( $D$ ) are related by the equation

$$\sigma = \frac{ne^2D}{kT} \quad (5.1)$$

where  $n$  is the number density of charge carrier,  $e$  represents electronic charge and  $k$  is the Boltzmann constant, and  $T$  is the absolute temperature. Furthermore, the diffusion coefficient is inversely proportional to the viscosity of the medium, which is given by Stokes-Einstein equation ( $D = \frac{kT}{6\pi\eta r}$ , equation 3A.2). By comparing equation (5.1) and (3A.2), it can be concluded that conductivity and viscosity follows a reciprocal relation. Hence, by lowering the viscosity, the electrical conductivity of a medium can be increased. Recently Maroncelli and Co-workers<sup>218</sup> have shown that the average solvation time and electrical conductivity of a medium are intricately related to each other. Through dielectric continuum model, they have shown that faster solvation (smaller  $\langle\tau_s\rangle$ ) favours the electrical conductivity of a medium. Looking at Table 5.3, we can see that for ethaline medium, both viscosity, as well as average solvation times are smaller as compared to glyceline medium. Further with addition upto 0.2 mole fraction of lithium salt to neat ethaline, the increase in  $\langle\tau_s\rangle$  value observed to be not very large ( $\sim 0.16$  ns) than that for neat ethaline. Moreover, and the  $\langle\tau_s\rangle$  of these solvent system found to be low as compared to ILs and ILs +  $\text{LiNTf}_2$  mixture.<sup>272</sup> These observations suggest that as compared to ILs ethaline medium containing lithium salt has the potential to serve as a relatively better medium for electrolytic applications.

### 5.3.3. Rotational Relaxation Dynamics

In order to get further insight into the microenvironment surrounding a probe solute, the time-resolved fluorescence anisotropy measurement has been performed in all the concerned solvent systems by employing three different probe solutes. In the present study also, the choice of the three probes is primarily governed by the fact that depending on different chemical characteristics of the probe molecule, they locate themselves in different regions of a particular solvent system, which, in turn, may allow us to probe those selective micro-regions (polar, non-polar) of the concerned solvent system.<sup>229, 274</sup>

**5.3.3.1. C153:** The fluorescence anisotropy decay profile of C153 in ethaline at 298 K is provided in Figure 5.7(a), and the rotational relaxation time ( $\tau_r$ ) of C153 in both DESs in the absence and presence of lithium salt are collected in Table 5.4 & Table 5.5. From the tables, it can be observed that, for both DESs, at a particular temperature, the  $\tau_r$  value of C153 is found to increase with an increase in mole fraction of lithium salt. This has happened due to the increase in bulk viscosity of the medium upon addition of lithium salt. Again, for a particular solvent system, with an increase in temperature,  $\tau_r$  value is found to decrease. The decrease in  $\tau_r$  value in all media with an increase in temperature is consistent with the lowering in the bulk viscosity of the corresponding medium. Upon careful inspection of Table 5.5, we can also see that upon going from neat ethaline to (ethaline + lithium salt (0.3 mole fraction)) mixture, the increase in bulk viscosity is estimated to be  $\sim 4$  times, whereas the  $\tau_r$  value is found to increase only by  $\sim 2$  times. This observation indicates that microviscosity felt by the probe in the media is different from the bulk viscosity of the media. This relatively faster rotation of C153 also reflects the lowering in solute-solvent interaction in (DESs + Li) salt mixture as compared to that in only neat DESs. The relatively larger increase in  $\tau_r$  value of C153 in glyceline than that in ethaline can be attributed to the higher viscosity of the latter than the former. It has been

noticed that with addition of lithium salt to the glyceline medium, no significant change in  $\tau_r$  value in the medium has been observed.

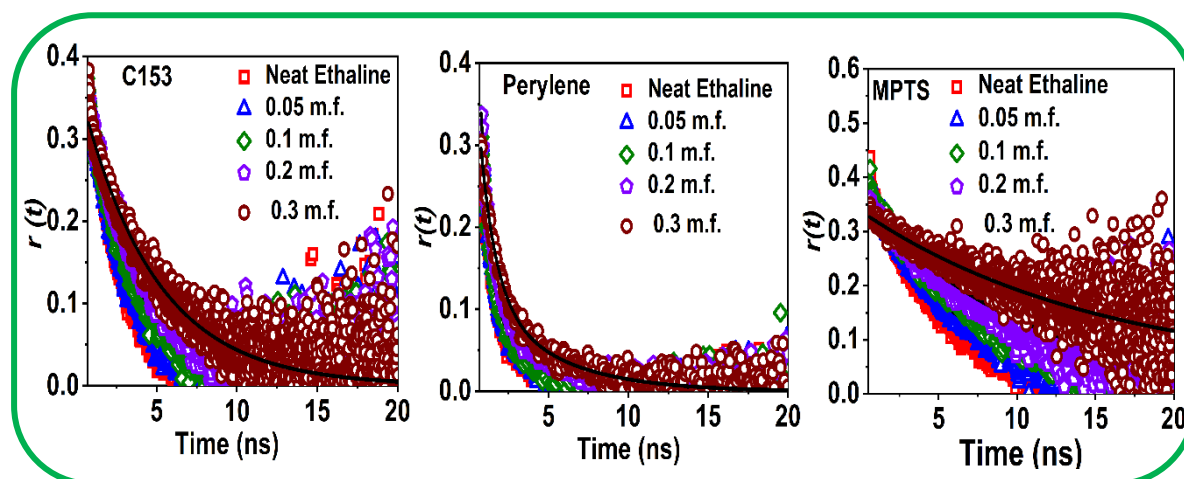


**Figure 5.7.** Time-resolved fluorescence anisotropy decay for C153, perylene and MPTS in ethaline in the absence and presence of LiNTf<sub>2</sub> at 298 K.

**Table 5.4.** Rotational relaxation parameter of different probes in glyceline.

System	$\eta$ (cP)/T (K)	C153		Perylene		MPTS	
		$\tau_r$ (ns)	$C_{obs}$	$\tau_r$ (ns)	$C_{obs}$	$\tau_r$ (ns)	$C_{obs}$
Neat Glyceline	345.7/(298)	11.07	0.40	3.2	0.13	18.7	0.68
	242.3/(303)	8.84		2.51		14.2	
	180.5/(308)	7.01		2.14		11.81	
	100.7/(318)	4.4		1.58		8.38	
	60.2/(328)	2.77		1.18		6.02	
Glyceline + 0.05 m.f. LiNTf <sub>2</sub>	377.8/(298)	11.79	0.41	3.35	0.12	22.15	0.57
	265.7/(303)	10.07		2.76		17.7	
	191.5/(308)	7.49		2.2		14.1	
	106.7/(318)	4.7		1.65		10.67	
	63.7/(328)	2.96		1.26		7.19	
Glyceline + 0.08 m.f. LiNTf <sub>2</sub>	409.9/(298)	12.36	0.41	3.54	0.13	23.41	0.50
	285.1/(303)	10.36		2.95		18.43	
	205.4/(308)	8.38		2.35		15.4	
	113.8/(318)	4.97		1.76		11.78	
	66.3/(328)	3.2		1.3		7.88	

**Table 5.5.** Rotational relaxation parameter of different probes in ethaline.

System	$\eta$ (cP)/T (K)	C153		Perylene		MPTS	
		$\tau_r$ (ns)	$C_{obs}$	$\tau_r$ (ns)	$C_{obs}$	$\tau_r$ (ns)	$C_{obs}$
Neat Ethaline	38.8/(298)	2.36	0.65	0.99	0.30	4.77	1.29
	30.8/(303)	1.92		0.82			
	24.7/(308)	1.58		0.70			
	16.7/(318)	1.10		0.51			
	12.3/(328)	0.82		0.36			
Ethaline + 0.05 m.f. LiNTf <sub>2</sub>	51/(298)	2.75	0.59	1.15	0.27	5.98	1.31
	37.9/(303)	2.18		0.92			
	31.4/(308)	1.79		0.80			
	20.9/(318)	1.22		0.57			
	14.2/(328)	0.88		0.40			
Ethaline + 0.1 m.f. LiNTf <sub>2</sub>	68/(298)	3.43	0.55	1.25	0.22	7.67	1.24
	52.2/(303)	2.68		1.02			
	41.9/(308)	2.20		0.88			
	27.5/(318)	1.54		0.62			
	18.3/(328)	1.07		0.44			
Ethaline + 0.2 m.f. LiNTf <sub>2</sub>	116/(298)	4.69	0.45	1.66	0.18	10.28	1.07
	88.1/(303)	3.71		1.31			
	69.7/(308)	3.10		1.10			
	35.1/(318)	2.05		0.77			
	28.9/(328)	1.45		0.58			
Ethaline + 0.3 m.f. LiNTf <sub>2</sub>	172.7/(298)	5.77	0.40	2.14	0.16	15.26	1.05
	128.2/(303)	4.77		1.74			
	100.7/(308)	3.90		1.40			
	61.5/(318)	2.58		0.94			
	39.2/(328)	1.80		0.76			

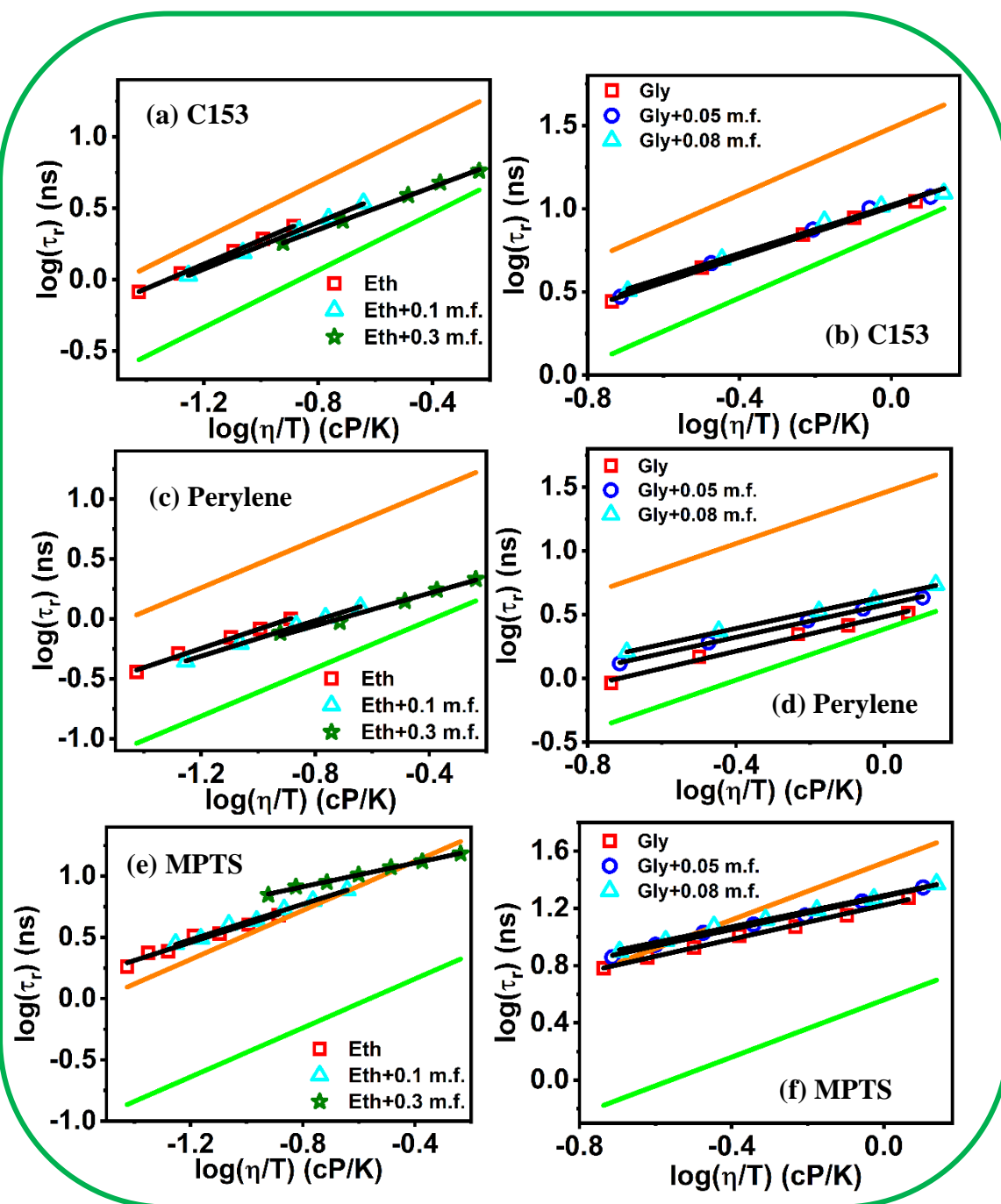


**Figure 5.8.** log- log plot of  $\tau_r$  versus  $\eta/T$  of C153 (a), (b); Perylene (c), (d) and MPTS (e), (f). Left side panel is for ethaline and right-side panel is for glyceline. Different mole fraction of LiNTf<sub>2</sub> added to both DESs are shown in the legends. Solid Brown and green line represent the slip and stick boundary condition respectively. Solid black line represents linear fit to the data points.

In order to get further insight into the rotational behaviour of C153 in these given media, the time-resolved fluorescence anisotropy data has been analyzed based on Stokes-Einstein-

Debye (SED) hydrodynamic theory.<sup>193, 232, 277</sup> Figures 5.8(a)&(b) represent the log-log plot of  $\tau_r$  versus  $\eta/T$  of C153 in both DESs respectively. From Figure 5.8, we can observe that the rotation of C153 in both media in neat condition as well as in the presence of lithium salts, falls within the broad limits predicted by the SED theory. However, it can also be noticed from the plot that the rotational dynamics of C153 in both DESs are somewhat different from one another. This change in the rotational behaviour of C153 in these media is also reflected in the estimated  $C_{obs}$  values. For ethaline medium, with increase in the concentration of lithium salt, a gradual decrease in the  $C_{obs}$  value is observed, whereas for glyceline medium, the value of  $C_{obs}$  remains almost the same throughout (Table 5.5).

Further analysis of the rotational behaviour of C153 in both aforesaid media has also been done in light of the empirical relation<sup>175-185</sup>  $\tau_r = A(\eta/T)^p$ , as this can provide an idea about the dependence of  $\tau_r$  to  $\eta/T$ , where both  $A$  and  $p$  are constant. Hence, the departure of the exponent  $p$  from unity signifies the extent of non-linearity in the  $\tau_r$  versus  $\eta/T$  plot. This fractional dependence of viscosity to rotational relaxation time has been attributed to the viscosity-diffusion decoupling of the solute molecule in the concerned solvent systems. It has been already mentioned in previous chapters that the decoupling of rotational motion of solute with the medium viscosity happens due to heterogeneity of the medium. Table 5.6 summarizes the fitted value of  $A$  and  $p$ . From the table, it can be seen that the deviation of  $p$  value from unity is more in case of glyceline medium ( $p = 0.76$ ) as compared to ethaline medium ( $p = 0.85$ ). Interestingly, with addition of lithium salts to both media, more departure of  $p$  value from unity is observed (Table 5.6). This clearly suggests that addition of higher amount of lithium salt induces more dynamic heterogeneity in the medium.

**Table 5.6.** Parameters A and  $p$  obtain from the fits of  $\log \langle \tau_r \rangle$  vs  $\log \langle \eta/T \rangle$ 

System	C153		Perylene		MPTS	
	A	$p$	A	$p$	A	$p$
Ethaline	$13.5 \pm 0.01$	$0.85 \pm 0.01$	$5.14 \pm 0.04$	$0.80 \pm 0.04$	$23.45 \pm 0.02$	$0.77 \pm 0.02$
Ethaline + 0.05 m.f. LiNTf <sub>2</sub>	$12.33 \pm 0.02$	$0.84 \pm 0.02$	$4.47 \pm 0.02$	$0.76 \pm 0.02$	$22.95 \pm 0.04$	$0.73 \pm 0.03$
Ethaline + 0.1 m.f. LiNTf <sub>2</sub>	$11.5 \pm 0.01$	$0.82 \pm 0.01$	$3.81 \pm 0.01$	$0.74 \pm 0.01$	$21.89 \pm 0.02$	$0.70 \pm 0.02$
Ethaline + 0.2 m.f. LiNTf <sub>2</sub>	$10.00 \pm 0.01$	$0.79 \pm 0.01$	$3.17 \pm 0.02$	$0.71 \pm 0.02$	$19.5 \pm 0.02$	$0.63 \pm 0.03$
Ethaline + 0.3 m.f. LiNTf <sub>2</sub>	$8.95 \pm 0.02$	$0.75 \pm 0.02$	$3.02 \pm 0.02$	$0.67 \pm 0.04$	$19.97 \pm 0.01$	$0.57 \pm 0.01$
Glyceline	$10.25 \pm 0.01$	$0.76 \pm 0.02$	$3.02 \pm 0.02$	$0.53 \pm 0.01$	$16.6 \pm 0.01$	$0.60 \pm 0.02$
Glyceline + 0.05 m.f. LiNTf <sub>2</sub>	$10.5 \pm 0.01$	$0.75 \pm 0.04$	$3.81 \pm 0.01$	$0.52 \pm 0.02$	$19.1 \pm 0.01$	$0.58 \pm 0.02$
Glyceline + 0.08 m.f. LiNTf <sub>2</sub>	$10.5 \pm 0.02$	$0.72 \pm 0.04$	$4.47 \pm 0.01$	$0.52 \pm 0.01$	$19.5 \pm 0.01$	$0.55 \pm 0.03$

**5.3.3.2. Perylene.** Figure 5.7 provides the fluorescence anisotropy decay profile of a non-polar probe perylene in ethaline in the absence and presence of lithium salts at 298K, and the  $\tau_r$  values of perylene in both DESs in neat as well as after the addition of lithium salts are also collected in Table 5.4 and Table 5.5. From Figure 5.7, we can see that the rotation of perylene is much faster as compared to C153 and MPTS (*vide infra*), indicating that the solute-solvent interaction is relatively less than that for the other two probes. From the tables, we can also see that upon going from ethaline to glyceline, the bulk viscosity increases by nearly 10 times while the increase in  $\tau_r$  values is estimated to be just above 3 times. This faster rotation of perylene in glyceline medium as compared to that in ethaline medium indicates the significant differences in the microscopic structural organization of both DESs. It may be noted here that Lawler et al.<sup>303</sup> have also reported the faster rotational diffusion of perylene in [BMIM][Tf<sub>2</sub>N]-LiTf<sub>2</sub>N mixture with increase in lithium salt concentration. The authors have rationalized the

---

---

faster diffusion of perylene with increase concentration of lithium salt in the ionic liquids by considering the change in the structural organization of ionic liquids upon addition of lithium salt. From the log-log plot of  $\tau_r$  versus  $(\eta/T)$  (Figures 5.8(c)&(d)) for ethaline and glyceline medium we can see that the rotational relaxation time falls well within the limits as predicted by SED theory. However, on careful inspection of the SED plot of perylene, it can be observed that the rotation of perylene is getting faster with an increase in the lithium-ion concentration in ethaline whereas  $\tau_r$  value almost remains same with respect to glyceline. This fact is also evident from the estimated  $C_{obs}$  value also. For example, addition of 0.3 mole fraction of lithium salt to ethaline, the  $C_{obs}$  value become half of neat ethaline ( $C_{obs} = 0.26$ ) at 298K. However, with addition of 0.08 mole fraction lithium salt to glyceline the  $C_{obs}$  value almost remains unchanged. This clearly depict that addition of lithium salt to both systems induces different structural changes due to which perylene experiences different microenvironment for different (DES + Li salt) mixture solvent systems.

**5.3.3.3. MPTS.** MPTS being a charged species generally located in the polar region and has the ability to form hydrogen-bonding interactions with the solvent molecule. From the fluorescence anisotropy decay curve (Figure 5.7), one can see that the rotational diffusion of MPTS is significantly slower as compared to perylene. For example, the  $\tau_r$  value is observed to increase nearly by a factor of  $\sim 5$  upon going from perylene to MPTS in ethaline medium. The slower rotation of MPTS as compared to perylene in ethaline indicates that solute-solvent interaction is more for the former than the latter. Furthermore, there is  $\sim 9$  folds increase in viscosity upon going from ethaline to glyceline, whereas the increase in  $\tau_r$  value of MPTS is  $\sim 4$  folds. This indicates that MPTS experiences less amount of solute-solvent interaction in glyceline medium as compared to that in ethaline medium. This observation subsequently signifies that solvent-solvent interaction is more in glyceline medium, whereas solute-solvent

interaction is more in ethaline medium. In order to get more idea regarding the rotational behaviour of MPTS in (DES + Li salt) mixture, data have been analyzed by SED hydrodynamic theory. The log-log plot of  $\tau_r$  versus  $\eta/T$ , along with the stick and slip line of MPTS, are provided in Figures 5.8(e)&(f) for both ethaline and glyceline medium. From Figures 5.8(e)&(f), it can be observed that for ethaline medium the experimentally calculated  $\tau_r$  value lies above the stick line. But for glyceline medium, the experimental  $\tau_r$  value lies below it, but is more close to the stick line. When the experimental  $\tau_r$  lies above the stick line, it is called as superstick behaviour in hydrodynamic terminology.<sup>233</sup> This superstick behaviour generally arises due to strong solute-solvent interaction. Similar kind of superstick behaviours have also been observe in case of room temperature ionic liquids have also been observed by different groups.<sup>226, 227, 229-231, 233, 276</sup> Furthermore, Samanta and co-worker<sup>185</sup>, while working on ethaline also encountered the superstick behaviour of both Rhodamine123 and Fluorescein. The authors have attributed the superstick behaviour of these probes to specific solute-solvent interactions, such as hydrogen bonding interaction between these probe molecules and the constituents of ethaline. Therefore, in the present scenario, the hindered rotation of MPTS perhaps is also suggesting the strong solute-solvent interaction between the sulphite groups of MPTS with the constituent of DES. Moreover, the increase in  $C_{obs}$  value of MPTS for ethaline medium with the increase in lithium salt concentration indicates the increase in specific solute-solvent interaction between solute and solvent molecules.

#### 5.3.4. PFG-NMR Studies

To explore a more detailed understanding about the mobility of different components present in the DES pulse field gradient (PFG) NMR technique has also been employed in the present work. This experiment is done to measure the translational diffusion coefficients ( $D$ ) of the DES and (DES+ Li salt) mixture independently. Measurement of  $D$  value not only provides

idea about the shape, size, and mass of the diffusive species but also indicates the cationic-anionic interaction and microscopic structural organization of the solvent system.<sup>163, 164, 247, 277</sup>

**Table 5.7.** Estimated translational diffusion coefficient of DESs with varying mole fraction of LiNTf<sub>2</sub>

System	$D \times 10^{-11} \text{ m}^2/\text{s}$		
	298 K	308 K	318 K
Ethaline	2.2	3.38	4.99
Ethaline + 0.05 m.f. LiNTf <sub>2</sub>	1.97	3.04	4.57
Ethaline + 0.1 m.f. LiNTf <sub>2</sub>	1.54	2.37	3.63
Ethaline + 0.2 m.f. LiNTf <sub>2</sub>	1.08	1.81	2.8
Ethaline + 0.3 m.f. LiNTf <sub>2</sub>	0.65	1.16	1.79
Glyceline	0.40	0.76	1.35
Glyceline + 0.05 m.f. LiNTf <sub>2</sub>	0.34	0.67	1.2
Glyceline + 0.08 m.f. LiNTf <sub>2</sub>	0.32	0.63	1.12

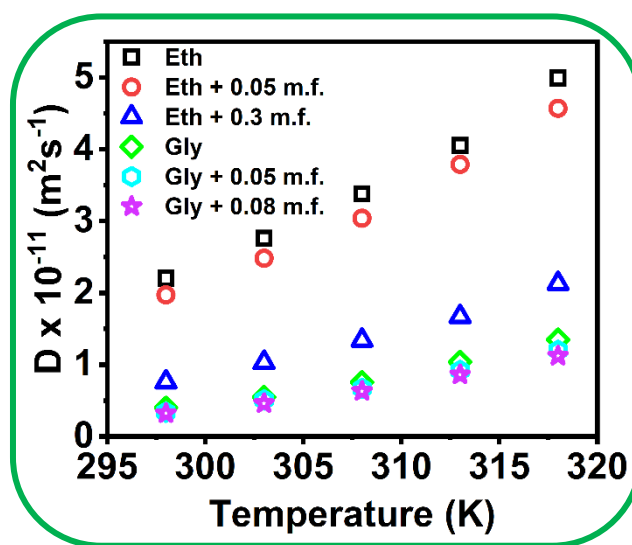


**Figure 5.9.** Temperature-dependent variation of the self-diffusion coefficients of neat DES and (DES + Li salt) mixture.

The values of  $D$  for both DESs in the absence and presence of LiNTf<sub>2</sub> at various temperatures are measured by fitting the data through Stejskal–Tanner equation.<sup>264</sup> Since choline cation is common in all solvent systems under consideration, its diffusion coefficients

have been monitored and are collected in Table 5.7. The  $D$  values (Table 5.7) obtained for both DESs are consistent with previously reported value.<sup>163, 164</sup> Further, we can see that for all solvent systems, the  $D$  value increases with increase in temperature which can be ascribed to the lowering of viscosity of the medium. With addition of lithium salt to both medium there is a lowering of  $D$  value which is also in accordance with the increase in bulk viscosity of the medium. However, it is interesting to note that the change in  $D$  value for both DESs with viscosity does not follow linear correlation. For example, upon going from ethaline to glyceline the viscosity change is nearly  $\sim 10$  times, whereas the decrease in  $D$  value is found to be smaller than 5 times. This disproportionate change in  $D$  value with bulk viscosity of the medium clearly indicates the dissimilarities in the microscopic structural organization of the DESs. The lower diffusion coefficient of glyceline than ethaline is accounted for the presence of more extensive hydrogen bonding network between the HBD and HBA as well as within the HBD itself.<sup>163-164</sup>

### 5.3.5 Arrhenius Behaviour

In order to get an idea about the rate of change of translational and rotational diffusion as well as viscous flow of the (DES + Li salt) mixture with respect to temperature, the data have been further analysed through Arrhenius equation. Similar analysis are often found to be useful for various ILs and DESs solvent systems.<sup>163, 164, 272</sup> Fitting of the data through Arrhenius equation provide the value of activation energy for viscous flow, translational and rotational diffusion which in turn provide information regarding the microenvironment of the diffusive species. The temperature dependence of translational diffusion and viscous flow are usually fitted by employing Arrhenius equation.<sup>64</sup> The rotational relaxation time ( $\tau_r$ ) of C153 (Table 5.4 & Table 5.5) in neat DES as well as in presence of lithium salt at various temperatures have also been analysed through Arrhenius equation.<sup>272</sup>

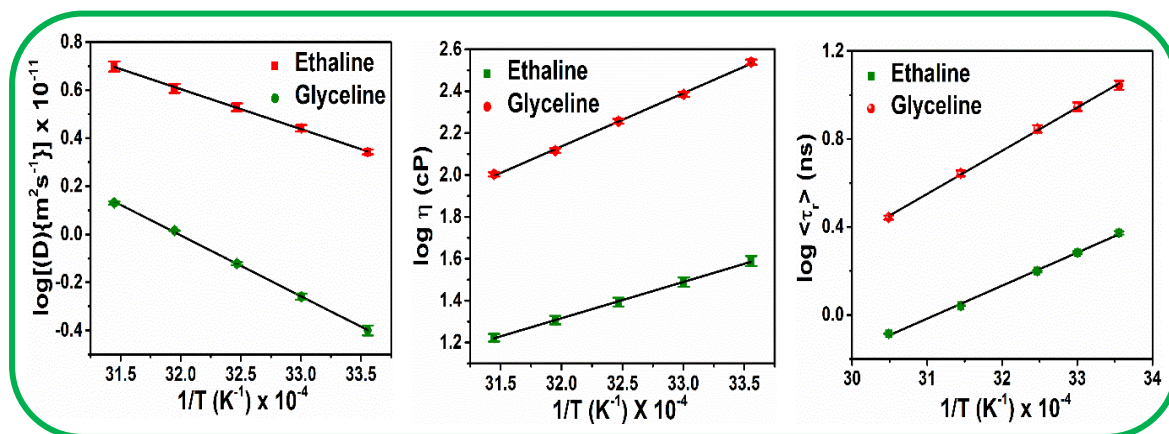


**Figure 5.10.** Arrhenius fitting to (a) translational diffusion coefficient, (b) Viscosity (c) rotational diffusion coefficient of C153 in both DESs.

**Table 5.8.** Activation energy for viscous flow ( $E_\eta$ ), translational Diffusive flow of choline cation, ( $E_{D,CH^+}$ ) and Rotational diffusive flow ( $E_r$ ) for C153 in DESs and DES + Li Mixture

System	Viscous flow ( $E_\eta$ ) (kJ/mol)	Translational Diffusive flow ( $E_{D,CH^+}$ ) (kJ/mol)	Rotational diffusive flow $E_r$ (kJ/mol) for C153
Ethaline	$33.16 \pm 0.40$	$31.87 \pm 0.50$	$28.74 \pm 0.60$
Ethaline + 0.05 m.f. LiNTf <sub>2</sub>	$35.05 \pm 0.70$	$33.22 \pm 0.37$	$30.79 \pm 0.58$
Ethaline + 0.1 m.f. LiNTf <sub>2</sub>	$35.32 \pm 0.66$	$33.61 \pm 1.40$	$31.04 \pm 0.66$
Ethaline + 0.2 m.f. LiNTf <sub>2</sub>	$38.10 \pm 0.46$	$37.82 \pm 1.60$	$31.77 \pm 0.48$
Ethaline + 0.3 m.f. LiNTf <sub>2</sub>	$40.29 \pm 0.77$	$40.01 \pm 1.51$	$31.90 \pm 0.43$
Glyceline	$48.65 \pm 0.94$	$47.44 \pm 0.75$	$37.64 \pm 0.65$
Glyceline + 0.05 m.f. LiNTf <sub>2</sub>	$49.72 \pm 0.95$	$48.04 \pm 0.69$	$38.29 \pm 1.34$
Glyceline + 0.08 m.f. LiNTf <sub>2</sub>	$50.23 \pm 0.96$	$48.32 \pm 0.74$	$37.52 \pm 1.54$

Figures 5.10(a)&(b) represents the Arrhenius behaviour in terms of diffusion coefficients ( $D$ ) and viscosity ( $\eta$ ) respectively. Table 5.8 collects the activation energy values that are estimated separately for both diffusive and viscous flow. Form Table 5.8 it can be seen that for all DES the activation energies for viscous flow are little higher than the activation energies

for translational diffusive flow. However, for rotational diffusion, the activation energy is comparatively low. This indicates that the translational diffusion is more closely associated with the viscosity of the medium as compared to rotational diffusion of a probe molecule. Furthermore, with increase in lithium salt concentration, the deviation of activation energy of rotational diffusion from the activation energy of bulk viscosity of the medium has also found to increase. These observations also supports the fact that the structural organisation of both media are different and addition of lithium salts also change the microstructural organisation of the media.

#### **5.4. Conclusion**

In the present report the behaviour of two deep eutectic solvents in their neat condition and their mixture with lithium salt have been investigated through several spectroscopic techniques such as steady state, time resolved fluorescence, EPR and NMR measurements so as to realise the potential of these solvent systems as electrolytic media for electrochemical uses. Several interesting results have been obtained from these studies. EPR spectral measurements have revealed that the polarities of the medium are closed to aliphatic poly-hydroxy alcohol and polarity of the medium found to increase with increase in the concentration of lithium salt. Studies on dynamic of solvation have shown an increase in average solvation time with increase in concentration of lithium salt. Interestingly, correlation of average solvation time and conductivity of the concerned media have indicated that ethaline, as compared to glyceline, may serve as a relatively better candidate for electrochemical uses. Investigation of rotational dynamics through time resolved fluorescence anisotropy and measurements of self-diffusion coefficient through NMR of both DESs have suggested significant perturbation in the structural organisation of these solvent systems in presence of lithium salt. The present study demonstrate that the structural organisation of both ethaline and glyceline are significantly different from

each other and addition lithium salt considerably perturb the nano/micro structural organisation of the solvent systems. The outcome of present study is expected to be helpful to understand the microscopic behaviour of (DES + Li salt) mixtures and thereby enable us to realise the potential of these media in electrochemical applications including application in lithium-ion battery.

# CHAPTER 6

---

## Assessing the Influence of Deep Eutectic Solvents on the Structure and Conformational Dynamics of BSA

---

Barik, S.; Mahapatra, A.; Preeyanka, N.; Sarkar, M.; *Phys. Chem. Chem. Phys.*, 2023, 25, 20093-20108.

**Abstract**

Although deep eutectic solvents (DESs) are regarded as useful substitutes for both ionic liquids and common organic solvents for storage and applications of biomolecules, it is still unclear whether all DESs or only specific types of DES will be suitable for the said purpose. In view of this, the work of the present chapter aims to report on the structure and conformational dynamics of BSA in the presence of two DESs, namely Ethaline (Choline chloride: ethylene glycol) and BMEG (benzyltrimethyl ammonium chloride: ethylene glycol), having the same hydrogen bond donor but with distinct hydrogen bond acceptor, so that how small changes in one constituent of a DES alter the protein-DES interaction at the molecular level can be understood. The protein-DES interaction is investigated by exploiting both ensemble-averaged measurements like steady-state and time-resolved fluorescence spectroscopy, circular dichroism (CD) spectroscopy, and single-molecule measurement technique like fluorescence correlation spectroscopy (FCS). Interestingly, the results obtained from these studies have demonstrated that while a very small quantity of BMEG completely unfolds the native structure of the protein, it remains in a partially unfolded state even at very high ethaline content. More interestingly, it has been found that at very high concentrations of BMEG, the unfolded protein undergoes enhanced protein-protein interaction resulting in the aggregation of BSA. All of the results obtained from these investigations have essentially suggested that both protein-DES interaction and interspecies interaction among the constituent of DESs play a crucial role in governing the overall stability and conformational dynamics of the protein in DESs.

---

**6.1. Introduction**

The quest for suitable reaction media for biocatalytic and biotransformation reactions that can maintain the three-dimensional structure of the protein while allowing effective substrate

---

---

binding, complex formation, and product release is a persistent need in the pharmaceutical and food processing sectors.<sup>305-307</sup> Therefore, scientific research activity to obtain environmentally benign solvents which can maintain the structural and functional integrity of protein, even at very harsh conditions (such as in the presence of denaturant, high temperature, very high/very low pH, etc.), is rapidly accelerating.<sup>9, 308</sup> In this regard, both ionic liquids and common organic solvents have had their fair share of history and hype, and within that ecosystem, deep eutectic solvents (DESs) have come to light as a better feasible option as compared to both of them.<sup>16, 18-20, 64</sup> DESs are known to compensate several of the drawbacks of ILs, including toxicity, biodegradability, biocompatibility, and so on, making them even a superior media for enzymatic reactions, storage, and boosting the stability of various biomacromolecules.<sup>21, 109, 110</sup> However, the behavior of biomolecules in these media has been poorly understood in terms of their intermolecular interaction and dynamics with DESs, perhaps due to very less number of literature on this issue. Moreover, it is still unclear whether all types of DESs or only certain kinds of DESs are suitable for bio-related applications. Therefore, it is important to have a molecular-level understanding of protein-DES interaction so that proper design and development of new DESs, which can maintain the structural and functional integrity of the protein in the presence of DESs, can be done.

Whilst a substantial number of studies on the activity and stability of biomacromolecules in the presence of ILs have been thoroughly investigated<sup>263, 309-312</sup>, very few reports on the same issues by employing DESs, have been documented.<sup>313-323</sup> Huang et al.<sup>317</sup> have thoroughly studied the activity, stability, and toxicity of choline chloride (ChCl) and acetylcholine chloride (AchCl)-based DESs in neat as well as in their aqueous solution on some proteins and enzymes. Esquembre et al.<sup>315</sup> have reported that no change in the native structure of lysozyme can be seen in the presence of neat and hydrated ChCl-based DESs. Further,

Stamatis and colleagues<sup>320</sup> have also observed high stability of cytochrome c (cyt c) in the presence of 30% v/v aqueous solution of different ammonium salt based-DESs. They have also reported that the nature of the ammonium salt and the hydrogen bond donor used for the formation of DES, as well as their quantity in the reaction mixture, had a significant impact on the catalytic activity of heme-dependent proteins. While working on the same objective, Venkatesu and co-workers<sup>313, 314, 322</sup> demonstrated high stability of different biomacromolecules such as haemoglobin, bovine serum albumin (BSA), and  $\alpha$ -chymotrypsin in the presence of ChCl-based DESs, suggesting that the enhanced stability of these proteins is due to the formation of DESs complexes rather than the synergistic effect of individual components. Moreover, enhanced thermal and pH stability of DNA backbone in the presence of DESs has also been reported by some researchers.<sup>318, 323</sup> In addition, some computational studies have also been documented on the stability of various proteins in the presence of ChCl-based DESs.<sup>319, 324</sup> Many of the results have essentially suggested DESs as non-toxic and better-stabilizing media. However, there are also a few reports which have proposed that DESs may cause disruption in the secondary structure of the protein and can destabilize it. For instance, Antalik and co-workers<sup>325</sup> have reported that DES made from guanidinium salts and urea has been discovered to completely denature the secondary and tertiary structure of the enzyme cyt c. In a similar line, Samanta and co-workers<sup>316</sup>, while working on the structural stability of cyt c in the presence of DESs, reported that while AchCl-glycerol-based DES maintains the structural stability of cyt c, AchCl-ethylene glycol-based DES completely unfolds the protein secondary and tertiary structure.

In view of all these above discussions, it is clear that the behaviour of protein-DES interaction in terms of maintaining the structural integrity and biocatalytic activity of protein is still ambiguous. These reports have also suggested that it is almost impossible to anticipate

the behaviour of the protein in the presence of DESs in advance since it relies heavily on the chemical nature of a DES in general and interspecies interactions between the various constituents of that DES in particular. Further, most of these studies report on the influence of DESs on protein's stability and activity using CD (circular dichroism) spectroscopy and other ensemble average measurements and do not give any information regarding the structure and conformational dynamics of the protein at single-molecular resolution. Apart from these, practically all of these researches have been conducted on the impact of choline chloride or acetylcholine chloride-based DESs on protein's structure and conformations, leaving many other types of DESs, such as hydrophobic DES, alkyl/benzyl phosphonium based DES, or natural DESs (NADES), unexplored. Considering this, it is essential to acquire a thorough knowledge of the protein-DES interaction by applying various types and classes of DESs by single-molecule and ensemble-average measurements.

Keeping the above issue in mind, in the present study, an attempt has been made to investigate the impact of two chemically distinguishable DESs on the structural stability and conformational dynamics of BSA (bovine serum albumin). BSA was chosen selectively because its structure and conformation are very sensitive to external additives, and it is frequently used as a model protein to investigate protein-ligand interaction.<sup>326</sup> Apart from this, easy labelling of the protein with external dyes while retaining its structure and conformation makes it even a better choice for understanding protein-ligand interaction at a single-molecular level.<sup>327, 328</sup> The two DESs employed in this investigation are Ethaline (Choline chloride: ethylene glycol) and BMEG (benzyl trimethyl ammonium chloride: ethylene glycol), both of which have the same HBD but distinct HBAs.<sup>19-20, 186, 329</sup> The two DESs used in the study were also chosen expressly to understand how changes in one component (HBAs) of DESs affect the protein-DES interaction and alter the structure and conformation of the protein. Initially,

the behaviour of protein-DES interaction has been studied by using steady-state and time-resolved fluorescence spectroscopic techniques. Additionally, investigations have also been done by exploiting FCS and CD spectroscopy techniques so that a molecular-level understanding of the alternation in the structure and conformational dynamics of the protein in the presence of DESs can be obtained. The results obtained from the studies have revealed that changes in even one component of the DES mixture have a considerable effect on DES-protein interaction, suggesting that both protein-DES interaction and interaction with the DES components govern the overall structure and conformation of the protein in the presence of DESs. Chart 6.1 depicts the native structure of BSA and the chemical structures of the components of the DESs employed in this investigation.

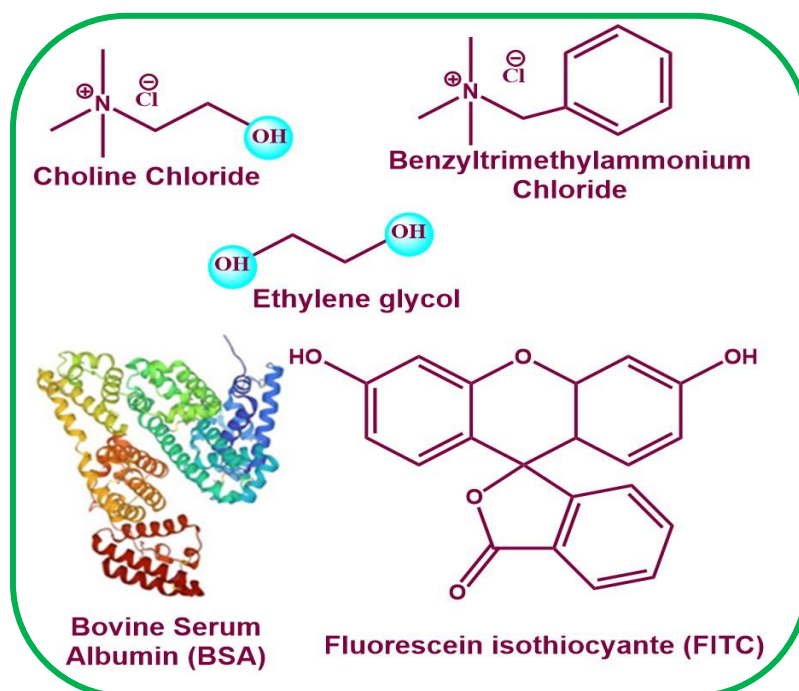


**Chart 6.1.** (a) Molecular structure of different constituents of DESs, (b) BSA in native state and (c) fluorescein isothiocyanate (FITC) dye.

## 6.2. Experimental Sections

The detail about the synthesis and characterization of both DESs are provided in APX 6.1. The protein stock solution was made by dissolving the BSA powder in the 10 mM phosphate buffer

of pH 7.4. and stirring gently at room temperature. All the samples were prepared fresh and allowed to settle for 15 minutes before being introduced into the instrument. The addition of different quantities of DESs to the protein solution is represented in weight/volume percentage (% w/v), and the amount of DESs varies from 00 % w/v to 90 % w/v. For the steady-state, time-resolved spectroscopy, and CD spectroscopy measurements, the concentration of BSA (without dye tagged) was 2  $\mu$ M in the experimental buffer. For the CD spectroscopy measurement, the highest concentration of Ethaline and BMEG is 50% and 20 %, respectively, so as to keep the HT voltage below 700V. For the studies involving the dye-tagged protein, the concentrations of BSA-FITC were 4  $\mu$ M and 4 nM for ensemble average (steady-state and time-resolved spectroscopy) and single-molecule measurements, respectively. Following the literature-reported method, the dye-to-protein ratio in the labelled protein was calculated using absorbance and molar extinction coefficient values (43824  $M^{-1}cm^{-1}$  for BSA at 280 nm and 68000  $M^{-1}cm^{-1}$  for FITC at 495 nm) and was found to be  $\sim$ 1.2.

### 6.3. Results and Discussions

#### 6.3.1. Quenching of the Intrinsic Fluorescence of BSA in the Presence of DES

The intrinsic fluorescence of albumin proteins is highly sensitive to its structural conformation and local microenvironment surrounding it, and because of this, the intrinsic protein fluorescence has been frequently used to study the interaction of proteins with various organic molecules, drugs, surfactants, ionic liquids, etc.<sup>330-332</sup> Considering this in mind, in the present study also the intrinsic fluorescence of BSA in absence and presence of DESs have been exploited to get information on the interactions between DES and protein. Note that the fluorescence of BSA appears at 340 nm due to the  $n \rightarrow \pi^*$  transition of different fluorophore amino acid residues (tryptophan (Trp), tyrosine (Tyr), and phenylalanine (Phe)) in the protein.<sup>330-332</sup> However, the intrinsic fluorescence of BSA is observed to be primarily

dominated by the Trp residue as both Tyr and Phe residues have very less quantum yield in the aqueous medium.<sup>330-332</sup> Furthermore, by fixing the excitation wavelength at 295 nm, not only the contribution of Tyr and Phe residue can be eliminated, but also the charge and energy transfer in BSA to the indole side chain of tryptophan moiety can also be avoided.<sup>330</sup> Since the present DESs systems (Ethaline and BMEG) also show negligible absorbance at 295 nm (Figure APX6.2), in the present study, the fluorescence of BSA has been recorded by exciting the samples at 295 nm. However, since the possibility of the inner filter effect cannot be ruled out in the present case, the correction for the same is done by using the following standard equation<sup>193, 225</sup>

$$F^{Corr}(\lambda_E, \lambda_F) = F(\lambda_E, \lambda_F) \times \frac{A(\lambda_E)}{A_{tot}(\lambda_E)} \quad (6.1)$$

where,  $F^{Corr}(\lambda_E, \lambda_F)$  is the corrected fluorescence intensity at the excitation wavelength ( $\lambda_E$ ) and emission wavelength ( $\lambda_F$ ),  $F(\lambda_E, \lambda_F)$  is the observed fluorescence intensity at  $\lambda_E$  and  $\lambda_F$ ,  $A$  represents the optical density of the free protein and  $A_{tot}$  is the total optical density of the solution at the excitation wavelength ( $\lambda_E$ ).

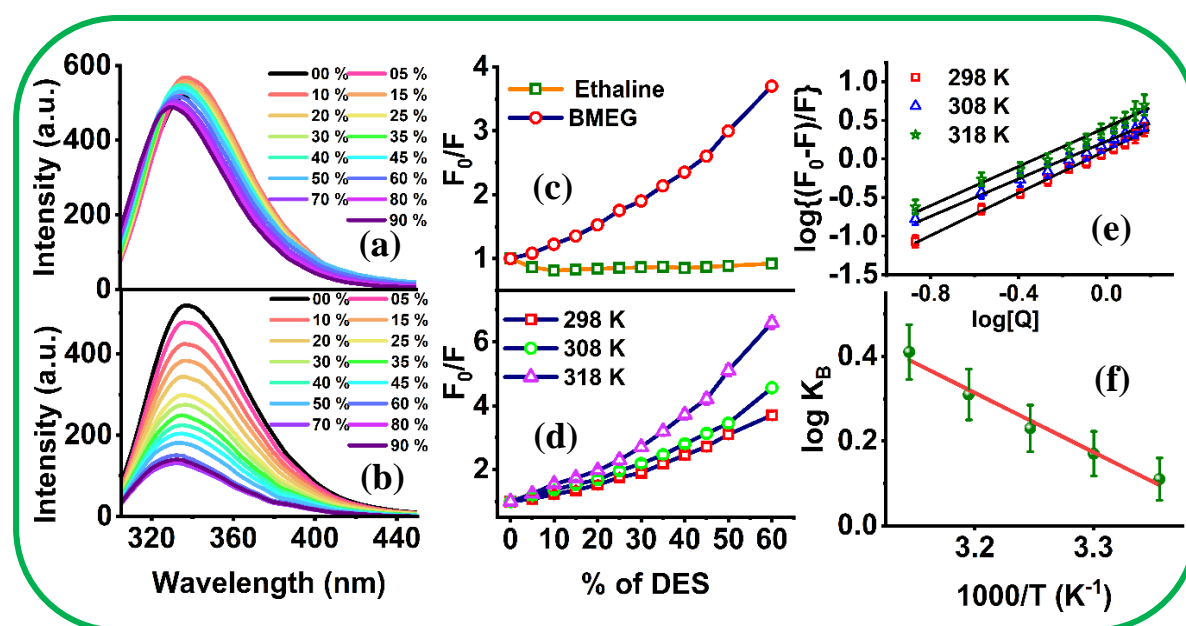


**Figure 6.1.** Fluorescence emission spectra ( $\lambda_{ex} = 295\text{nm}$ ) of BSA in absence and presence of gradual addition of (a) ethaline and (b) BMEG. (c) Stern-Volmer plot for BSA-BMEG and

BSA-ethaline at 298K. (d) Stern-Volmer plot for BSA-BMEG at 3 different temperatures. (e) Double logarithmic plot at three different temperatures for BSA-BMEG (solid black line shows the linear fit). (f) Binding constant versus temperature for BSA-BMEG (solid red line shows the linear fit of the data points).

The corrected fluorescence spectra of BSA at 298K in the absence and presence of different percentages of DESs are given in Figure 6.1(a) & (b). From Figure 6.1(b), one can clearly observe that the intrinsic fluorescence of BSA gradually decreases with the addition of BMEG, and a similar trend has been seen when studies are performed at other temperatures (Figure APX6.3). The intrinsic fluorescence of BSA is found to be quenched by around 75% when 60% of BMEG is added to the aqueous solution of BSA (Figure 6.1(b) & (c)). However, no appreciable decrease in fluorescence intensity has been seen with further increase in the BMEG concentration (70-90%) has been increased further. In contrast to this, the addition of 60% ethaline has hardly any effect on the intrinsic fluorescence of BSA. In fact, only a very slight reduction in the fluorescence of BSA is seen when 90% ethaline is added to the aqueous solution of BSA. In addition to this, the fluorescence spectra of BSA show a blueshift of 8 nm with the addition of 60% BMEG as compared to a shift of 2 nm of the same when same quantity of ethaline is added to the BSA solutions. The shift in fluorescence maxima and the decrease in the fluorescence intensity of BSA are indicative features of the change in the microenvironment around the fluorophore and the folding alteration of the protein.<sup>310, 333, 334</sup> The observation of a blue shift of the protein fluorescence in the presence of BMEG indicates a more hydrophobic environment around the fluorescence amino acid residues.<sup>310, 333, 334</sup> This early study demonstrates that while the BMEG considerably affects both the structure and microenvironment of BSA, ethaline cannot induce appreciable changes in the native structure of BSA.

Since a number of processes, including collisional quenching, molecular rearrangement, excited state reaction, and ground state complex formation, may also be

responsible for the fluorescence quenching phenomenon of BSA, it is crucial to fully comprehend the underlying mechanism of quenching of BSA fluorescence in the presence of BMEG.<sup>193, 225</sup> Therefore, the fluorescence quenching data are analyzed by the classical Stern-Volmer (SV) models, which is given as follows

$$\frac{F_0}{F} = 1 + K_S \cdot [Q] \quad 6.2a$$

$$\frac{\tau_0}{\tau} = 1 + K_D \cdot [Q] \quad 6.2b$$

where  $F_0$  ( $\tau_0$ ) is the fluorescence intensity (lifetime) in the absence of quencher and  $F$  ( $\tau$ ) is the same in the presence of quencher,  $[Q]$  is the quencher concentration,  $K_s$  and  $K_D$  are the static and dynamic quenching constants respectively.

Representative SV plots of quenching of the protein fluorescence in the presence of DESs at 298K are provided in Figure 6.1(c). As can be seen from the figure,  $\frac{F_0}{F}$  versus percentage of DES plot for ethaline is observed to be a straight line and almost parallel to the X-axis, indicating no change in the protein fluorescence in the presence of ethaline. However, for BMEG, the SV plot exhibits an upward curvature with increasing concentration of BMEG. Please note that similar upward curvatures have also been observed for BMEG-induced quenching of BSA fluorescence at other temperatures (Figure 6.1(d)). This type of upward curvature data in  $\frac{F_0}{F}$  plots may be explained by considering the simultaneous involvement of both static and dynamic quenching processes during the quenching events.<sup>193, 225</sup> In the static quenching process, the fluorescence lifetime of the fluorophore does not alter in the presence of quencher molecule, whereas in the dynamic quenching process, the fluorescence lifetime decreases continuously with the increase in the concentration of the quencher.<sup>193, 225</sup> Keeping the above points in mind, time-resolved fluorescence decay experiments have been performed so that a clearer picture about the nature of quenching mechanism observed in the present study can be obtained. Here, we would like to point out that time-resolved fluorescence measurement

is a very useful technique to quantitatively estimate the extent of exposure of the buried tryptophan moieties to the aqueous phase at any concentration of the quencher by examining the lifetimes and the associated amplitude of the two Trp residues.<sup>330</sup>

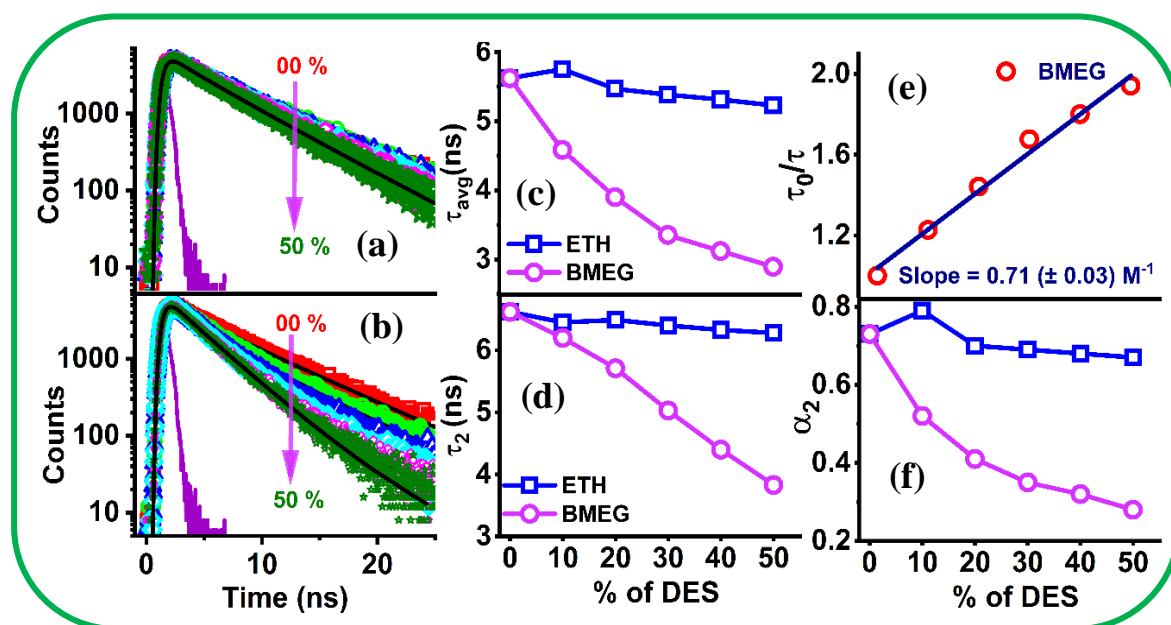


**Figure 6.2.** Representative fluorescence decay traces ( $\lambda_{ex}=295\text{nm}$ ) of BSA in absence and presence of gradual addition (a) Ethaline and (b) BMEG DESs at 298 K. The instrument response functions (IRF) are shown in solid violet lines and the biexponential fit of the fluorescence decay traces are shown in solid back line. Variation of (c) average lifetime and (d) longer decay component for BSA fluorescence decay in presence of different amount of Ethaline and BMEG. (e) Stern-Volmer plot with respect to lifetime for BSA in presence of BMEG. (f) Variation of amplitude ( $\alpha_2$ ) associated with longer component of BSA fluorescence decay in presence of Ethaline and BMEG.

The representative fluorescence decay curves of BSA titrated against a different percentage of DESs at 298K are shown in Figure 6.2(a) & (b). As can be seen from Figure 6.2(a), the fluorescence decay traces of the protein remain intact even at 50% of Ethaline content, and a very marginal change has been observed upon addition of 90% of Ethaline to the BSA solution (Figure APX6.4). On the other hand, a faster fluorescence decay of BSA in the presence of BMEG has been observed, indicating the quenching of the intrinsic fluorescence of BSA (Figure 6.2(b)). The fluorescence decays of BSA in the absence and

presence of the DESs are fitted to bi-exponential decay functions, and the relevant decay parameters are collected in Table 6.1.

**Table 6.1.** Fluorescence decay parameters of BSA in the absence and presence of DESs

Systems	$\tau_1$	$\alpha_1$	$\tau_2$	$\alpha_2$	$\tau_{avg}$
BSA in Buffer	2.92	0.27	6.62	0.73	5.62
10 % ETH	3.12	0.21	6.45	0.79	5.75
20% ETH	3.3	0.30	6.33	0.7	5.49
30% ETH	3.12	0.31	6.37	0.69	5.42
40% ETH	3.34	0.32	6.29	0.68	5.35
50% ETH	3.04	0.34	6.23	0.66	5.15
70% ETH	3.12	0.35	6.17	0.65	5.10
90% ETH	3.15	0.35	6.11	0.65	5.07
10% BMEG	2.83	0.48	6.2	0.52	4.58
20% BMEG	2.64	0.59	5.71	0.41	3.90
30% BMEG	2.45	0.65	5.03	0.35	3.35
40% BMEG	2.52	0.68	4.4	0.32	3.12
50% BMEG	2.53	0.72	3.83	0.28	2.89
70% BMEG	2.64	0.74	3.76	0.26	2.93
90% BMEG	2.81	0.75	3.97	0.25	3.1

As can be seen from the table, the fluorescence lifetimes of BSA exhibit two decay components, i.e., 2.92 ( $\tau_1$ ) and 6.62 ( $\tau_2$ ) ns, with an average lifetime of 5.62 ( $\tau_{avg}$ ) ns. The longer decay component is assigned to Trp-214, while the shorter decay component is attributed to Trp-135.<sup>330</sup> Any increase or decrease in the lifetime component with the addition of quencher is indicative of the unfolding/change in the protein's native structure. From Table 6.1, one can notice that with the gradual addition of BMEG there is a steep decrease in  $\tau_2$  values (Figure 6.2(d)), whereas the decrease in  $\tau_1$  value is marginal (Table 6.1). Moreover, with the gradual addition of BMEG, the amplitude associated with Trp-135 is found to increase,

while the same for Trp-214 decrease. This observation of decrease in the longer decay component of BSA lifetime in the presence of BMEG with a simultaneous reduction in the corresponding amplitude clearly shows the presence of a dynamic quenching mechanism to the protein fluorescence. Here we would like to mention that Kumaran et al.<sup>330</sup>, while investigating the time-resolved fluorescence of BSA in the presence of denaturant, also observed similar kind of results. They have proposed that the quenching of the fluorescence lifetime of tryptophan of BSA on the addition of formamide is because of the denaturation of the protein, which results due to the gradual exposure of the Trp-214 moiety to the aqueous phase. Therefore, in the present case also, the decrease in the fluorescence lifetimes of BSA in the presence of BMEG can be attributed to the denaturation of the protein due to the exposure of Trp-214 to the aqueous phase. Moreover, upon a careful look, one can clearly notice that the product of ( $\alpha_2 \times \tau_2$ ) decreases from 4.83 ns to 1.07 ns upon addition of 50% BMEG indicating a 78% denaturation of the protein. However, the time-resolved measurement data show no appreciable change in the individual fluorescence lifetimes components as well as in their corresponding amplitudes when ethaline is added to the BSA solution. This observation essentially suggests that even after addition of 90% of ethaline to BSA aqueous solution, the native structure of the protein almost remains unaltered.

Now, based on the estimated average lifetimes of BSA in the absence and presence of BMEG, the  $\frac{\tau_0}{\tau}$  vs concentration of BMEG has been plotted and fitted through equation 6.2(b). The dynamic quenching constant ( $K_D$ ) value estimated from the slope of Figure 6.2(e) is found to be  $0.70 (\pm 0.05) M^{-1}$ . Additionally, the bimolecular quenching constant ( $k_q$ ) value for BSA-BMEG is calculated by using  $K_D = k_q \tau_0$  (where  $\tau_0$  is the lifetime of the fluorophore in the absence of the quencher)<sup>193, 225</sup>, and the value is found to be  $1.05 \times 10^8 M^{-1} s^{-1}$ . Given that the estimated  $k_q$  value is comparatively smaller than the largest possible values of the bimolecular quenching

constant ( $2 \times 10^{10} \text{ M}^{-1}\text{s}^{-1}$ ) in the aqueous medium, the dynamic quenching is also operating on the overall quenching events as observed in the present case.<sup>193, 225</sup> Moreover, since the quenching mechanism is also not purely diffusion controlled, this prompted us to analyze the quenching data by invoking the “sphere of quenching action” model (equation 6.3), where it is assumed that both static and dynamic quenching processes are active at the same time during the overall quenching events.<sup>333-335</sup>

$$\frac{F_0}{F} = (1 + K_D[Q]) \cdot e^{V[Q]} \quad (6.3)$$

where  $[Q]$  is the quencher concentration  $V$  and  $K_D$  are the static and dynamic quenching constants, and  $F_0$  and  $F$  are the fluorescence intensity in the absence and presence of quencher, respectively. The value of  $V$  is obtained from the non-linear fitting of  $\frac{F_0}{F}$  versus  $[Q]$  by equation 6.3, and the value of  $V$  is found to be  $0.86 (\pm 0.02) \text{ M}^{-1}$ , at 298 K (Figure APX6.5). Interestingly, the value of  $V$  and  $K_D$  are found to be almost similar for BMEG-induced quenching of BSA fluorescence, suggesting that both static and dynamic quenching processes contribute to the overall quenching process of BSA fluorescence in presence of BMEG.<sup>333-335</sup>

After that, the binding interaction between proteins and BMEG is further investigated by analyzing the intrinsic protein fluorescence in the presence of BMEG at various temperatures. The associated parameters of the binding interaction between BSA and BMEG have been calculated by using the double logarithm plot (equation 6.4) which is given below<sup>336</sup>

$$\log \left[ \frac{F_0 - F}{F} \right] = \log K_B + n \log [Q] \quad (6.4)$$

where  $[Q]$  is the quencher concentration,  $K_B$  is the equilibrium binding constant, and  $n$  is the number of binding sites in the protein,  $F_0$  and  $F$  are the fluorescence intensity in the absence and presence of quencher, respectively. Please note that analysis of the data through double logarithm plot are often found to be useful as it allows the experimentalist to obtain useful parameters such as  $K_B$  and  $n$  value. The double logarithm linear plots for the interaction of

BMEG with the protein at some selected temperatures are shown in Figure 6.1(e), whereas the same plots for other temperatures are shown in the Appendix 6.5 (Figure APX6.6).  $K_B$  and  $n$  values for BSA-BMEG interaction have been calculated from the intercept and slope of the simulated linear line of the double logarithm plot (Figure 6.1(e) and Figure APX6.6) at different temperatures, and the corresponding data are summarized in Table 6.2. As noted in Table 6.2, BMEG has an average of more than one binding site per macromolecule ( $n$  values), which may indicate that more than one fluorophore amino acid residue (Trp and Tyr) is involved in the protein binding interaction.<sup>310, 311, 336</sup> Additionally, as can be seen from Table 6.2, the value of binding constants for the BSA-BMEG binding events is relatively weaker as compared to the binding of BSA with other surfactants and longer alkyl chains containing ILS.<sup>337, 338</sup> It should be noted that the interaction between a protein and its ligands can be influenced by a variety of weak intermolecular forces, including electrostatic interaction, hydrogen bond formation, van der Waals interaction, hydrophobic and steric interactions, etc.<sup>339</sup> Therefore, it is important to analyse the thermodynamic parameters such as enthalpy ( $\Delta H$ ) and entropy ( $\Delta S$ ) for BSA-BMEG interaction events in order to get an idea about the specific factor that might be responsible for governing the stability of protein-ligand complex. In order to achieve this, the relevant thermodynamic parameters for the current protein-BMEG binding events are determined using the van't Hoff relation (equation 6.5a). The van't Hoff relation can be used to link  $K_B$  values to temperature on the assumption that the variation of  $\Delta H$  for the protein-BMEG binding process is negligible over the temperature range investigated (equation 6.5a). The  $K_B$  values obtained from temperature-dependent fluorescence titration experiments at different temperature have been used in the van't Hoff relation. The van't Hoff plot for binding events of BSA-BMEG is shown in Figure 6.1(f). The  $\Delta H$  and  $\Delta S$  values are calculated from the slope and intercept of the simulated linear line of the van't Hoff plot (Figure 6.1(f)), respectively. Finally, the free energy of binding ( $\Delta G$ ) is calculated for all

the experimental temperatures with the help of equation 6.5b by using estimated  $\Delta H$  and  $\Delta S$  values. All the estimated thermodynamic parameters are compiled in Table 6.2.

$$\log K_B = \left(-\frac{\Delta H}{2.303R}\right) \cdot \frac{1}{T} + \frac{\Delta S}{2.303R} \quad (6.5a)$$

$$\Delta G = \Delta H - T \cdot \Delta S \quad (6.5b)$$

The negative values of  $\Delta G$  in the interaction events are an indicative of the spontaneous binding interaction of these BMEG to the protein. For the investigation of protein-ligand interaction, Ross and Subramanian proposed that both positive values for  $\Delta H$  and  $\Delta S$  are generally suggestive of the hydrophobic interaction.<sup>340</sup> Similar hydrophobic interactions of protein-IL binding have also been documented earlier.<sup>18, 310, 333, 334, 338</sup> Thus, the observation of an endothermic binding process accompanied with positive  $\Delta S$  value, in the present study, essentially indicates that the BSA-BMEG interaction is primarily mediated by hydrophobic interaction.

**Table 6.2.** Binding constant ( $K_B$ ), number of binding sites ( $n$ ), and other relative thermodynamic parameters for the Interaction of BMEG with BSA

Temp. /K	BSA-BMEG				
	$K_B$ ( $M^{-1}$ )	$\Delta H$ ( $kJ\ mol^{-1}$ )	$\Delta S$ ( $J\ K^{-1}mol^{-1}$ )	$\Delta G$ ( $kJ\ mol^{-1}$ )	$n$
298	1.29 $\pm$ 0.04	26.79 $\pm$ 3.12	91.71 $\pm$ 7.13	-0.54 $\pm$ 0.04	1.39 $\pm$ 0.04
303	1.48 $\pm$ 0.05			-1.00 $\pm$ 0.05	1.31 $\pm$ 0.05
308	1.70 $\pm$ 0.06			-1.46 $\pm$ 0.07	1.25 $\pm$ 0.08
313	2.04 $\pm$ 0.08			-1.92 $\pm$ 0.08	1.28 $\pm$ 0.04
318	2.57 $\pm$ 0.10			-2.38 $\pm$ 0.08	1.42 $\pm$ 0.06

### 6.3.2. Steady-State and Time-Resolved Fluorescence of BSA-FITC

In order to study the conformational dynamics and the unfolding of protein in the presence of DESs at single molecular resolution, the protein must be strongly fluorescent, and the fluorescence from the protein must be sensitive to the conformational changes of the protein

---

---

molecule. Here it is to be noted that the brightness (product of molar extinction coefficient and quantum yield) of Trp residue of a protein is comparatively low as compared to common organic dye.<sup>341</sup> In addition to this, Trp must be excited with UV lights, which requires UV microscope optics that are not frequently accessible. As a result, the fluorescence from Trp is usually not investigated through FCS. To overcome this issue, protein molecules are generally labelled covalently or non-covalently with fluorescent probe molecules to study the conformational changes through FCS. Therefore, to analyze the conformational changes/protein unfolding through FCS in the presence of DESs, BSA tagged with FITC dye (BSA-FITC) is employed in the current work.

Prior to the study of the interaction of the dye-tagged BSA (BSA-FITC) with the concerned DESs at single-molecule level (FCS), the steady-state and time-resolved data have also been recorded for BSA-FITC in the absence and presence of different percentage of DESs. The emission spectra of BSA-FITC at various DESs percentages are shown in Figure 6.3(a) & (b). As can be seen from the figure, the fluorescence intensity of BSA-FITC in the buffer solution (in the absence of any additives) is very low. However, with the gradual addition of BMEG, the fluorescence intensity increases sharply. Here, we would like to note that in the absence of any additives, the dye-tagged protein remains in the folded state, and as a result, the fluorescence intensity of BSA-FITC in buffer solution is quenched because of the interaction of FITC with the side chains of the nearby amino acids.<sup>342</sup> Similar suppression of fluorescence of fluorescein attached to an intestinal fatty acid binding protein (IFABP) was also noticed by Frieden and Co-workers.<sup>342</sup> Additionally, photoinduced electron transfer between the FITC dye molecule and side chain amino acid residues (such as Trp, Tyr, etc.) can also reduce the fluorescence of FITC-tagged proteins.<sup>341, 342</sup> However, the unfolding of the protein not only exposed the fluorescein group to the solvent but also suppressed the PET process, which resulted in a significant rise in fluorescence intensity. As it is well known that common

denaturants like guanidinium hydrochloride (GdHCl) unfold the protein through chemical interactions, we have also recorded the fluorescence of BSA-FITC in the presence of GdHCl and found that addition of more than 2M of GdHCl the fluorescence intensity increases sharply (Figure APX6.7(a)). However, the fluorescence intensity of the dye (FITC) alone does not exhibit any enhancement in fluorescence in the presence of the relevant DESs (Figure APX6.7(b) & (c)). This demonstrates that the alteration in the native structure of the protein is what causes the fluorescence intensity of BSA-FITC to rise in the presence of BMEG. As can be seen from Figure 6.3(b) & (c), the fluorescence of BSA-FITC increases significantly up to 60% of BMEG concentration, revealing the unfolding of the native structure of BSA. However, the fluorescence intensity of BSA-FITC is found to decrease abruptly with further increases in BMEG concentration (70–90%). This abrupt drop in fluorescence intensity of BSA-FITC perhaps indicates the aggregation of BSA at higher BMEG concentrations (70–90%). It is important to note in this context that several prior studies have shown that partially or totally unfolded proteins are more likely to aggregate due to enhanced protein-protein interaction.<sup>343-</sup>  
<sup>345</sup> Additionally, the aggregation of BSA due to thermal and/or chemical unfolding of its native structure has also been documented earlier.<sup>343-345</sup> Due to aggregation of BSA, significant crowding of the protein increases the hydrophobicity around the fluorophore, which ultimately results in the quenching of the fluorescence of FITC by the amino acid residues and thereby causes a sudden decrease in the fluorescence intensity.<sup>343-345</sup> On the other hand, there is a slight increase in the fluorescence intensity of BSA-FITC in the presence of the other DES, ethaline. For instance, nearly 1.4 times increase in fluorescence intensity is seen for BSA-FITC in presence of 50% more ethaline compared to a nearly 5 times rise for the same amount of BMEG. In fact, the fluorescence intensity of BSA-FITC increases only by about two times even at very large concentrations of ethaline (90%). All These findings suggest that in comparison to ethaline, BMEG considerably alters the native structure of the protein.

Furthermore, the time-resolved fluorescence spectra of BSA-FITC recorded in the presence of different quantities of DESs are shown in Figure 6.3(b) & (c). The fluorescence decay profiles of BSA-FITC (in the absence of DESs) show a biexponential decay behaviour (Table 6.3) with a shorter lifetime component ( $\tau_1$ ) associated with a larger amplitude ( $\alpha_1$ ) and a longer lifetime component ( $\tau_2$ ) associated with a smaller amplitude ( $\alpha_2$ ). These two lifetime components represent the lifetime of the native and unfolded state of the dye-tagged protein with  $\alpha_1$  and  $\alpha_2$  as their corresponding amplitude, respectively. With the addition of Ethaline to the aqueous solution of BSA-FITC, no significant change in the average lifetime ( $\tau_{avg}$ ) as well as in the individual component and amplitude have been observed (Table 6.3). However, with the gradual increase in the percentage of BMEG, even though the individual lifetimes do not show appreciable change, the amplitude associated with each component changes significantly, ultimately changing the average lifetime. For example, the amplitude associated with the shorter component decreases from 87% (in buffer) to 54% in the presence of 50% BMEG, which results in the increase of average lifetime from 0.83 ns to 1.86 ns. This decrease in the amplitude of the shorter component and the concomitant increase in the amplitude of the longer component with the gradual addition of BMEG further indicates the gradual unfolding of the protein.<sup>316</sup> However, with further addition of BMEG (70-90%), a sudden decrease in the  $\tau_{avg}$  have been observed, which is also consistent with the steady-fluorescence behaviour of BSA-FITC. This observation also further points out the possibility of aggregation of BSA at higher concentrations of BMEG. In order to shed further light on the aforementioned findings, FCS methods have been used to explore the effects of both DESs on the structure and conformation of BSA at a single molecule level.

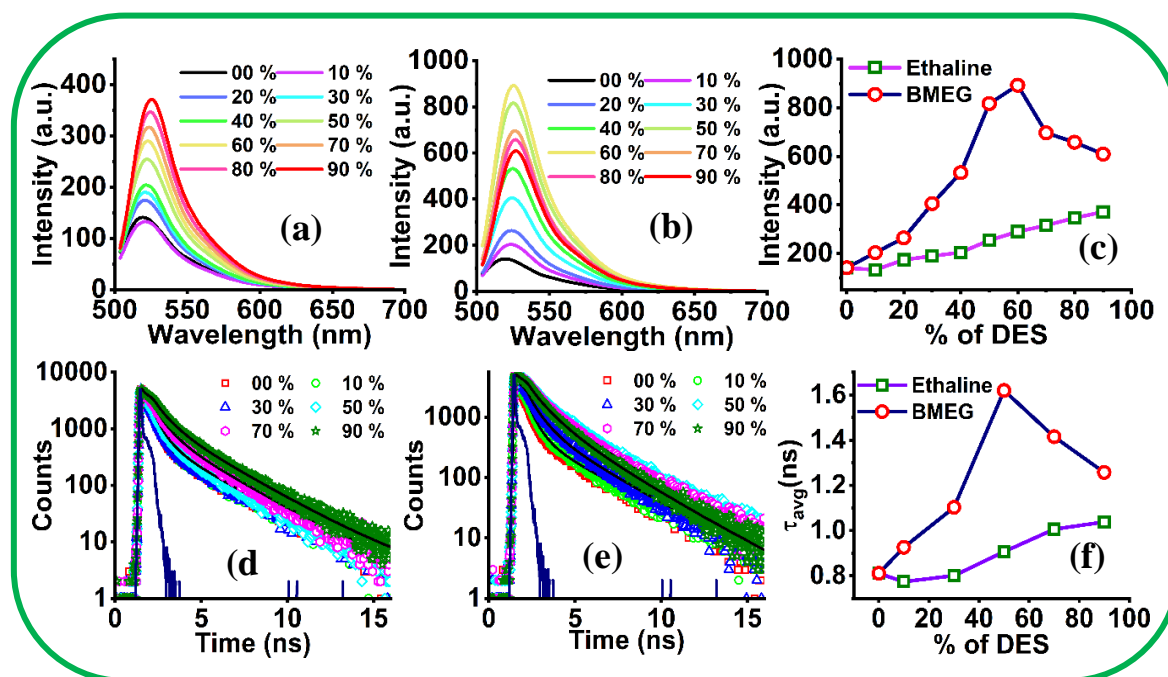


**Figure 6.3.** Fluorescence emission spectra ( $\lambda_{ex} = 485\text{nm}$ ) of BSA-FITC in absence and presence of gradual addition of (a) ethaline and (b) BMEG (dotted line). (c) Variation of fluorescence intensity of BSA-FITC in presence of different amount of DESs. Fluorescence decays ( $\lambda_{ex} = 485\text{nm}$ ) of BSA-FITC in presence of different quantity of (d) Ethaline and (e) BMEG. The solid navy blue represents the IRF and the solid black line represents the biexponential fits of the fluorescence decay traces. (f) Variation of average lifetime BSA-FITC in presence of different amount of DESs.

**Table 6.3.** Fluorescence decay parameters of FITC-BSA in the absence and presence of DESs.

Systems	$\tau_1$	$\alpha_1$	$\tau_2$	$\alpha_2$	$\tau_{avg}$
BSA-FITC in Buffer	0.53	0.87	2.69	0.13	0.81
10 % ETH	0.47	0.86	2.64	0.14	0.77
30% ETH	0.48	0.85	2.62	0.15	0.80
50% ETH	0.55	0.82	2.53	0.18	0.91
70 % ETH	0.63	0.8	2.51	0.2	1.00
90 % ETH	0.58	0.76	2.49	0.24	1.04
10% BMEG	0.55	0.83	2.76	0.17	0.93
30% BMEG	0.62	0.75	2.55	0.25	1.10
50% BMEG	0.69	0.54	2.71	0.46	1.62
70 % BMEG	0.67	0.61	2.58	0.39	1.42
90 % BMEG	0.63	0.67	2.53	0.33	1.26

### 6.3.3. FCS Studies of BSA-FITC

FCS is an elegant and sensitive technique where the analysis of the time-dependent fluorescence intensity fluctuation provided crucial information about diffusion as well as dynamics of diffusing species in sub-microsecond-to-second time scales.<sup>193, 263, 341, 342</sup> Moreover, one can easily and precisely examine the folding and unfolding of a dye-tagged protein in the presence of additives or denaturants by simply measuring the diffusion time of the protein through FCS.<sup>193, 263, 341, 342</sup> Therefore, in the present study, we have made use of FCS methods to gather important information on the interaction between the protein and concerned DESs at single molecule resolution. Figure 6.4(a) & (b) represents the FCS traces of BSA-FITC in the absence and presence of different quantities of Ethaline and BMEG, respectively. When these FCS traces are fitted through a single component diffusion model, by using equation 2.24, it does not provide a good fit to the data (Figure APX6.8(a)). So, we have fitted the FCS data with a modified form of equation 2.24, which contain a single component diffusion along with a stretched exponential relaxation component (equation 6.6). The fitting of the FCS traces with the latter one provides the best fit to our experimental results. A comparison of the fitting results with one component diffusion and one component diffusion coupled with a stretched exponential relaxation component is provided in the Appendix (Figure APX6.8).

$$G(\tau) = \frac{1-A+A\exp(-\tau/\tau_R)^\beta}{N(1-A)} \left(1 + \frac{\tau}{\tau_D}\right)^{-1} \left(1 + \frac{\tau}{\kappa^2\tau_D}\right)^{-1/2} \quad (6.6)$$

where  $\tau$ ,  $N$ ,  $\tau_d$ , and  $\kappa$  represent the lag-time, the number of molecules in the observation volume, the diffusion time, and structure parameter of the observation volume, respectively.  $A$  is the amplitude of the relaxation time ( $\tau_R$ ) representing the fraction of molecules in the non-fluorescent state and  $\beta$  ( $0 < \beta < 1$ ) is the stretching exponent representing the distribution of  $\tau_R$ .

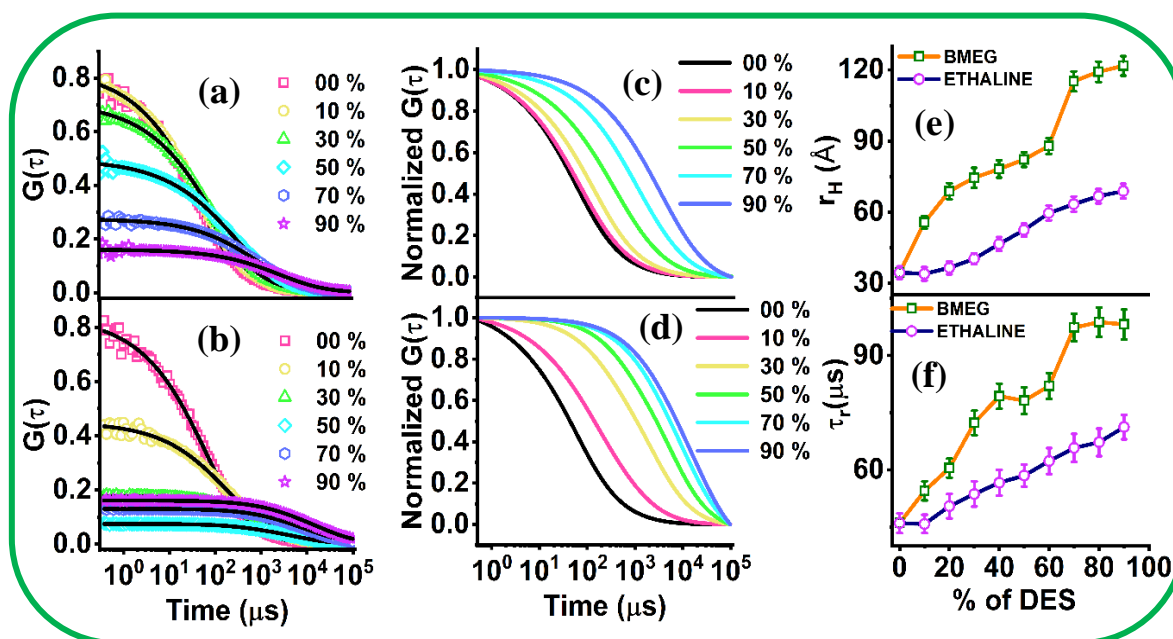


**Figure 6.4.** FCS traces of BSA-FITC in presence of (a) Ethaline and (b) BMEG, solid black line shows the fitting of the FCS traces. Normalized fitted FCS traces of BSA-FITC in (c) Ethaline and (d) BMEG. Variation of (e) hydrodynamic radii and (f) conformational time ( $\tau_R$ ) in presence of different quantity of DES.

**Table 6.4.** Estimated fitted parameters of FCS data of BSA-FITC in presence of DESs

Systems	A	$\tau_R$ ( $\mu$ s)	$\beta$	$\tau_D$ (ms)	$r_H$ ( $\text{\AA}$ )
00 %	$0.75 \pm 0.04$	$46.1 \pm 2.4$	$0.50 \pm 0.03$	$0.31 \pm 0.02$	$34.7 \pm 1.4$
10 % ETH	$0.71 \pm 0.04$	$45.8 \pm 2.8$	$0.51 \pm 0.03$	$0.34 \pm 0.02$	$33.9 \pm 1.2$
30 % ETH	$0.67 \pm 0.02$	$53.7 \pm 3.4$	$0.50 \pm 0.04$	$0.54 \pm 0.04$	$40.3 \pm 1.7$
50 % ETH	$0.58 \pm 0.02$	$58.5 \pm 2.6$	$0.53 \pm 0.05$	$1.21 \pm 0.09$	$52.4 \pm 2.6$
70 % ETH	$0.46 \pm 0.02$	$65.6 \pm 2.1$	$0.56 \pm 0.05$	$2.72 \pm 0.15$	$63.3 \pm 2.6$
90 % ETH	$0.39 \pm 0.03$	$71.2 \pm 3.2$	$0.58 \pm 0.04$	$5.96 \pm 0.34$	$68.8 \pm 2.8$
10 % BMEG	$0.55 \pm 0.03$	$54.5 \pm 3.7$	$0.53 \pm 0.04$	$0.68 \pm 0.05$	$55.6 \pm 2.1$
30 % BMEG	$0.27 \pm 0.02$	$72.3 \pm 4.4$	$0.72 \pm 0.05$	$2.15 \pm 0.16$	$74.5 \pm 3.1$
50 % BMEG	$0.22 \pm 0.02$	$78.1 \pm 3.9$	$0.82 \pm 0.05$	$5.30 \pm 0.37$	$82.2 \pm 3.1$
70 % BMEG	$0.32 \pm 0.03$	$97.3 \pm 4.6$	$0.77 \pm 0.04$	$13.3 \pm 0.93$	$115.2 \pm 4.2$
90 % BMEG	$0.35 \pm 0.02$	$98.1 \pm 3.9$	$0.77 \pm 0.05$	$21.9 \pm 1.12$	$121.7 \pm 4.8$

It is important to note here that the fitting of the FCS with equation 6.6 reveals that the fluorescence intensity fluctuation, in the present case, is not only happening due to the diffusion of the dye-tagged protein in and out of the confocal region but also caused by some additional

relaxation process.<sup>263, 341, 342, 345</sup> Some past studies have shown that a similar model can be employed quite effectively while multiple overlapping relaxation kinetics contribute to the FCS data.<sup>263, 341, 342, 345</sup> Moreover, The fact that the additional relaxation component is not artefactual has also been established by several control experiments.<sup>263, 341, 342, 345</sup> Chattopadhyay et al., while working on FITC bound IFABP (intestinal fatty acid binding protein), also used similar fitting model for analysis of their FCS traces and carried out a number of control experiments to ensure that the extra component is not an artefact.<sup>342</sup> They have suggested that when the conformational change of the protein is sufficiently fast ( $\tau_R \ll \tau_D$ ), then the quenching of the FITC fluorescence by the amino acids (Trp) can cause additional fluctuation in the fluorescence intensity, which can be observed in FCS. So, the overall FCS traces will represent a combination of both diffusion and conformational motion of the protein. Considering this, in the present analysis, the observation of the additional stretched exponential relaxation term ( $\tau_R$ ) reflects the conformational dynamics of the protein with diverse time scales. Thus, analysis and estimation of the  $\tau_D$  value of BSA-FITC will provide information about the structure of the protein (hydrodynamic radius of the folded or unfolded protein), whereas the  $\tau_R$  value will delineate about the conformational motion of the proteins.

One can see from Figure 6.4(a) & (b) that the correlation traces are shifted to a longer time scale with the increasing addition of DESs, suggesting slower diffusion of BSA-FITC. This observation is quite evident from the normalized fitted traces (Figure 6.4(c) & (d)) and the steady rise in the estimated diffusion time ( $\tau_D$ ) (Table 6.4) of BSA-FITC estimated from the fitting of the FCS traces in the presence of both DESs. This increase in the diffusion time of BSA-FITC may be due to the increase in the viscosity and /or increase in the hydrodynamic radius of the protein. By carefully examining Table 6.4, it becomes apparent that adding 50% ethaline increases the  $\tau_D$  value by almost six times, but adding the same amount of BMEG

increases the  $\tau_D$  value by more than sixteen times. Since the addition of DES also increases the viscosity of the solution, which likewise raises the  $\tau_D$  value, it is challenging to determine which DESs have a larger impact on the native state of the protein. Therefore, it is important to estimate the hydrodynamic radius of the protein in absence and presence of different amount of DES. The hydrodynamic radius ( $r_H$ ) of the protein is generally calculated from the Stokes-Einstein equation which is as follows

$$r_H = \frac{k_B T}{6\pi\eta D} \quad (6.7)$$

where  $\eta$  is the viscosity coefficient of the solution,  $k_B$  is the Boltzmann constant,  $T$  is the absolute temperature, and  $D$  is the diffusion coefficient of the protein, which can be estimated from the following equation 2.25. Nevertheless, because the  $D$  value and the  $\tau_D$  value are inversely correlated, the hydrodynamic radius is eventually overestimated due to changes in the viscosity and refractive index of the medium after the addition of DESs. In order to fix the discrepancy in refractive index and viscosity, corrections have been done by following the literature method as suggested by Sherman et al.<sup>346</sup> They utilized Rh6G as the diffusion standard since it's  $r_H$  is independent of both viscosity and refractive index, and they employed the ratio approach to get rid of mistakes brought on by viscosity and refractive index mismatches, as shown below<sup>346</sup>,

$$\frac{R_h^{protein}}{R_h^{Rh6G}} = \frac{\tau_D^{protein}}{\tau_D^{Rh6G}} \quad (6.8)$$

where  $R_h^{protein}$  and  $R_h^{Rh6G}$  are the hydrodynamic radius of the protein and Rh6G respectively, while,  $\tau_D^{protein}$  and  $\tau_D^{Rh6G}$  are the diffusion time of the protein and Rh6G respectively. Similar method has also been used by other researchers to estimate the  $r_H$  value of protein through FCS.<sup>312, 333, 341, 342, 345, 347-349</sup>

Table 6.4 compiles the estimated  $r_H$  values of the protein in the absence and presence of various DES concentrations. As can be seen from Table 6.4, the  $r_H$  values of the protein in its native condition in the absence of any additives is estimated to be 34.7 Å, which is consistent with earlier literature results.<sup>345</sup> Moreover, Wilkins et al.<sup>350</sup> have demonstrated that the empirical relationship,  $r_H = 4.75N^{0.29}$  where N is the number of amino acids (for BSA, N = 583), may be used to theoretically predict the  $r_H$  value of a protein in its natural state. The  $r_H$  value of the protein in its native form, as determined by the aforementioned relation, is 30.1 Å, which is very close to our experimentally observed value. Table 6.4 also demonstrates that the  $r_H$  value of the protein increases as both DESs are gradually added, which can be further visualized from Figure 6.4(e). As can be seen from the figure, the increase in the  $r_H$  value of the protein in the presence of BMEG is steeper as compared to the same for Ethaline. For example, the  $r_H$  value of the protein in presence of 50% ethaline is almost estimated to be the same as that in 10% of BMEG, signifying that BMEG affects the native structure of the protein more as compared to Ethaline. The increase in the  $r_H$  value of the protein essentially indicates the unfolding of the protein in the presence of DESs. As it is well known that common denaturant like GdHCl, urea, etc., also unfolds the protein and thereby increase the  $r_H$  value of the protein, we have also estimated the  $r_H$  value of the protein in the presence of GdHCl by employing FCS techniques so that a clear understanding of the protein unfolding mechanism can be obtained.<sup>349</sup> The FCS traces and the estimated  $r_H$  value of the protein in the presence of GdHCl are shown in Figure APX6.9 and Table APX6.1, respectively. For GdHCl, it has been found that with the addition of 6M GdHCl, the protein is completely unfolded with an estimated  $r_H$  value of 80.8 Å (Table APX6.1), which is close to the theoretically predicted (by using equation,  $r_H = 2.11N^{0.57}$ )  $r_H$  value (79.6 Å) of the unfolded protein.<sup>350</sup> The denaturation of BSA due to the complete unfolding of BSA in presence of 5 to 6M of GdHCl have also been

reported earlier.<sup>351</sup> Interestingly, the  $r_H$  value (75-85 Å) of the protein in presence of 30 to 60% of BMEG (Table 6.4 and Table APX6.1) is found to be almost comparable to the  $r_H$  value of the unfolded protein. However, upon addition of 70% of BMEG, the  $r_H$  value of the protein is estimated to be 115.2 Å, which is significantly larger than the  $r_H$  value of a completely unfolded protein. Interestingly, the  $r_H$  value (119.2-121.1 Å) of the protein does not show any appreciable change with further increase in the concentration of BMEG (80-90%). More interestingly, these  $r_H$  values of the protein at higher BMEG concentrations are found to be closely related to the  $r_H$  value of BSA in aggregated conditions. Pabbathi et al.<sup>345</sup> have also observed a sudden increase in the  $r_H$  value of BSA in the presence of 50% of DMSO through FCS studies. They have suggested that DMSO completely unfolds the native structure of BSA and favourable interaction among the unfolded protein results in the aggregation of protein. In light of this, in the present scenario also, the sudden rise in the  $r_H$  value of BSA in presence of 70% BMEG essentially signifies the aggregation of the protein due to enhanced protein-protein interaction as a result of complete unfolding of the protein. On the other hand, the  $r_H$  value of the protein is found to be close to 68.8 Å even after the addition of 90% ethaline, suggesting that the protein has not fully unfolded. All of these findings demonstrate that while a little amount of BMEG can cause complete unfolding and denaturation of the protein structure, they can remain in a partly unfolded state even in presence of high concentration of Ethaline.

Now upon concentrating on the conformational relaxation of the protein, the  $\tau_R$  values of the protein, like the  $\tau_D$  value, are also affected by the change in viscosity. Hence, the mismatch that appears due to the change in viscosity of the solvent is corrected by following the literature procedure<sup>263</sup>, and the corrected  $\tau_R$  values for BSA-FITC in the absence and presence of both DESs are summarized in Table 6.4. The  $\tau_R$  value of the protein in its native state is found to be 46.1  $\mu$ s, which is consistent with the previous-literature reported value.<sup>345</sup>

<sup>347</sup> Samanta and co-workers<sup>345</sup> have reported a  $\tau_R$  value of 35  $\mu\text{s}$  for FITC labelled BSA due to conformational dynamics of the protein, which changes to 81  $\mu\text{s}$  with addition of 40% DMSO. Later on, Sarkar and co-workers<sup>347</sup> have observed three temporal components of conformational dynamics for Alexa-labeled BSA in the range of 2–650  $\mu\text{s}$  in absence and presence of graphene oxide and ascribed them to the protein chain dynamics (faster components) and coordinated chain motion (slower component). Similarly, Yadav et al.<sup>349</sup> have also reported a relaxation time constant of 27–80  $\mu\text{s}$  for TMR (tetramethyl rhodamine) labelled HSA and ascribed this due to the concerted chain motions or interchain diffusion of side chains of HSA. In view of all these prior reports, one can reasonably say that the observed  $\tau_R$  value in the present study can be assigned to the conformational dynamics of the protein due to concerted chain motions and/or interchain interactions of the protein. Moreover, the observation of a steady increase in the  $\tau_R$  value of the protein with gradual addition of DESs, indicates the slowing down of the conformational dynamics of the protein. Interestingly, this slowing down of conformational dynamics is found to be more pronounced for BMEG as compared to that for Ethaline (Figure 6.4(f), Table 6.4). For example, a nearly two-fold increase in the  $\tau_R$  value of the protein can be observed in presence of 50% BMEG. Additionally, the estimated  $\tau_R$  value corresponding to the presence of 50% BMEG is found to be comparable to the  $\tau_R$  value in presence of 6M GdHCl (Table APX6.1). As it has been already mentioned that BSA completely unfolds in presence of 6M GdHCl, the slowing down of conformational dynamics of the protein in presence of 50% BMEG arises due to the complete unfolding of the protein. As a consequence of the protein unfolding, the amino acids of the protein (Trp, Tyr, etc.) are required to diffuse across a longer distance so as to quench the fluorescence of the FITC, resulting in an increase in the  $\tau_R$  value of the unfolded protein.<sup>263, 316</sup> However, when more than 70% of BMEG is added to the aqueous solution of BSA-FITC, a sharp increase in the  $\tau_R$  value has been observed, and this value remains almost constant with the further increase

---

---

in BMEG concentration. This happens due to aggregation of the protein at a very high concentration of BMEG. Because of the aggregation of the protein, the flexibility of the side chain residue is significantly reduced, which ultimately slows down the conformational motion of the aggregated protein.<sup>345</sup>

Apart from this, the  $\tau_R$  value is also associated with a stretching exponent ( $\beta$ ), which represents the distribution of the conformational relaxation time scale. This distribution of  $\tau_R$  value suggests that the conformational motions of the protein are heterogeneous and occur over a range of time scales as a result of several short- and long-range fluctuations in the dye-tagged protein.<sup>352, 353</sup> Many other proteins have also been shown to exhibit this heterogeneous conformational dynamics, and the flexibility of the protein structure is thought to be the primary factor contributing to the observed heterogeneity in the conformational dynamics of the protein.<sup>316, 353</sup> From Table 6.4, one can notice that the  $\beta$  value increase significantly in presence of BMEG (0.50 to 0.82 in presence of 50% BMEG), whereas the increase of the same is very less for ethaline (0.50 to 0.57 in presence of 50% Ethaline). Notably, the  $\beta$  value in presence of 50% BMEG is also found to be close to the value observed in presence 6M GdHCl. This increase in  $\beta$  value indicates the decrease in the distribution of the conformational fluctuation time scales. It should be noted here that when the protein unfolds, the distance between the side chain residues of the amino acids and the dye moiety increases, which subsequently decreases the effective fluctuations of the unfolded protein resulting in the increased  $\beta$  value.<sup>316</sup> In the present case also, the significant increase in the  $\beta$  value in BMEG as compared to that in Ethaline suggests the complete unfolding of the protein in the presence of the former. In this context, it is also important to notice that the fitting parameter ( $A$ ) associated with the  $\tau_R$  value represents the fraction of molecules in the non-fluorescent state due to quenching of FITC by the amino acid residues. In the native state of the protein, the self-quenching of FITC by the amino acids is very efficient, due to which the dark fraction is very

high (75%). However, when the protein unfolds, the quenching of FITC fluorescence is suppressed, which results in a decrease in the A value. From the Table, it can be seen that the A value decrease from 75% to 40% in 90% Ethaline and 22% in 50 % BMEG, where the latter value runs parallelly with the estimated A value in presence of 6M GdHCl (27%, Table APX6.1), indicating complete and partially unfolding of the protein in presence of BMEG and Ethaline respectively. Moreover, since the  $G(0)$  value (i.e., the value of  $G(\tau)$  at zero time delay) is correlated with N via the relationship  $G(0) = 1/N(1-A)$ , a reduction in the A value corresponds to a decrease in the  $G(0)$  value. This drop in  $G(0)$  suggests that there are more molecules in the confocal volume that are undergoing conformational fluctuations as a result of protein unfolding. Figure 6.4 (a & b) shows that the  $G(0)$  value for BMEG drops more than it does for ethaline, which also advocates that the former causes larger protein unfolding than the latter. However, when more than 70% of BMEG is added, both the A and  $G(0)$  value increases. For instance, the observed number of molecules dropped from 18 in presence of 60 % BMEG to 10 in presence of 70 % BMEG. This observation also clearly points to the aggregation of BSA at a very high concentration of BMEG. All of the results obtained from the analysis of FCS data are found to be in agreement with the findings obtained from the steady-state and time-resolved fluorescence studies, and it has been found that BMEG significantly altered protein structure even at low concentrations and caused aggregation of the protein at higher concentration, whereas the protein can remain in a partially unfolded state even in the presence of higher Ethaline content. The outcome of this study further delineates that the extent and nature of the interaction of protein with different DESs are significantly different from each other.

#### **6.3.4. Conformational Studies of BSA through CD Spectroscopy**

To further ascertain our findings and comment on the extent and nature of protein-DES interaction, we have also performed CD experiments. CD spectroscopy is a very informative

tool to evaluate the conformational changes in protein structure and its stability in presence of external additives.<sup>330, 338</sup> It has been documented that the Far-UV CD spectroscopy can be used to understand the alteration induced in the secondary structure ( $\alpha$ -helical,  $\beta$ -sheet) of proteins due to unfolding or refolding of proteins as well as to quantitatively estimate the  $\alpha$ -helical of the protein. The CD spectra of BSA exhibit two distinctively negative peaks due to the transition of the amide group of the peptide bond of the protein.<sup>315, 330, 338</sup> The two peaks at wavelengths of 208 nm and 222 nm represent the  $\pi \rightarrow \pi^*$  transition and  $n \rightarrow \pi^*$  transition of the protein.<sup>315, 330, 338</sup> In the present study, the far UV-CD spectra of BSA in the absence and presence of different quantities of both DESs at 298 K are shown in Figure 6.5. From the figure, it can be noticed that the spectral shape of the CD signals does not change significantly even after addition of 50% of ethaline, despite the fact that a decrease in the negative CD signal value is observed. However, while the CD spectral shape gets abruptly changed in presence of only 20% of BMEG, the  $\alpha$ -helical peak (peak at 208 nm) is completely vanished, indicating the structural denaturation of the protein.<sup>315, 330, 338</sup> To estimate the  $\alpha$ -helix content of BSA quantitatively in the absence and presence of both DESs, following equation<sup>354</sup> have been used,

$$MRE = \frac{\theta_{obs}}{10ncl} \quad (6.9)$$

where, MRE is the mean residue ellipticity,  $\theta_{obs}$  is the observed ellipticity in millidegrees,  $n$  is the number of amino acid residues (583 for BSA),  $l$  is the path length of the cell (0.2 cm),  $C$  is the molar concentration of BSA.

$$\alpha - helix (\%) = \frac{(-MRE_{208} - 4000)}{33000 - 4000} \times 100 \quad (6.10)$$

where,  $MRE_{208}$  is the calculated MRE value at 208 nm, 4000 is the MRE value of the  $\beta$ -form and random coil conformation cross at 208 nm, and 33000 is the MRE value of a pure  $\alpha$ -helix at 208 nm.

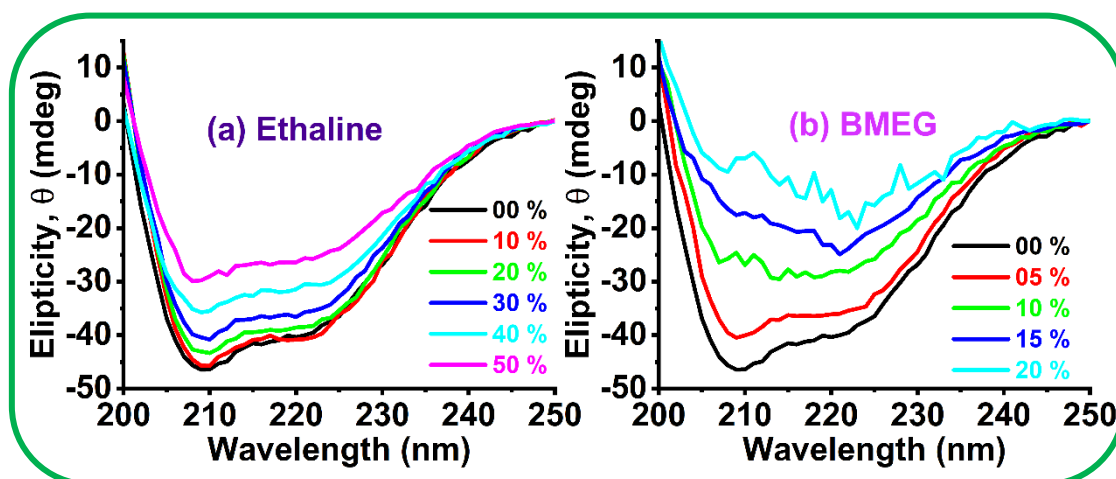


**Figure 6.5.** Far-UV CD spectra of 2  $\mu\text{M}$  BSA in the absence and presence of different quantity of (a) Ethaline and (b) BMEG.

**Table 6.5.** Variation in the Secondary Structure ( $\alpha$ -Helical) of BSA in the presence of different quantity of DESs

ETHALINE	% of $\alpha$ -Helix	BMEG	% of $\alpha$ -Helix
00 %	53.7	00 %	53.7
10 %	52.1	05 %	44.6
20 %	49.3	10 %	24.3
30 %	44.7	15 %	11.9
40 %	38.1	20 %	03.8
50 %	31.6		

The percentages of  $\alpha$ -helix of BSA as estimated from equation 6.10 are provided in Table 6.5. The value of the  $\alpha$ -helical content of the native form of BSA in the aqueous buffer is found to be 53.7% (Table 6.5), which is very close to the literature-reported value.<sup>337, 338</sup> Analysis of the data in Table 6.5 reveals that the  $\alpha$ -helical content of BSA decreases gradually in the presence of both DESs indicating the unfolding of the protein due to the interaction between the protein and DESs. However, the decrease is found to be relatively more effective in BMEG as compared to that in Ethaline. For instance, the  $\alpha$ -helical content of the protein decreases from  $\sim 54\%$  to 6% in presence of 20% BMEG, whereas the same remains almost

---

---

unaffected in the presence of same amount Ethaline. The large decrease in the percentages of  $\alpha$ -helix of BSA in the presence of BMEG indicates the complete unfolding of the protein, which is also consistent with results obtained from the steady-state and time-resolved fluorescence as well as from the FCS studies. Interestingly, the  $\alpha$ -helical composition of the protein is still decent even in the presence of higher quantity (50%) of ethaline (Table 6.5) which shows that protein retains a partially unfolded state even at higher ethaline content.

The majority of the findings obtained from steady-state and time-resolved measurements, FCS studies, and CD studies show that the addition of BMEG significantly changes the native structure of the protein and causes complete denaturation, whereas ethaline has only a little impact on the protein, allowing it to remain in a partially unfolded state even at very high ethaline concentrations. This finding is particularly intriguing since, except from a very few numbers of reports<sup>316,325</sup>, several prior investigations have shown that the structures of various biomolecules, such as lysozyme and bovine serum albumin, are essentially unaltered in aqueous mixtures of ChCl-based DESs.<sup>317-322</sup> For instance, Bhakuni et al.<sup>314</sup> have shown that the DES made of ChCl and urea significantly stabilizes the protein despite having a denaturant as its primary component due to the stronger interaction between ChCl and urea as compared to protein and urea. Additionally, since a DES is formed by combining two distinct components, many previous studies have also examined whether the impact of DESs in aqueous solutions on the biocatalytic activity and protein stability is caused by DES dissociation in water, the combined effects of their individual components, or by the DES complex itself.<sup>313-316, 320, 322</sup> For example, Venktesu and co-workers<sup>322</sup>, while working on the stability and activity of  $\alpha$ -chymotrypsin, have demonstrated that even at a significant dilution of DESs, the effect imparted by the ChCl-based DESs on  $\alpha$ -chymotrypsin is by virtue of DES itself rather than its individual constituent. Similarly, Stamatis and colleagues<sup>320</sup> discovered that DESs significantly affect the biocatalytic activity of cyt c when compared to the mixture

of individual components, implying that the effect of DES on enzyme activity is due to the presence of DES complex in the reaction mixture rather than the effect of its individual components. Considering all of these arguments, it is reasonable to conclude that the interaction of BSA with BMEG and Ethaline heavily relies on the interspecies interactions between the constituents (HBA and HBD) of each DESs system and the observed effect of both DESs on proteins results from DES formation rather than from the synergetic effects contributed by individual constituents.

In this context, it is also important to note here that the difference in the influence of BMEG and Ethaline towards the protein structure is also very interesting in a sense that both DESs only differ in having different HBAs and share the same HBD (ethylene glycol). This observation clearly shows how changes in just one DES component can significantly affect the stability and conformational dynamics of a protein. Furthermore, despite the fact that the HBD (ethylene) of DESs is anticipated to interact with proteins via hydrogen bonds, it is still referred to be an excellent protein stabilizer, which retains the structure and conformation of the protein.<sup>355</sup> This suggests that the unfolding of the protein ultimately depends on the variation in the molecular structure of the HBAs of both DESs and their extent of interaction with both the protein and the HBD. Since HBAs of BMEG majorly differs from Ethaline in a sense that it has a hydrophobic cationic group (benzyl group), it's interaction with the HBD as well as with the protein secondary structure, is believed to be critical in governing the overall destabilization of BSA. It should be mentioned here that a number of earlier research have shown that ILs and surfactants with long alkyl chains denature proteins as a result of hydrophobic and van der Waals interactions.<sup>309-312</sup> Yet, in the current situation, the protein's denaturation by BMEG, despite in the absence of a longer hydrophobic chain, is rather unusual. Nevertheless, it has also been noted that benzyl group can involve in  $\pi$ - $\pi$  stacking, cation-  $\pi$  interaction, and/or CH- $\pi$  interaction, which may eventually lead to compaction or

destabilization of the protein depending upon the extent of interaction.<sup>356</sup> However, alternation of the protein structure due to the above mentioned interactions between protein and external additives also heavily dependent on the strength of other factors such as solute–solvent, protein–solvent, solute–protein and protein–protein interactions, which ultimately govern the fate of the protein.<sup>330</sup> This has been rightly pointed out by Saddam et al.<sup>316</sup> in their recent publication, where they have recently shown that the composition of the protein solvation shell and the interactions between the DES and protein are both determined by the relative strength of the interspecies hydrogen bonds that are formed between the constituents of DESs and with the surrounding water molecules. In view of all these reports, it is reasonable to conclude that at lower concentration of ethaline, where one can expect a large disruption in the hydrogen bonding network, both the constituents of ethaline involve in strong interaction with surrounding water molecules and hence their interaction with protein is minimal due to which the protein structure remains unchanged as observed from our data. However, with the increase in DES concentration, it is expected that more DES–protein interaction would significantly alter the structure and conformation of the protein. But at higher ethaline concentrations, the protein–DES interaction is now in competition with the interspecies hydrogen bonding network interaction inside the DES (interaction among the constituents of ethaline), which results in the partial unfolding of the protein. Strong interspecies hydrogen bonding interaction in ethaline has already been documented in earlier reports.<sup>186, 284</sup> But for BMEG, even a very small quantity of the DES causes significant alternation in the protein secondary structure, which suggests that the benzyl group of the HBA must be involved in the hydrophobic interaction with the protein. In addition to this, the positive value of the thermodynamic parameters also essentially justified our finding that despite the presence of hydrogen bond donor substitutes, the interaction of BMEG and protein is mediated through hydrophobic interaction. With the increase in BMEG concentration, the complete unfolding protein essentially suggests that the

benzyl groups of BMEG have a higher propensity to interact with protein hydrophobically. Moreover, at very high BMEG content, the favourable interaction among the unfolded protein results in the aggregation of the protein, suggesting significant protein-protein interaction.

#### **6.4. Conclusion**

In summary, the structure and conformational dynamics of BSA in the presence of two structurally and chemically different DESs have been examined in order to have a molecular level of understanding of how the nature of constituents of DESs can affect the protein-DES interaction. This work is also done with an objective to find out whether all types of DESs or only certain kinds of DESs can be used as suitable media for the storage of proteins and biomolecules. For this purpose, the behaviour of BSA in the presence of two DESs (i.e., Ethaline and BMEG) has been investigated by employing both ensemble average and single molecule spectroscopic techniques. Both steady-state and time-resolved fluorescence measurements show that the intrinsic fluorescence of the protein gets quenched in the presence of BMEG, while no change in the fluorescence is observed in the presence of Ethaline, indicating strong BSA-BMEG interaction as compared to BSA-Ethaline interaction. Further, the thermodynamic parameters estimated from the steady-state fluorescence measurements have confirmed the predominant involvement of hydrophobic interaction during BSA-BMEG interaction, and the BSA-BMEG interaction is mostly entropy-driven. Interestingly, a thorough examination of FCS data has revealed that while a small quantity of BMEG can completely unfolds the protein's native structure, the protein remains in a partially unfolded state even in the presence of very high ethaline content. More interestingly, it has also been observed that at very high BMEG concentrations, favourable interaction among the unfolded protein, results in the aggregation of BSA due to enhanced protein-protein interaction. All the results obtained from both ensemble average and single molecule measurements, which are in perfect agreement, suggest that both protein-DES interaction and interspecies interaction among the

constituent of DESs regulate the overall stability and conformational dynamics of the protein in DESs. Moreover, as BMEG causes aggregation of the protein and protein aggregations are linked with many neurodegenerative disorders, the outcome of the current study also clearly points out that not all DESs can be treated as an alternative media for the storage of biomolecules. The current investigations at both single molecular and ensemble average conditions are expected to be helpful in the judicious selection, design, and development of novel DESs for protein storage and applications.

---

## 6.5. Appendix

### 6.5.1. Synthesis of DESs

Both DESs were synthesized using the typical literature technique.<sup>19-20,186,329</sup> Briefly, in a conical flask, ethylene glycol (3 mol) and choline chloride or benzyltrimethylammonium chloride (1 mol) were mixed and heated in an oil bath at 353 K with continual stirring until a transparent homogenous liquid was formed. The liquids were then slowly cooled down to the room temperature (298 K) and dried 323 K for several hours and stored in an inert atmosphere prior to experiments. The purity of the prepared DESs was checked through  $^1\text{H}$  NMR spectroscopy in  $\text{D}_2\text{O}$  as solvent.

$^1\text{H}$  NMR ( $\delta_{\text{H}}$ , ppm) of Ethaline: 5.15 brs (1H, OH), 4.65 brs (6H, OH), 3.55 m (14H, O-CH<sub>2</sub>), 3.45 m (2H, N-CH<sub>2</sub>), 3.12 s (9H, N-(CH<sub>3</sub>)<sub>3</sub>). 14H, O-CH<sub>2</sub>

$^1\text{H}$  NMR ( $\delta_{\text{H}}$ , ppm) of BMEG: 7.4 m (5H, -C<sub>6</sub>H<sub>5</sub>), 4.7 brs (6H, OH), 4.35 s (2H, N-CH<sub>2</sub>), 3.5 m (12H, O-CH<sub>2</sub>), 2.95 s (9H, N-(CH<sub>3</sub>)<sub>3</sub>).

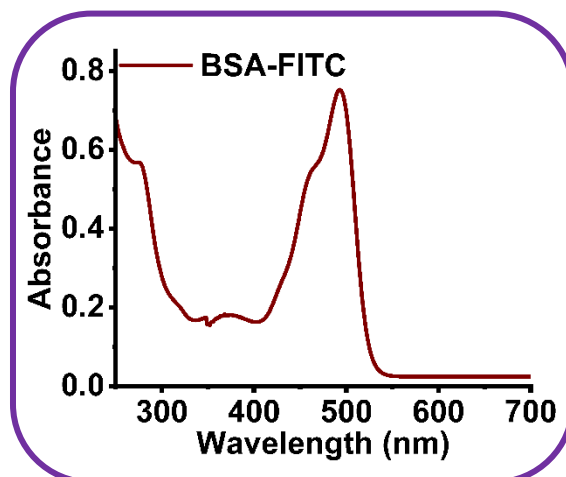


**Figure APX6.1.** Steady-state absorption spectra of BSA-FITC in 10mM phosphate buffer.

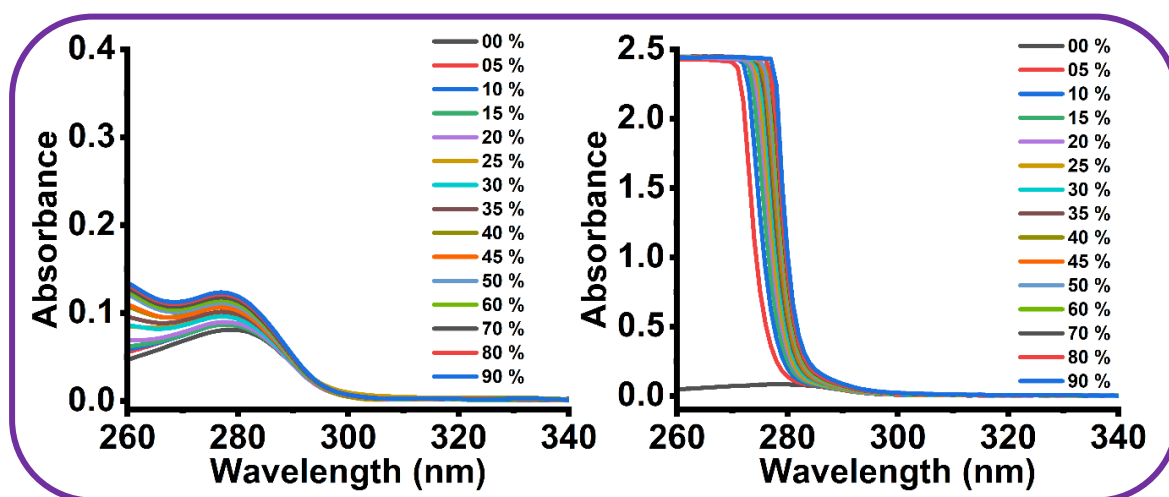


**Figure APX6.2.** Steady-state absorption spectra of 2  $\mu\text{M}$  of BSA in presence of (a) Ethaline and (b) BMEG.

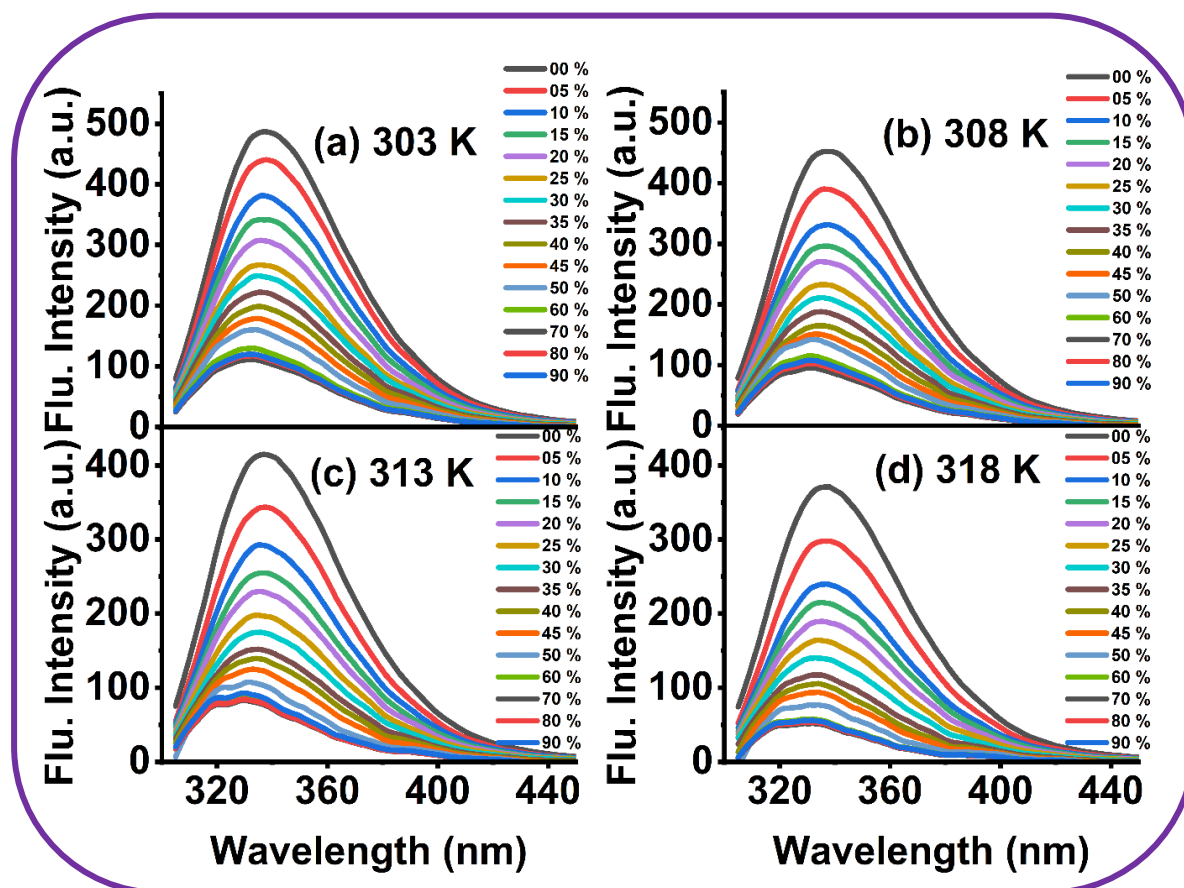


**Figure APX6.3.** Steady-state fluorescence spectra of BSA (2 $\mu$ M) in presence of different quantity of BMEG at 303 to 318K.

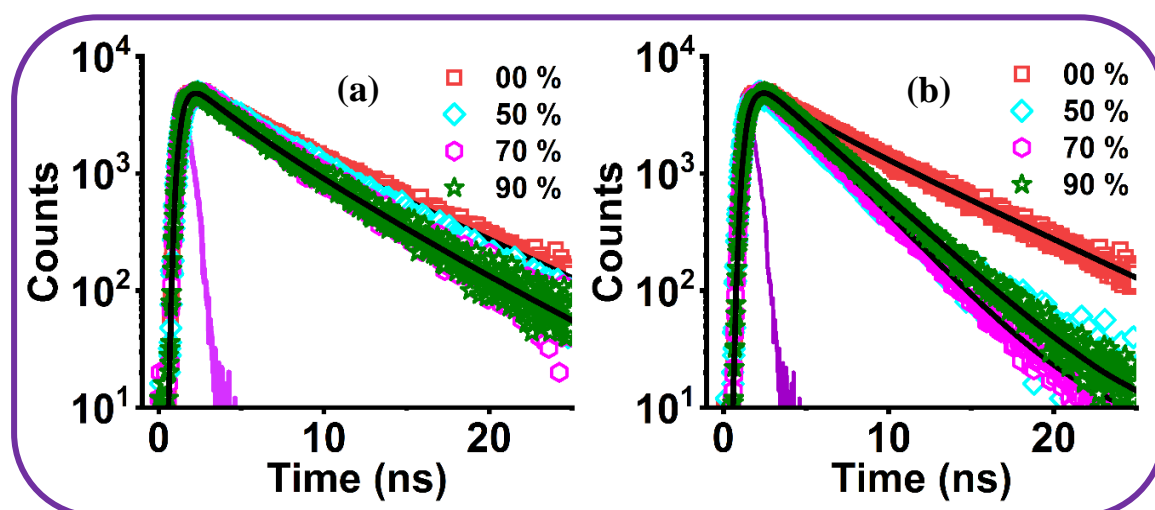


**Figure APX6.4.** Fluorescence decay traces ( $\lambda_{ex} = 295\text{nm}$ ) of BSA in absence and presence of different quantity of (a) Ethaline and (b) BMEG DESs at 298 K.

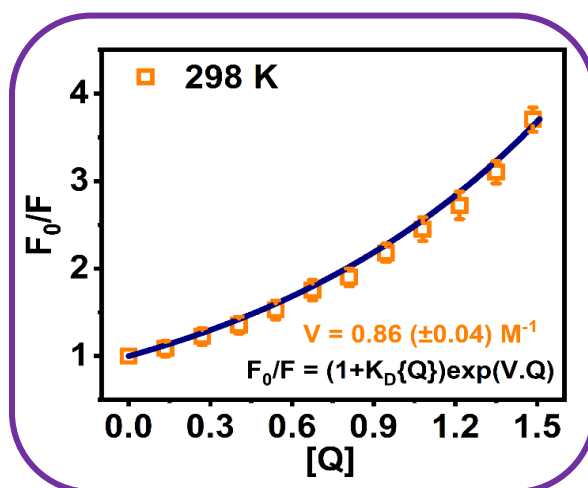


**Figure APX6.5.** Stern-Volmer plots for quenching of intrinsic BSA fluorescence by BMEG at 298 K. The solid line represents the simulated curve obtained by using equation 6.3.

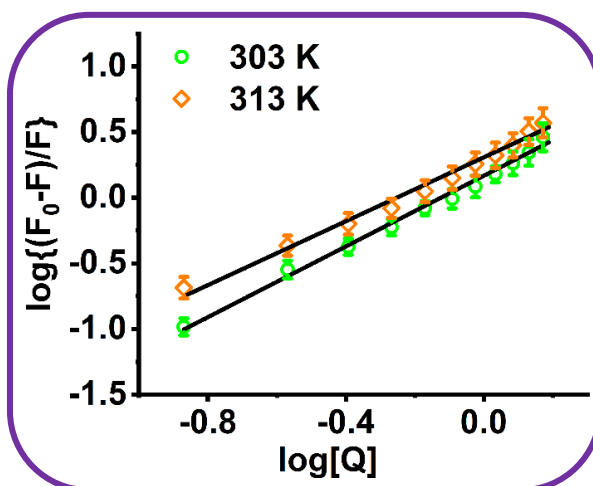


**Figure APX6.6.** Double logarithmic plot at 303K and 313K for BSA-BMEG.

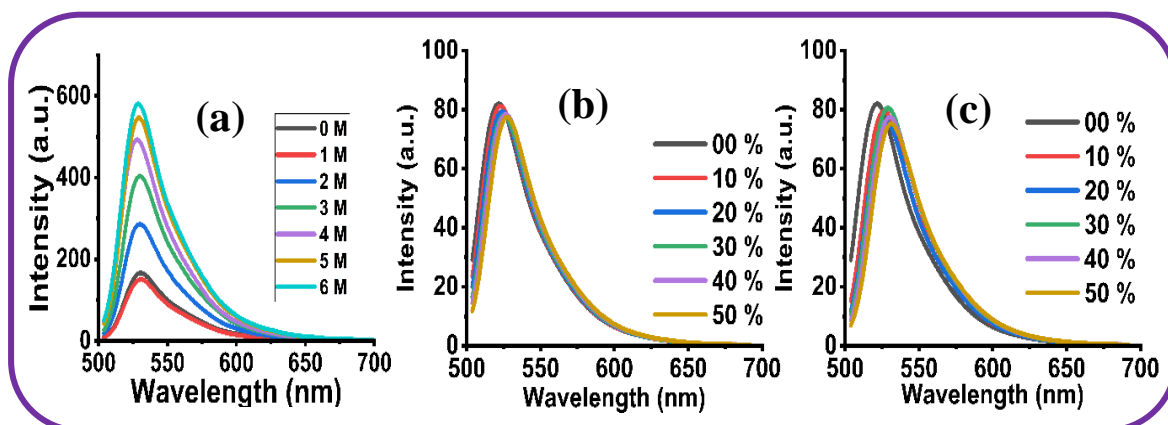


**Figure APX6.7.** Steady-state fluorescence spectra of (a) BSA-FITC in presence of GdHCl. Steady-state fluorescence spectra of FITC dye only in presence of (b) Ethaline and (c) BMEG respectively.

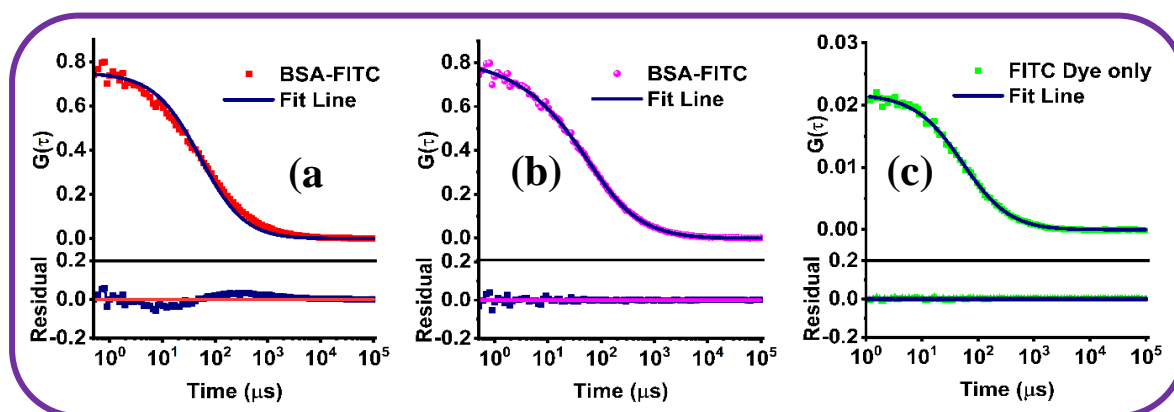


**Figure APX6.8.** Fitting of the FCS trace of BSA-FITC in 10 mM phosphate buffer through (a) single component diffusion model (equation), and (b) single component diffusion model along with stretched relaxation component (equation). (c) Fitting of FITC dye only in buffer through single component diffusion model. The corresponding residual shows the goodness of the fit.

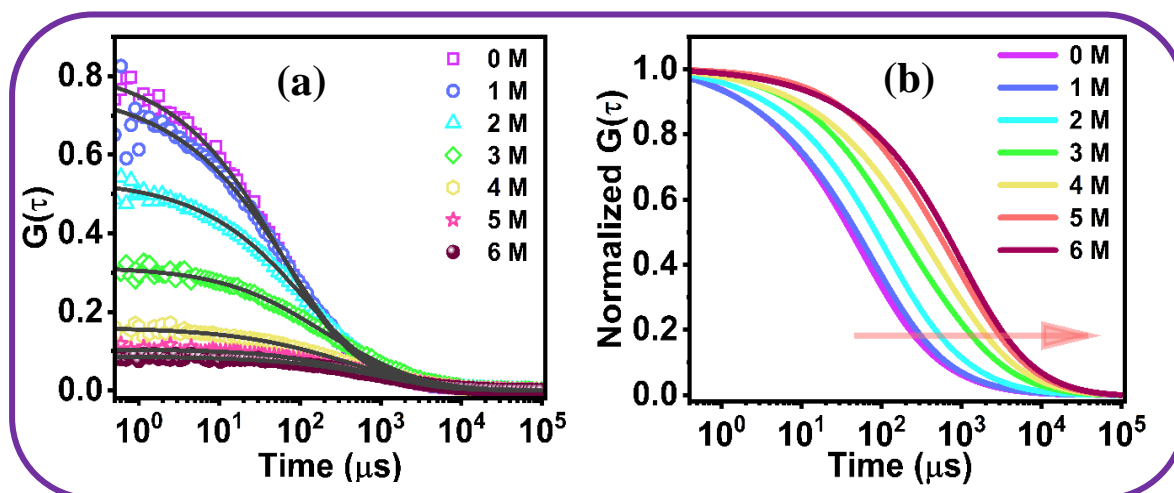


**Figure APX6.9.** (a) FCS traces of BSA-FITC in presence of GdHCl. (b) Normalized fitted FCS traces of BSA-FITC in GdHCl.

**Table APX6.1.** Estimated fitted parameters of FCS data of BSA-FITC in presence of GdHCl

Systems	A	$\tau_R$ ( $\mu$ s)	$\beta$	$\tau_D$ (ms)	$r_H$ ( $\text{\AA}$ )
00 %	$0.75 \pm 0.04$	$46.1 \pm 2.4$	$0.50 \pm 0.03$	$0.31 \pm 0.02$	$34.8 \pm 1.4$
1 M GdHCl	$0.73 \pm 0.03$	$45.2 \pm 2.2$	$0.56 \pm 0.04$	$0.37 \pm 0.03$	$35.7 \pm 1.5$
2 M GdHCl	$0.65 \pm 0.03$	$57.9 \pm 3.1$	$0.59 \pm 0.04$	$0.51 \pm 0.05$	$46.2 \pm 1.8$
3 M GdHCl	$0.49 \pm 0.03$	$62.1 \pm 3.6$	$0.64 \pm 0.06$	$0.78 \pm 0.05$	$65.6 \pm 2.4$
4 M GdHCl	$0.42 \pm 0.02$	$69.5 \pm 2.9$	$0.67 \pm 0.05$	$0.99 \pm 0.08$	$76.7 \pm 2.9$
5 M GdHCl	$0.29 \pm 0.02$	$77.6 \pm 3.9$	$0.76 \pm 0.05$	$1.13 \pm 0.09$	$81.2 \pm 2.8$
6 M GdHCl	$0.27 \pm 0.03$	$78.9 \pm 3.7$	$0.73 \pm 0.04$	$1.29 \pm 0.07$	$80.8 \pm 2.7$

---

---

### **Summary and Future Prospects**

In summary, in the present thesis work, we have made an attempt to understand structure and dynamical behavior of several DESs and RTILs in absence and presence of electrolytes and biomolecules. Specifically, attempts have been made to understand the differences in the intermolecular interaction, structural organization and dynamics between DESs and RTILs having similar functional groups. The influence of increasing numbers of hydroxyl groups on the structure and dynamics of ammonium-based RTILs have also been investigated. Additionally, in order to realize the potential of DESs for electrochemical applications, structural and dynamical behavior of DESs have been investigated in absence and presence of lithium salt. Moreover, studies on the effects of DESs on the structure and conformational dynamics of BSA have also been carried out. All the aforementioned investigations are done by employing various spectroscopic techniques such as steady-state fluorescence, time-resolved fluorescence (TCSPC and FLUPs), the confocal spectroscopy (FCS), EPR, NMR etc. Several interesting results in relation to understanding the basics of solute-solvent and solvent-solvent interaction, solvent-protein and solvent-electrolytes interaction and its relationship with the structural organization of the media have emerged from the present work. The key findings of the present thesis are summarized below.

- The microscopic behavior such as solute-solvent and solvent-solvent interactions, and structural heterogeneity are found to be considerably different for both DESs and RTILs. Moreover, the solvent relaxations of DESs are found to be much faster than RTILs. Interestingly, it has also been observed that even at faster time scale, the different motions related to solvent relaxation are significantly different for both DESs and RTILs

- 
- 
- It has also been observed that the increase in the number of hydroxyl groups on the cation head of RTILs can considerably alter the local structural organisation and dynamics of the solvent systems.
  - The addition of electrolytes such as lithium salts can significantly affects the rotation, translation and solvation dynamics of the DESs and importantly, perturb the nano structural organization of the DESs.
  - It has also been observed that the interspecies interaction between the constituents of DESs significantly alter the DES-protein interaction. Moreover, as BMEG causes aggregation of the protein and protein aggregation are linked with many neurodegenerative disorders, the outcome of the current thesis work also clearly points out that all DESs cannot be treated as an alternative media for the storage of biomolecules.

The current thesis work provides several new and interesting physical insights. The knowledge obtained from the current thesis work is expected to be useful in understanding the structural organization, intermolecular interaction and dynamics of DESs and RTILs in better fashion. The thesis work also suggests that the structure and dynamical behavior of DESs and RTILs are different, and DESs may not necessarily be considered as a sub class of ILs, rather DESs should be treated as a separate class of solvent with their own identity. Moreover, the current thesis work also highlights the importance of judicious selection of DESs for various bio-related applications. The current outcome of the present thesis work is expected to advance our existing understanding of behavior of DESs and functionalized RTILs at microscopic level.

The potential for DESs to go well beyond the realm of academia is enormous because of their many advantageous properties over traditional solvents. Moreover, DESs have shown immense potential in material design and bio-related applications. However, the numbers of

DESs available for their use in these fields are currently limited, and only a few specific DESs have been utilized. Therefore, in the coming years, new types of DESs having different types of constituents (HBAs and HBDs) need to be developed to broaden their scope for application in various other fields.

## REFERENCES

1. A. D. McNaught and A. Wilkinson, *Compendium of chemical terminology*, Blackwell Science Oxford, **1997**.
2. P. Ball, *PNAS*, **2017**, 114, 13327-13335.
3. R. Makitra, *Russian journal of general chemistry*, **2005**, 75, 664-664.
4. Y. Marcus, *Properties of solvents*, Wiley, **1998**.
5. C.-J. Li and B. M. Trost, *PNAS*, **2008**, 105, 13197-13202.
6. G. Wypych, *Handbook of solvents*. William Andrew Publishing, Toronto, **2001**.
7. W. M. Nelson, *Green solvents for chemistry: perspectives and practice*, Oxford University Press, **2003**.
8. L. Pfaltzgraff and J. Clark, *Advances in Biorefineries*, **2014**, 3-33.
9. R. A. Sheldon, *Green Chem.*, **2017**, 19, 18-43.
10. M. Tobiszewski, A. Mechlińska and J. Namieśnik, *Chem. Soc. Rev.*, **2010**, 39, 2869-2878.
11. F. M. Kerton and R. Marriott, *Alternative solvents for Green Chem.*, Royal Society of chemistry, **2013**.
12. J. M. DeSimone, *Science*, **2002**, 297, 799-803.
13. A. Jordan, P. Stoy and H. F. Sneddon, *Chem. Rev.*, **2020**, 121, 1582-1622.
14. R. A. Sheldon, *Green Chem.*, **2005**, 7, 267-278.
15. P. G. Jessop and W. Leitner, *Chemical synthesis using supercritical fluids*, John Wiley & Sons, **2008**.
16. R. D. Rogers and K. R. Seddon, *Science*, **2003**, 302, 792-793.
17. D. A. Alonso, A. Baeza, R. Chinchilla, G. Guillena, I. M. Pastor and D. J. Ramón, *Eur. J. Org. Chem.*, **2016**, 612-632.
18. A. Schindl, M. L. Hagen, S. Muzammal, H. A. Gunasekera and A. K. Croft, *Front. Chem.*, **2019**, 7, 347.
19. E. L. Smith, A. P. Abbott and K. S. Ryder, *Chem. Rev.*, **2014**, 114, 11060-11082.
20. Q. Zhang, K. D. O. Vigier, S. Royer and F. Jérôme, *Chem. Soc. Rev.*, **2012**, 41, 7108-7146.
21. A. P. Abbott, R. C. Harris, K. S. Ryder, C. D'Agostino, L. F. Gladden and M. D. Mantle, *Green Chem.*, **2011**, 13, 82-90.
22. J. S. Wilkes, *Green Chem.*, **2002**, 4, 73-80.
23. T. Welton, *Chem. Rev.*, **1999**, 99, 2071-2084.

24. P. Wasserscheid and W. Keim, *Angew. Chem. Int. Ed.*, **2000**, 39, 3772-3789.
25. K. R. Seddon, A. Stark and M.-J. Torres, *Pure Appl. Chem.*, **2000**, 72, 2275-2287.
26. R. Atkin and G. G. Warr, *J. Phys. Chem. B*, **2008**, 112, 4164-4166.
27. Y. Umebayashi, W.-L. Chung, T. Mitsugi, S. Fukuda, M. Takeuchi, K. Fujii, T. Takamuku, R. Kanzaki and S.-i. Ishiguro, *J. Comput. Chem., Japan*, **2008**, 7, 125-134.
28. R. Hayes, S. Imberti, G. G. Warr and R. Atkin, *J. Phys. Chem. C*, **2014**, 118, 13998-14008.
29. R. Hayes, G. G. Warr and R. Atkin, *Chem. Rev.*, **2015**, 115, 6357-6426.
30. H. J. Jiang, R. Atkin and G. G. Warr, *Curr. Opin. Green Sustain. Chem.*, **2018**, 12, 27-32.
31. Y.-L. Wang, B. Li, S. Sarman, F. Mocci, Z.-Y. Lu, J. Yuan, A. Laaksonen and M. D. Fayer, *Chem. Rev.*, **2020**, 120, 5798-5877.
32. R. Sheldon, *ChemComm.*, **2001**, 2399-2407.
33. G. Imperato, B. König and C. Chiappe, *Eur. J. Org. Chem.*, **2007**, 1049-1058.
34. R. D. Rogers and G. A. Voth, *Acc. Chem. Res.*, **2007**, 40, 1077-1078.
35. N. V. Plechkova and K. R. Seddon, *Chem. Soc. Rev.*, **2008**, 37, 123-150.
36. J. P. Hallett and T. Welton, *Chem. Rev.*, **2011**, 111, 3508-3576.
37. J. F. Wishart, *Energy Environ. Sci.* **2009**, 2, 956-961.
38. Walden, P., *Bull. Acad. Imper. Sci. St. Petersburg*, **1914**, 1800.
39. F. H. Hurley and T. P. Wier, *J. Electrochem. Soc.*, **1951**, 98, 203.
40. J. S. Wilkes and M. J. Zaworotko, *J. Chem. Soc., ChemComm.*, **1992**, 965-967.
41. O. G. Polyakov, S. M. Ivanova, C. M. Gaudinski, S. M. Miller, O. P. Anderson and S. H. Strauss, *Organometallics*, **1999**, 18, 3769-3771.
42. M. Picquet, I. Tkatchenko, I. Tommasi, P. Wasserscheid and J. Zimmermann, *Adv. Synth. Catal.*, **2003**, 345, 959-962.
43. A. S. Larsen, J. D. Holbrey, F. S. Tham and C. A. Reed, *J. Am. Chem. Soc.*, **2000**, 122, 7264-7272.
44. W. Xu, L.-M. Wang, R. A. Nieman and C. A. Angell, *J. Phys. Chem. B*, **2003**, 107, 11749-11756.
45. J. L. Anderson, R. Ding, A. Ellern and D. W. Armstrong, *J. Am. Chem. Soc.*, **2005**, 127, 593-604.
46. J. Y. Kim, T. H. Kim, D. Y. Kim, N.-G. Park and K.-D. Ahn, *J. Power Sources*, **2008**, 175, 692-697.
47. M. Moosavi and F. Khashei, *Fluid Phase Equilib.*, **2018**, 460, 135-145.

48. S. Tang, G. A. Baker and H. Zhao, *Chem. Soc. Rev.*, **2012**, 41, 4030-4066.
49. G. Yu, S. Zhang, G. Zhou, X. Liu and X. Chen, *AIChE journal*, **2007**, 53, 3210-3221.
50. B. E. Gurkan, J. C. de la Fuente, E. M. Mindrup, L. E. Ficke, B. F. Goodrich, E. A. Price, W. F. Schneider and J. F. Brennecke, *J. Am. Chem. Soc.*, **2010**, 132, 2116-2117.
51. S. Kirchhecker and D. Esposito, *Curr. Opin. Green Sustain. Chem.*, **2016**, 2, 28-33.
52. H. Ohno and K. Fukumoto, *Acc. Chem. Res.*, **2007**, 40, 1122-1129.
53. R. L. Gardas, R. Ge, P. Goodrich, C. Hardacre, A. Hussain and D. W. Rooney, *J. Chem. Eng. Data*, **2010**, 55, 1505-1515.
54. A. E. Visser, R. P. Swatloski, W. M. Reichert, R. Mayton, S. Sheff, A. Wierzbicki, J. H. Davis Jr and R. D. Rogers, *ChemComm.*, **2001**, 135-136.
55. R. Giernoth, *Angew. Chem. Int. Ed.*, **2010**, 49, 2834-2839.
56. Y. S. Sistla and A. Khanna, *J Ind Eng Chem*, **2014**, 20, 2497-2509.
57. Y. Yu, J. Mai, L. Wang, X. Li, Z. Jiang and F. Wang, *Sci. Rep.*, **2014**, 4, 5997.
58. B.-S. Lee and S.-g. Lee, *Bulletin of the Korean Chemical Society*, **2004**, 25, 1531-Scientific reports 1537.
59. K.-S. Kim, D. Dembereinyamba and H. Lee, *Langmuir*, **2004**, 20, 556-560.
60. X. Yuan, N. Yan, S. A. Katsyuba, E. E. Zvereva, Y. Kou and P. J. Dyson, *Phys. Chem. Phys. Chem.*, **2012**, 14, 6026-6033.
61. Y. Bai, R. Yan, W. Tu, J. Qian, H. Gao, X. Zhang and S. Zhang, *ACS Sustain. Chem. Eng.*, **2018**, 6, 1215-1224.
62. T. J. de Souza Ramos, G. H. Berton, T. M. Cassol and S. A. Júnior, *J. Mater. Chem. C*, **2018**, 6, 6270-6279.
63. A. P. Abbott, G. Capper, D. L. Davies, R. K. Rasheed and V. Tambyrajah, *ChemComm.*, **2003**, 70-71.
64. A. P. Abbott, D. Boothby, G. Capper, D. L. Davies and R. K. Rasheed, *J. Am. Chem. Soc.*, **2004**, 126, 9142-9147.
65. A. Banerjee, K. Ibsen, T. Brown, R. Chen, C. Agatemor and S. Mitragotri, *PNAS*, **2018**, 115, E11000-E11001.
66. M. A. Martins, S. P. Pinho and J. A. Coutinho, *J. Solution Chem.*, **2019**, 48, 962-982.
67. A. Alhadid, L. Mokrushina and M. Minceva, *Molecules*, **2019**, 24, 2334.
68. A. P. Abbott, G. Capper, D. L. Davies, H. L. Munro, R. K. Rasheed, V. Tambyrajah, *Chem. Commun.* **2001**, 2010.
69. A. P. Abbott, G. Capper, D. L. Davies and R. K. Rasheed, *Chem. Eur. J.*, **2004**, **10**, 3769-3774.

70. A. P. Abbott, J. C. Barron, K. S. Ryder and D. Wilson, *Chem. Eur. J.*, **2007**, 13, 6495-6501.
71. D. O. Abranches, M. A. Martins, L. P. Silva, N. Schaeffer, S. P. Pinho and J. A. Coutinho, *ChemComm.*, **2019**, 55, 10253-10256.
72. N. Schaeffer, D. O. Abranches, L. P. Silva, M. A. Martins, P. J. Carvalho, O. Russina, A. Triolo, L. Paccou, Y. Guinet and A. Hedoux, *ACS Sustain. Chem. Eng.*, **2021**, 9, 2203-2211.
73. B. B. Hansen, S. Spittle, B. Chen, D. Poe, Y. Zhang, J. M. Klein, A. Horton, L. Adhikari, T. Zelovich and B. W. Doherty, *Chem. Rev.*, **2020**, 121, 1232-1285.
74. H. Shirota, T. Mandai, H. Fukazawa and T. Kato, *J. Chem. Eng. Data*, **2011**, 56, 2453-2459.
75. S. V. Dzyuba and R. A. Bartsch, *ChemPhysChem*, **2002**, 3, 161-166.
76. Y. Cao and T. Mu, *Ind. Eng. Chem. Res.*, **2014**, 53, 8651-8664.
77. M. T. Clough, K. Geyer, P. A. Hunt, J. Mertes and T. Welton, *Phys. Chem. Phys. Chem.*, **2013**, 15, 20480-20495.
78. J. Gonzalez-Rivera, E. Husanu, A. Mero, C. Ferrari, C. Duce, M. R. Tine, F. D'Andrea, C. S. Pomelli and L. Guazzelli, *J. Mol. Liq.*, **2020**, 300, 112357.
79. W. Chen, Z. Xue, J. Wang, J. Jiang, X. Zhao and T. Mu, *Acta Phys. Chim. Sin.*, **2018**, 34, 904-911.
80. N. Rodriguez Rodriguez, A. van den Bruinhorst, L. J. Kollau, M. C. Kroon and K. Binnemans, *ACS Sustain. Chem. Eng.*, **2019**, 7, 11521-11528.
81. Z.-B. Zhou, H. Matsumoto and K. Tatsumi, *Chem. Lett.*, **2004**, 33, 1636-1637.
82. Z. B. Zhou, H. Matsumoto and K. Tatsumi, *Chem. Eur. J.*, **2006**, 12, 2196-2212.
83. H. Wang, J. Wang and S. Zhang, *J. Chem. Eng. Data*, **2012**, 57, 1939-1944.
84. K. Shahbaz, F. Mjalli, M. Hashim and I. AlNashef, *Thermochim. Acta*, **2011**, 515, 67-72.
85. K. A. Omar and R. Sadeghi, *J. Mol. Liq.*, **2022**, 119524.
86. P. Bonhote, A.-P. Dias, N. Papageorgiou, K. Kalyanasundaram and M. Grätzel, *Inorg. Chem.*, **1996**, 35, 1168-1178.
87. G. Yu, D. Zhao, L. Wen, S. Yang and X. Chen, *AIChE Journal*, **2012**, 58, 2885-2899.
88. K. Padaszynski and U. Domanska, *J. Chem. Inf. Model.*, **2014**, 54, 1311-1324.
89. K. Tochigi and H. Yamamoto, *J. Phys. Chem. C*, **2007**, 111, 15989-15994.
90. L. C. Branco, J. N. Rosa, J. J. Moura Ramos and C. A. Afonso, *Chem. Eur. J.*, **2002**, 8, 3671-3677.

91. A. Bakhtyari, R. Haghbakhsh, A. R. C. Duarte and S. Raeissi, *Fluid Phase Equilib.*, **2020**, 521, 112662.
92. F. S. Mjalli and J. Naser, *ASIA-PAC J CHEM ENG*, **2015**, 10, 273-281.
93. A. Fröba, M. Rausch, K. Krzeminski, D. Assenbaum, P. Wasserscheid and A. Leipertz, *Int. J. Thermophys.*, **2010**, 31, 2059-2077.
94. T. L. Greaves, A. Weerawardena, C. Fong, I. Krodkiewska and C. J. Drummond, *J. Phys. Chem. B*, **2006**, 110, 22479-22487.
95. D. R. Macfarlane, P. Meakin, J. Sun, N. Amini and M. Forsyth, *J. Phys. Chem. B*, **1999**, 103, 4164-4170.
96. R. K. Gautam and D. Seth, *J. Therm. Anal.*, **2020**, 140, 2633-2640.
97. H.-Z. SU, J.-M. YIN, Q.-S. LIU and C.-P. LI, *Acta Physico-Chimica Sinica*, **2015**, 31, 1468-1473.
98. A. M. O'Mahony, D. S. Silvester, L. Aldous, C. Hardacre and R. G. Compton, *J. Chem. Eng. Data*, **2008**, 53, 2884-2891.
99. Q. Li, J. Jiang, G. Li, W. Zhao, X. Zhao and T. Mu, *Sci China Chem.*, **2016**, 59, 571-577.
100. C. Reichardt, *Chem. Rev.*, **1994**, 94, 2319-2358.
101. C. Reichardt, *Green Chem.*, **2005**, 7, 339-351.
102. M. A. Ab Rani, A. Brant, L. Crowhurst, A. Dolan, M. Lui, N. H. Hassan, J. Hallett, P. Hunt, H. Niedermeyer and J. Perez-Arlandis, *Phys. Chem. Phys. Chem.*, **2011**, 13, 16831-16840.
103. S. Zhang, X. Qi, X. Ma, L. Lu and Y. Deng, *J. Phys. Chem. B*, **2010**, 114, 3912-3920.
104. C. Ruß and B. König, *Green Chem.*, **2012**, 14, 2969-2982.
105. A. Pandey, R. Rai, M. Pal and S. Pandey, *Phys. Chem. Phys. Chem.*, **2014**, 16, 1559-1568.
106. J. Płotka-Wasyłka, M. De la Guardia, V. Andruch and M. Vilková, *Microchem. J.*, **2020**, 159, 105539.
107. Y. Dai, J. Van Spronsen, G.-J. Witkamp, R. Verpoorte and Y. H. Choi, *J. Nat. Prod.*, **2013**, 76, 2162-2173.
108. H. Zhang, X. Lu, L. González-Aguilera, M. L. Ferrer, F. Del Monte and M. C. Gutiérrez, *J. Chem. Phys.*, **2021**, 154, 184501.
109. A. Romero, A. Santos, J. Tojo and A. Rodríguez, *J. Hazard. Mater.*, **2008**, **151**, 268-273.
110. A. S. Wells and V. T. Coombe, *Org. Process Res. Dev.*, **2006**, 10, 794-798.

111. T. Torimoto, T. Tsuda, K. i. Okazaki and S. Kuwabata, *Adv. Mater.*, **2010**, 22, 1196-1221.
112. M. Armand, F. Endres, D. R. MacFarlane, H. Ohno and B. Scrosati, *Nat. Mater.*, **2009**, 8, 621-629.
113. T. Itoh and Y.-M. Koo, *Application of Ionic Liquids in Biotechnology*, Springer, **2019**.
114. Y. P. Mbous, M. Hayyan, A. Hayyan, W. F. Wong, M. A. Hashim and C. Y. Looi, *Biotechnol. Adv.*, **2017**, 35, 105-134.
115. J. Wu, Q. Liang, X. Yu, Q. F. Lü, L. Ma, X. Qin, G. Chen and B. Li, *Adv. Funct. Mater.*, **2021**, 31, 2011102.
116. F. Shi, Y. Gu, Q. Zhang and Y. Deng, *Catal. Surv. from Asia*, **2004**, 8, 179-186.
117. J. L. Shamshina, P. S. Barber and R. D. Rogers, *Expert Opin. Drug. Discov.*, **2013**, 10, 1367-1381.
118. S. Emami and A. Shayanfar, *Pharm. Dev. Technol.*, **2020**, 25, 779-796.
119. Q. Zeng, Y. Wang, Y. Huang, X. Ding, J. Chen and K. Xu, *Analyst*, **2014**, 139, 2565-2573.
120. L. Feng, H. Meng, Y. Lu and C. Li, *Sep. Purif. Technol.*, **2022**, 281, 119994.
121. M. Hasib-ur-Rahman, M. Siaj and F. Larachi, *Chem. Eng. Process*, **2010**, 49, 313-322.
122. M. Watanabe, M. L. Thomas, S. Zhang, K. Ueno, T. Yasuda and K. Dokko, *Chem. Rev.*, **2017**, 117, 7190-7239.
123. D. R. MacFarlane, N. Tachikawa, M. Forsyth, J. M. Pringle, P. C. Howlett, G. D. Elliott, J. H. Davis, M. Watanabe, P. Simon and C. A. Angell, *Energy Environ. Sci.* **2014**, 7, 232-250.
124. K. M. Jeong, M. S. Lee, M. W. Nam, J. Zhao, Y. Jin, D.-K. Lee, S. W. Kwon, J. H. Jeong and J. Lee, *J. Chromatogr. A*, **2015**, 1424, 10-17.
125. I. Juneidi, M. Hayyan and M. A. Hashim, *Process Biochem.*, **2018**, 66, 33-60.
126. D. D. Patel and J. M. Lee, *Chem. Rec.*, **2012**, 12, 329-355.
127. H. Zhao and S. V. Malhotra, **2002**.
128. K.-S. Kim, N. D. Demberelnyamba, S.-W. Yeon, S. Choi, J.-H. Cha and H. Lee, *Korean J. Chem. Eng.*, **2005**, 22, 717-720.
129. K. Richter, P. S. Campbell, T. Baecker, A. Schimitzek, D. Yaprak and A. V. Mudring, *Phys. Status Solidi B*, **2013**, 250, 1152-1164.
130. H. G. Liao, Y. X. Jiang, Z. Y. Zhou, S. P. Chen and S. G. Sun, *Angew. Chem. Int. Ed.*, **2008**, 47, 9100-9103.

131. M. Chirea, A. Freitas, B. S. Vasile, C. Ghitulica, C. M. Pereira and F. Silva, *Langmuir*, **2011**, 27, 3906-3913.
132. J.-Y. Dong, Y.-J. Hsu, D. S.-H. Wong and S.-Y. Lu, *J. Phys. Chem. C*, **2010**, 114, 8867-8872.
133. P. Halli, J. Hamuyuni, H. Revitzer and M. Lundström, *J. Clean. Prod.*, **2017**, 164, 265-276.
134. Y. Wang, X. Liu, A. Yang, P. Lv, L. Zhang, Y. Li and Y. Yang, *J. Mol. Liq.*, **2022**, 353, 118846.
135. A. E. Visser, R. P. Swatloski, W. M. Reichert, R. Mayton, S. Sheff, A. Wierzbicki, J. H. Davis and R. D. Rogers, *Environ. Sci. Technol.*, **2002**, 36, 2523-2529.
136. E. D. Bates, R. D. Mayton, I. Ntai and J. H. Davis, *J. Am. Chem. Soc.*, **2002**, 124, 926-927.
137. A. Zhu, T. Jiang, B. Han, J. Zhang, Y. Xie and X. Ma, *Green Chem.*, **2007**, 9, 169-172.
138. D. Yang, M. Hou, H. Ning, J. Zhang, J. Ma, G. Yang and B. Han, *Green Chem.*, **2013**, 15, 2261-2265.
139. J.-H. Shin, W. A. Henderson and S. Passerini, *Electrochem. solid-state lett.*, **2005**, 8, A125.
140. P. Wang and S. Zakeeruddin, *Chem. Commun*, **2002**, 2972-2973.
141. A. Noda, M. A. B. H. Susan, K. Kudo, S. Mitsushima, K. Hayamizu and M. Watanabe, *J. Phys. Chem. B*, **2003**, 107, 4024-4033.
142. H.-R. Jhong, D. S.-H. Wong, C.-C. Wan, Y.-Y. Wang and T.-C. Wei, *Electrochem. Comm.*, **2009**, 11, 209-211.
143. X. Wu, H. Zhang, S. He, Q. Yu, Y. Lu, W. Wu, N. Ding, Q. Zhu, Z. Chen and Y. Ma, *Int. J. Biol. Macromol.*, **2020**, 150, 528-535.
144. A. Banerjee, K. Ibsen, T. Brown, R. Chen, C. Agatemor and S. Mitragotri, *PNAS*, **2018**, 115, 7296-7301.
145. J. K. Lee and M.-J. Kim, *J. Org. Chem.*, **2002**, 67, 6845-6847.
146. J. T. Gorke, F. Srienc and R. J. Kazlauskas, *ChemComm.*, **2008**, 1235-1237.
147. W. A. Henderson, P. Fylstra, C. Hugh, P. C. Trulove and S. Parsons, *Phys. Chem. Phys. Chem.*, **2012**, 14, 16041-16046.
148. E. Bodo, S. Mangialardo, F. Ramondo, F. Ceccacci and P. Postorino, *J. Phys. Chem. B*, **2012**, 116, 13878-13888.
149. H.-o. Hamaguchi, S. Saha, R. Ozawa and S. Hayashi, ACS Publications, **2005**.

150. S. Laschat, A. Baro, N. Steinke, F. Giesselmann, C. Hägele, G. Scalia, R. Judele, E. Kapatsina, S. Sauer and A. Schreivogel, *Angew. Chem. Int. Ed.*, **2007**, 46, 4832-4887.
151. C. Tschierske, *Prog. Polym. Sci.*, **1996**, 21, 775-852.
152. A. Bradley, C. Hardacre, J. Holbrey, S. Johnston, S. McMath and M. Nieuwenhuyzen, *Chem. Mater.*, **2002**, 14, 629-635.
153. A. G. Avent, P. A. Chaloner, M. P. Day, K. R. Seddon and T. Welton, *J. Chem. Soc., Dalton Trans.*, **1994**, 3405-3413.
154. M. A. Gebbie, M. Valtiner, X. Banquy, E. T. Fox, W. A. Henderson and J. N. Israelachvili, *PNAS*, **2013**, 110, 9674-9679.
155. R. Bini, O. Bortolini, C. Chiappe, D. Pieraccini and T. Siciliano, *J. Phys. Chem. B*, **2007**, 111, 598-604.
156. D. Wakeham, A. Nelson, G. G. Warr and R. Atkin, *Phys. Chem. Phys. Chem.*, **2011**, 13, 20828-20835.
157. D. Wakeham, P. Niga, C. Ridings, G. Andersson, A. Nelson, G. G. Warr, S. Baldelli, M. W. Rutland and R. Atkin, *Phys. Chem. Phys. Chem.*, **2012**, 14, 5106-5114.
158. T. L. Greaves, D. F. Kennedy, S. T. Mudie and C. J. Drummond, *J. Phys. Chem. B*, **2010**, 114, 10022-10031.
159. C. J. Margulis\*, *Mol. Phys.*, **2004**, 102, 829-838.
160. S. Schrödle, G. Annat, D. R. MacFarlane, M. Forsyth, R. Buchner and G. Hefter, *ChemComm.*, **2006**, 1748-1750.
161. Y. Dai, G.-J. Witkamp, R. Verpoorte and Y. H. Choi, *Food chem.*, **2015**, 187, 14-19.
162. Y. Dai, J. van Spronsen, G.-J. Witkamp, R. Verpoorte and Y. H. Choi, *Anal. Chim. Acta*, **2013**, 766, 61-68.
163. C. D'Agostino, R. C. Harris, A. P. Abbott, L. F. Gladden and M. D. Mantle, *Phys. Chem. Phys. Chem.*, **2011**, 13, 21383-21391.
164. C. D'Agostino, L. F. Gladden, M. D. Mantle, A. P. Abbott, I. A. Essa, A. Y. Al-Murshedi and R. C. Harris, *Phys. Chem. Phys. Chem.*, **2015**, 17, 15297-15304.
165. A. Pandey and S. Pandey, *J. Phys. Chem. B*, **2014**, 118, 14652-14661.
166. D. V. Wagle, G. A. Baker and E. Mamontov, *J. Phys. Chem. Lett.*, **2015**, 6, 2924-2928.
167. O. S. Hammond, D. T. Bowron and K. J. Edler, *Green Chem.*, **2016**, 18, 2736-2744.
168. P. K. Mandal, M. Sarkar and A. Samanta, *J. Phys. Chem. A*, **2004**, 108, 9048-9053.
169. Z. Hu and C. J. Margulis, *PNAS*, **2006**, 103, 831-836.
170. H. Jin, X. Li and M. Maroncelli, *J. Phys. Chem. B*, **2007**, 111, 13473-13478.

171. A. Adhikari, K. Sahu, S. Dey, S. Ghosh, U. Mandal and K. Bhattacharyya, *J. Phys. Chem. B*, **2007**, 111, 12809-12816.
172. Z. P. Zheng, W. H. Fan, S. Roy, K. Mazur, A. Nazet, R. Buchner, M. Bonn and J. Hunger, *Angew. Chem. Int. Ed.*, **2015**, 54, 687-690.
173. B. Guchhait, H. Al Rasid Gazi, H. K. Kashyap and R. Biswas, *J. Phys. Chem. B*, 2010, 114, 5066-5081.
174. B. Guchhait, S. Daschakraborty and R. Biswas, *J. Chem. Phys.*, **2012**, 136, 174503.
175. A. Das and R. Biswas, *J. Phys. Chem. B*, **2015**, 119, 10102-10113.
176. T. Pal and R. Biswas, *Chem. Phys. Lett.*, **2011**, 517, 180-185.
177. A. Das, S. Das and R. Biswas, *J. Chem. Phys.*, **2015**, 142, 034505.
178. K. Mukherjee, S. Das, E. Tarif, A. Barman and R. Biswas, *J. Chem. Phys.*, **2018**, 149, 124501.
179. E. Tarif, J. Mondal and R. Biswas, *J. Phys. Chem. B*, **2019**, 123, 9378-9387.
180. N. Subba, P. Sahu, N. Das and P. Sen, *J. Chem. Sci.*, **2021**, 133, 1-10.
181. N. Das and P. Sen, *Phys. Chem. Phys. Chem.*, **2021**, 23, 15749-15757.
182. N. Subba, N. Das and P. Sen, *J. Phys. Chem. B*, **2020**, 124, 6875-6884.
183. N. Subba, E. Tarif, P. Sen and R. Biswas, *J. Phys. Chem. B*, **2020**, 124, 1995-2005.
184. N. Subba, K. Polok, P. Piatkowski, B. Ratajska-Gadomska, R. Biswas, W. Gadomski and P. Sen, *J. Phys. Chem. B*, **2019**, 123, 9212-9221.
185. S. S. Hossain and A. Samanta, *J. Phys. Chem. B*, **2017**, 121, 10556-10565.
186. S. S. Hossain and A. Samanta, *Phys. Chem. Phys. Chem.*, **2018**, 20, 24613-24622.
187. S. S. Hossain, S. Paul and A. Samanta, *J. Phys. Chem. B*, **2020**, 124, 2473-2481.
188. Y. Cui, J. C. Rushing, S. Seifert, N. M. Bedford and D. G. Kuroda, *J. Phys. Chem. B*, **2019**, 123, 3984-3993.
189. S. Kaur, A. Gupta and H. K. Kashyap, *J. Phys. Chem. B*, **2016**, 120, 6712-6720.
190. L. Percevault, A. Jani, T. Sohler, L. Noirez, L. Paquin, F. Gauffre and D. Morineau, *J. Phys. Chem. B*, **2020**, 124, 9126-9135.
191. J. B. Birks, **1970**.
192. J. R. Lakowicz and J. R. Lakowicz, *Principles of fluorescence spectroscopy*, **1999**, 445-486.
193. J. R. Lakowicz, *Principles of fluorescence spectroscopy*, Springer, 2006.
194. B. Valeur and G. Weber, *Chem. Phys. Lett.*, **1977**, 45, 140-144.
195. G. Weber and M. Shinitzky, *PNAS*, **1970**, 65, 823-830.

196. P. K. Mandal, A. Paul and A. Samanta, *J. Photochem. Photobiol. A*, **2006**, 182, 113-120.
197. B. Bagchi and B. Jana, *Chem. Soc. Rev.*, **2010**, 39, 1936-1954.
198. M. Maroncelli and G. R. Fleming, *J. Chem. Phys.*, **1987**, 86, 6221-6239.
199. H. Jin, G. A. Baker, S. Arzhantsev, J. Dong and M. Maroncelli, *J. Phys. Chem. B*, **2007**, 111, 7291-7302.
200. R. Jimenez, G. R. Fleming, P. Kumar and M. Maroncelli, *Nature*, **1994**, 369, 471-473.
201. P. K. Chowdhury, M. Halder, L. Sanders, T. Calhoun, J. L. Anderson, D. Armstrong, X. Song and J. Petrich, *J. Phys. Chem. B*, **2004**, 108, 10245-10255.
202. M. Horng, J. Gardecki, A. Papazyan and M. Maroncelli, *J. Phys. Chem.*, **1995**, 99, 17311-17337.
203. J. Ingram, R. Moog, N. Ito, R. Biswas and M. Maroncelli, *J. Phys. Chem. B*, **2003**, 107, 5926-5932.
204. N. Ito, S. Arzhantsev, M. Heitz and M. Maroncelli, *J. Phys. Chem. B*, **2004**, 108, 5771-5777.
205. N. Ito, S. Arzhantsev and M. Maroncelli, *Chem. Phys. Lett.*, **2004**, 396, 83-91.
206. R. Karmakar and A. Samanta, *J. Phys. Chem. A*, **2002**, 106, 4447-4452.
207. R. Karmakar and A. Samanta, *J. Phys. Chem. A*, **2003**, 107, 7340-7346.
208. H. K. Kashyap and R. Biswas, *J. Phys. Chem. B*, **2008**, 112, 12431-12438.
209. H. K. Kashyap and R. Biswas, *J. Phys. Chem. B*, **2010**, 114, 254-268.
210. M. N. Kobrak, *J. Chem. Phys.*, **2006**, 125, 064502.
211. M. N. Kobrak, *J. Chem. Phys.*, **2007**, 127, 184507.
212. M. N. Kobrak and V. Znamenskiy, *Chem. Phys. Lett.*, **2004**, 395, 127-132.
213. A. Samanta, *J. Phys. Chem. B*, **2006**, 110, 13704-13716.
214. A. Samanta, *J. Phys. Chem. Lett.*, **2010**, 1, 1557-1562.
215. S. Sarkar, R. Pramanik, C. Ghatak, P. Setua and N. Sarkar, *J. Phys. Chem. B*, **2010**, 114, 2779-2789.
216. D. Seth, S. Sarkar and N. Sarkar, *J. Phys. Chem. B*, **2008**, 112, 2629-2636.
217. X.-X. Zhang, M. Liang, N. P. Ernsting and M. Maroncelli, *J. Phys. Chem. B*, 2013, 117, 4291-4304.
218. X.-X. Zhang, M. Liang, N. P. Ernsting and M. Maroncelli, *J. Phys. Chem. Lett.*, **2013**, 4, 1205-1210.
219. V. Znamenskiy and M. N. Kobrak, *J. Phys. Chem. B*, **2004**, 108, 1072-1079.
220. K. Bhattacharyya, *ChemComm.*, **2008**, 2848-2857.

221. R. Fee and M. Maroncelli, *Chem. Phys.*, **1994**, 183, 235-247.
222. Y. Shim, J. Duan, M. Choi and H. J. Kim, *J. Chem. Phys.*, **2003**, 119, 6411-6414.
223. Y. Shim, M. Choi and H. J. Kim, *J. Chem. Phys.*, **2005**, 122, 044511.
224. A. H. Turner and D. Kim, *J. Chem. Phys.*, **2018**, 149, 174503.
225. B. Valeur and M. N. Berberan-Santos, *Molecular fluorescence: principles and applications*, John Wiley & Sons, **2012**.
226. G. Dutt, *ChemPhysChem*, **2005**, 6, 413-418.
227. G. Dutt, *J. Phys. Chem. B*, **2010**, 114, 8971-8977.
228. G. Dutt and S. Raman, *J. Chem. Phys.*, **2001**, 114, 6702-6713.
229. V. Gangamallaiyah and G. Dutt, *J. Phys. Chem. B*, **2012**, 116, 12819-12825.
230. L. Karve and G. Dutt, *J. Phys. Chem. B*, **2011**, 115, 725-729.
231. K. Mali, G. Dutt and T. Mukherjee, *J. Chem. Phys.*, **2005**, 123, 174504.
232. C. M. Hu and R. Zwanzig, *J. Chem. Phys.*, **1974**, 60, 4354-4357.
233. K. Fruchey and M. Fayer, *J. Phys. Chem. B*, **2010**, 114, 2840-2845.
234. A. Gierer and K. Wirtz, *Zeitschrift für Naturforschung A*, **1953**, 8, 532-538.
235. J. L. Dote, D. Kivelson and R. N. Schwartz, *J. Phys. Chem.*, **1981**, 85, 2169-2180.
236. K. G. Spears and L. E. Cramer, *Chem. Phys.*, **1978**, 30, 1-8.
237. T. W. Nee and R. Zwanzig, *J. Chem. Phys.*, **1970**, 52, 6353-6363.
238. R. Biswas and B. Bagchi, *J. Chem. Phys.*, **1997**, 106, 5587-5598.
239. P. Kumar Sahu, A. Ghosh and M. Sarkar, *J. Phys. Chem. B*, **2015**, 119, 14221-14235.
240. S. K. Das, P. K. Sahu and M. Sarkar, *J. Phys. Chem. B*, **2013**, 117, 636-647.
241. D. Majhi, S. Seth and M. Sarkar, *Phys. Chem. Phys. Chem.*, **2018**, 20, 7844-7856.
242. S. S. Hossain, S. Paul and A. Samanta, *J. Phys. Chem. B*, **2019**, 123, 6842-6850.
243. J. H. Werner, S. N. Baker and G. A. Baker, *Analyst*, **2003**, 128, 786-789.
244. D. K. Sasmal, A. K. Mandal, T. Mondal and K. Bhattacharyya, *J. Phys. Chem. B*, **2011**, 115, 7781-7787.
245. J. Guo, G. A. Baker, P. C. Hillesheim, S. Dai, R. W. Shaw and S. M. Mahurin, *Phys. Chem. Phys. Chem.*, **2011**, 13, 12395-12398.
246. S. Patra and A. Samanta, *J. Phys. Chem. B*, **2012**, 116, 12275-12283.
247. K. Damodaran, *Annu. Rep. NMR Spectrosc.*, **2016**, 88, 215-244.
248. N. Dias, K. Shimizu, P. Morgado, E. J. Filipe, J. N. Canongia Lopes and F. n. Vaca Chávez, *J. Phys. Chem. B*, **2014**, 118, 5772-5780.
249. D. Kruk, R. Meier, A. Rachocki, A. Korpała, R. Singh and E. Rössler, *J. Chem. Phys.*, **2014**, 140, 244509.

250. T.-Y. Wu, S.-G. Su, K.-F. Lin, Y.-C. Lin, H. P. Wang, M.-W. Lin, S.-T. Gung and I.-W. Sun, *Electrochimica acta*, **2011**, 56, 7278-7287.
251. A. M. o. de Ferro, P. M. Reis, A. A. Freitas, J. N. Canongia Lopes, L. P. N. Rebelo, K. Shimizu and J. M. Esperança, *J. Chem. Eng. Data*, **2019**, 64, 4932-4945.
252. K. Rohatgi-Mukherjee, *Fundamentals of photochemistry*, New Age International, **1978**.
253. D. O'Connor, *Time-correlated single photon counting*, Academic press, **2012**.
254. E. P. Farr, J. C. Quintana, V. Reynoso, J. D. Ruberry, W. R. Shin and K. R. Swartz, *J. Chem. Edu.*, **2018**, 95, 864-871.
255. W. Becker, *Advanced time-correlated single photon counting techniques*, Springer Science & Business Media, **2005**.
256. D. Magde, E. Elson and W. W. Webb, *Phys. Rev. Lett.*, **1972**, 29, 705.
257. E. L. Elson, *Biophysical journal*, **2011**, 101, 2855-2870.
258. R. Rigler and E. S. Elson, *Fluorescence correlation spectroscopy: theory and applications*, Springer Science & Business Media, **2012**.
259. P. R. Bevington and D. K. Robinson, *McGraw-Hill, New York*, **2003**.
260. A. McKinnon, A. Szabo and D. Miller, *J. Phys. Chem.*, **1977**, 81, 1564-1570.
261. D. O'Connor, W. Ware and J. Andre, *J. Phys. Chem.*, **1979**, 83, 1333-1343.
262. E. C. Wu, H. J. Kim and L. A. Peteanu, *The J. Phys. Chem. B*, **2017**, 121, 1100-1107.
263. S. Sen Mojumdar, R. Chowdhury, S. Chattoraj and K. Bhattacharyya, *J. Phys. Chem. B*, **2012**, 116, 12189-12198.
264. E. O. Stejskal and J. E. Tanner, *J. Chem. Phys.*, **1965**, 42, 288-292.
265. J. M. Klein, H. Squire, W. Dean and B. E. Gurkan, *J. Phys. Chem. B*, **2020**, 124, 6348-6357.
266. P. K. Mandal and A. Samanta, *J. Phys. Chem. B*, **2005**, 109, 15172-15177.
267. A. Kawai, T. Hidemori and K. Shibuya, *Chem. Lett.*, **2004**, 33, 1464-1465.
268. Y. Akdogan, J. Heller, H. Zimmermann and D. Hinderberger, *Phys. Chem. Phys. Chem.*, **2010**, 12, 7874-7882.
269. B. Y. Mladenova, D. R. Kattnig and G. n. Grampp, *J. Phys. Chem. B*, **2011**, 115, 8183-8198.
270. C. Reichardt, *Angew. Chem. Int. Ed. in English*, **1979**, 18, 98-110.
271. A. P. Demchenko, *J. Lumin.*, **2002**, 17, 19-42.
272. R. S. Dhale, P. K. Sahu and M. Sarker, *J. Phys. Chem. B*, **2017**, 121, 7934-7945.
273. S. Das, R. Biswas and B. Mukherjee, *J. Phys. Chem. B*, **2015**, 119, 274-283.

274. K. Mali, G. Dutt and T. Mukherjee, *J. Chem. Phys.*, **2008**, 128, 054504.
275. A. Triolo, M. E. Di Pietro, A. Mele, F. Lo Celso, M. Brehm, V. Di Lisio, A. Martinelli, P. Chater and O. Russina, *J. Chem. Phys.*, **2021**, 154, 244501.
276. S. R. Prabhu and G. Dutt, *J. Phys. Chem. B*, **2014**, 118, 13244-13251.
277. J. T. Edward, *J. chem. edu.*, **1970**, 47, 261.
278. A. Knorr, K. Fumino, A.-M. Bansa and R. Ludwig, *Phys. Chem. Phys. Chem.*, **2015**, 17, 30978-30982.
279. M. Yoshizawa-Fujita, Y. Kousa, K. Kidena, A. Ohira, Y. Takeoka and M. Rikukawa, *Phys. Chem. Phys. Chem.*, **2011**, 13, 13427-13432.
280. S. K. Das, D. Majhi, P. K. Sahu and M. Sarkar, *ChemPhysChem*, **2017**, 18, 198-207.
281. A. Paul and A. Samanta, *J. Phys. Chem. B*, **2007**, 111, 4724-4731.
282. S. Barik, M. Chakraborty and M. Sarkar, *J. Phys. Chem. B*, **2020**, 124, 2864-2878.
283. Y. Kimura, A. Kobayashi, M. Demizu and M. Terazima, *Chem. Phys. Lett.*, **2011**, 513, 53-58.
284. S. Barik, M. Chakraborty, A. Mahapatra and M. Sarkar, *Phys. Chem. Phys. Chem.*, **2022**, 24, 7093-7106.
285. P. J. Carlson, S. Bose, D. W. Armstrong, T. Hawkins, M. S. Gordon and J. W. Petrich, *J. Phys. Chem. B*, **2012**, 116, 503-512.
286. Y. Cui, K. Fulfer, J. Ma, T. Weldeghiorghis and D. Kuroda, *Phys. Chem. Phys. Chem.*, **2016**, 18, 31471-31479.
287. D. Reuter, P. Münzner, C. Gainaru, P. Lunkenheimer, A. Loidl and R. Böhmer, *J. Chem. Phys.*, **2021**, 154, 154501.
288. E. W. Castner Jr, J. F. Wishart and H. Shirota, *Acc. Chem. Res.*, **2007**, 40, 1217-1227.
289. H. Weingärtner, *Angew. Chem. Int. Ed.*, **2008**, 47, 654-670.
290. G. Cui, C. Wang, J. Zheng, Y. Guo, X. Luo and H. Li, *ChemComm.*, **2012**, 48, 2633-2635.
291. P. Wasserscheid and T. Welton, *Ionic liquids in synthesis*, Wiley Online Library, **2008**.
292. S. K. Panja, B. Haddad, M. Debdab, J. Kiefer, Y. Chaker, S. Bresson and A. Paolone, *ChemPhysChem*, **2019**, 20, 936-940.
293. S. Palchowdhury and B. Bhargava, *J. Phys. Chem. B*, **2015**, 119, 11815-11824.
294. F. S. Menges, H. J. Zeng, P. J. Kelleher, O. Gorlova, M. A. Johnson, T. Niemann, A. Strate and R. Ludwig, *J. Phys. Chem. Lett.*, **2018**, 9, 2979-2984.
295. J. Neumann, D. Paschek, A. Strate and R. Ludwig, *J. Phys. Chem. B*, **2020**, 125, 281-286.

296. T. Niemann, J. Neumann, P. Stange, S. Gärtner, T. G. Youngs, D. Paschek, G. G. Warr, R. Atkin and R. Ludwig, *Angew. Chem. Int. Ed.*, **2019**, 58, 12887-12892.
297. T. Niemann, D. Zaitsau, A. Strate, A. Villinger and R. Ludwig, *Sci. Rep.*, **2018**, 8, 1-7.
298. C. A. Nkuku and R. J. LeSuer, *J. Phys. Chem. B*, **2007**, 111, 13271-13277.
299. A. Boisset, S. Menne, J. Jacquemin, A. Balducci and M. Anouti, *Phys. Chem. Phys. Chem.*, **2013**, 15, 20054-20063.
300. D. Dhingra, Bhawna, A. Pandey and S. Pandey, *J. Phys. Chem. B*, **2019**, 123, 3103-3111.
301. T. Mendez-Morales, J. Carrete, O. Cabeza, O. Russina, A. Triolo, L. J. Gallego and L. M. Varela, *J. Phys. Chem. B*, **2014**, 118, 761-770.
302. S. R. Prabhu and G. Dutt, *J. Phys. Chem. B*, **2015**, 119, 6311-6316.
303. C. Lawler and M. D. Fayer, *J. Phys. Chem. B*, **2013**, 117, 9768-9774.
304. R. Younesi, G. M. Veith, P. Johansson, K. Edström and T. Vegge, *Energy Environ. Sci.* **2015**, 8, 1905-1922.
305. M. C. Deller, L. Kong and B. Rupp, *Acta Crystallogr. F: Struct. Biol. Commun.*, **2016**, 72, 72-95.
306. T. W. Johannes and H. Zhao, *Curr. Opin. Microbiol.*, **2006**, 9, 261-267.
307. S. Rahuel-Clermont, R. Bchini, S. Barbe, S. Boutserin, I. André and F. Talfournier, *ACS Catalysis*, **2019**, 9, 1337-1346.
308. J. M. Woodley, *Trends Biotechnol.*, **2008**, 26, 321-327.
309. D. Kumar Das, A. Kumar Das, A. Kumar Mandal, T. Mondal and K. Bhattacharyya, *ChemPhysChem*, **2012**, 13, 1949-1955.
310. T. Singh, P. Bharmoria, M.-a. Morikawa, N. Kimizuka and A. Kumar, *J. Phys. Chem. B*, **2012**, 116, 11924-11935.
311. U. K. Singh and R. Patel, *Mol. Pharm.*, **2018**, 15, 2684-2697.
312. A. Pabbathi, S. Ghosh and A. Samanta, *J. Phys. Chem. B*, **2013**, 117, 16587-16593.
313. H. Arora, D. Dhiman, K. Kumar and P. Venkatesu, *Phys. Chem. Phys. Chem.*, **2022**, 24, 29683-29692.
314. K. Bhakuni, N. Yadav and P. Venkatesu, *Phys. Chem. Phys. Chem.*, **2020**, 22, 24410-24422.
315. R. Esquembre, J. M. Sanz, J. G. Wall, F. del Monte, C. R. Mateo and M. L. Ferrer, *Phys. Chem. Phys. Chem.*, **2013**, 15, 11248-11256.
316. S. S. Hossain, S. Paul and A. Samanta, *J. Phys. Chem. B*, **2021**, 125, 5757-5765.

317. Z. L. Huang, B. P. Wu, Q. Wen, T. X. Yang and Z. Yang, *J. Chem. Technol. Biotechnol.*, **2014**, 89, 1975-1981.
318. D. Mondal, M. Sharma, C. Mukesh, V. Gupta and K. Prasad, *ChemComm.*, **2013**, 49, 9606-9608.
319. H. Monhemi, M. R. Housaindokht, A. A. Moosavi-Movahedi and M. R. Bozorgmehr, *Phys. Chem. Phys. Chem.*, **2014**, 16, 14882-14893.
320. A. A. Papadopoulou, E. Efstathiadou, M. Patila, A. C. Polydera and H. Stamatis, *Ind. Eng. Chem. Res.*, **2016**, 55, 5145-5151.
321. A. Sanchez-Fernandez, K. Edler, T. Arnold, D. A. Venero and A. Jackson, *Phys. Chem. Phys. Chem.*, **2017**, 19, 8667-8670.
322. N. Yadav, K. Bhakuni, M. Bisht, I. Bahadur and P. Venkatesu, *ACS Sustain. Chem. Eng.*, **2020**, 8, 10151-10160.
323. H. Zhao, *J. Chem. Technol. Biotechnol.*, **2015**, 90, 19-25.
324. M. Kumari, P. Kumari and H. K. Kashyap, *Phys. Chem. Phys. Chem.*, **2022**, 24, 5627-5637.
325. J. Parnica and M. Antalík, *J. Mol. Liq.*, **2014**, 197, 23-26.
326. Y. Shu, M. Liu, S. Chen, X. Chen and J. Wang, *J. Phys. Chem. B*, **2011**, 115, 12306-12314.
327. G. Hungerford, J. Benesch, J. F. Mano and R. L. Reis, *Photochem. Photobiol. Sci.*, **2007**, 6, 152-158.
328. C. Wischke and H.-H. Borchert, *Pharmazie* ., **2006**, 61, 770-774.
329. A. Basaiahgari, S. Panda and R. L. Gardas, *J. Chem. Eng. Data*, **2018**, 63, 2613-2627.
330. R. Kumaran and P. Ramamurthy, *J. Lumin.*, **2014**, 148, 277-284.
331. C. A. Royer, C. J. Mann and C. R. Matthews, *Protein Science*, **1993**, 2, 1844-1852.
332. J. Steinhardt, J. Krijn and J. G. Leidy, *Biochem.*, **1971**, 10, 4005-4015.
333. M. M. Islam, S. Barik, N. Preeyanka and M. Sarkar, *J. Phys. Chem. B*, **2020**, 124, 961-973.
334. M. M. Islam, S. Barik and M. Sarkar, *J. Phys. Chem. B*, **2019**, 123, 1512-1526.
335. P. Pierre, N. Ennaji and N. Françoise, **2014**.
336. K. A. Connors, *Binding constants: the measurement of molecular complex stability*, Wiley-Interscience, **1987**.
337. E. L. Gelamo and M. Tabak, *Spectrochim. Acta A Mol. Biomol. Spectrosc.*, **2000**, 56, 2255-2271.

338. M. Kumari, J. K. Maurya, M. Tasleem, P. Singh and R. Patel, *J. Photochem. Photobiol. B, Biol.*, **2014**, 138, 27-35.
339. D. Leckband, *Annu. Rev. Biophys. Biomol. Struct.*, **2000**, 29, 1-26.
340. P. D. Ross and S. Subramanian, *Biochem.*, **1981**, 20, 3096-3102.
341. K. Chattopadhyay, S. Saffarian, E. L. Elson and C. Frieden, *Biophys. J.*, **2005**, 88, 1413-1422.
342. K. Chattopadhyay, S. Saffarian, E. L. Elson and C. Frieden, *PNAS*, **2002**, 99, 14171-14176.
343. E. Y. Chi, S. Krishnan, T. W. Randolph and J. F. Carpenter, *Pharm. res.*, **2003**, 20, 1325-1336.
344. M. Silow, Y.-J. Tan, A. R. Fersht and M. Oliveberg, *Biochem.*, **1999**, 38, 13006-13012.
345. A. Pabbathi, S. Patra and A. Samanta, *ChemPhysChem*, **2013**, 14, 2441-2449.
346. E. Sherman, A. Itkin, Y. Y. Kuttner, E. Rhoades, D. Amir, E. Haas and G. Haran, *Biophys. J.*, **2008**, 94, 4819-4827.
347. J. Kuchlyan, N. Kundu, D. Banik, A. Roy and N. Sarkar, *Langmuir*, **2015**, 31, 13793-13801.
348. S. M. Supratik, C. Rajdeep, C. Shyamtanu and B. Kankan, 2012.
349. R. Yadav, B. Sengupta and P. Sen, *J. Phys. Chem. B*, **2014**, 118, 5428-5438.
350. D. K. Wilkins, S. B. Grimshaw, V. Receveur, C. M. Dobson, J. A. Jones and L. J. Smith, *Biochem.*, **1999**, 38, 16424-16431.
351. M. ud din Parray, S. Y. AlOmar, A. Alkhuriji, F. A. Wani, Z. A. Parray and R. Patel, *Colloids Surf. A: Physicochem. Eng. Asp.*, **2021**, 610, 125737.
352. B. Pradhan, C. Engelhard, S. Van Mulken, X. Miao, G. W. Canters and M. Orrit, *Chem. Sci.*, 2020, **11**, 763-771.
353. A. Gupta, T. J. Aartsma and G. W. Canters, *J. Am. Chem. Soc.*, **2014**, 136, 2707-2710.
354. Y.-H. Chen, J. T. Yang and H. M. Martinez, *Biochem.*, **1972**, 11, 4120-4131.
355. P. Huang, A. Dong and W. S. Caughey, *J. Pharm. Sci.*, **1995**, 84, 387-392.
356. E. A. Meyer, R. K. Castellano and F. Diederich, *Angew. Chem. Int. Ed.*, **2003**, 42, 1210-1250.